Development and characterization of a colloidal fluorescent ZIF derivative acting as a bio-label for immunoassays

Dissertation

zur Erlangung des akademischen Grades

doctor rerum naturalium

(Dr. rer. nat.)

im Fach: Chemie

Spezialisierung: Anorganische und Allgemeine Chemie

eingereicht an der

Mathematisch-Naturwissenschaftlichen Fakultät der Humboldt-Universität zu Berlin

Von

M.Sc. Ander Chapartegui Arias

Präsidentin der Humboldt-Universität zu Berlin

Prof. Dr.-Ing. Dr. Sabine Kunst

Dekan der Mathematisch-Naturwissenschaftlichen Fakultät

Prof. Dr. Elmar Kulke

Gutachter

Prof. Dr. Rüdiger Tiemann; Dr. Franziska Emmerling; Dr. Rudolf Schneider; Prof. Dr. Klaus Rademann; Prof. Dr. Thomas Braun; Dr. Sebastian Beyer

Tag der Verteidigung

30. September 2021

Abstract

Improvements in bioanalytical technologies are driven by evolving threats and challenges to the global community, like emerging diseases, the need for substance screening and increasing environmental pollution. On-site quick and simple analytical methodologies are key to adapt to threatening situations in time. Immunoanalytical methodologies, like Lateral Flow Immunoassays (LFIA), are one key group of analytical methodologies that has shown success when it comes to quick, reliable, and easy-to-use detection. However, some samples present difficulties to be detected with the traditional immunoanalytical tools. The bottleneck for detecting very small amounts of any given analyte in immunoanalysis-based systems can predominantly be due to the inability to develop an antibody capable of targeting an analyte of interest. Another factor affecting the use of immunoassays is the reduced sensitivity of the signalling label. Classical luminescent labels are rarely employed in LFIA systems. This is due to their relatively small improvement of sensitivity and their high price. Therefore, there is a need to develop new, cost-efficient colloids that will increase the signal intensity and/or improve the interaction with the sample, allowing a lowering of the detection limits in LFIA systems significantly.

On this context, this work explores a new bioanalytical concept that employs nanosized Zeolite Imidazolate Frameworks (ZIFs) particles as labels for antibody-based analytical methods, including enzyme-linked immunosorbent assay (ELISA) and lateral flow immunoassay (LFIA). The advantage of ZIFs as labels over established materials is their versatile, facile, and cheap synthesis. This includes the ability to encapsulate low molecular weight substances for additional sensing purposes and for stable conjugation to biomacromolecules for high selectivity. As a model target analyte of relevance Phthalate acyl esters (PAEs) have been selected. The relevance of the detection of PAEs is due to their properties as endocrine disrupting chemicals (EDCs) and carcinogenic. Combined with PAEs being abundant on the environment because of their use as plasticizers in plastic-made tableware for children, toys, drinking bottles and other polyvinylchloride-based products, shows the importance or their routine detection of drinking water or foods being so critical.

To use ZIFs as bio-label, a methodology to include a fluorescent functionality on its crystal structure was developed. The approach comprises covalently attaching 1-aminopyrene to the framework of a ZIF. This is achieved by forming an imine between aminopyrene and 2-imidazolecarboxaldehyde. The methodology was also tuned to obtain nanoscale colloidal particles of the system by using different modulating agents during the precipitation technique. The fluorescent properties of the modified ZIF were studied via fluorescence spectroscopy, and their use as optical sensing platforms against PAEs was stablished. The feasibility of a novel bioanalytical concept that employs this colloidal ZIF particles as bio-labels for immunoassay was subsequently explored. For this, a strategy for covalently linking antibodies to form stable, colloidal ZIFs conjugates is developed. The formation of the bond was proven by LC/MS-MS quantification of the fragments of the digested conjugate. The proof of principle for their use in ELISA and LFIA, preserving their mobility and the antibodies' affinity and selectivity is presented.

Abstrakt

Verbesserungen der bioanalytischen Technologien werden durch die sich entwickelnden Bedrohungen und Herausforderungen für die globale Gemeinschaft vorangetrieben, wie z. B. neu auftretende Krankheiten, die Notwendigkeit des Substanz-Screenings und die zunehmende Umweltverschmutzung. Schnelle und einfache Analysemethoden vor Ort sind der Schlüssel zur rechtzeitigen Anpassung an bedrohliche Situationen. Immunoanalytische Methoden, wie z. B. Lateral Flow Immunoassays (LFIA), sind eine wichtige Gruppe von analytischen Methoden, die sich als schnell, zuverlässig und einfach zu handhabend erwiesen haben. Einige Proben lassen sich jedoch nur schwer mit den herkömmlichen immunanalytischen Werkzeugen nachweisen. Der Engpass für den Nachweis sehr kleiner Mengen eines bestimmten Analyten in immunoanalytischen Systemen kann in erster Linie auf die Unfähigkeit zurückzuführen sein, einen Antikörper zu entwickeln, der in der Lage ist, einen interessierenden Analyten zu erfassen. Ein weiterer Faktor, der den Einsatz von Immunoassays beeinträchtigt, ist die geringere Empfindlichkeit der Signalmarkierung. Klassische Lumineszenzmarker werden in LFIA-Systemen nur selten eingesetzt. Dies ist auf ihre relativ geringe Verbesserung der Empfindlichkeit und ihren hohen Preis zurückzuführen. Daher besteht die Notwendigkeit, neue, kosteneffiziente Kolloide zu entwickeln, die die Signalintensität erhöhen und/oder die Wechselwirkung mit der Probe verbessern, wodurch die Nachweisgrenzen in LFIA-Systemen deutlich gesenkt werden können.

Vor diesem Hintergrund wird in dieser Arbeit ein neues bioanalytisches Konzept untersucht, das nanoskalige Zeolith-Imidazolat-Frameworks (ZIFs) als Marker für antikörperbasierte Analysemethoden einsetzt, einschließlich Enzyme-Linked-Immunosorbent-Assay (ELISA) und Lateral Flow Immunoassay (LFIA). Der Vorteil von ZIFs als Marker gegenüber etablierten Materialien ist ihre vielseitige, einfache und kostengünstige Synthese. Dazu gehört die Möglichkeit, niedermolekulare Substanzen für zusätzliche Sensorzwecke zu verkapseln und für eine hohe Selektivität stabil an Biomakromoleküle zu konjugieren. Als modellhafter Zielanalyt von Relevanz wurden Phthalat-Acylester (PAEs) ausgewählt. Die Relevanz des Nachweises von PAEs ergibt sich aus ihren Eigenschaften als endokrin wirksame Chemikalien (EDCs) und krebserregend. In Kombination mit der Tatsache, dass PAEs aufgrund ihrer Verwendung als Weichmacher in Kindergeschirr, Spielzeug, Trinkflaschen und anderen Produkten auf Polyvinylchlorid-Basis in der Umwelt reichlich vorhanden sind, zeigt, wie wichtig der routinemäßige Nachweis von PAEs in Trinkwasser oder Lebensmitteln ist.

Um ZIFs als Bio-Label zu verwenden, wurde eine Methode entwickelt, um eine fluoreszierende Funktionalität in ihre Kristallstruktur einzubauen. Der Ansatz umfasst die kovalente Anlagerung von 1-Aminopyren an das Gerüst eines ZIFs. Dies wird durch die Bildung eines Imins zwischen Aminopyren und 2-Imidazolcarboxaldehyd erreicht. Die Methodik wurde auch abgestimmt, um nanoskalige kolloidale Partikel des Systems zu erhalten, indem verschiedene Modulationsmittel während der Fällungstechnik verwendet wurden. Die fluoreszierenden Eigenschaften der modifizierten ZIF wurden mittels Fluoreszenzspektroskopie untersucht und ihre Verwendung als optische Sensorplattformen gegen PAEs wurde etabliert. Anschließend wurde die Machbarkeit eines neuartigen bioanalytischen Konzepts untersucht, das diese kolloidalen ZIF-Partikel als Bio-Labels für Immunoassays einsetzt. Hierfür wurde eine Strategie zur kovalenten Bindung von Antikörpern zu stabilen, kolloidalen ZIFs-Konjugaten entwickelt. Die Bildung der Bindung wurde durch LC/MS-MS-Quantifizierung der Fragmente des verdauten Konjugats nachgewiesen. Der Grundsatzbeweis für die Verwendung in ELISA und LFIA unter Beibehaltung der Mobilität sowie der Affinität und Selektivität der Antikörper wird vorgestellt.

Abbreviations

1-AP	1-Aminopyrene
2-mim	2-Methylimidazolate
DMP	Dimethyl phthalate
DBP	Dibutyl phthalate
DBB	Benzyl butyl Phthalate
DEHP	Diethyl hexyl phthalate
DMSO	Dimethylsulphoxide
EDS	Energy-dispersive x-ray spectroscopy
ELISA	Enzyme-Linked ImmunoSorbent Assay
FTIR	Fourier-transform infrared spectroscopy
HPLC	High-performance liquid chromatography
HRP	Horseradish peroxidase
i2ca	Imidazol-2-carboxaldehyde
ICP-OES	Inductively coupled plasma atomic emission spectroscopy
IgG	Immunoglobulin type G
MeONa	Sodium methoxide
Na_2HPO_4	Disodium hydrogen phosphate
$NaBH_3CN$	Sodium cyanoborohydride
NaH_2PO_4	Sodium phosphate monobasic
OD	Optical density
PBS (buffer)	Phosphate-buffered saline solution
PFA	Perfluoroalkoxy alkane
PVDF	Polyvinylidene fluoride
PXRD	Powder x-ray diffractometry
Sheep IgG	Immunoglobulin type G from sheep
S-TEM	Scanning transmission electron microscopy
TEM	Transmission electron microscopy
TMB	3,3',5,5'-tetramethylbenzidine
TRIS (buffer)	tris(hydroxymethyl)aminomethane
Z8P	Pyrene-modified ZIF-8/ZIF-90 hybrid
Z8P–IgG	Z8P IgG antibody conjugate
Z90–IgG	ZIF-90 IgG antibody conjugate
Z90P	Pyrene-modified ZIF-8/ZIF-90 hybrid
RT	Retention time
a.u.	Arbitrary Units

Table of Contents

1. Introduction

The use of Phthalate Acyl Esters (phthalic acid esters, PAEs) as plasticizers has led to their widespread presence on the environment. PAEs are widely present on the environment due to them being part of plastics. Plastic garbage in oceans and soil releases PAEs to the water and the ground, which can lead to eventual poisoning of the human population. The quick and easy detection of PAEs in samples such as drinking waters or soil is therefore of significant relevance. Literature research has shown gaps in the easy and in-situ detection of short chained PAEs. These gaps are due, in part, to the absence of antibodies that are capable of interacting with the more hydrophobic members of the PAEs, DEHP (Di-2-ethylhexyl phthalate), BBP (Benzyl butyl phthalate), DBP (Dibutyl phthalate) and DMP (Dimethyl phthalate). Not having antibodies available to detect PAEs inhibits the development of a portable detection methodology base in immunoassays.

Taking advantage of this hydrophobicity of the PAEs, the possibility of developing a new system capable of detecting PAEs was plausible. This new system is based on Zeolite Imidazolate Frameworks (ZIFs), a sub-family of Metal-Organic Frameworks (MOFs). ZIFs are formed by imidazolates as organic building blocks, and the chemical and physical properties of ZIFs can be tuned by selecting the right imidazolate organic ligand. ZIF-8, formed by 2-methyl imidazole, and ZIF-90, formed by imidazole 2-carboxaldehyde, were selected as the parent structures to develop a new ZIF. ZIF-8 brings an extend body of work that is already presented on the literature, that demonstrates how to tune particle size and shape. ZIF-90 brings the presence of the aldehyde functionality on its constituting imidazole moiety, a key aspect of the post-synthetic functionalization of the ZIF. This aldehyde functionalization is also key to introduce a fluorescence functionality on the ZIF, fluorescent element that is capable of detecting and quantifying the presence of PAEs. Furthermore, this ZIF systems can be made compatible with immunoassays, something already presented on the current literature, but not yet optimized. For this, a colloidal ZIF system is proposed and successfully prepared. The colloidal nature of the ZIF particles is necessary to maximize the interaction of the ZIF with the antibodies, while maximizing the mobility of the system in solution. An additional key advantage of using this new ZIF is that it links covalently with antibodies, stabilizing the conjugate even further. This covalent linkage can be achieved thanks to the aldehyde functionalities that are part of the ZIF particles.

Another gap that was found in the literature was the accurate and easy quantification of multicomponent MOFs. The new colloidal ZIF that was developed includes more than one organic ligand in its crystal structure. To fully understand the properties of the system, specifically the fluorescence response and the particle size and shape, an accurate quantification of the new ZIF was necessary. The quantification of multicomponent MOFs in the literature is rarely presented, but where it is done, it is often mentioned with little significance. To fill in this gap, the use of HPLC as a routine analytical technique is proposed, presenting a new HPLC methodology to quantify ZIF composition. The extensive use of HPLC as a routine analytical technique is used to obtain accurate chemical composition of the organic ligands forming the presented modified ZIFs. By simultaneous use of HPLC, PXRD and TEM for the synthesised ZIFs, important insight on how the fluorescent functionality is part of the system, as well as how it affects the ZIF formation, is gained.

Finally, a methodology for the formation of a stable ZIF-antibody conjugate is explored, as well as the potential of ZIFs as bio-compatible materials. The conjugation methodology for the formation

of a stable a ZIF-antibody conjugate is based on the formation of an amine bond between the amino functionality of the antibody and the aldehyde functionality of the ZIF, and the formation of a stable covalent linkage is demonstrated. The potential of ZIFs as compatible biomaterials is shown in a variety of analytical and diagnostic applications such as ELISA and LFIA. The combination of the activity and selectivity of antibodies with the versatility of structure and composition of ZIFS (chemical reactivity, capture of biological species, a porous carrier, etc) on a final system that is stable and mobile in dispersion has been presented. Moreover, the colloidal nature of the ZIF-antibody conjugate is explored via NTA (Nanoparticle Tracking Analysis) and the long-term stability is assessed by PXRD.

2. Literature review

2.1. Phthalates and endocrine disruptors

Phthalate esters are esters of phthalic acid (1,2-Benzenedicarboxylic acid) with various alcohols (phthalic acid esters, PAEs). They are a group of chemicals used mainly as plasticisers (substances added to a material to make it softer and more flexible, to increase its plasticity, decrease its viscosity, or decrease friction during its handling in manufacture) for plastics. Their addition is required to give the inherently hard and brittle plastic polyvinyl chloride (PVC) elastic properties and allows it to be used as a soft plastic. They are used, for example, in cables, films, floor coverings, hoses, wallpaper, and sports and leisure articles. This leads the chemical industry to produce about one million tons of phthalates in Western Europe every year[1].

Plastic garbage in oceans and soil releases PAEs, since they are not chemically attached to the polymer chains of the plastic, leaving the polymer through migration, evaporation or extraction by liquids[2]. This loss is problematic, since it leads to eventual contamination of the surrounding medium[3-10], and to ingestion by the human population[11]. The presence of this PAEs in the environment is a big issue, since many plasticizers have been identified as hazardous for human health and development; specifically, in this work, short chained phthalates (SC-PAE) are targeted (Figure 1). Increased level of phthalates is associated with severe consequences in the developmental biology of children, decreased fertility, increased risk of diabetes and increased malignancy of cancer in adults[12]. They are also endocrine disrupting chemicals (EDCs)[13], substances that disturb the hormonal balance in complex biological life forms[14].

Even though the use of phthalates in industry is more restricted, especially in Europe, were the ECHA (European Chemicals Agency) included them in the list of chemicals that require authorization for their production and use[15]. Despite the production of short-chained phthalates decreases each year, the presence of phthalates in soils and waters continues to pose problems since they decompose slowly[16]. Thus, the development of analytical methodologies to determine the presence and concentration of phthalates in environmental samples is more relevant than ever.

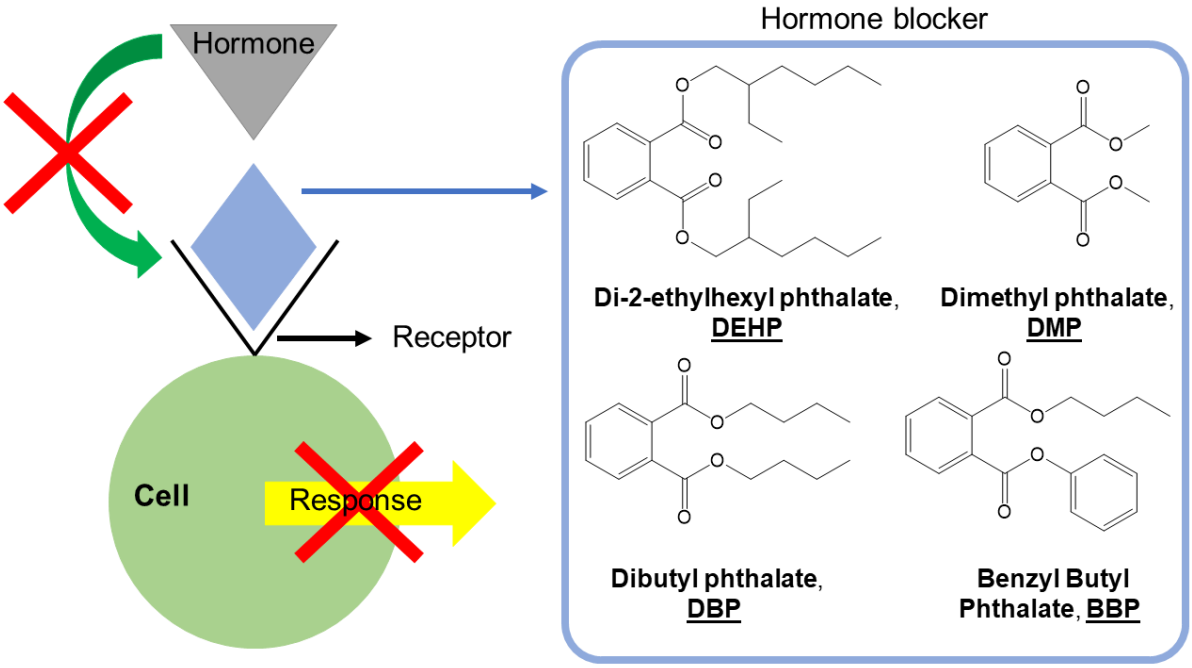

Figure 1 Scheme representing the anti-androgen endocrine disrupting activity of the short-chained phthalates (SC-PAEs); these chemical species can irreversibly block the androgen receptor on the cell membranes. The four SC-PAEs of interest are also shown.

Currently, the standard methodologies to test for the presence of phthalates in a given sample require sophisticated analytical methods, e.g. techniques such as liquid chromatography coupled to mass spectrometry[17]. This technology is immobile, restricting the routine on-site monitoring of the presence of phthalates to ensure consumer safety. The availability of a sensor capable of measuring on-site, without the requirement of specialized personnel implies a big advantage for safety, quality control and would have considerable economic impact. While specific antibodies could be generated for short-chained phthalates (dibutyl phthalate, DBP[18-20]; dimethyl phthalate, DMP[21]), it was not the case for the much more important, long-chained phthalates (diethyl hexyl phthalate or bis(2-ethylhexyl) phthalate, DEHP; benzyl butyl phthalate, BBP) or their substitutes, such as diisononyl 1,2-cyclohexanedicarboxylic acid, DINCH[22], due to the phthalates non-polar nature, their hydrophobicity increasing with chain length. Because there are limited on site measurement possibilities the development of alternative sensing technologies is important. Therefore, there is a need to develop new, cost-efficient methodologies that will increase the signal intensity and/or improve the interaction with the sample, allowing the development of an in-situ detection methodology. In this context the use of zeolitic imidazolate frameworks (ZIFs) is taken on this work.

2.2. Metal-Organic Frameworks (MOFs)

Metal-organic frameworks (MOFs)[23] are a class of compounds consisting of metal ions or metallic clusters coordinated to organic ligands to form one-, two-, or three-dimensional crystalline structures[24] (Figure 2). Since their discovery[25], MOFs have been widely studied and many applications have been developed[24], from their use as extracting subtracts of analytes from environmentally relevant samples[26], their capacity as catalysts[27], as part of fuel-cell and metal-air batteries[28], and even as drug delivery materials[29], to name a few. A key aspect of MOFs is their porous nature, and in some of MOFs, the pores are stable during elimination of the guest molecules (often solvents) and could be refilled with other compounds. This porosity causes MOFs to be of interest for applications on which traditionally porous materials, such as aluminosilicate zeolites[30] or perovskites[31] are desirable.

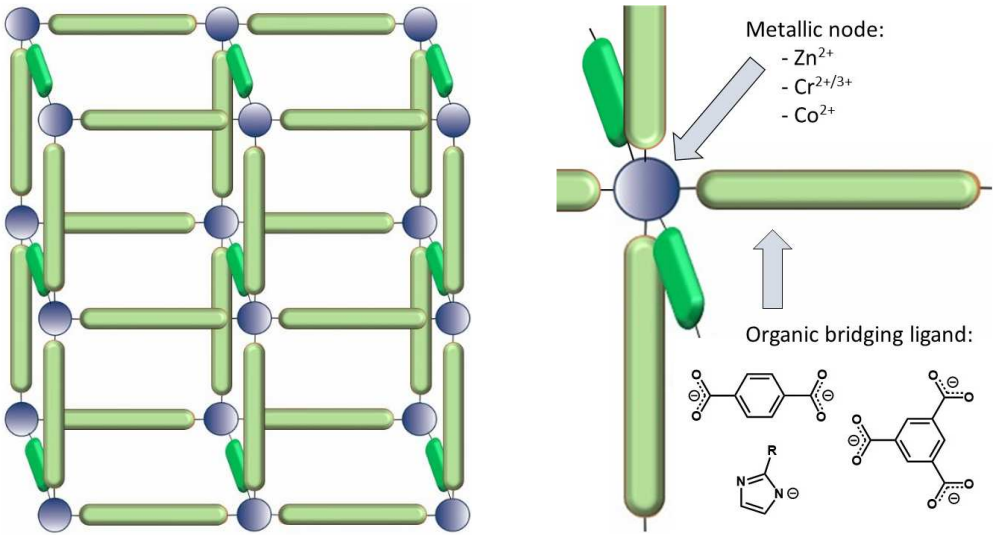

Figure 2 Simple representation of a MOF structure. The violet spheres represent the metalic nodes, and the green bars represent the organic bridging ligands.

The synthesis of MOFs is achieved by borrowing concepts from metal carboxylate cluster chemistry[32], were metal-carboxylate clusters act as secondary building units (SBU) for the assembly of extended open frameworks. This applicability is expanded even further considering the variability of metal node and functionality of organic linker that formed them[33]. Owing to the richness of the MOF composition, many of their properties can be tuned by modifying the chemical composition or structure of their metallic and organic constituents[34-36]. As such, MOFs are very versatile. Also, many chemical species can be trapped inside of the pores of the structures[37], expanding even further their versatility. The number of MOFs is quite extensive and is ever-growing. Amongst the most well-known and used MOFs in literature some highlight are MOF-5[24, 38-41], MIL-100[42-44], UiO-66[45-48] and ZIFs.

MOF architecture can be tuned by using a variety of organic bridging ligands, forming multicomponent MOFs[35, 49-52]. For example, Yaghi *et al.*,[53] demonstrated that up to eight benzene dicarboxylic acid (BDC) ligands with different chemical functional groups can be simultaneously incorporated into the MOF-5 framework, creating a multi-component MOF. Multi-component MOFs are known to expand the potential of the frameworks[54]. For crystalline MOFs containing just one organic ligand, X-ray diffraction (XRD) suffices to identify the chemical and crystalline composition. Multi-component MOFs require the use of other techniques to have an accurate composition confirmation. A few analytical techniques have been used to explore the chemical composition of MOFs, including Fourier transform infrared spectroscopy (FTIR)[55, 56] and solid state nuclear magnetic resonance (ssNMR)[57, 58] spectroscopy. However, the chemical composition of MOFs is obtained indirectly by both analytical techniques and the analysis become quickly intractable for complex, poorly defined compositions, or for material available at low concentrations. There is, then, a gap for other more suitable quantitative analytical techniques to obtain an accurate composition for those MOFs with several organic ligands or when organic substrates become trapped within the MOF.

2.2.1 Zeolite Imidazolate Frameworks (ZIFs)

Zeolite imidazolate frameworks (ZIFs)[59, 60] are a family of MOFs with a variety of applications[61]. Structurally, ZIFs are comprised of tetrahedral metallic nodes connected through bridging imidazolate anions[62] (Figure 3). ZIFs are grown from imidazolate tetrahedra constructed by the coordination between metallic cations and imidazolate anions[62], where imidazole and imidazole derivative units constitute the bridges for connecting the metal centres. The structural properties of ZIFs make them excellent materials for next generation technologies, like surface and/or pore tunability[59, 60]. They are attractive due to their high porosity, excellent mechanical stability, tuneable surface properties, and their exceptional chemical and thermal stabilities[60]. ZIFs are exceptionally easy to synthesize through precipitation reactions from aqueous and organic solvents[63]. The pore size and the adsorption properties of ZIFs can be tailored by changing or chemically modifying the anionic imidazolate linker[64]. ZIFs share a similar crystal structure with aluminosilicate zeolites, since the crystal structure of some of the most relevant MOFs is consistent with the sodalite crystal structure for zeolites[65].

The intrinsic properties of ZIFs have led to their use in a broad range of applications including sensing[66], catalysis[67] and extraction[68], to name a few. This last example as extraction materials is critical to choose ZIF-8 as a base for hydrophobic analytes of interest, since the hydrophobic nature of the pore of the ZIF has the potential to preconcentrate these analytes in solution, potentially increasing its sensitivity. However, unlike aluminosilicate zeolites, MOFs count with very high sorption capacities and complex sorption behaviour not seen in aluminosilicate zeolites, giving them an additional edge, edge that is even further exacerbated when the chemical function ability intrinsic to the MOFs comes into play[35-37].

ZIFs can be synthesized through precipitation reactions from aqueous and organic solvents[63], as well as mechanochemically[69]. Their particle size can be tuned during the synthetic process[70], key

since the size of the particles plays a determining role influencing the mobility of the system[71]. From all the ZIF members, ZIF-8, formed by using zinc coordinated to 2-methylimidazole (2mim)[59, 60], shows the most extensive research. ZIF-90 is isostructural with ZIF-8, but it includes an available aldehyde functionality that allows the crystal to be part of chemical reactions, and for ZIF-90 is imidazole-2-carboxaldehyde (i2ca)[55, 72, 73], opening the window to create modified ZIFs with a pursued functionality of interest. Moreover, the hydrophobicity or hydrophilicity of ZIFs can also be tuned[74] by varying the bridging imidazole species, which in turn can improve the interaction for the ZIF particles with organic species.

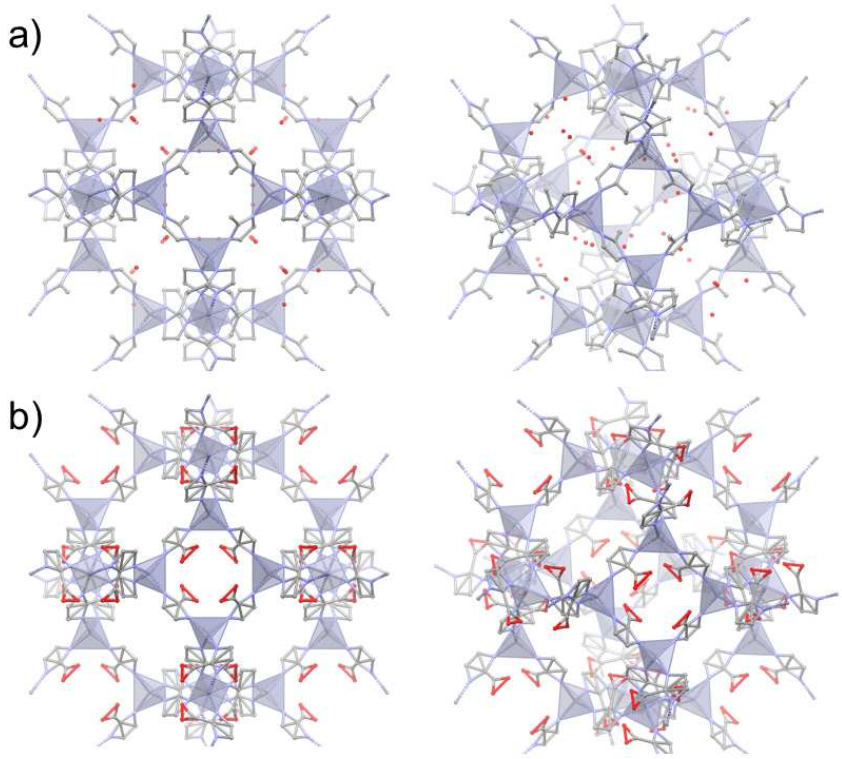

Figure 3 Crystal structure of ZIF-8 (a) and ZIF-90 (b). with the same LTA topology as zeolite A. The centre of the tetrahedra contains the Zn^{2+} atoms, oxygen atoms are represented in red, nitrogen atoms in blue and carbon in gray. The oxigen atoms in the ZIF-90 structure appear double because of the crystallographic disorder; there are two possitions that are equivalent, thus they are resolved as one.

The use of ZIFs as a platform for sensing has been growing the last years[75]. There are two main ways ZIFs are used as sensors. As electrochemical sensors, ZIFs have shown successes detecting gases, commonly as hybrid materials[76, 77], combining high sensitivity and selectivity of carbon nanotubes with the thermal and physic-chemical stability of ZIFs. The ZIF is used to enhance or modify a property of the second material, like an In_2O_3 and ZIF-8 heterostructures designed as efficient sensing materials for NO_2 detection[77]. The material shows a remarkably high response to 1 ppm NO_2 and high humidity resistance due to the hydrophobicity of ZIF-8 in comparison with those of the pristine In_2O_3 NF sensor. This is an interesting approach to take to detect small organic molecules, since it presents a potential high selectivity and sensitivity. However, sample

preparation for PAEs should also be heavily optimized, since it presents itself and complex and dangerous. There are some examples of the use of ZIF within hybrid materials, like the synthesis of MOFs around metal oxide particles as electrochemical sensors in solution, for example. An electrochemiluminescence immunosensor for the detection of cardiac troponin I (cardiac regulatory protein) was developed by using zeolitic imidazolate frameworks, with encapsulated spherical graphite crystals as luminophore[78]. As luminescent sensors ZIFs have been used as a base structure on which fluorophores have been captured. Abuzalat *et. al.*[79] synthesized a fluorescent metal–organic framework for the highly selective and sensitive detection of nitroaromatic explosives. ZIF-8 was synthesized and enhanced with the fluorescent 8-hydroxyquinoline zinc. The synthesized material shows visible colour changes upon exposure to TNT from ivory to light red. Zhang et.al.[80] reported a luminescent chemo sensors for detecting antibiotics in water, based on ZIF-8) loaded with rhodamine B and fluorescein disodium salt as dyes. These examples show that modifying a ZIF to develop a fluorescent response is not as complicated as creating a hybrid material for electro sensing.

Lastly, in the context of biochemical, miniaturized assays, is critical that the ingredients behave as "quasi-solutions", i.e, colloidal dispersions. Particulate systems like colloidal solutions are best for these applications to obtain highly reproducible results (high precision, small standard deviations). So, an understanding of the ZIF formation mechanisms is key for developing a system compatible in immunoassays.

2.2.2 MOF formation mechanism

Particle formation in solution is governed by two elementary processes[81], nucleation[82, 83] and particle growth[84]. Nucleation in solution is a phase transition, generating a new phase (like a solid crystal) from a parent phase (chemical species in solution), phase change driven by a reduction on the free energy from a transition from a high free energy phase to an organized structure or pattern with a lower free energy. The original model to explain this is known as Classical Nucleation Theory (CNT). On this model nucleation, defined simply as the first random formation of a distinct thermodynamic new phase that has the ability to irreversibly grow into larger sized nucleus within the body of a metastable parent phase, is the first step in the spontaneous formation of a new thermodynamic phase or a new structure, starting from a state of metastability. The time to nucleate can vary by orders of magnitude, from negligible to exceedingly large, far beyond reach of experimental timescales. One of the key achievements of classical nucleation theory is to explain and quantify this immense variation. CNT is based on kinetic equations that describe the formation of clusters as a step-by-step process with two assumptions: 1) the formation of cluster can be expressed within capillarity approximation, meaning only molecules in close spatial proximity can form nuclei, and 2) the number of molecules available on the initial liquid phase does not change in time. Under these limitations the appropriate analytical solutions of nucleation rate and the number of supercritical sizes can be obtained. This offers analytical approaches easy to use, which is why CNT is widely applied in the analysis of available experimental data. However, in some cases the assumptions are not fulfilled and—as a consequence—the predictions of CNT theory fail.

An example is the relative nucleation rates for fluid bubbles of nanometer dimensions in polymer matrices; this case shows that classical nucleation theory predictions are off by many orders of magnitude. The main cause of the failure of classical nucleation theory can be traced to its representation of a bubble surface as a flat interface. For nanoscopic bubbles, the curvature of the bubble surface is comparable to the size of the polymer molecules.

Nowadays, for many applications and studies, a nonclassical pathway is considered as a dominating mechanism in solution crystallization. This nonclassical approach occurs via an intermediate step previous to nucleation, first explained as Oswald's rule of stages[85], and it states that the system does not go directly to the most stable conformation, but through an intermediate stage with closest free energy to the initial state rather than the final. LaMer model of nanoparticle growth[86] has been used as a primary tool for understanding MOF NP formation. According to this model, the process of nucleation and growth occurs in four successive steps: 1) Rapid increase in the concentration of reactive monomers in solution, 2) Homogeneous nucleation "burst" as the concentration of reactive monomers exceeds the critical nucleation concentration (C_{nuc}), 3) Rapid reduction in the concentration of monomers in solution, halting further nucleation events, 4) Extended crystal growth upon reaching the saturation concentration. The short nucleation period of the LaMer mechanism, which temporally separates crystal nucleation from crystal growth, is critical for the synthesis of uniform NPs. The faster the reagents form the MOF of interest, the more favoured is the formation of MOF nuclei, hence the smaller the particles will end up becoming.

When it comes to the ZIF formation mechanism, only little is known. The most widely accepted model for ZIF formation was originally proposed by Cravillon et al[87] (Figure 4), and has been reinforced with subsequent research[88-92]. It builds upon the LaMer model of crystallization, and explains that the ZIF crystal formation has roughly four main steps: first the zinc-imidazole coordination complexes form, then these complexes oligomerize into nanosized amorphous clusters, these clusters turn to amorphous particles that grow via monomer addition, and finally these systems crystallize and grow, forming the ZIF crystals. The Zn-imidazole intermediate species have been successfully identified by Lim et al. [89], were they describe a systematic approach to synthesize well-defined ZIF-8 crystals at different nucleation rates by adjusting zinc to 2-methylimidazole ratios, and they identify discrete chemical species during ZIF-8 synthesis and trace their transition using ESI-MS, providing evidence of the first step of formation proposed by Cravillon. The change from amorphous to crystalline particles has been also captured experimetnally[88, 93] Terban et al,[88] for example, observed X during the synthesis of ZIF-8 *via* synchrotron X-ray scattering and the atomic pair distribution function (PDF) analysis. They observed that despite rapid formation of the crystalline product, a high concentration of $Zn(2mim)_4$ (2mim = 2-methylimidazolate) initially forms and persists as stable clusters over long times, while a secondary, amorphous phase also pervades during the synthesis, which has a structural similarity to the final ZIF-8 and may act as an intermediate to the final product, providing evidence of the last step proposed by Cravillon. There is also evidence of the workings for the molecular assembly leading to the shift from amorphous polymer to crystalline ZIF, proposed by Cravillon, Moh et al.[92], through atomic force microscopy (AFM), revealed that the growth process for ZIF-8 occurs through the nucleation and spreading of successive metastable unenclosed Zinc imidazolate polymers to eventually form stable crystalline ZIF surface, and that this process is reliant on the

presence of species not yet part of the framework to bridge the developing pores during growth. This gave more support to the ZIF formation model proposed by Cravillon.

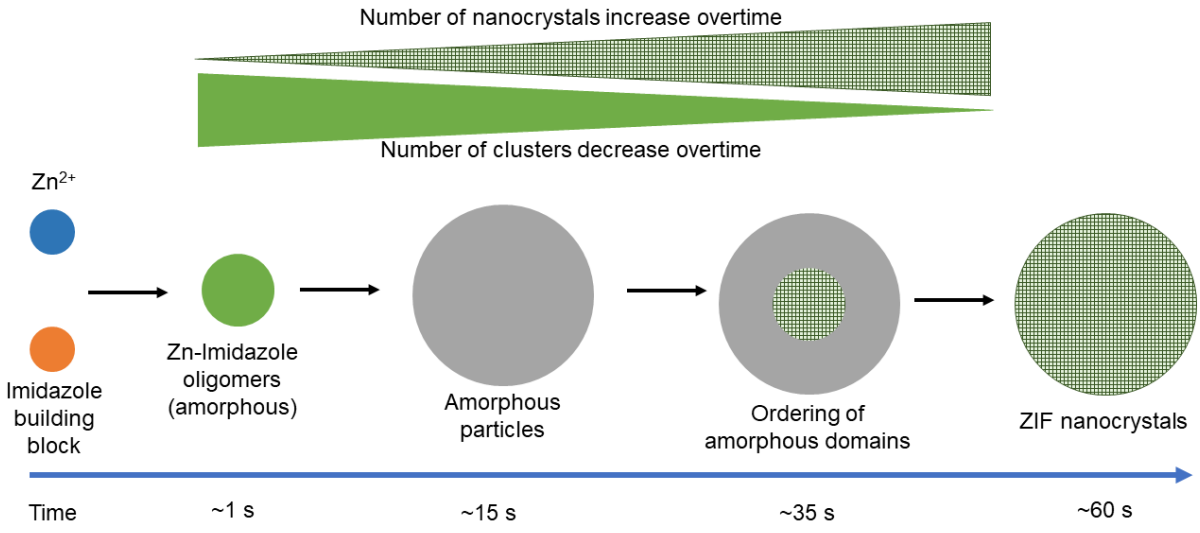

Figure 4 *Basic scheme summarizing the proposed ZIF formation methodology by Cravillon[87].*

This model also provides insight into the formation of ZIF nanoparticles. Cravillon also presented simple methodologies that lead to the wet synthesis of colloidal ZIF-8 dispersions[94]. He observed that, as a general guideline to obtain this colloidal ZIF solutions, the synthetic conditions must work on a way that formation of nanocrystals happens favouring nucleation over crystal growth; this can be achieved by controlling many aspects of the synthetic process:

- Concentrations of all precursors: The first reported methodology to obtain colloidal ZIFs comes from Cravillon et. at[94]. They achieved a colloidal dispersion by adding 2mim (2-methylimidazole) in excess related to the zinc source, with a final $Zn(NO_3)_2 \cdot 6H_2O$, 2mim, and methanol a molar ratio of approximately 1:8:700.Yeung et al. reported that an increase of the reagent concentration, keeping the Zn:2mim ratio constant, led to a decrease in crystallization rate and, ultimately, to larger particles[95]. Their explanation to this phenomenon was to assume that there had been a pre-equilibrium of metastable intermediate clusters with different Zn/2-mim ratios; thus, increasing the concentration would inhibit nucleation by favouring over-coordinated species, generating larger ZIF-8 particles. The ratio in which the species are present during synthesis play a key role on final particle size. Cravillon et al.[94] achieved the first synthesis of colloidal ZIF-8 (45 nm average), by simply stirring a mixture of $Zn(NO_3)_2$ and 2mim in methanol at a molar ratio of $Zn(NO_3)_2$: 2mim : MeOH = 1 : 8 : 1000. Excess ligand proved essential for promoting faster nucleation and stabilizing the initial colloids. Zhang et al.[96] were able to synthesize smaller ZIF-8 particles in methanol by increasing the $Zn(NO_3)_2$: 2mim : MeOH molar ratio, ranging from 1 : 4 : 500 to 1 : 16 : 500; they reported that the average particle size gradually

decreased from 1 mm to 100 nm, but the excess of 2mim resulted in aggregation of the ZIF-8 nanocrystals. Cravillon found a solution to this, by decreasing the ratio between $Zn(NO_3)_2$: 2mim but including modulating agents on the synthesis[70].

- Zinc salt precursor: Schejn et al[97] reported crystal size and morphology of ZIF-8 nanocrystals synthesized with a synthetic methodology that mirrors that of Cravillon in molar ratios, and keeping all conditions constant while changing only the source of zinc. All products were obtained with a sodalite-like crystal phase (SOD) and both particle size and morphology were found to be dependent on the reactivity of the Zn^{+2} salt (reactivity in this context means the dissociative strength of the Zinc salt species, a higher dissociation leading to a higher). Zinc salts like $Zn(acac)_2$,$Zn(NO_3)_2$, $ZnSO_4$ or $Zn(ClO_4)_2$ yield crystals with diameters varying between 50 and 200 nm were obtained; $ZnCl_2$, $Zn(OAc)_2$ or ZnI_2 afforded crystals with sizes varying between ca. 350 and 650 nm; low reactive $ZnBr_2$ salt was found to generate micro sized crystals. This dependency is associated to the dissociative capacity of the zinc salt, as well as the reactivity of the zinc counter-ion in the media.

- Solvent used: Wet synthesis of ZIF-8 is highly dependent on the solvent used. Bustamante et al.[98] showed how different solvents affect crystallinity and crystallite size during the synthesis of ZIF-8.The solvent can exert thermodynamic and kinetic effects in the assembly of MOFs[99]. For ZIF sodalite like structures Park et al.[60] showed that the solvent is critical in directing the formation of the frameworks. Similarly, Tian et al.[100]noted that some organic solvents play a key role as template agents in the synthesis of imidazolates with zeolitic topologies. It is also important to consider that the porous nature of the ZIFs leads to the solvent being frequently trapped within the confines of the pore itself. Depending on the interactions between the solvent and the pore, removing this excess solvent can be difficult. For instance, in the preparation of ZIF-8 in dimethylformamide (DMF) it has been observed that DMF is not easily removed even under aggressive drying conditions[101]; not so for methanol[102], who interacts rather weakly with the ZIF itself.

- Modulating agents (capping agents): The simplest definition of a modulating, or capping, agent is a chemical species that interferes with the growth of particles, affecting their total size and shape. Modulators can act as capping ligands that compete with the organic linker, leading to two possible outcomes: i) reducing the number of nucleation points, leading to increased crystal size; ii) limiting the crystal growth, decreasing the crystal size. Given these opposing effects, the net effect of a modulator depends on its coordination strength to the metal, its concentration, and its basicity (the organic bridging ligands must be deprotonated to be successfully coordinated by the metal). Cravillon et al. evaluated the effects of formate, 1-methylimidazole and n-butylamine as modulators in the synthesis of ZIF-8 in methanol[70]. They observed that in the presence of formate or 1-methylimidazole, monodisperse microcrystals (1-3 mm) were formed, while with n-butylamine the average size was 18 nm. This was attributed to the higher basicity of n-butylamine, which can deprotonate the intermediate Zn:2mim species to accelerate the nucleation rate. On the other hand, formate and 1-methylimidazole, which are less basic, cannot deprotonate the

intermediate, and instead, compete with 2-mim, thus leading to a low nucleation rate and consequently, to larger crystals.

2.2.3 Pyrene as quenchable chromophore

Fluorescence as a phenomenon was first observed and described by Nicolás Monardes[103], a Spanish physician and botanist. Monardes published in 1565 his "*Historia medicinal de las cosas que se traen de nuestras Indias Occidentales*", in which he describes the bluish opalescence of the water infusion from the wood of a small Mexican tree. In 1845 Fredrick W. Herschel[104] described and characterized the phenomena when he discovered that UV light could excite a quinine solution to emit blue light. Sir George G. Stokes[105] further studied this phenomenon, discovering that fluorescence emission from an object comprises a longer wavelength than the UV light that originally excited the object.

Fluorescence occurs when a molecule absorbs light in the visible or ultraviolet range of the spectrum, exciting it from the electronic ground state to an excited state. From there it can return to the ground state by releasing the absorbed energy in the form of heat and by radiation in the visible or near-infrared spectral range. The energy emitted has a lower energy than the one absorbed, which occurs because the molecules transits to an intermediate state of energy between the exited state and the ground state before it emits the absorbed radiation. In addition to the change of electronic structure absorption can also lead to the excitation of vibrational levels, which requires more energy or light of shorter wavelength. In some molecules like benzene, this leads to a distinct pattern (vibrational progression) in the absorption spectrum.

Fluorescence can be detected with very high sensitivity even from single molecules and it is used in a large number of chemical and biochemical applications, including medicine[106, 107], chemical sensors[108-110] and biological detectors[111-113]. The sensitivity of fluorescence-based sensing relies on the fact that the emitted light usually has a longer wavelength (lesser energy radiation) than the intense light used for excitation, which can therefore be easily suppressed by filters or monochromators. This difference between absorption and fluorescence wavelength (maxima) is also known as the Stokes shift. In the case of solution, the vibrational energy is very quickly dissipated by collisions with the solvent and the molecule adopts a new equilibrium configuration before emission takes place, which can lead to fluorescence quenching[114]. A variety of molecular interactions can result in quenching, and there are three main mechanism for quenching to occur: Förster resonance energy transfer (FRET or FET)[115] is a dynamic quenching mechanism because energy transfer occurs while the donor is in the excited state. FRET is based on classical dipole-dipole interactions between the transition dipoles of the donor and acceptor and is extremely dependent on the donor-acceptor distance. It also depends on the donor-acceptor spectral overlap and the relative orientation of the donor and acceptor transition dipole moments; Dexter electron transfer (also known as Dexter exchange or collisional energy transfer, colloquially known as Dexter Energy Transfer)[116] is a short-range phenomenon that falls off exponentially with and depends on a resonant and spatial overlap of the donor and the quencher molecular orbitals. In most

fluorophore–quencher situations, the Förster mechanism is more important than the Dexter mechanism. However, the Dexter mechanism can be dominant between the dye and the solvent especially when hydrogen bonds are formed between them. Excimers (a short-lived homo or heterodimeric molecule formed from two species, at least one of which has a valence shell completely filled with electrons) formed by more than two different species. Often, they are composed of two atoms or molecules that would not bond if both were in the ground state. The lifetime of an excimer is very short, on the order of nanoseconds. Exciplexes provide one dynamic mechanisms by which fluorescence is quenched, and a regular exciplex has some charge-transfer between donor and acceptor.

Fluorescence quenching has been widely studied both as a fundamental phenomenon, and as a source of information about biochemical systems. Fluorescence can occur via both dynamic and static quenching, both requiring molecular spatial proximity between the fluorophore and quencher. In the case of dynamic collisional quenching, the quencher must diffuse to the fluorophore within the lifetime of the excited state. Upon contact, the fluorophore returns to the ground state, without emission of a photon. In general, quenching occurs without any permanent change in the molecules, that is, without a photochemical reaction. In static quenching a complex is formed between the fluorophore and the quencher, and this complex is nonfluorescent. To use fluorescence quenching as a detection methodology requires a mathematical model of molecular contact. The Stern-Volmer equation (equation 1) for collisional fluorescence quenching[117] establishes a functional relationship between quencher concentration and fluorescence intensity loss.

$$\frac{F_0}{F_Q} = (1 + K_D \times Q)$$

Equation 1 Stern-Volmer equation for collisional fluorescence quenching

Were F_0 is the fluorescence intensity for the fluorophore with no quencher in solution, F_Q is the fluorescence intensity for the fluorophore in presence of the concentration Q for the quencher, and "K_D" is the Stern-Volmer quenching constant for the system. This equation assumes collisional quenching to be predominant over static quenching. But that may not be the case for the system; it must be considered that there is also static quenching during the sensing process. If both quenching processes are contributing, then the equation must consider both contributions. This leads to a modified version of Equation X, which includes both static and dynamic quenching (equation 2).

$$\frac{F_0}{F_Q} = (1 + K_D \times Q)(1 + K_S \times Q)$$

Equation 2 Stern-Volmer equation for collisional and static fluorescence quenching

where "K_S" is the association constant of the fluorophore-quencher complex. As a potential exciplexing donor, pyrene is very promising[118, 119]. Pyrene is known for its ability to form excimers with aromatic components[120, 121]. The high quantum yield and long fluorescence lifetime makes

pyrene an ideal candidate for sensing of aromatic molecules. Rochat et al proposed a promising strategy to functionalize the ZIF and make it able to detect the presence of SC-PAEs[122]. In their work a commercially available pyrene-based fluorescence dye (8-hydroxypyrene1,3,6-trisulfonate) was successfully used as a selective molecular probe for the detection of caffeine in aqueous solution. This development has inspired my selection to explore the modification of colloidal ZIFs with the analogue, 1-aminopyrene (1ap)

2.3. Immunoassays

The pursuit of new, selective, and sensitive detection techniques is an active area of research in the analytical sciences. Since the discovery of antibodies in 1890 by Emil von Behring[123], who used them to successfully treat diphtheria in humans, leading to him winning the Noble Price in Medicine in 1901, antibodies have shown a wide array of uses, both therapeutically[124, 125] and analytically. Antibodies offer numerous advantages over other analytical techniques[126-129].

Immunoassays are antibody-based analytical methods for quantitative and qualitative analysis[130] (Figure 5). Based on specific antigen-antibody interactions, immunoassays are used widely for diagnosis, pharmacokinetic studies by drug monitoring, and quality control of commercially available products[131-133]. For these applications, high-specificity antibodies such as polyclonal (a heterogeneous mixture of antibodies against the whole antigen) and monoclonal (a single antibody against one antigenic determinant) antibodies are required. Many such antibodies are available, offering broad design space to tune the analytical method towards virtually any biological or chemical analyte[134]. By using several conjugation and modification techniques, these antibodies can be modified to form an antibody-label conjugate to allow easy tracking in complex mixtures[135, 136].

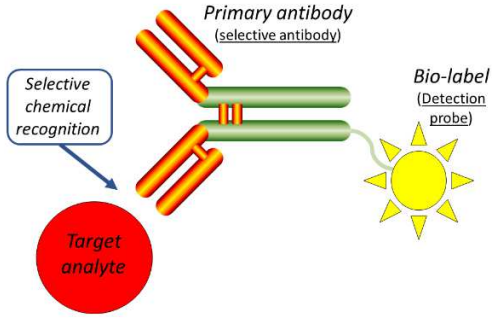

Figure 5 *Basic scheme for the use of an antibody as a detection system.*

The most common uses of antibodies as analytical tools are enzyme-linked immunosorbent assays (ELISA)[137, 138] and lateral flow immunoassay (LFIA)[139]. These assays have found significant applications in many bioanalytical areas, such as diagnosis of diseases, therapeutic drug monitoring, clinical pharmacokinetic and bioequivalence studies in drug discovery and pharmaceutical industries[138, 140, 141].

ELISA has been used as a diagnostic tool in medicine[137, 140], plant pathology[130, 131], and biotechnology[140, 142], as well as a quality control check in various industries[143]. In the simplest form, the targets on the sample to be tested are attached to a surface. Then, a complementary antibody is deposited over the surface so it can bind the target. This antibody is linked to an enzyme and then any unbound antibodies are removed by washing with suitable buffers. In the final step, the enzyme's substrate is added. If there was binding the subsequent reaction produces a detectable signal, most commonly a colour change.

Lateral flow tests, also known as immunochromatographic assays[144] or lateral flow immunoassays (LFIA)[139], are simple devices intended to detect the presence of a target substance in a liquid sample without the need for specialized and costly equipment (Figure 6). These tests are widely used in medical diagnostics for home testing, point of care testing, or laboratory use. The most common example are home pregnancy tests, where a hormone, human chorionic gonadotropin, is targeted. Many lab-based applications increase the sensitivity of simple lateral flow tests by employing additional dedicated equipment. These lateral flow tests operate on the same principles as ELISA, but the liquid sample runs along the surface of a pad with reactive molecules that show a visual positive or negative result. The pads are based on a series of capillary beds, such as pieces of porous paper, microstructure polymer, or sintered polymer. Each of these pads has the capacity to transport fluid (e.g., urine, blood, saliva) spontaneously.

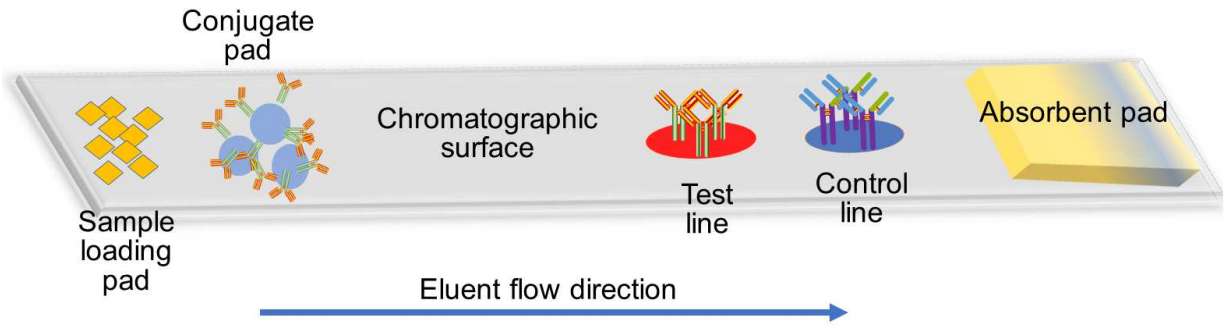

Figure 6 Simple representation of Lateral Flow Immunoassay. A liquid sample containing the analyte of interest moves due to capillary action through various zones of the polymeric strips, on which molecules that can interact with the analyte are attached. The sample is applied at one end of the strip, on the adsorbent sample pad, which is impregnated with buffer salts and surfactants that make the sample suitable for interaction with the detection system. The sample pad ensures that the analyte present in the sample will be capable of binding to the capture reagents of conjugates and on the membrane. The treated sample migrates through the conjugate release pad, which contains antibodies that are specific to the target analyte and are conjugated to coloured or fluorescent particles. The sample, together with the conjugated antibody bound to the target analyte, migrates along the strip into the detection zone. This is a porous membrane (usually composed of nitrocellulose) with specific biological components (mostly antibodies or antigens) immobilized in lines. Their role is to react with the analyte bound to the conjugated antibody. Recognition of the sample analyte results in an appropriate response on the test line, while a response on the control line indicates the proper liquid flow through the strip. The read-out, represented by the lines appearing with different intensities, can be assessed by eye or using a dedicated reader.

When it comes to the substrate, there is also a significant amount of variety. The antibodies are bonded, either actively (covalent bond) or passively (electrostatic interactions) to the sensing element of the system[145, 146], the substrate or "bio-label". There is a wide selection of bio-labels, from gold[147, 148] and latex[149] nanoparticles[150, 151], to organic dyes[152, 153] or quantum dots[154, 155]. The use of metal-organic frameworks (MOFs) bears the potential to expand the application range by combining the versatility of structure and functionality of MOFs with the selectivity and affinity

of antibodies. Kumar et al[40] used mesoscopic MOF-5 particles and serum albumin to demonstrate that conjugation between MOFs and proteins is feasible. A common approach to creating conjugates involves covalently binding an antibody amino functionality to a host aldehyde group[156, 157] via imine bond through a Schiff base formation. Consequently, a host particle (*i.e* the ZIF nanoparticle) must exhibit both a desired property and a free aldehyde functionality, leading to choosing ZIF-90 as a model system, a structural analogue of ZIF-8. ZIF-90 forms through bridging of 2-imidazolecarboxaldehyde (i2ca) molecules between the tetrahedral zinc nodes[55, 158]. This conjugation methodology is especially compatible with the ZIFs due to the fact that the ZIF nanoparticles can easily include the necessary functionality (free aldehyde groups). Also, the conjugation via imine formation occurs at alkaline conditions (pH 8-9), allowing the ZIF particles to be chemically stable; ZIFs tend to quickly hydrolyse on acidic conditions since the acidity protonates the imidazolate building blocks.

3. Materials and methods

3.1. Chemicals

Zinc nitrate hexahydrate (CAS: 10196-18-6) was purchased from Roth (100% purity); 2-methylimidazole (CAS: 693-98-1) was purchased from Acros Organics (100% purity); 1-Aminopyrene (CAS: 1606-67-3; 95% purity) and Imidazolate-2-carboxaldehyde (CAS: 10111-08-7; 97% purity) were purchased from Sigma-Aldrich (Figure 7). Sodium methoxide (CAS: 124-41-4; 95% purity) was purchased from Merck. Sodium cyanoborohydride solution (CAS: 25895-60-7) 5.0 M in 1 M NaOH, n-Butylamine 99.5% were purchased from Sigma-Aldrich. Methanol and dimethylformamide HPLC grade where purchased at CHEMSOLUTE. All materials were used as received without further purification.

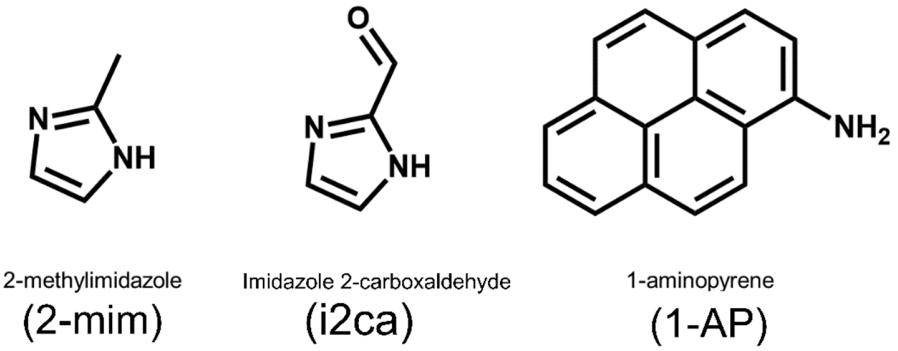

Figure 7 Chemical structures of the constituents to form Z8P, and their proposed abbreviations.

The Phthalate Acyl Esthers (PAEs) where obtained from Sigma-Aldrich: dimethylphthalate ≥99% (DMP), dibutylphthalate 99% (DBP), benzylbutylphthalate 98% (BBP) and diethylhexylphthalate ≥99.5% (DEHP).

All HPLC solvents used were of high purity HPLC grade. Water was acquired from a Milli-Q® Direct Water Purification System [18.2 MΩ•cm (25°C)]. Methanol for HPLC was purchased from CHEMSOLUTE as HPLC grade and TFA was purchased from Sigma Aldrich as Reagent-Plus 99 %. Disodium phosphate (Na_2HPO_4 Reagent grade, CAS: 10028-24-7) and Monosodium phosphate (NaH_2PO_4 Reagent grade, CAS: 10049-21-5) were purchased from Sigma-Aldrich. Nitric acid (HNO_3 65% grade for analysis EMSURE® Reag. PhEur, ISO) was purchased from Merck. Ultrapure deionized water (18.2MΩ cm−1, 25°C) was used for dilutions on sample and standard preparations (Milli-Q Gradient, Merck Millipore).

To quantify during ICP-OES an external standard solution of Zn is used, directly traceable to the NIST SRM 3168a (Certipur® Certified Reference Material, $Zn(NO_3)_2$ in HNO_3 2-3% Suprapur® Merck, Germany). All solvents and additives (acetonitrile, ammonium formate, formic acid) were

of LC-MS grade (CHEMSOLUTE,). Water was obtained from an ultrapure water purification system (Elga).

For NMR measurements d6-DMSO (CAS: 2206-27-1, 99.9%) in 0.75 ml ampules was purchased from Sigma-Aldrich

All reagents for buffer preparation, and casein, were purchased from Merck. Di-sodium tetraborate decahydrate (Ph Eur,BP,JP,NF grade, CAS: 1303-96-4), Sodium chloride (Reagent grade, CAS: 7647-14-5), Sodium azide solution (10% w/v in water, CAS: 26628-22-8), $NaH_2PO_4 \cdot 2H_2O$ (Reag. Ph Eur grade, CAS: 10049-21-5), $Na_2HPO_4 \cdot 2H_2O$ (Ph Eur,BP,USP grade, CAS: 10028-24-7), $C_4H_{11}NO_3$ (TRIS, Ph Eur grade, CAS: 77-86-1), Sodium dihydrogen citrate (Reagent grade, CAS: 18996-35-5), KH_2PO_4 (molecular biology grade, CAS: 7778-77-0), K_2HPO_4 (Analysis grade, CAS: 7758-11-4), $C_6H_7KO_2$ (potassium sorbate, Ph Eur,BP,NF,FCC,E 202 grade, CAS: 24634-61-5), 0.05% (v/v) Tween™ 20 solution (CAS: 9005-64-5), Tetrabutylammonium borohydride (synthesis grade, CAS: 33725-74-5), 3,3′,5,5′-tetramethylbenzidine (TMB, analysis grade, CAS: 54827-17-7), Casein (technical grade, CAS: 9000-71-9).

Antibodies

HRP-conjugated donkey anti-sheep-IgG (A3415), 1.8 mg/mL, in buffer (50 mM Na_2HPO_4, 20 mM Na_2HPO_4, TRIS HCl 0.1 M, pH 7.4, azide 0.02% w/v), was purchased from Sigma-Aldrich. Anti-mouse IgG from sheep (R1256P), 2 mg/mL, in PBS buffer, was purchased from Acris Antibody GmbH (Herford, Germany).

3.1.1 Preparation of buffers and solutions

Preparation of the phosphate buffer (PBS) for HPLC (pH 8.8)

Na_2HPO_4 (9.83 mmol, 1.75±0.0005 g) and NaH_2PO_4 (0.12 mmol, 16.29±0.5 mg) were weighed and dissolved into 1 L Milli-Q water. After dissolution, the PBS buffer was filtered through a 0.45 µm nylon membrane) to remove un-dissolved micro-crystal. The pH was determined to be 8.60 using a pH meter.

Preparation of the EDTA solution for digestion:

Na_2EDTA (1116±0.5 mg) and NaOH (800±0.5 mg) were dissolved in Milli-Q water (4 mL). The solid was dissolved by stirring and resulted in a highly viscous clear solution that was hot to the

touch. MeOH (12 mL) was subsequently added and mixed. and the mixture prepared in this way was found to be stable for 24 hours, after which the solution was found to turn into a gel.

Buffers for ELISA and LFIA

Borate buffer

Di-sodium tetraborate decahydrate (9.64±0.0005 g) and sodium chloride (8.29±0.0005 g) were dissolved in 1L of Milli-Q water. After full dissolution 1 mL of a sodium azide solution (10% w/v in water) was added and mixed. The final pH of the buffer was determined to be 9.05.

Phosphate buffered saline (PBS)

$NaH_2PO_4 \cdot 2H_2O$ (1.56±0.0005 g), $Na_2HPO_4 \cdot 2H_2O$ (12.46±0.0005 g) and NaCl (8.47±0.0005 g) were dissolved in 1 L of Milli-Q water. The final pH was determined to be 7.60.

TRIS buffer

$C_4H_{11}NO_3$ (TRIS, 1.21±0.0005 g) and NaCl (8.77±0.0005 g) were dissolved in 1 L of Milli-Q water. The final pH was determined to be 8.50.

Citrate buffer

Sodium dihydrogen citrate (47.10±0.0005 g) was dissolved on 1L of Milli-Q water, and the pH was determined to be 4.00. For reasons of stability, the buffer was kept in the fridge at 4°C.

Wash buffer

KH_2PO_4 (6.124±0.0005 g), K_2HPO_4 (65.32±0.0005 g) and $C_6H_7KO_2$ (0.225±0.0005 g) was dissolved on 1L of Milli-Q water. 30 ml of a 0.05% (v/v) Tween™ 20 solution was added. The final pH of the buffer was determined to be pH 7.60.

TMB solution

Tetrabutylammonium borohydride (102.93±0.5 mg) and 3,3′,5,5′-tetramethylbenzidine (TMB, 480.7±0.5 mg) were dissolved on 1L of Milli-Q water added. For stability, the buffer was kept in the fridge at 4°C.

3.2. Synthesis and characterization the imine

1ap (1-aminopyrene) and **i2ca** (2-imidazolecarboxaldhyde) were made to react on a 1 mol to 1 mol ratio inside an aluminium-capped sealable glass flask in methanol (0.8755mmol for each species / 10ml of methanol). The solution was then heated at 80 °C for 30 min with slow stirring (300 rpm) on a magnetic stirrer. The **imine** [IUPAC name= *(E)-1-(1H-imidazol-2-yl)-N-(pyren-1-yl)methanimine*] started precipitating as an intense cadmium yellow solid after 10 mins, and his precipitation evolved reaching the end after 30 mins. After this reaction time, the suspension was allowed to cool down to room temperature while stirring. The suspension was transferred quantitatively to a 15 mL Falcon tube and the solid sedimented via centrifugation (4000 rpm, 5 min). The supernatant was carefully removed and discarded. At this stage there maybe residual starting materials.

To wash the solid small amounts of cold and fresh methanol was added to the sedimented residue and redispersed by strong agitation; the suspension was then centrifuged to sediment the solid. After removing the supernatant, the open Falcon tube was subjected to vacuum for 3 hours at 5 mbar and 60°C in a vacuum oven.

Caution: Perform the wash procedure with methanol only once to prevent the imine from dissolving in methanol, hence reducing the final yield of the imine.

3.3. Preparation of the fluorescent modified nanoparticulated ZIFs

The basic protocol for all variants of the modified ZIFs on this work was as described next, adapting the masses required for each chemical and the reaction times as needed for each individual modified ZIF (Figure 8). The synthetic process is a two-step one-pot reaction. The first step of the reaction is the Schiff base condensation of 1ap with excess of i2ca in MeOH at 85°C. The second step is the in-situ addition of the alkaline catalyst (MeONa or n-$BuNH_2$) and the zinc salt to produce the modified ZIF. As an optional step, just before the addition of the Zinc salt is possible to add the 2mim to be included on the structure.

The required masses for **1ap** (1-aminopyrene) and **i2ca** (imidazolate-2-carboxaldehyde) were transferred into a sealable glass flask and sealed with an aluminium cap, then heated at 80°C for 30-210 min with stirring. After cooling the solution to ambient temperature, the alkaline catalyst (n-butylamine or sodium methoxide [MeONa] dissolved in methanol) was added; 2-methylimidazole was optionally added to the solution. Finally, a $Zn(NO_3)_2{\cdot}6{\cdot}H_2O$ methanolic solution was added. Almost immediately after the addition of the Zn salt solution, a yellow solid appeared dispersed in the solution. Stirring was stopped. The mixture was left undisturbed for 18 hours. A yellow solid sedimented to the bottom of the vial. The sedimented mixture is extracted

via centrifugation. The solid residue was washed with either DMF or methanol and extracted again via centrifugation, discarding the liquid supernatant. This washing procedure was repeated until the supernatant became colourless. The solid residue was finally dried overnight at 5 mbar and 75°C and let to cool down under vacuum.

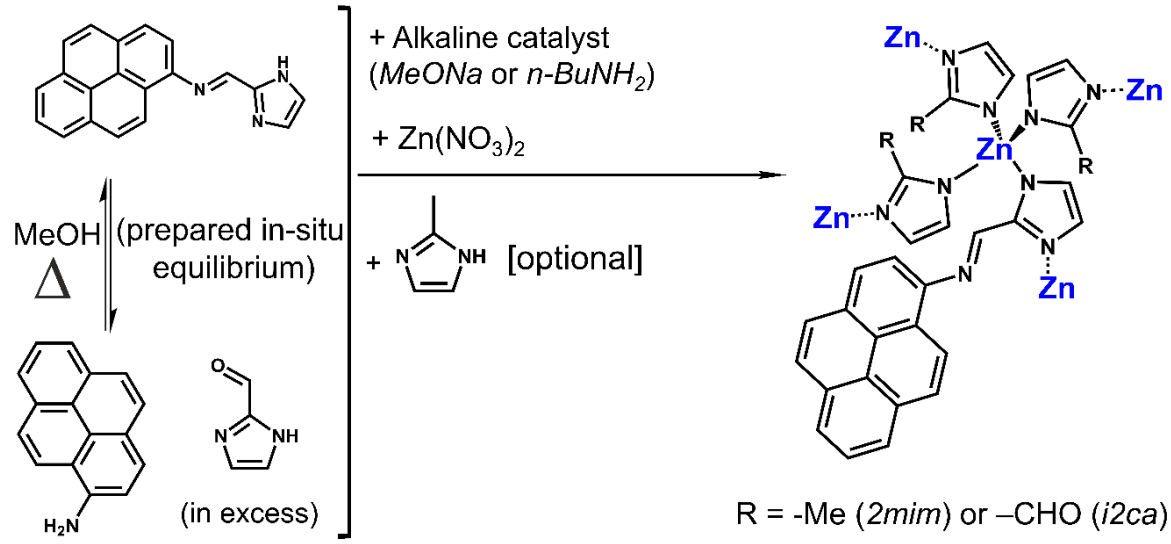

Figure 8 *Scheme summarizing the synthesis process to obtain the modified ZIFs.*

Preparation of the ZIF-8/ZIF-90 hybrid (Z8P-5$^{30}_{NbuAm,1:2}$):

"**Z8P-5$^{30}_{NbuAm,1:2}$**" will also referred to as "**Z8P-5"** along the work. This modified ZIF was achieved using the synthetic proportions 1 : 2 : 14.3 : 0.004 for Zn : imidazole species (2mim and i2ca) : MeOH : n-butylamine. The imine reaction time was let to evolve for 30 minutes at 80°C.

From literature work, $Zn(NO_3)_2$ as the Zn source offers the smallest sized ZIF-8 particles[97], methanol as the ideal solvent to form a non-aggregated colloidal solution[94], and n-butylamine as the best capping alkaline agent[70]. The molar ratio between species was chosen as a compromise between particle size and reaction yield. The inclusion of 2mim was done to facilitate the reaction of the ZIF, since 2mim showed a higher reactivity that the one for i2ca. This difference in reactivity between both imidazolates was attributed to 2mim being a stronger acid than i2ca, thus deprotonating more easily and complexing with Zn^{2+} atoms faster.

Preparation of the ZIF-8/ZIF-90 hybrid (Z8P-15$^{30}_{MeONA,1:2}$):

"**Z8P-15^{30}$_{MeONA,1:2}$**" will also be referred to as **Z8P-15** along the work. This modified ZIF was achieved using the synthetic proportions 1 : 2 : 14.3 : 0.004 for Zn : imidazole species (2mim and i2ca) : MeOH : MeONa. The imine reaction time was let to evolve for 30 minutes at 80°C.

Compared to the Z8P-5^{30}$_{NbuAm,1:2}$ synthesis, the biggest change was the substitution of n-butylamine by MeONa (Sodium Methoxide) as a capping agent. n-Butylamine blocks free aldehyde functionalities on nanoparticles, hindering any possible antibody conjugation since there were not enough available reaction points. The replacement by MeONa eliminates this aldehyde functionality blockage. The rest of the synthetic conditions remain unchanged.

Preparation of the family of modified ZIF-90 (Z90P-(5-30)^{210}$_{MeONA,1:4}$):

"**Z90P-(5-30)^{210}$_{MeONA,1:4}$**" will also referred to as **Z90P-5 to 30** along the work. This is achieved using the synthetic proportions 1 : 4 : 71.83 : 0.004 for Zn : imidazole species (i2ca) : MeOH : MeONa. The imine reaction time was let to evolve for 210 minutes at 80°C.

Compared to the synthesis for Z8P-5^{30}$_{NbuAm,1:2}$ and Z8P-15^{30}$_{MeONA,1:2}$, the biggest changes were: 1) elimination of 2mim as a structural agent on the ZIF, to study only the inclusion of i2ca; 2) the change of the molar ratios of Zn : i2ca. Literature suggests shows that a change on the molar ratios towards an equimolar ratio between Zn and the imidazole building blocks generates smaller particles (section 3.2.2). The increase on the ratio on this system will allow the particle to be slightly bigger in size. This increase in particle size will give more freedom to the imine to choose are to be incorporated on the ZIF particles, bulk, or surface, providing more information on the incorporation of the system.

NOTE: The difference on the molar proportions when compared to the previous synthesis protocols, specifically the increase on the amount of methanol used, is due to the low solubility of the imine in methanol and the necessity to increase the presence of the imine on these particular ZIFs.

Table 1 Amount of the starting materials of interest on the proportion of interest for each one of the variants of the modified ZIF, expressed in mmol. The final reaction volume for each ZIF is 11 ml.

MOF	$Zn(NO_3)_2$	i2ca	1ap	*% Imine targeted*
	mmol	mmol	mmol	*% mol/mol*
Z90P-5	0.110	0.440	0.022	*5.0*
Z90P-10	0.110	0.440	0.044	*10.0*
Z90P-15	0.110	0.440	0.066	*15.0*
Z90P-20	0.110	0.440	0.088	*20.0*
Z90P-25	0.110	0.440	0.110	*25.0*
Z90P-30	0.110	0.440	0.132	*30.0*

Preparation of the nanoparticulated ZIF-90

The general synthetic method described in section 4.3 was employed, using as alkaline catalyst for this system MeONa. The molar proportions between the chemicals to obtain this modified ZIFs are **1 : 2 : 14.3 : 0.004** for **Zn : i2ca : MeOH : MeONa**.

Preparation of ZIF-8

The general synthetic method described in section 4.3 was employed, using as alkaline catalyst for this system MeONa. The molar proportions between the chemicals to obtain this modified ZIFs are **1 : 2 : 14.3 : 0.004** for **Zn : 2mim : MeOH : MeONa**.

3.4. X-Ray diffraction of modified ZIFs

Capillary geometry: Powder X-ray diffractometry (PXRD) patterns were collected with Cu Kα radiation (λ= 1.50406 Å) on a D8 Advanced diffractometer (Bruker AXS, Germany) equipped with a LYNXEYE-XE detector with a Johansson-Monochromator. Samples were measured in reflection geometry in a 2Θ range from 4° to 60° with a step size of 0.009°. As sample holder glass capillaries with a width of 0.5 mm was used.

Bragg-Brentano geometry: Powder X-ray diffractometry patterns were collected with Cu Kα radiation (λ = 1.50406 Å) on a D8 Advanced diffractometer (Bruker AXS, Germany) equipped with a LYNXEYE XE-T (energy dispersive) detector with no monochromator. Samples were measured in reflection geometry in a 2Θ range from 4° to 50° with a step size of 0.009° with spinning setup. As sample holder a PVC (Polyvinylchloride) sample holder compatible with Bragg-Brentano, with a cavity with an opening of 0.8 cm in diameter

To prepare the powder samples for PXRD analysis, each powder was softly ground with an agar pestle on an agate mortar and pestle, the homogeneous fine powder was then placed on the sample holder.

X-Ray diffraction of conjugated ZIFs

For each ZIF-antibody conjugate samples, a small volume of the of the stock solution for each ZIF-IgG conjugate was freshly added to an Eppendorf tube, centrifuged (15000 rpm, 3 min) to reduce

its volume by removing excess supernatant, and then this dispersion was placed on a zero background silicon monocrystalline sample holder. The measurement was started with the sample still wet. All diffractograms were obtained with a 2θ range of 5-50°.

To assess that the crystallinity of the ZIFs within the conjugates was not severely damaged over time we measured the crystallite size for each system, applying the Scherrer equation (equation 3) to the first three reflections, (110), (200) and (211), for all diffractograms. The Scherrer equation is a formula that relates the size of sub-micrometre crystallites in a solid to the broadening of a peak in a diffraction pattern and was used in the determination of size of crystals in the powder[159].

$$\tau = \frac{K\lambda}{\beta cos\theta}$$

Equation 3 . Scherrer equation for calculating the crystallite size, where "τ" is the mean size of the ordered (crystalline) domains, "K" is a dimensionless shape factor [we took 1], "λ" is the x-ray wavelength (1.50406 nm), "β" is the line broadening at half the maximum intensity (FWHM) in radians, "θ" the Bragg angle. We calculated all the FWHM for each diffraction peak after background subtraction and applying a Gaussian fitting model with Origin.

3.5. Fluorescence characterization of the ZIF particles

Fluorescence spectra were obtained on an all-in-one microplate reader Synergy H1 with dispenser (BioTek). The software used was Gen5. The spectra were acquired from 380 to 600 nm, with a step of 2 nm, measurement time of 10 ms, delay between measurements of 100 ms. The samples were handled in a Polypropylene 96-well black plate from Greiner Bio-One.

In each well of a black non-binding polypropylene 96-well black microtiter plate, a small constant volume of the standards dispersion solution of the modifies fluorescent ZIF (Either in methanol of in borate buffer, depending of the system being characterize) is transferred. Then aliquots with different concentrations of the phthalates being tested are placed on the wells (in water or borate buffer, depending of the system being tested). Then each well is taken to the same total volume of 200 µl. The excitation wavelength was 335 nm, emission wavelength was observed at 445 nm. The gain was set to 100%.

3.6. HPLC protocol for ZIF quantification

High performance liquid chromatography analysis of the Z90P sample was performed using a modular Agilent 1100 Series HPLC system composed of a high pressure binary pump, auto-sampler with injector programming capabilities, Peltier type column oven with 6 µL heat

exchanger and a Diode Array Detector with a micro flow cell to reduce peak dispersion when using short columns (50 x 4.6 mm dimensions) as in this case. The flow-path was connected using 0.12 mm ID stainless steel tubing to minimize peak dispersion. ChemStation software was used to process the HPLC data.

A reversed-phase HPLC system with a silica covalently linked C18 pentafluoro-phenyl column was used. This Excel C18-PFP column has been manufactured to be stable up to pH 10. However, to avoid unnecessary damage to the column and the HPLC system, both should be flushed after use for at least 20 minutes at a low flow rate with water/methanol to remove damaging residues from buffer which could crystalize in the HPLC equipment and column and also to avoid subjecting the silica-based column to damaging alkaline conditions. Both the column and the HPLC system were flushed before and after use for at least 20 minutes at a flowrate of 1 ml/min with water/methanol to remove damaging residues from the HPLC equipment and column and to equilibrate the column prior to use. PBS (phosphate buffer) was eluted to equilibrate the column with the working alkaline buffer prior to any sample injection.

The two methodologies used have the following parameters:

- Water-methanol system:

Solvent A = Phosphate buffer 10 mmol, pH=8.8 ; Solvent B = MeOH ;0-4 min; 10-95 % B;

run time of 7 min; post time of 2 min; equilibration time of 1 min

Flow rate 2 mL/min; column temperature of 45 °C; 1 µL injection.

Maximum working pressure: 390 bar (close to the upper limit) at approx. 5 min

- Water-acetonitrile system:

Solvent A = (phosphate buffer 10 mmol, pH=8.8) ; Solvent B = (Acetonitrile:Solvent A in a 65:35 proportion) ; **1)** 0-0.6 min; 5 % B; **2)** 0.6-2 min; 100 % B;

run time of 5 min; post time of 2 min; equilibration time of 1 min

Flow rate is 2.5 mL/min; column temperature of 45 °C; 1 µL injection.

Maximum working pressure: 290 bar at approx. 2 min

Note: when preparing the solvent B, exercise caution. Any ratio > 70% MeCN: 30% PBS can result on the sudden precipitation of phosphate crystals on the solution, clogging the column and HPLC system and can even destroy the column during measurements.

3.7. Quantification of Zn^{2+} content on ZIFs by ICP-OES

The digestion procedure for the ZIFs was performed using HNO_3 30 %v/v, that was previously purified by sub-boiling it. The disintegrated ZIF sample in concentrated HNO_3 was then diluted with ultrapure deionized water to a volume of 10 mL and mixed well. The ICP determination of Zn^{2+} in the samples was performed against an external standard solution of a Zn^2 which is directly traceable to the NIST SRM 3169 (Certipur© Certified Reference Material, Merck, Germany).

ICP-OES parameter for analysis of disintegrated Z8P

The operating conditions for the ICP-OES (Agilent 5110 VDV) are listed on Table 2.

Table 2 Operational conditions for the ICP OES analysis

Parameter	Operating condition
RF power (kW)	1.2
Auxiliary gas flow rate ($L \cdot min^{-1}$)	1.00
Plasma gas flow rate ($L \cdot min^{-1}$)	12.00
Nebulizer gas flow rate ($L \cdot min^{-1}$)	0.70
Viewing height (mm)	8
Pump speed (rpm)	15
Stabilization time (s)	30
Integration time (s)	5
Replicates	5
Viewing mode	Radial
Wavelength (nm)	202.548 (Zn II)

3.8. LC-MS methodology to identify the conjugate imidazole-Lys fragment

Sample preparation: digestion of the conjugate

To a distinct amount of sample 1 mL of an aqueous solution of HCl 6N was added, the air was purged with the use of a Schlenk line with vacuum and Argon, and then heated to 107 °C for 24 h. After the digestion, the samples were cooled down and transferred to a 1.5 mL Eppendorf tube, and the solvent was removed using a SpeedVac.

LC-MS:

Liquid chromatography-mass spectrometry analysis was performed on a 1290 UHPLC system (Agilent, Germany) coupled to a 6600 TripleTOF mass spectrometer (SCIEX, Germany).

Samples were separated on a 2.1 mm × 75 mm × 1.8 µm BEH amide column (Waters, Germany) using a hydrophilic liquid interaction chromatography (HILIC) mode.

Solvent A: acetonitrile/water 50:50, 10 mM ammonium formate, 0.125% formic acid.

Solvent B: acetonitrile/water 95:5, 10 mM ammonium formate, 0.125% formic acid.

Solvent gradient (%B): 0 min 100%, 1 min 100%, 10 min 0%, 12 min 0%, 12.1 min 100%, 15 min 100%.

Flow rate: 0.5 mL/min. Column temperature: 35 °C.

Positive and negative electrospray ionization (ESI+/-) was carried out at 320 °C using capillary voltages of 5500 V and 4500 V, respectively. Mass spectrometric detection was performed in full-scan mode (m/z 50-600) at a scan rate of 4 s^{-1} using data-dependent MS/MS acquisition (DDA Top-4). For data analysis, raw data files were converted to mzML format and imported into an R workspace. Peak pre-processing was performed using package xcms[160]. For MS/MS fragment substructure annotation, competitive fragmentation modelling was used[161] (CFM-ID).

3.9. Conjugation of Z8P and ZIF-90 with IgG antibodies

Conjugation of ZIF-90 and Z8P with anti-mouse IgG protocol

Disperse a known mass for the ZIF (**ZIF-90** or **Z8P**) in borate buffer solution (1 mg/mL as approximate concentration). Seal the glass vial with the cap, and sonicate for 15 min. Then add **sheep anti-mouse IgG** (for each 1mg of ZIF/mL of borate buffer add 35 µL of a 2 mg/mL solution approximately) to this dispersion without any previous purification step. After stirring the mixture for 15 min at room temperature, add a commercially prepared aqueous solution of **Na[BH_3(CN)]** (5 M) in 1 M NaOH (for each 1mg of ZIF/mL of borate buffer add 35 µL of the Na[BH_3(CN)] solution approximately) and allow to react for an additional 4 hours at room temperature.

Warning: Exercise extreme care when handling cyanoborohydride. Always wear gloves, glasses and work in a properly enclosed fume hood.

 GHS05, GHS06, GHS08, GHS09

Protocol for washing the freshly prepared ZIF-90-IgG or Z8P-IgG

The next steps were designed to remove any anti-mouse IgG not covalently bonded to ZIF-90 or Z8P. The washing protocol of this conjugation reaction is as follows:

The ZIF-IgG suspension was centrifuged at 15000 rpm. The supernatant was removed and reserved for later use in case the ELISA experiment fails, suggesting unsuccessful binding between the IgG and the ZIF. The wash will help to investigate if the free IgG in the wash was active or inactive. The ZIF-IgG conjugate was washed with borate buffer, sonicating the suspension for 2 min to ensure full dispersion of the solid particles, then centrifuged again. The washing step was repeated with TRIS buffer three times, then two additional times with borate buffer. The ZIF-IgG was then dispersed on borate buffer. This is the **ZIF-IgG stock solution** (0.75 mg/mL) used in all the ELISA, LFIA, LC/MS and PXRD characterization.

> **Addendum**: The amount of washing steps was developed so that only the covalently bound antibody remains on the ZIF particles.

3.10. Dynamic laser scattering (DLS) of the Z90-IgG conjugates:

Dispersant phase preparation

To measure on DLS it is critical that the dispersion has no dust particles present. To eliminate all non-desired particles from the dispersion, the dispersant (borate buffer) was double filtered before use. This was done my making the dispersant go through a double filter setup, using two different filters:

- Filter A: "*CHROMAFIL® Xtra H-PTFE-45/25*". A Hydrophobic PTFE/hydrophilic PTFE filter for polar and unpolar solvents, with a pore size of 0.45 µm and filter diameter of 25 mm.
- Filter B: "*WHATMAN® GD/X Sterile*". A PES filter media for polar and unipolar solvents, with a pore size of 0.2 µm and filter diameter of 25 mm.

DLS sample preparation and results

A dispersion on double filtered borate buffer of Z90-IgG with a concentration for approximately 0.2 mg/mL was prepared. Before the measurement on DLS is critical to sonicate the sample for at least 5 min, to break all the micro aggregates. This, however, must be performed carefully, since ultrasonicating can lead to fragmentations and exfoliation of the particles[63].

3.11. Nanoparticle tracking of the Z90-IgG conjugates:

Nanoparticle tracking analysis was performed on a Malvern Panalytical NanoSight LM14.
NTA Version: NTA 3.2 Dev Build 3.2.16
Script Used: SOP Standard Measurement 11-48-23AM 25J~
Capture Settings: Camera Type: sCMOS; Laser Type: Blue405; Camera Level: 11; Slider Shutter: 890; Slider Gain: 146; FPS 25.0; Number of Frames: 1498; Temperature: 22.8 - 23.0°C; Viscosity: (Water) 0.931 - 0.934 cP;

Analysis Settings: Detect Threshold: 15; Blur Size: Auto; Max Jump Distance: Auto: 7.5 - 14.3 pix.

Dispersant phase preparation

To measure on DLS it is critical that the dispersion has no dust particles present. To eliminate all non-desired particles from the dispersion, the dispersant (borate buffer) was double filtered before use. This was done my making the dispersant go through a double filter setup, using two different filters:

- Filter A: "*CHROMAFIL® Xtra H-PTFE-45/25*". A Hydrophobic PTFE/hydrophilic PTFE filter for polar and unpolar solvents, with a pore size of 0.45 µm and filter diameter of 25 mm.
- Filter B: "*WHATMAN® GD/X Sterile*". A PES filter media for polar and unipolar solvents, with a pore size of 0.2 µm and filter diameter of 25 mm.

NTA Sample preparation

A dispersion on double filtered borate buffer of Z90-IgG with a concentration for approximately 20µg Z8P/mL was prepared. Before the measurement on DLS is critical to sonicate the sample for at least 5 min, to break all the micro aggregates. This, however, must be performed carefully, since ultrasonicating can lead to fragmentations and exfoliation of the particles[63].

3.12. Studies on conjugated antibody residual activity

Protocol of the non-competitive indirect ELISA for the anti-sheep IgG primary

In this version of the protocol the activity of the base ELISA system [mouse IgG (target) / sheep anti-mouse IgG (from sheep, primary, selective antibody) / anti-sheep IgG-HRP (from donkey, enzyme-labelled detector antibody)] was assessed.

The standard curve was prepared by making serial dilutions of one known concentration of the primary (sheep anti-mouse IgG) across a range of concentrations (0.25-750 ng/mL), while keeping every other parameter of the system constant. Each well was treated under the same conditions, and each measurement was done in quadruplicate.

The protocol is performed at follows:

Coat a 96 well transparent high-binding microtiter plate (flat-bottom, Nunc MaxiSorp™) with the mouse IgG (target). Seal the plates with Parafilm® to prevent evaporation and incubate for 4 h on a microplate shaker. Wash the wells of the microtiter plates with a 3-repetition cycle automatized microtiter washer using a PBS-based washing buffer. Ensure that the remaining binding sites on the MTP are blocked using a casein solution into each well. Seal the plates with Parafilm® to prevent evaporation and incubate for 1 h on a microplate shaker. Wash the plates again as described previously. Add the sheep anti-mouse IgG (primary, selective antibody) solutions to the corresponding wells. Seal the plates with Parafilm® to prevent evaporation and incubate for 18 hours on a microplate shaker. Wash the plates again as described previously. Add the anti-sheep IgG-HRP (enzyme-labelled detector antibody) to each well. Seal the plates with Parafilm® to prevent evaporation and incubate for 1 hour on a microplate shaker. Wash the plates again as described previously. Add the TMB solution (TMB-based substrate solution) to each well and incubate for 15 min on a microplate shaker. Each well's solution will turn from transparent to blue in colour. Add the stop solution (1 M sulphuric acid) to each well. The colour will change from blue to yellow. Measure the optical density (OD) of the wells.

The calibration curves were obtained by fitting a four-parameter logistic function to the data points obtained from OD measurements using the software Origin™. The sigmoidal shape of calibration curves is expected when the binding occurs via intact antibody binding sites and not,

e.g., due to non-specific binding. The calibration standard solutions were prepared by making serial dilutions from a stock solution of the antibody species to be assessed (anti-mouse IgG), while keeping the rest of the solution constituents at constant concentrations. In order to compare the amounts of soluble antibodies, each well was processed under the same conditions, and 4 replicates of each measurement were performed.

Preparation of Capture antibody solution

1.5 µL of mouse IgG were dissolved in 20 mL of borate buffer. The glass vial was sealed and homogenized using a mechanical shaker.

Preparation of Casein blocking solution

20 mg of casein were dissolved in 20 mL of PBS buffer. The glass vial was sealed and homogenized using a mechanical shaker.

Preparation of sheep anti-mouse IgG solutions in borate buffer

Preparation of 3 stock solutions

In total 3 stock solutions of sheep anti-mouse IgG were prepared. Stock solution MS1 was prepared from the original stock solution of the sheep anti-mouse IgG (2 mg/mL). Stock solution MS2 was prepared by dilution from MS1; Stock solution MS3 was prepared by dilution from MS2.

MS1 was prepared as follows:

25 µL of the original stock solution of the sheep anti-mouse IgG were dissolved in 1.5 mL of borate buffer. The glass vial was sealed and homogenized using a mechanical shaker.

MS2 was prepared as follows:

100 µL of the MS1 stock solution were dissolved in 1.5 mL of borate buffer. The glass vial was sealed and homogenized using a mechanical shaker.

MS3 was prepared as described for MS2 but using MS2 as the stock solution

The concentration for the MS solutions were:

MS1 = 50 µg/mL;
MS2 = 5 µg/mL;
MS3 = 0.5 µg/mL;

Preparation of the dilution series for assessing antibody activity of anti-mouse IgG

Eleven new solutions from these four stock solutions (MS1, MS2 and MS3) were prepared in borate buffer, with a varying concentration for sheep anti-mouse IgG, from 0.25 to 750 ng/mL. To keep the antibodies stable during the whole process all solutions were kept on ice.

Preparation of the solution of HRP-labelled detection antibody

1.5 µL of anti-sheep IgG, HRP labelled, were dissolved in 10 mL of PBS buffer. The glass vial was sealed and homogenized using a mechanical shaker.

Preparation of the solution of TMB-based substrate

550 µL of the TMB solution and 8.5 µL of H_2O_2 (30% v/v) were dissolved in 22 mL of citrate buffer. The glass vial was sealed and homogenized using a mechanical shaker.

Protocol of the non-competitive indirect ELISA for the ZIF-IgG conjugates

In this version of the protocol the residual activity of the antibodies bound to both the ZIF-IgG conjugates by a modified ELISA system [mouse IgG (target) / ZIF-IgG (Z8P-IgG and Z90-IgG, primary, selective antibody) / anti-sheep IgG–HRP (from donkey, enzyme-labelled detector antibody)] was assessed.

The standard curve was prepared by making serial dilutions of one known concentration of the analyte (ZIF–IgG conjugates, both Z90-IgG and Z8P-IgG) across a range of concentrations (0-150 ng/mL), while keeping every other parameter of the system constant. Each well was treated under the same conditions, and each measurement was done in quadruplicate.

The protocol previously described was performed with the modification of adding the ZIF-IgG conjugate solutions (ZIF-IgG solutions in borate buffer) to the corresponding wells instead of the mouse IgG.

Preparation of ZIF−IgG solutions in borate buffer:

Preparation of 4 stock solutions of **ZIF-IgG**

In total 4 stock solutions of Z8P-IgG and Z90-IgG were prepared. Stock solution MS1 was prepared from the initial stock solution of Z8P-IgG (0.75 mg/mL) and Z90-IgG (0.75 mg/mL); Stock solution MS2 was prepared by dilution from MS1; Stock solution MS3 was prepared by dilution from MS2.

MS1 was prepared as follows:

10 µL of the original stock solution of the ZIF-IgG (Z90-IgG or Z8P-IgG) was dissolved in 1.5 mL of borate buffer. The glass vial was sealed and homogenized using a mechanical shaker.

MS2 was prepared as follows:

100 µL of the MS1 stock solution was dissolved in 1.5 mL of borate buffer. The glass vial was sealed and homogenized using a mechanical shaker.

MS3 was prepared as described for MS2 but using MS2 as the stock solution

The concentration for the MS solutions will be:

MS1 = 7.5 µg/mL;
MS2 = 0.75 µg/mL;
MS3 = 0.075 µg/mL;

Preparation of the dilution series for assessing antibody activity of ZIF-IgG

23 new solutions were prepared from these four stock solutions (MS1, MS2, MS3 and MS4) to varying concentrations for ZIF-IgG (both Z90-IgG and Z8P-IgG), from 0.015 to 150 ng/mL. In order to keep the antibodies stable during the whole process all solutions were kept on ice.

Protocol of the non-competitive ELISA for the antibody conjugates Z8P-IgG / non-competitive fluorescent ELISA parallel tests

To study the viability of the fluorescently modified ZIF-8/ZIF-90 hybrid as a fluorescent bio label in immunoassays, a new ELISA was designed by modifying the previous methodology, comparing

the response for Z8P-IgG between non-competitive ELISA and non-competitive fluorescent ELISA.

In both these ELISAs the standard curve was prepared by making serial dilutions of one known concentration of the primary, Z8P-IgG, across a range of concentrations (0-1500 ng/mL), while keeping every other parameter of the system constant. Each well was treated under the same conditions, and each measurement was done in quadruplicate. Both ELISA protocols took place using the exact same concentration for all species. Two measurements took place in parallel:

- Non-competitive ELISA: On a high-binding transparent microtiter plate, where OD was measured as a final step
- Non-competitive fluorescent ELISA: On a high-binding black microtiter plate, were fluorescence was measured as a final step

Note: the significant increase on the concentrations for the target and the primary is due to the fact that the fluorescence sensitivity is not high enough to work on the previously used range of concentrations, thus we are forced to increase them to reasonably detect and quantify fluorescence.

Preparation of Capture antibody solution

5.0 μL of mouse IgG (2mg/mL) were dissolved in 20 mL of borate buffer. The glass vial was sealed and homogenized using a mechanical shaker.

Preparation of 4 stock solutions

In total 4 stock solutions of Z8P-IgG were prepared. Stock solution MS1 was prepared from the initial stock solution of Z8P-IgG (0.75 mg/mL); Stock solution MS2 was prepared by dilution from MS1; Stock solution MS3 was prepared by dilution from MS2.

MS1 was prepared as follows:

100 μL of the original stock solution of Z8P-IgG were dissolved in 1.5 mL of borate buffer. The glass vial was sealed and homogenized using a mechanical shaker.

MS2 was prepared as follows:

100 μL of the MS1 stock solution were dissolved in 1.5 mL of borate buffer. The glass vial was sealed and homogenized using a mechanical shaker.

MS3 was prepared as described for MS2 but using MS2 as the stock solution

The concentration for the MS solutions will be:

MS1 = 75 µg/mL;
MS2 = 7.5 µg/mL;
MS3 = 0.75 µg/mL;

Preparation of the dilution series for Z8P-IgG

Twenty-three new solutions were prepared from these four stock solutions (MS1, MS2, MS3 and MS4) to varying concentrations for Z8P-IgG, from 0.015 to 1500 ng/mL. In order to keep the antibodies stable during the whole process all solutions were kept on ice.

Protocol of the non-competitive ELISA for the antibody conjugates Z8P-IgG via non-competitive fluorescence immunoassay

A non-competitive indirect immunoassay for the assessment of the activity of the Z8P-IgG conjugate and its fluorescence capabilities was developed.

The protocol previously described was followed with the following modifications:

1) This experiment was performed on a 96 well black high-binding plate for fluorescence measurements (flat-bottom, Nunc MaxiSorp™).
2) After the incubation of the primary conjugate (ZIF-IgG), the fluorescence of each well was measured.
3) After the measurement, a three-cycle washing step using a PBS-based washing buffer took place and each well was filled with borate buffer
4) The fluorescence was then measured again
5) After this measurement, a three-cycle washing step using a PBS-based washing buffer took place and each well was filled with citrate buffer to disintegrate the ZIFs and liberate the fluorophores.
6) The plate was incubated in a plate shaker for 30 min
7) Fluorescence was then measured again

3.13. FTIR:

Fourier-transform infrared spectra were recorded on a Nicolet FT-IR NEXUS instrument with a Golden Gate-Diamond-ATR Unit and a DTGS KBr detector. For each measurement 32 sample scans and 32 background scans were recorded. The spectral range was from 200 cm^{-1} to 4000 cm^{-1} with a resolution of 4 cm^{-1}.

3.14. TEM:

Transmission electron microscopy (TEM) images were obtained in a Talos F200S Microscope (Thermo Fisher Scientific) by using a 200 kV microscopy technique in which a beam of electrons is transmitted through a specimen to form an image. A Ceta 16M camera (TEM mode) and a HAADF detector (STEM mode) were used to capture the images.

Additionally, a side-entry retractable Energy Dispersive X-ray Spectroscopy (EDS) detector were also used in the STEM mode to collect detailed elemental information.

The specimens were prepared by dropping sample solutions onto a 3 mm copper grid (Lacey Carbon, 400 mesh) and leaving them to air-dry at room temperature.

3.15. NMR:

Nuclear magnetic resonance measurements were performed on a 400 MHz NMR spectrometer (Mercury-400 BB) at 29.0 °C, with a relaxation delay of 2.000 sec, a pulse of 45.0°, an acquisition time of 2.274 sec and 16 repetitions. Solvent was deuterated DMSO.

3.16. Optical density (Absorption spectrometry):

Absorbance, with measurements in microtiter plates usually designated as optical density (OD), was measured on a SpectraMax Plus384 microplate reader (Molecular Devices, Ismaning, Germany) at 450 nm, referenced to 620 nm. All calibration standard solutions were determined in triplicate. SoftMax®Pro Software (v.5.3, Molecular Devices) was used for data acquisition.

4. Results and discussion

In this section of the thesis the experimental results are presented, and they are put into context to explain their relevance and conclusions.

Subsection 3.1 presents the developed HPLC methodology to digest and quantify ZIFs. Two digestion methodologies, suitable for the ZIFs, are explored and compared. Two HPLC mobile phase combinations are also explored and compared. The chromatograms for all the species involved on the synthesis of the modified ZIFs are presented. Finally, the mathematical equations to convert the data from HPLC into usable information is explained.

Subsection 3.2 presents the synthesis and characterization of the ZIFs. An overall explanation on how the synthesis of the ZIFs is approached is presented. The imine formation, one of the building blocks of the modified ZIFs, is presented and characterized. The two methodologies to obtain a nanosized ZIF with the imine incorporated is presented and compared. The advantages and disadvantages of the chosen capping ligands are explained.

Subsection 3.3 presents the final ZIF composition as a function of initial reagents. On this section it is shown how the use of HPLC quantification data, supported by TEM-EDS and ICP-OES, leads to a better understanding on how the imine incorporation within the ZIF structure occurs. A relationship between initial imine availability and final ZIF composition, and particle size and shape of the ZIFs, are presented.

Subsection 3.4 presents the fluorescence characterization of the modified ZIFs. A calibration curve based on a well known mathematical model for the fluorescence quenching of the ZIFs versus concentrations for four chosen Phthalate Acyl Esters (PAEs) is presented. A model on how the fluorescence quenching occurs within the ZIF particles, based on the obtained data, is presented.

Subsection 3.5 presents the creation and study of the ZIF-antibody conjugate. First, the conjugation methodology to create a ZIF-IgG conjugated is presented. The strength of this conjugation methodology is proven via the use of LC-MSMS of the digested mixture. The physical properties of the conjugate system are characterized via PXRD, DLS and NTA. The potential of the ZIF-IgG conjugation as a novel system is explored using ELISA and LFIA, complemented with fluorescence.

4.1. HPLC methodology to quantify ZIFs

To study the composition of the ZIFs a HPLC methodology to quantify digested ZIFs was developed. This methodology will allow to study the effect of different concentrations of imine during ZIF formation on particle size and shape. To quantify the composition of the ZIFs, the first step is the digestion of the solid powder into a clear and homogeneous solution. Two different methodologies were developed to digest this ZIFs, one acid-based and one alkaline-based.

Acid digestion methodology

This methodology digests the ZIFs by protonating the imidazolic building blocks that constitute the crystal structure of the ZIFs (Figure 9). The ZIF to be digested must be first dried well under vacuum (5 mbar, 70-80°C, 12-18 hours) to minimize errors during weighing. The dried ZIF sample is dispersed in a methanol/water mix and concentrated trifluoroacetic acid (TFA) is used as the digestion agent. The previously dispersed ZIF solid will quickly disappear, resulting in a transparent solution.

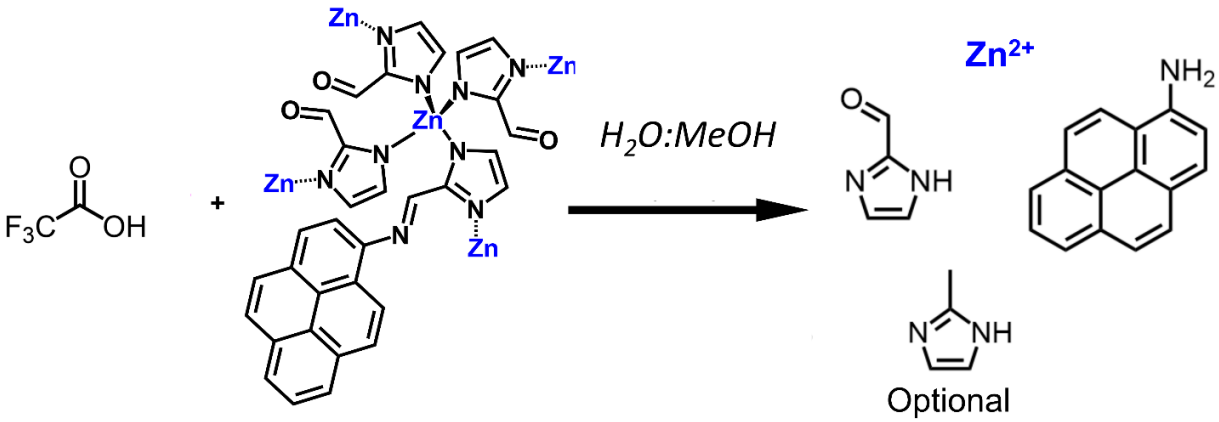

Figure 9 *Scheme representing the acid digestion methodology.*

Once the ZIF is completely digested (disappearance of all solid particles in dispersion) the as-made solution is too acidic for direct injection into the HPLC instrument. This acidity is not compatible with most HPLC columns, potentially irreversibly damaging them. Therefore, to neutralize the solution, it is neutralized using a NaOH water solution but leaving the solution slightly acidic to prevent reprecipitation of the ZIF.

This methodology poses a significant problem with the modified fluorescent ZIFs developed in this work: the imine will not survive the process as a whole molecule, suffering immediate hydrolysis. Correspondingly, this approach only allows to quantify indirectly the imine incorporated into the ZIFs, via the amount of 1ap that can be detected. However, this method leaves two open questions: (1) whether the imine was truly incorporated as a building block in the ZIF; and (2) whether 1ap is captured into ZIF pores during precipitation. To answer these questions a new digestion methodology was developed.

Alkaline digestion methodology

This methodology is based on the sequestration of the Zn^{2+} metallic nodes from the framework using a more favourable complexing agent ($EDTA^{4-}$) than the imidazolates that build the ZIFs (Figure 10). This sequestration happens in a highly alkaline media, since the pK_a value for EDTA to deprotonate all carboxylic groups is 10.4[162]. The total deprotonation of the EDTA is a necessity to favourably coordinate the zinc atoms.

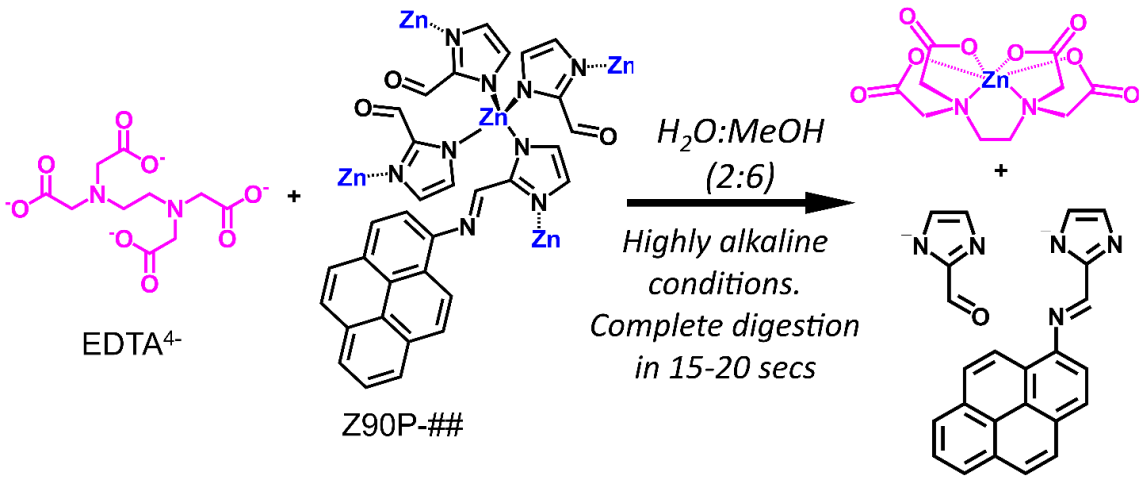

Figure 10 *Scheme representing the digestion methodology via Zn^{2+} sequestration by $EDTA^{4-}$ in alkaline conditions.*

It is important to first dry thoroughly the ZIF being investigated, followed by addition of the EDTA digestion solution. The powder dispersed in the solution quickly dissolves, and the solution becomes transparent with a yellow colour. The sample is ready to be injected on to the HPLC instrument. When preparing the EDTA digestion solution a 6:2 ratio for methanol:water works well to dissolve the EDTA homogeneously, but the EDTA solution will form gels in 24 hours, so it should be prepared freshly prior to the ZIF digestion. Increasing the methanol:water ratio in favour of the methanol will form EDTA gels on the solution faster than with a 6:2 ratio; a ratio of 7:2 forms gels in two hours, and a ratio of 8:2 forms gels within 10 minutes. To prepare the EDTA salt digestion solution it is important to try to keep it on a solvent with as much of organic proportion as possible, in the presented case methanol. The increase or organic solvent on the EDTA digestion will facilitate the dissolution of the organic components continuing the ZIFs. The solubility of the EDTA salt on organic solvents is extremely low, even on highly alkaline media; in order to dissolve properly the EDTA salt, the presence of water is mandatory.

HPLC methodology for quantifying ZIFs

The mobile phases used worked at alkaline pH, suitable for the analysis of imines. This alkaline pH will avoid the immediate hydrolysis of imines which would otherwise happen under acidic chromatographic conditions. This is critical for the quantification of the EDTA digested mixture,

to keep the imine undamaged. For the acidic digested mixture, since the acidic digestion has forced the imine to hydrolyse to its original constituents (1ap and i2ca), the alkaline buffer was not a critical factor. This alkaline mobile phase was also necessary to resolve the imidazole species 2mim and i2ca, and the chromophores 1ap and imine since they come close together in pairs (Figures 13 and 15). Both 2mim and i2ca are hydrophilic and elute first, close to the solvent front. To resolve the imidazolic species a pH value higher that their pKa (7.6) is chosen. 1ap and imine, both containing a pyrene fluorophore, are lipophilic and will be significantly retained. A pH value of 8.8 resolved 2mim from i2ca (Figure 13), as well as 1ap from the imine (Figure 15). To detect the presence of the analytes of interests, a Diode Array Detector (DAD) was used, that measures UV absorption. The absorptions spectra for all the analytes of interest was determine beforehand (Figure 11). To quantify 2mim a wavelength of 210±8 nm was selected, for i2ca a wavelength of 280±8 nm was selected, for 1ap a wavelength of 338±8 nm was selected and for the imine a wavelength of 380±8 nm was selected. These wavelengths are under the absorption bands for the UV for their respective analytes and they are far apart from each other, minimizing cross-detection.

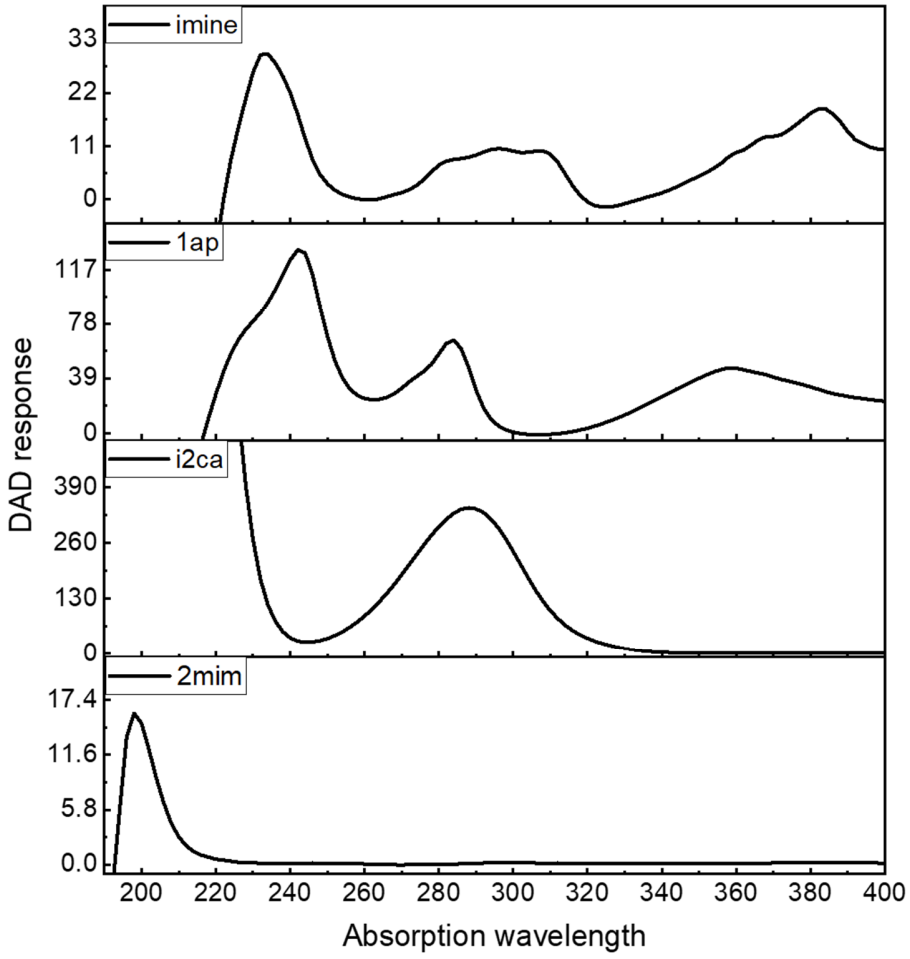

Figure 11. DAD absorption spectra for the analytes constituting the ZIFs of interest.

To have the organic species elute well an organic mobile phase is necessary. Methanol and acetonitrile were chosen as the organic phases since both are miscible with water and they have a low viscosity value. DMF and DMSO were not considered as an organic solvent since they present several issues with the HPLC instrument: (1) both absorb strongly in the UV, with the maximum of absorption at 240 nm[163]. This will interfere with the i2ca and 2mim quantification; (2) they are more viscous than typical HPLC solvents, so the pressure will spike up upon injection. The mixes of a water/organic phase will increase the working pressure[164], so minimizing this increase will allow a more stable HPLC quantification. This can also be rough on column packings; The column used on this method can withstand this pressure increase well but minimizing will render a more stable measurement with better resolved peaks. THF was also considered a candidate as the organic phase, but there is a big danger of the phosphate dissolved on the water buffer to precipitate when mixed with the THF, so it was avoided. Solvents such as Chloroform, or n-hexane are not miscible with water, making them not a feasible candidate.

- Water-methanol system:

This mobile phase combination allowed for the elution of the organic species, keeping them resolved and allowing a quantification (Figure 12). This method has two main disadvantages: first, methanol as a solvent and TFA as a digestion reagent had a significantly high amount of impurities (Figure 13b and c), that can make the quantification more complex. Second, the use of methanol mixed with water increased the working pressure of the HPLC instrument too close to the safe maximum value (400 bar). With methanol, between 3 and 4 min of elution time, the internal pressure reached a value of 390±10 bar, making it unsafe to the system and the detector. The reduction of the flow rate to reduce the working pressure will lead to the imidazolate chemicals and the aminopyrene and imine peaks to diffuse in the column as they elute, impeding a good resolution of their peaks.

- Water-acetonitrile system:

The acetonitrile:PBS mobile phase combination allowed for the elution of the organic species, keeping them resolved and allowing their quantification (Figure 14 and 15). The use of acetonitrile as the organic solvent provides two main advantages when compared to methanol: first, the retention times for the analytes were shorter (7 mins for one full quantification via methanol, compared to 5 mins with acetonitrile). Second, the working pressure of the system was significantly reduced as well, reaching the peak 290 bar at 3 mins. Also, acetonitrile was significantly cleaner than methanol, and EDTA (the digestion reagent) eluted with the eluent front, not interfering with the rest of the analytes (Figure 15). It is important to note that phosphate salts are insoluble in acetonitrile, however, so to make sure no accidental precipitation will happen inside the HPLC, the acetonitrile mobile phase was premixed with PBS (phosphate saline) buffer solution in a proportion of 65:35 of acetonitrile:PBS.

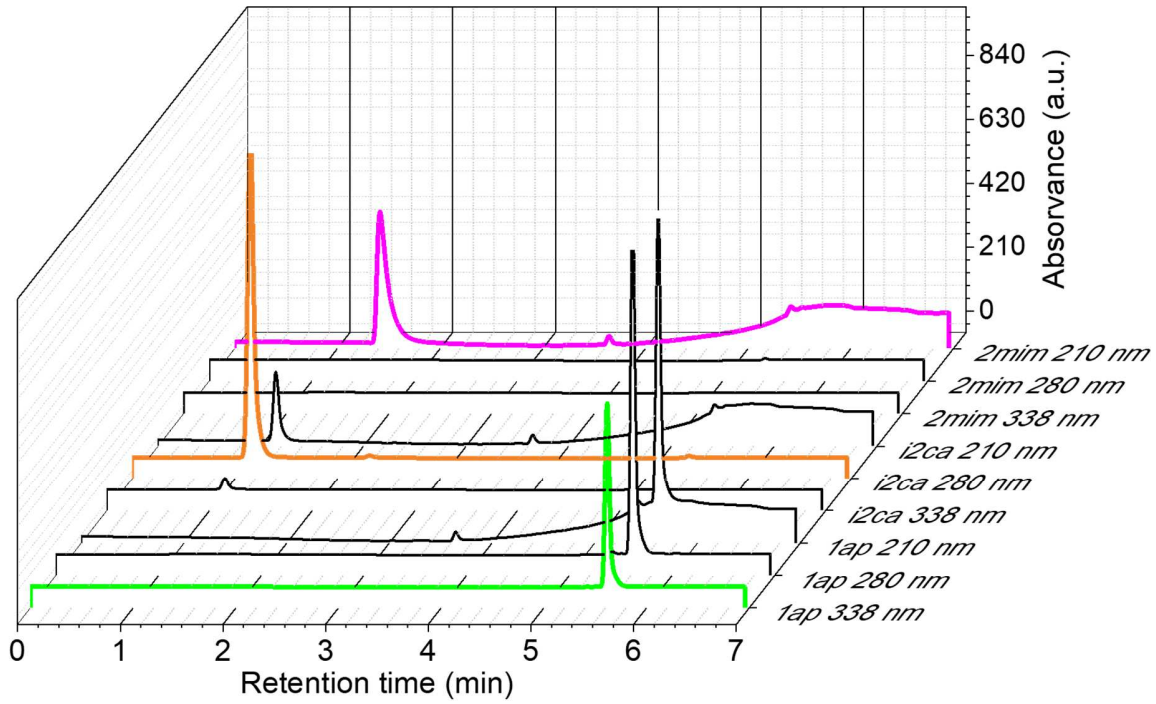

Figure 12 Chromatograms for 2mim, i2ca and 1ap with the methanol:PBS methodology, showing their response in all the chosen DAD wavelengths. Chosen response for 2mim is at 210 nm (purple line), for i2ca at 288nm (orange line) and for 1ap at 338 nm (green line).

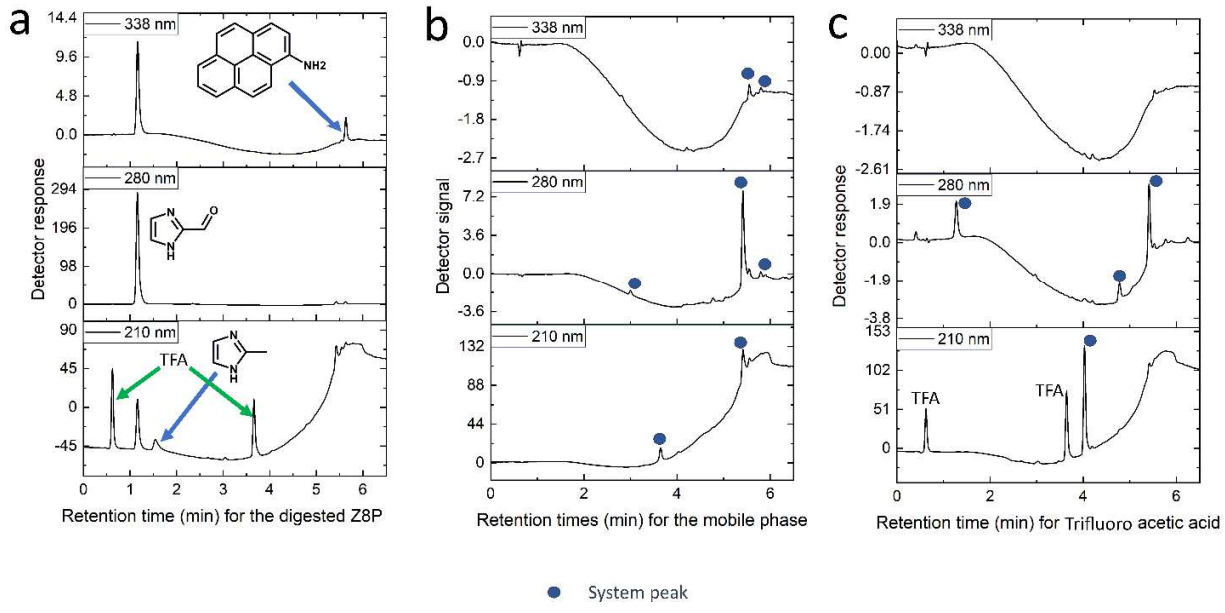

Figure 13. Chromatograms of the digested Z8P (a), the mobile phase (b), and the mobile phase with TFA (c). For all species all three chosen wavelengths are shown (from top to bottom; 338 nm, 280 nm and 210 nm). In Figure (a) the positions of all peaks on the digested ZIF is reported; the retention time for 2-mim is 1.53 min, for i2ca is 1.16 min, and for 1-AP is 5.63 min. TFA has two signals at 210 nm, one at 0.65 min and another one at 3.71 min.

- Water-acetonitrile system:

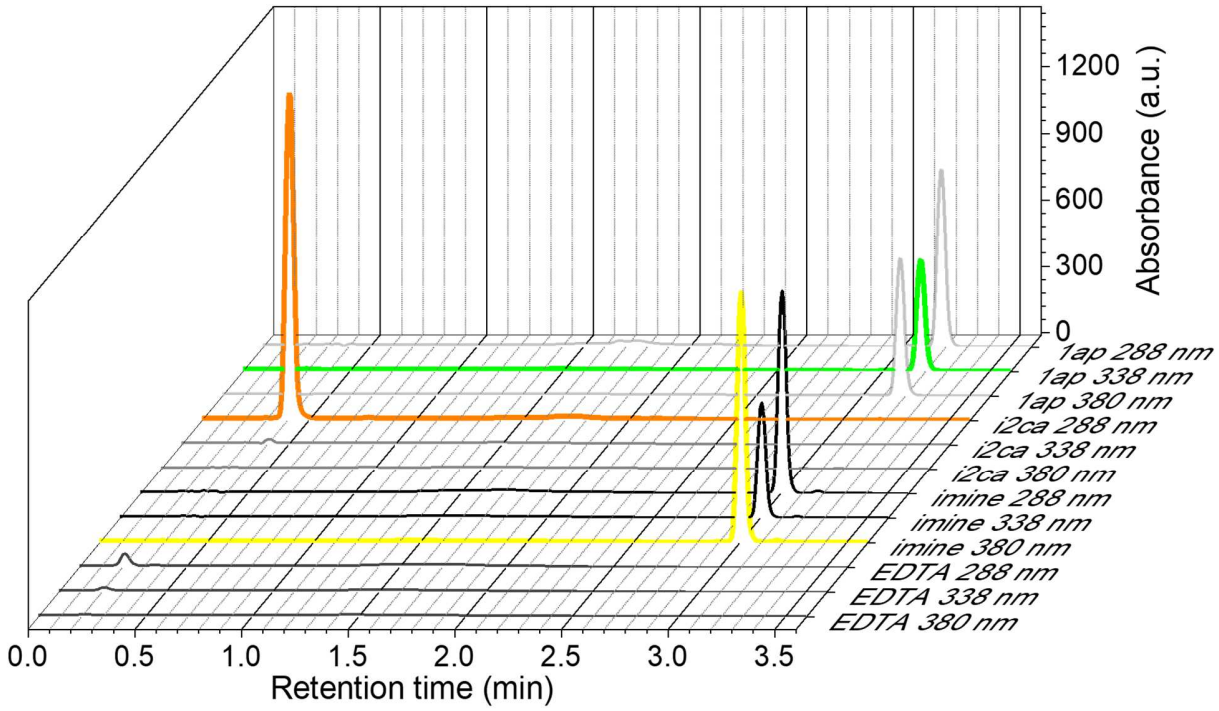

Figure 14 Chromatograms for i2ca, 1ap and imine with the acetonitrile:PBS method, showing their response in all the chosen DAD wavelengths. Best response for i2ca is at 288nm, for 1ap at 338 nm and for imine at 380 nm.

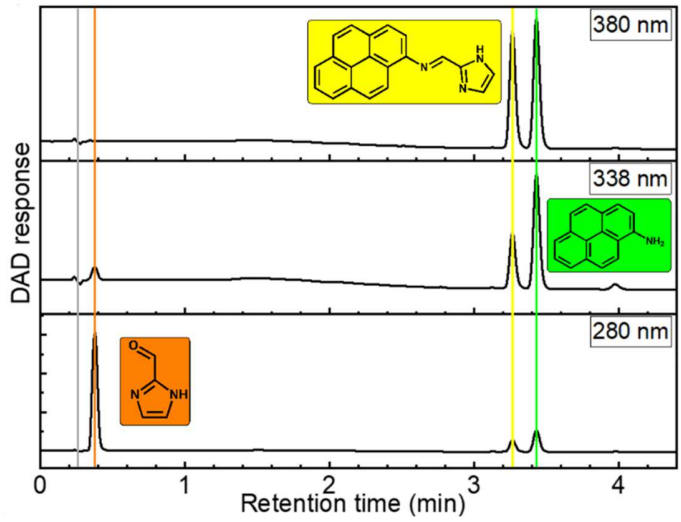

Figure 15 Chromatograms for a mixture of all the analytes of interest using the acetonitrile methodology, showing their response in all the chosen DAD wavelengths. Chosen response for i2ca is at 280 nm (orange bar), for 1ap at 338nm (green bar) and for imine at 30 nm (yellow bar).

For 2mim, i2ca and 1ap the standards were prepared from the commercially available starting materials, dissolved in methanol. Full dissolution for 1ap and i2ca was only achieved by heating each of them to 60 °C in a sealed glass flask. For the imine, standards for the quantification were prepared from the synthesised imine (section 4.2) dissolved in DMF. With these standards their concentration ranges where they show linearity were determined. The peak area obtained by HPLC for each working standard solution was plotted against the known concentration of the calibration standard solution. Once the concentration ranges where they show linearity has been determined for all analytes, all subsequent analyses was performed by using just one working standard solution prepared, ensuring that the concentration of the working standard and sample solutions were within the calibrated range of linearity.

To convert DAD peak area to working concentrations, Equation 4 was used, which converts the DAD peak area for each analyte, PA_X, to the concentration for the respective analyte as *(µmol of analyte X/mL reaction solution)*, with the DAD peak area for the standard solution of X, $PA_{stdX,}$as a reference. *Std X*" is the concentration for the standard solution of analyte used, and $MW_{analyte\ x}$ is the molecular weight for the analyte X.

Equation 4 Average concentrations in µg/mL calculated for each of the samples measured via HPLC. The concentrations expressed in %mol/mL solution are also expressed.

$$\left(\frac{\mu mol\ of\ analyte\ X}{ml\ reaction\ solution}\right) = \frac{(PA_X\ [counts]) \cdot (Std\ X\ [^{mg}/_{mL}]) \cdot (1000\ [^{\mu mol}/_{mmol}])}{(PA_{Std\ X}\ [counts]) \cdot MW_{analyte\ X}\ [^{mmol}/_{mg}]}$$

For convenient analysis, it is worth converting further the output of Equation 4 into a mol% of the analyte *via* Equation 5, which converts the concentration for the analyte X from *(µmol of analyte X/mL reaction solution)* to *(%mol)for analyte X*.

Equation 5 Average concentrations in µg/mL calculated for each of the samples measured via HPLC. The concentrations expressed in %mol/mL solution are also expressed.

$$\%mol\ for\ analyte\ X = \ 100 \cdot \frac{\left(^{\mu mol}/_{mL}\right) for\ analyte\ X}{\sum\left(^{\mu mol}/_{mL}\right) for\ all\ analytes}$$

To compare the composition of the modified ZIFs as a function of the analyte's contribution, it is convenient converting the DAD peak area to *(%g analyte X / g weighted ZIF).* Equation 6 is used, which converts the DAD peak area for each analyte, PA_X, to the concentration for the respective analyte as *(%g analyte X / g weighted ZIF),* with the DAD peak area for the standard solution of

X, $PA_{stdX,}$as a reference. *Std X* is the concentration for the standard solution of analyte used, and *weighted Z8P* is the mass for the modified ZIF digested expressed in mg.

Equation 6 Average concentrations in %g/g weighted ZIF calculated for each of the samples measured via HPLC.

$$\left({}^{\%g\ analite\ X}/_{g\ weighted\ ZIF}\right) = 100 \cdot \frac{(PA_X\ [counts]) \cdot (Std\ X\ [{}^{mg}/_{mL}]) \cdot (Vol.digestion\ [mL])}{(PA_{Std\ X}\ [counts]) \cdot (weighted\ Z8P\ [mg])}$$

Knowing the contribution on the mass for all organic elements, quantified directly from their respective DAD signals, then the Zn^{2+} composition contribution can be determined indirectly by HPLC as the mass difference of the weighted and digested ZIFs (equation 7).

Equation 7 Average concentrations in %g/g weighted ZIF calculated for each of the samples measured via HPLC.

$$\left({}^{\%g}/_{g\ weighted\ ZIF}\right) for\ Zn = 100 - \sum_{\substack{all\ organic \\ species}} \left[{}^{\%g\ analyte\ X}/_{g\ weighted\ ZIF}\right]$$

4.2. Synthesis and characterization of the modified ZIFs

This work focuses on a modified zeolitic imidazole framework (ZIF) that includes a fluorophore functionality covalently bound to its structure. These modified ZIFs were obtained using up to four basic building blocks: zinc as metallic nodes, 2mim (2-methylimidazole) as an structural organic linker between the zinc metal nodes, i2ca (imidazole 2-carboxaldehyde) as an organic linker between the zinc metal nodes that includes a chemically active functionality, and 1ap (1-aminopyrene) as the fluorescence moiety included in the form of an imine (Figure 16).

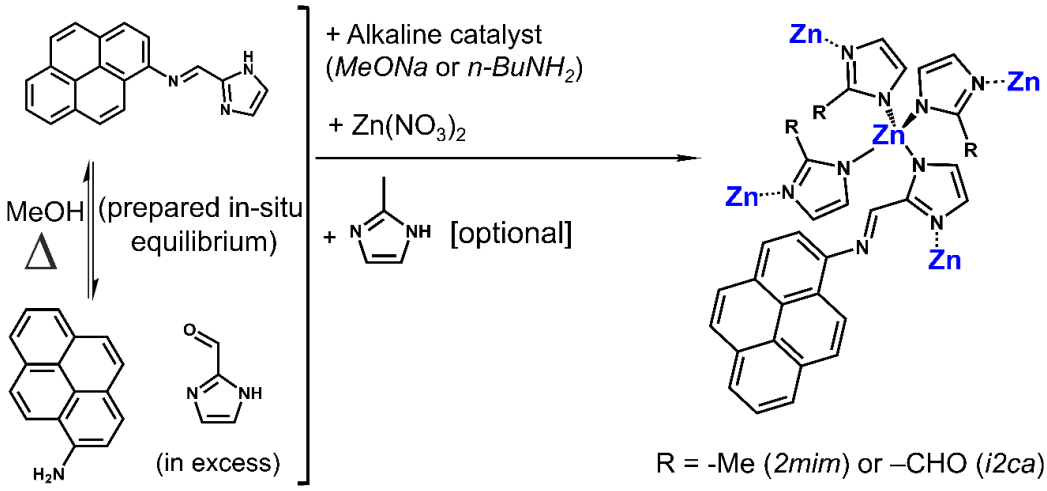

Figure 16 Scheme summarizing the synthesis process to obtain the modified ZIFs. The first step of the reaction is the Schiff base condensation of 1ap with excess of i2ca in MeOH at 85°C. The second step is the in-situ addition of the alkaline catalyst (MeONa or n-BuNH2) and the zinc salt to produce the modified ZIF. As an optional step, just before the addition of the Zinc salt is possible to add the 2mim to be included on the structure.

The synthetic procedure to form the modified ZIFs was performed as a one pot, two-step reaction. The first step consisted in forming the imine, *(E)-1-(1H-imidazol-2-yl)-N-(pyren-1-yl)methanimine*, via a Schiff base condensation between the amino functionality of the 1ap with the aldehyde functionality of the i2ca ligand (Figure 17).

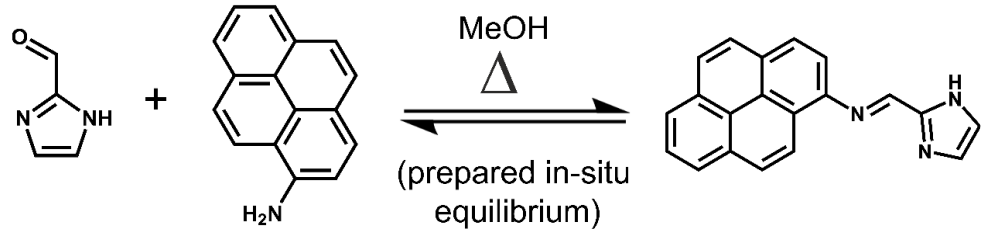

Figure 17 Scheme summarizing the synthesis process to obtain the imine to be incorporated on the final ZIF. The reaction is a Schiff base condensation of 1ap and i2ca in MeOH at 85°C.

The second step was the formation of the ZIF by adding the alkaline modulating agent, sodium methoxide or n-butylamine, and the metallic node, zinc. Additionally, before adding the zinc salt it was possible to add 2mim to be also incorporated on the final ZIF structure. This additional addition of the 2mim is performed to reduce even further the final size of the nanoparticles obtained. Given that the final goal was to form a conjugate with antibodies usable on ELISA and LFIA, the final particle size of the conjugate was a critical aspect of the system. In the context of biochemical, miniaturized assays, is critical that the ingredients behave as "quasi-solutions", i.e, colloidal dispersions. Particulate systems like colloidal solutions are best for these applications to obtain highly reproducible results (high precision, small standard deviations). This will mostly depend on the final particle size for the ZIF. Literature shows that the best solvent to obtain colloidal ZIF dispersions with the smaller possible particles, as well as to minimize particle aggregation and stable colloids, is methanol[70, 94]. This solvent selection was beneficial also for the characterization of the ZIFs composition by HPLC. The elimination of all trapped solvent on the pores is critical to minimize the error when weighting the ZIFs. This error is exacerbated when solvents such as DMF or water are used, since there is evidence that the solvent elimination from the ZIF, even on aggressive conditions, is not completely effective[165]. For this reason, methanol was chosen as the only solvent to obtain the modified ZIF nanoparticles.

The selection of methanol presented one key issue for the synthesis of the modified ZIFs: the low solubility of the formed imine on methanol. This low solubility for the imine conditioned the synthesis, since is not possible to synthesise and purify the imine prior the ZIF formation, since it could not be dissolved in a concentration high enough for the synthesis of the ZIFs. It was attempted to use THF and DMF during the synthesis of the ZIFs, that allow to use the synthesised and purified imine, but it led to micro sized ZIF particles (Figure 18). So, an approach on which the imine was formed in situ and kept dissolved in methanol was developed.

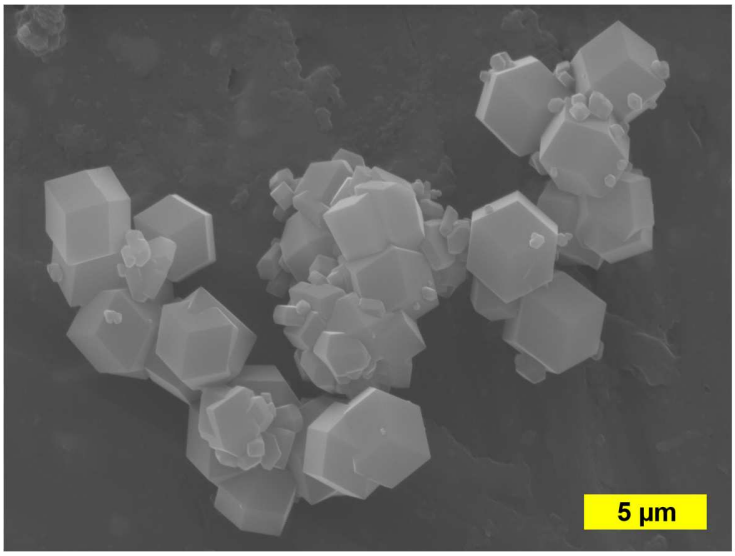

Figure 18 *SEM images of the modified ZIFs obtained using DMF as a solvent.*

- **Imine formation via Schiff base condensation: imine formation confirmation**

The first step on the synthesis of all the modified ZIFs on this works was the formation of the imine via Schiff base condensation. The formation of a Schiff base is an chemical equilibrium[166] (Figure 19).

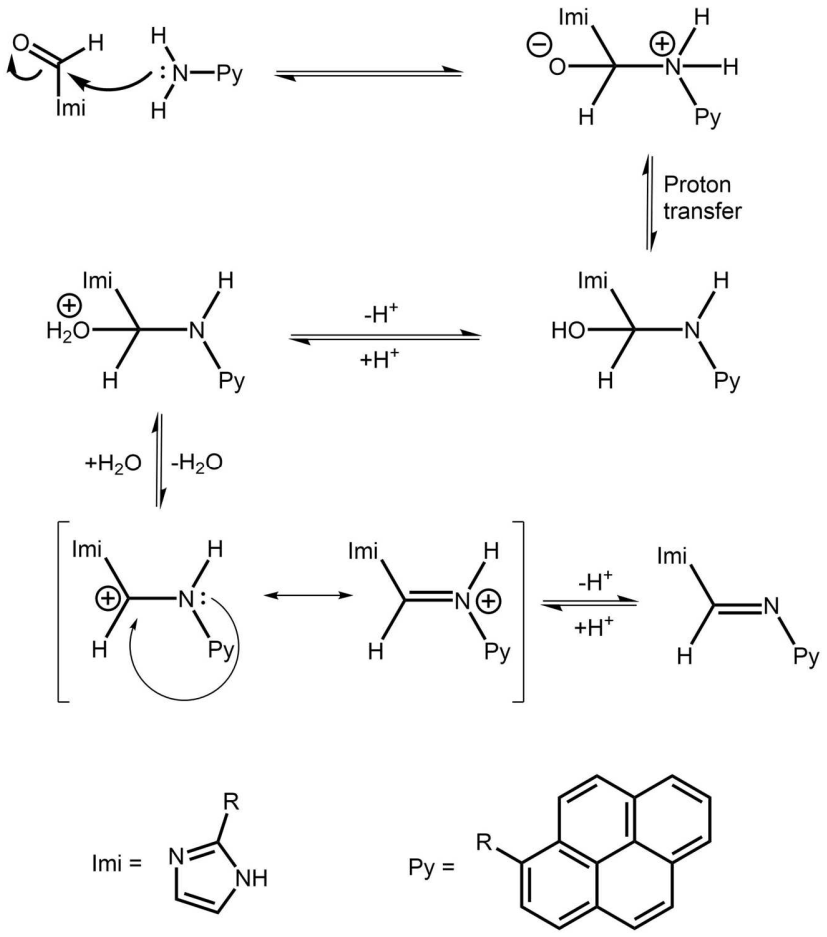

Figure 19 Mechanism of Schiff base formation for the imine of interest. The formation of a Schiff base is an equilibrium system[166]. The reaction begins with a nucleophilic attack at the carbonyl carbon of the aldehyde by the lone pair on the N atom of the incoming primary amine. A proton is moved from the positively charged nitrogen to the negatively charged oxygen producing a neutral carbinolamine. The OH group is then protonated by the acid, forming H_2O^+, which is a better leaving group than the OH group. This dehydration step leads to the formation of an iminium ion. The next step is the deprotonation of the nitrogen of the iminium ion by water and the formation of the final product, an imine. As the formation of water is one of the driving forces of the reaction, its removal should push the reaction to the right and maximize yields.

The comparison of the NMR spectra for all species involved in the imine synthesis, imine (Figure 21), 1ap and i2ca (Figure 20), provided information on the successful formation of the imine. Each spectra assignation can be found in section 7.1. The ^{1}H NMR spectrum for 1ap matched the one

reported in the literature[167], and it has a strong singlet that can be seen at 6.311 ppm, corresponding to the 2 protons of the amino group of aminopyrene. In the ^{1}H NMR spectrum of the imine the NH_2 peak at 6.311 ppm is barely visible (a small peak integrating for 0.07 can be seen due to impurities or slight hydrolyzation). When comparing the ^{1}H NMR spectra of i2ca and the imine, the peak corresponding to the proton on the aldehyde functionality on i2ca that can be seen at 9.647 ppm as a singlet is also vaguely present in the imine. A new singlet appears at 8.760 ppm on the imine ^{1}H NMR, corresponding to the proton on the carbon of the C=N bond of the imine. This result is a strong evidence of the successful formation of the imine.

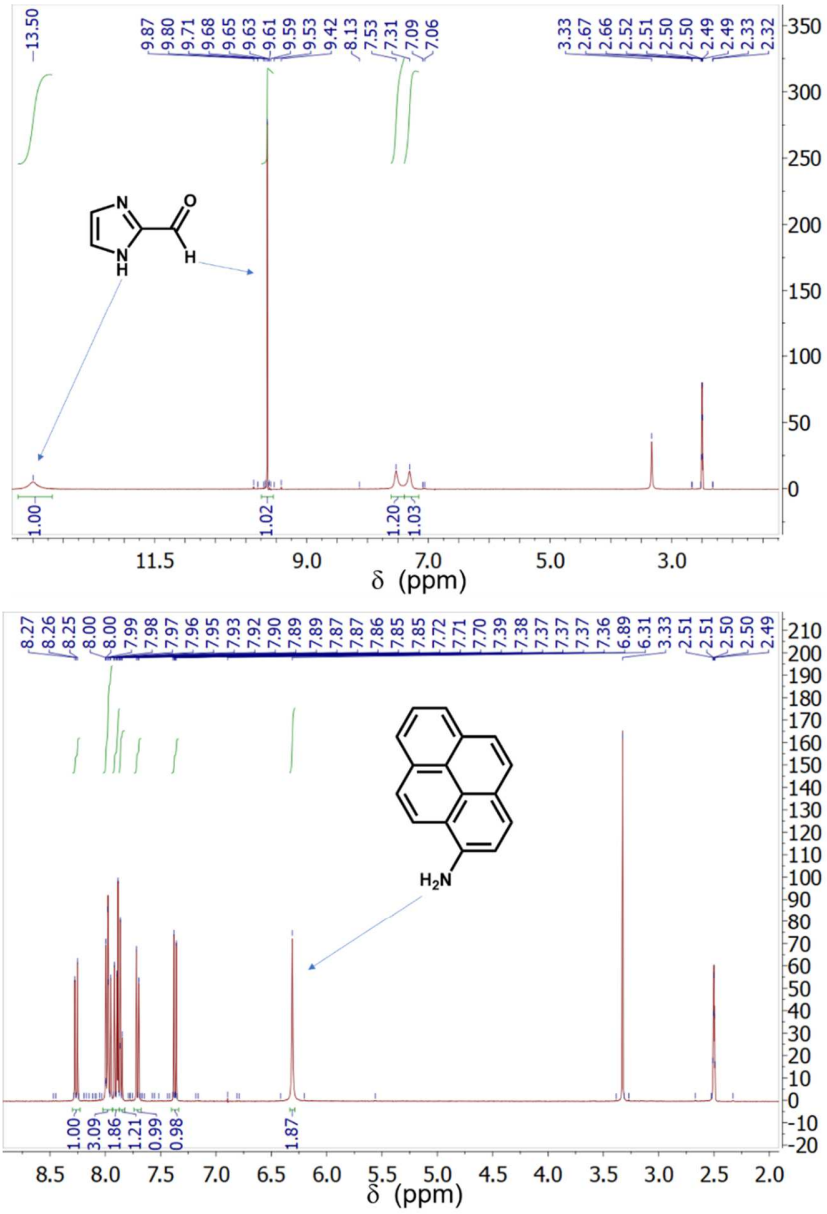

Figure 20 *^{1}H NMR spectra for 1-aminopyrene (1ap, bottom) and for imidazolate-2-carboxaldehyde (i2ca, top).*

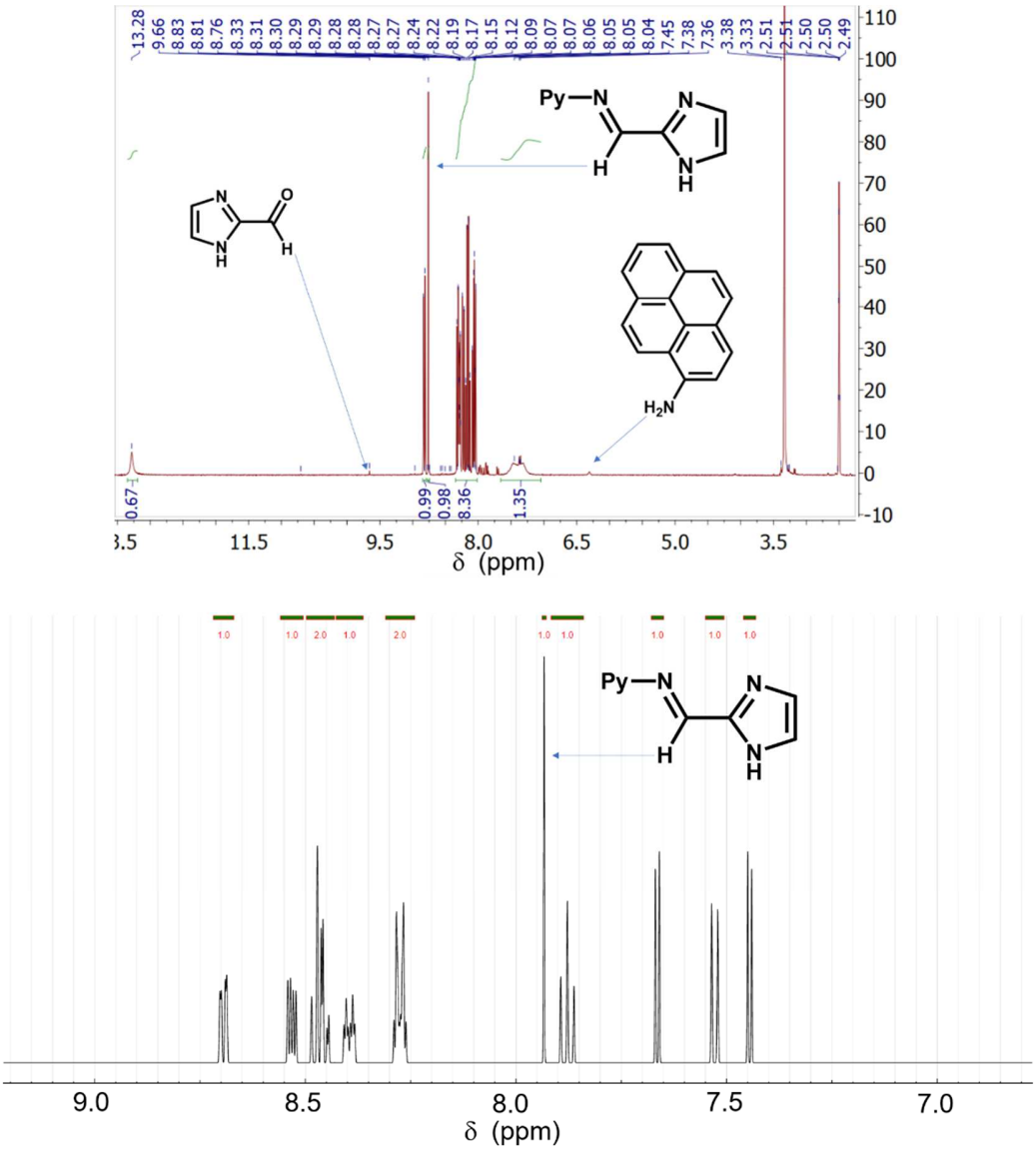

Figure 21 *Top: [1]H NMR spectra for the imine. Bottom: The simulated NMR spectra[168-170] for the newly formed imine[1].*

- **<u>Imine formation via Schiff base condensation: imine reaction characterization via HPLC</u>**

HPLC data support the fact that the synthesised imine was pure (Figure 22, see Figures 14 and 15 for the chromatograms for all species of interest), since only one peak could be observed on the

[1] https://www.nmrdb.org/new_predictor/index.shtml?v=v2.121.0

obtained imine solid dissolved on DMF. The purity of the synthesised imine showed that it could be used as a standard for the quantification of the composition of the modified ZIFs.

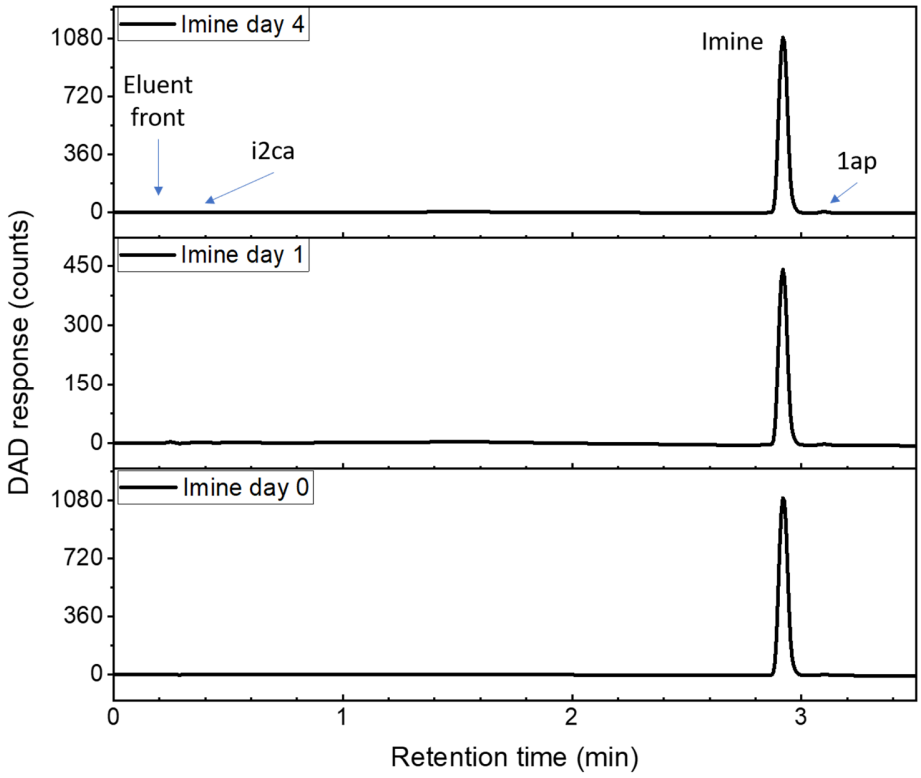

Figure 22 Chromatograms for the imine measured after the synthesis and purification (day 0) and the exact same sample kept at room temperature and protected for light for four days (day 4). A very small peak can be seen slowly appearing on the right of the main imine peak. The chromatograms are obtained using the acetonitrile-based methodology.

The equilibrium reaction time for the imine formation was studied by quantifying via HPLC the amount of imine, 1ap and i2ca present in different reaction solution for the Schiff base condensation while it evolves. In total five solutions with different levels of imine were let to react, with three replicates of each (Table 3). Once the reaction time was let to evolve, the composition of the mixture in equilibrium was quantified using the HPLC method developed (section 5.1). HPLC data for the imine formation (Figure 24) shows that the imine formation reaction reached equilibrium after 210 min, with a K_d value (Figure 23) calculated of $K_d = 12.10 \pm 0.91$ for the chosen conditions (80°C in methanol). The HPLC data for the imine equilibrium shows how the amount of imine obtained is directly dependant on the initial amount of 1ap (Figure 24 right).

Table 3 *Molar ratios for all constituents of the modified ZIFs at the starting of the synthetic process, expressed in mol. The obtained mass for the solid with a SOD crystal phase is shown as % mass*

MOF	i2ca	1ap	*% Imine targeted*
	mol	mol	*% mol/mol*
Z90P-5	4	0.2	*5.0*
Z90P-10	4	0.4	*10.0*
Z90P-15	4	0.6	*15.0*
Z90P-20	4	0.8	*20.0*
Z90P-25	4	1.0	*25.0*
Z90P-30	4	1.2	*30.0*

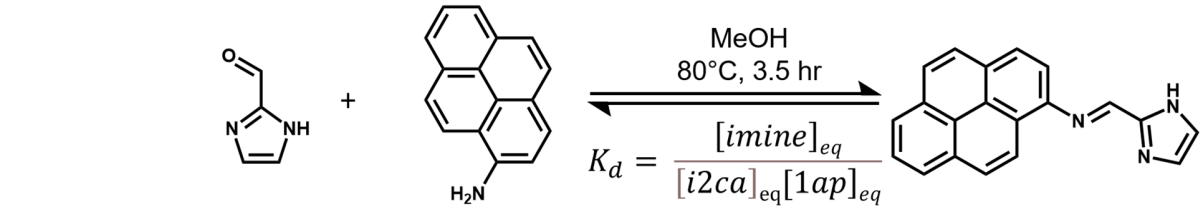

Initial (t=0.0 hr)	$[i2ca]_0$	$[1ap]_0$	
Equilibrium (t=3.5 hr)	$[i2ca]_{eq} = [i2ca]_0 - [imine]_{eq}$	$[1ap]_{eq} = [1ap]_0 - [imine]_{eq}$	$[imine]_{eq}$

$[i2ca]_0$ is kept constant on all ZIFs; $[1ap]_0$ is a function of $[i2ca]_0$

Figure 23 *Scheme of the formation of the imine via Schiff base condensation between 1ap and i2ca, with the chosen synthetic conditions and with the thermodynamic constant .*

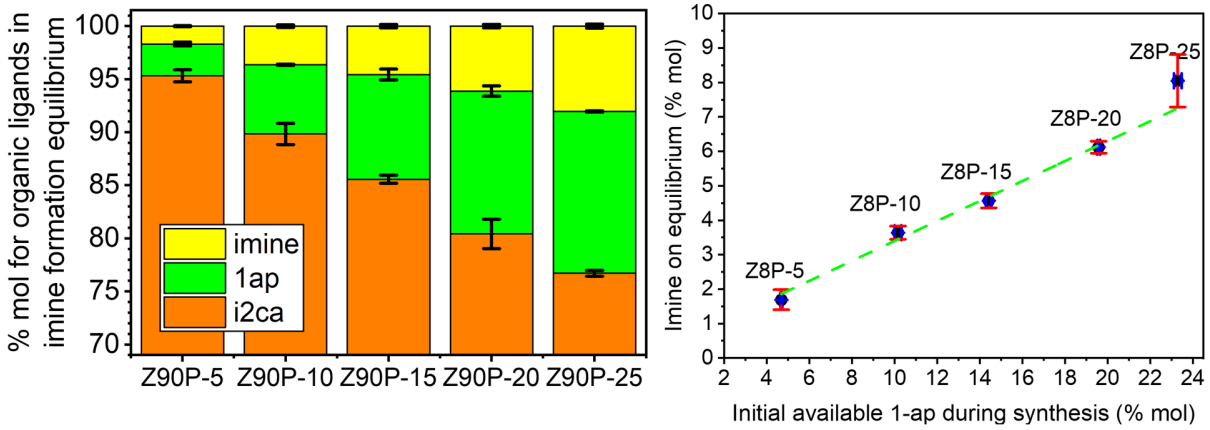

Figure 24 *Left: Averages for the amount for each of the chemicals of interest expressed as %mol/mL calculated from de HPLC data. It can be seen how an initial superior availability of 1ap during the imine formation leads to an increase on the final amount of available imine for the ZIF precipitation reaction. Right: Summary of the % mol for the imine in equilibrium plotted against the %mol for the initial available 1ap prior to the imine condensation reaction equilibrium. A quasi-linear tendency can be observed.*

Imines are sensitive to hydrolyzation when in the presence of water, leading to the imine bond reverting to its original constituents. To see how the imine in this work behaves, two control solutions were prepared, one dissolved in DMF (where the imine is stable for up to 4 days, Figure 22) and one in the EDTA digestion mixture. Both solutions were quantified via the HPLC methodology (section 5.1). The imine dissolved on the EDTA digestion mixture was quantified once every 15 mins, counted from the total dissolution of the imine in the solution, to check stability (Figure 25 left). HPLC quantification data shows that over time, and in the presence of H_2O, the imine suffers a relatively rapid hydrolyzation back to its original constituents, i2ca and 1ap. It is not possible to perform the measurement of the imine on the EDTA digestion solution without suffering some degree of hydrolyzation, since the presence of water to dissolve the EDTA is necessary. To prevent the imine hydrolyzation as much as possible the water contribution on the EDTA digestion solution was reduced as much possible. When preparing the EDTA digestion solution a 6:2 ratio for methanol:water rendered a homogeneous and clear solution, but the EDTA solution is found to gel within 24 hours. As such, EDTA solutions were prepared fresh prior to the ZIF digestion. Figure 25 shows that if the measurement was performed within 5 minutes after digestion the hydrolyzation observed is minimal. It must also be considered that the imine that is used as a starting standard for these hydrolyzation studies already had some degree of hydrolyzation, even stored in a desiccator and sealed in an Eppendorf tube under a nitrogen atmosphere for two weeks. The determination of the degradation speed of the imine on the EDTA digestion mixture showed that the imine can be quantified as a whole unit in the EDTA digestion solution.

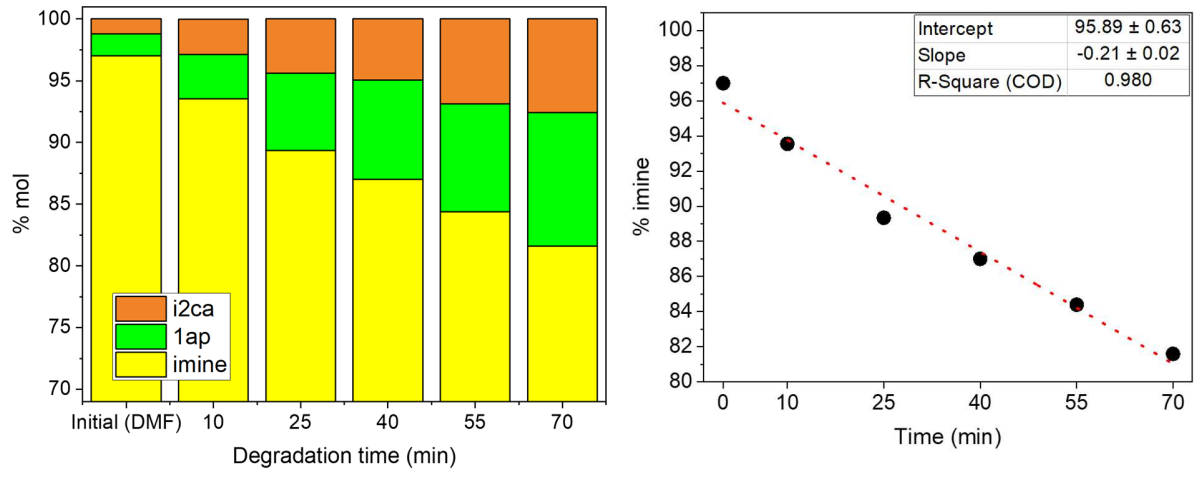

Figure 25 Left: Representation of the data of the imine hydrolyzation overtime in the presence of water (EDTA digestion mixture with water as cosolvent) at room temperature. Important to note that the imine that is used as a starting standard already had some degree of hydrolyzation, even though it is stored on a desiccator and sealed in an Eppendorf under nitrogen atmosphere for 2 weeks; Right: linear representation of the imine hydrolyzation overtime in the presence of water (EDTA digestion mixture with water as cosolvent) at room temperature, in %mol.

- **Synthesis of the fluorescent modified colloidal ZIFs**

Once the synthesis of the imine was established, a methodology to synthesise a nanoparticulated colloidal fluorescent modified ZIF was developed. As presented at the beginning of section 5.1, the synthesis for these ZIFs is a two-step one-pot reaction. To obtain a colloidal suspension in all cases methanol was used as solvent and $Zn(NO_3)_2$ as the source of zinc. Two different capping agents were used, n-butylamine (yielding Z8P-$5^{30}_{NbuAm,1:2}$) and sodium methoxide (yielding Z8P-$15^{30}_{MeONa,1:2}$). In both cases the ratios between the reagents was kept the same (1 : 2 : 14.3 : 0.004 for Zn : imidazole species (2mim and i2ca) : MeOH : caping agent). The two imidazole species were added in equimolar proportions. In both cases the synthetic methodology resulted in a yellow powdered solid, once it is separated via centrifugation and dried under vacuum and heat (section 4.3).

These powdered solids exhibited crystalline structures matching that of the sodalite (SOD) crystalline phase that has been reported for both ZIF-8 and ZIF-90 (Figure 26). From the TEM images the powder obtained with n-butylamine as capping agents was nanosized and non-aggregated (with an average size of around 35 nm, determined from TEM images only Figure 28 top). When using MeONa as capping agent also rendered nanosized and non-aggregated particles. The TEM images showed the rhombic dodecahedral shape reported for ZIF particles[171] (Figure 28 bottom). However, there is a significant increase in the particle size compared with the n-butylamine synthesis (range from 50 to 400 nm in diameter, also determined only from TEM images). Moreover, a higher size dispersity could also be seen when the particles obtained using the MeONa methodology is compared with the ones obtained with the butylamine methodology.

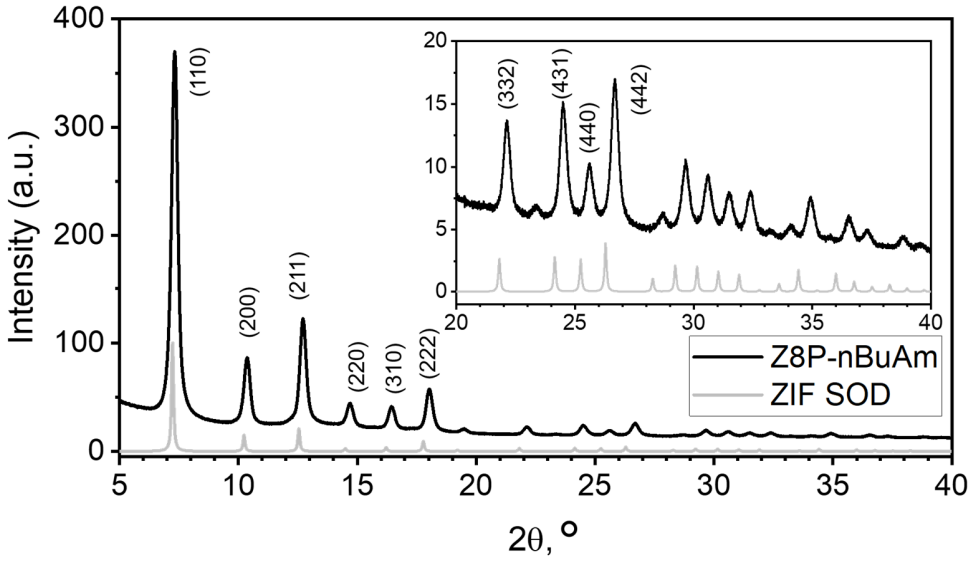

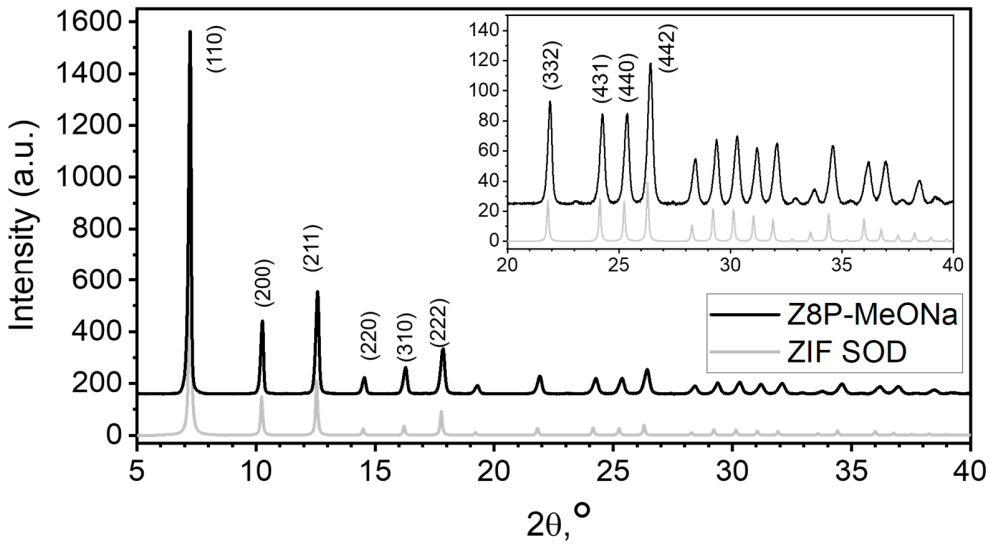

Figure 26 Top: Powder diffractogram for Z8P-5$^{30}_{NbuAm,1:2}$ measured in Bragg-Brentano geometry. Bottom: Powder diffractogram for Z8P-15$^{30}_{MeONa,1:2}$ measured in Bragg-Brentano geometry. The theoretical diffractogram for the SOD crystal phase, obtained from the CIF file for ZIF-8, is displayed on both diffractograms (grey line). The most relevant Miller indices are shown[172].

The use of n-butylamine yielded a smaller, monodisperse particle size when compared to the use of MeONa. However, the resulting ZIF can suffer from blocked aldehyde functionalities since the n-butylamine can form an imine via Schiff base condensation with the i2ca. Blocking any available aldehyde functionalities for the modified ZIFs will render the post-synthetic modification of the ZIFs less viable. ^{1}H NMR of the imine resulted of the Schiff base conjugation between the n-butylamine and i2ca is shown on Figure 27 top. The imine formation was performed on an equimolar ratio for both species involved, in methanol for 30 min at 80°C. A new compound was obtained, and the peak assignation were consistent with a new imine being formed, confirming the reaction between both reagents. To prevent the aldehyde functionality of the ZIF-90 crystal structure from being blocked by n-butylamine a capping agent that has no reactivity with the ZIFs functional groups was needed, hence the use of MeONa as alkaline capping agent.

MeONa showed the capacity to accelerate the formation of the ZIFs in solution by acting as a strong base and deprotonating the imidazole species. This alkaline acceleration during ZIF formation favoured the nucleation over the crystal growth, leading to an overall smaller particle size. Finally, MeONa yields methanol at the weak counter acid, which does not interfere with the ZIFs at all

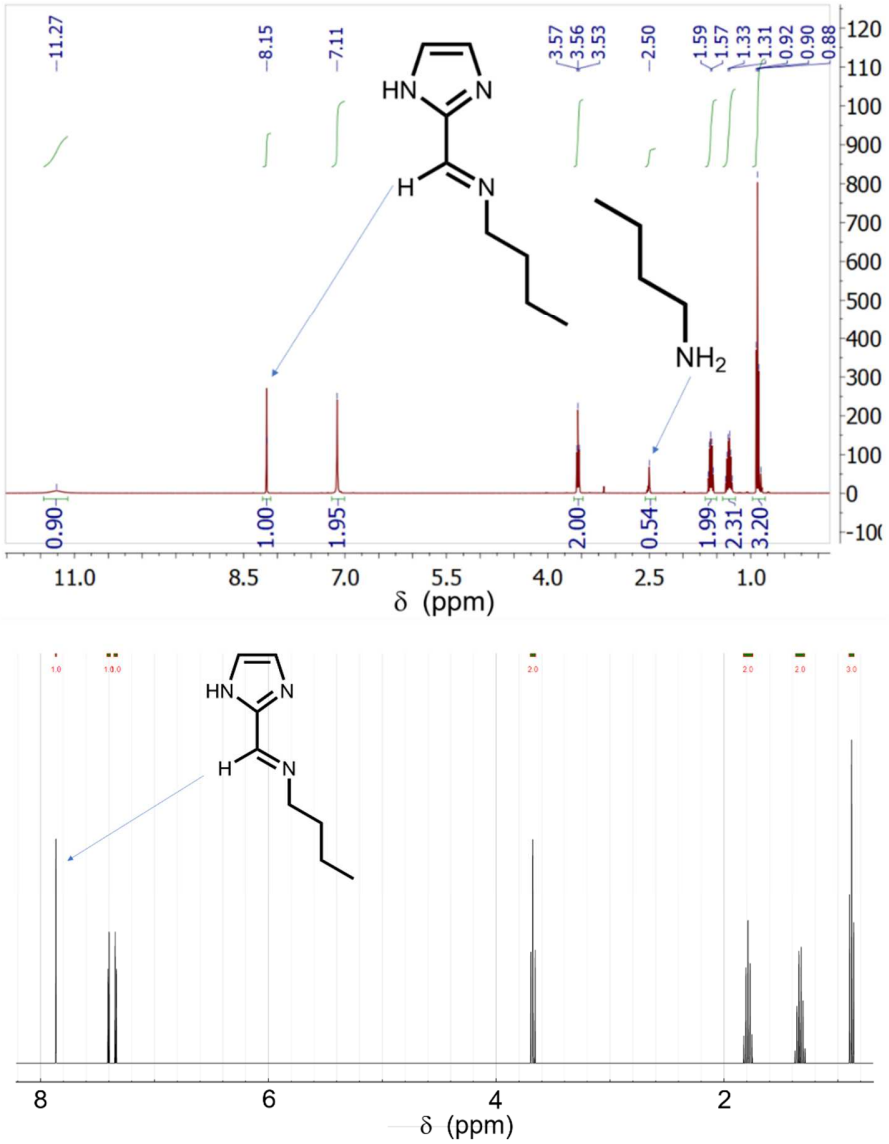

Figure 27 *[1]H NMR spectra for the imine formed between i2ca and n-Butylamine (top). The simulated NMR spectra[168-170] for the newly formed imine is also shown (bottom[2]).*

FTIR measurements of the modified ZIFs with ZIF-8 as a negative control and ZIF-90 as positive control showed that the aldehyde functionalities from i2ca were included in the modified ZIFs (Figure 29). All the characteristic peaks for each of the samples were consistent with the published spectra[173, 174] (Table 4). The band corresponding to the aldehyde functionality on the imidazolate-2-carboxaldehyde moiety (broad band at 1670 nm[55]) could only be observed on the ZIF-90 and the modified ZIF-8, Z8P and was not present in the unmodified ZIF-8.

[2] https://www.nmrdb.org/new_predictor/index.shtml?v=v2.121.0

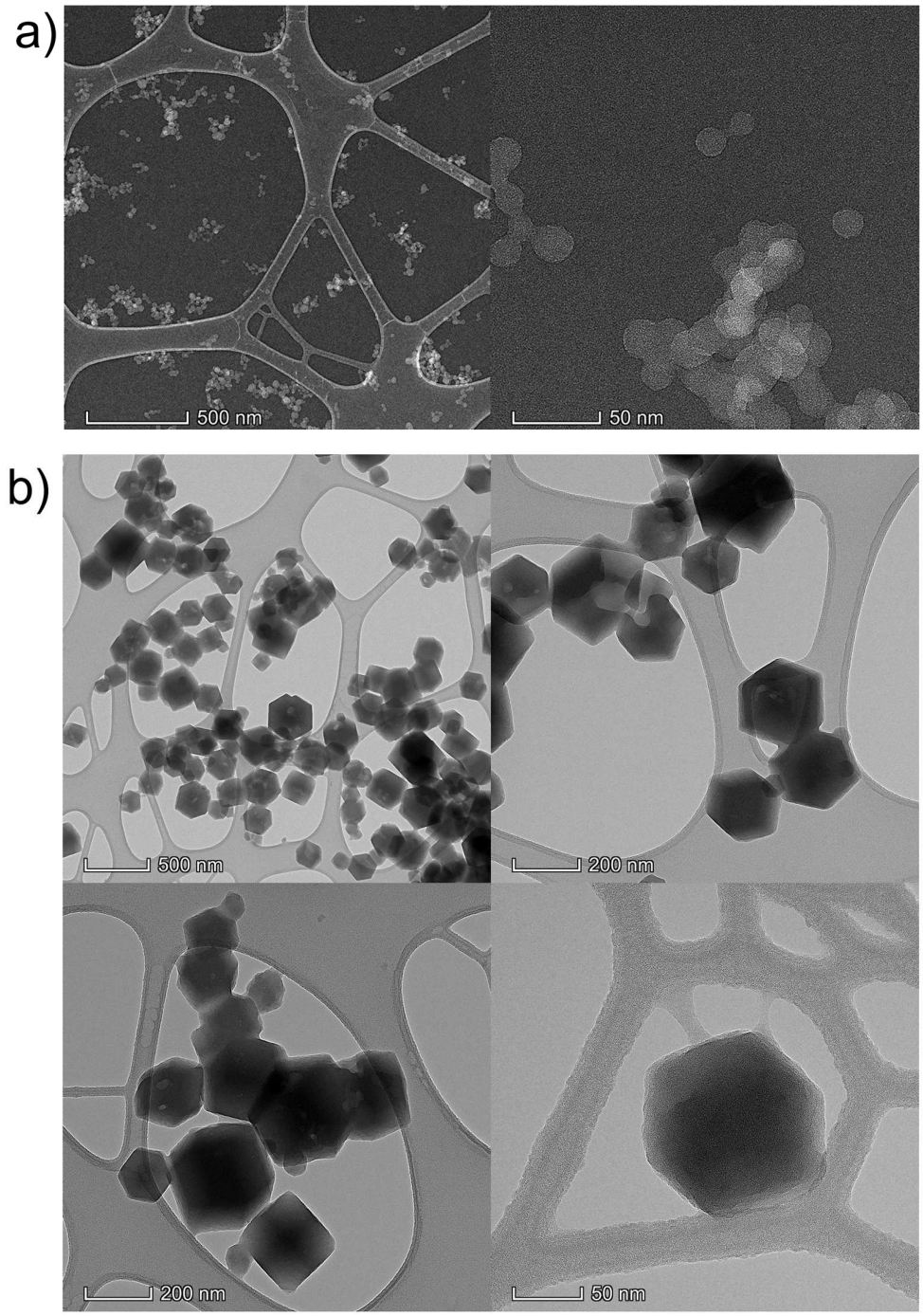

Figure 28 *a) TEM images for Z8P-15$^{30}_{NbuAm,1:2}$ dispersed in methanol.b) TEM Images for Z8P-15$^{30}_{MeONa,1:2}$.*

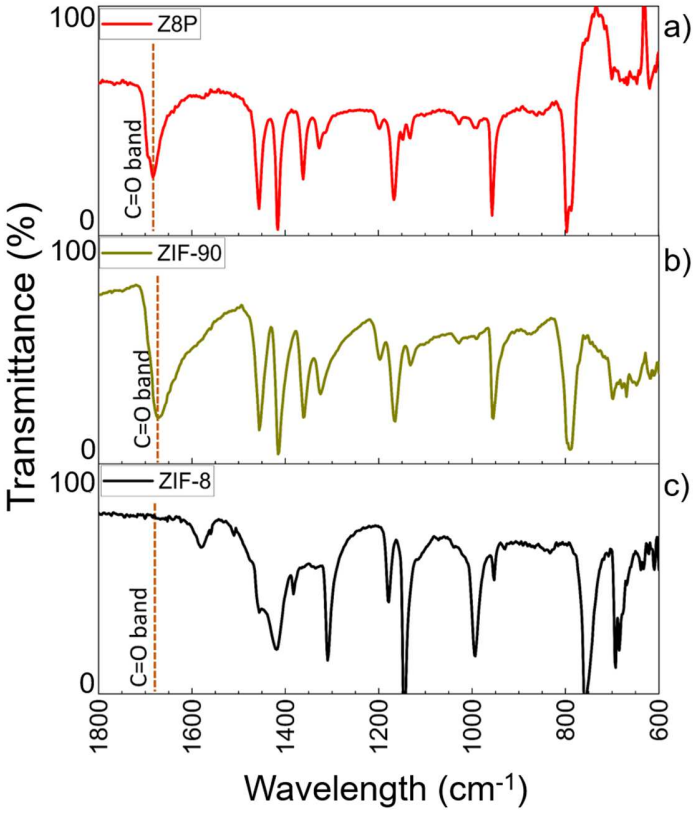

Peak position (cm^{-1})	Vibration assigned to
1670	free aldehyde on i2ca
1600	C=N imidazole ring
1457	imidazole ring stretching
1382	imidazole ring stretching
1145	C-N imidazole ring
995	C-N imidazole ring
760	aromatic sp^2 CH bending
690	aromatic sp^2 CH bending
421	Zn-N stretching

Figure 29 and Table 4 Left: FTIR spectra for a) Z8P (red line), b) ZIF-90 (green line) and c) ZIF-8 (black line). Right: Table with the FTIR band assignations. For the ZIF-8 particles, there are four characteristic peaks at 1600, 1145, and 995 cm^{-1}, assigned to vibrations of C=N, and C−N in the imidazole ring, respectively. The intense peaks at 1457 and 1382 cm^{-1} correspond to the entire ring stretching. Several spectral bands seen in the range 1350 to 900 cm^{-1} can be ascribed to the in-plane bending of the ring and the peaks at 760 and 690 cm^{-1} are associated with aromatic sp^2 C-H bending. Finally, a strong band at 421 cm^{-1} is observed that corresponds to the Zn-N stretching as the zinc atoms in the ZIF-8 structure connect to nitrogen atoms of the 2-mim linker during the formation of ZIF-8.

All the gathered data for the presented synthesis of the modified ZIFs strongly shows that a nanosized ZIF with available free aldehyde functionalities for posterior functionalization was obtained. The use of MeONa as capping agent has shown to be the most adequate choice since it allows to obtain non-aggregated nanoparticles while keeping the aldehyde functionalities free for any posterior functionalization.

4.3. ZIF composition as a function of initial reagents: Imine inclusion of the modified ZIFs

Synthesis of Z90P-(5-30) ZIFs and characterization via PXRD and HPLC

To explore further the imine inclusion of the ZIF obtained, as well as the relationship between the initial available 1ap during the imine reaction formation and the final imine inclusion, a new family of ZIFs was designed and synthesised (**Z90P-(5-30)$^{210}_{MeONA,1:4}$**, also Z90P). The Z90P family of ZIFs was synthesised by keeping all synthetic conditions constant (initial concentration for i2ca, $Zn(NO_3)_2$ and MeONa, time of reaction and reaction temperature), while increasing the initial amount of 1ap available (table 5). The imine formation reaction time was set to 3.5 hours before the ZIF formation is induced, since that is the time that was determined to reach a steady state of reaction (section 5.2).

Table 5 Molar ratios for all constituents of the modified ZIFs at the starting of the synthetic process, expressed in mol. The obtained mass for the solid with a SOD crystal phase is shown as % mass

MOF	$Zn(NO_3)_2$	i2ca	1ap	*% Imine targeted*	SOD mass obtained
	mol	mol	mol	*% mol/mol*	(% mass)
Z90P-5	1	4	0.2	*5.0*	96.97
Z90P-10	1	4	0.4	*10.0*	90.57
Z90P-15	1	4	0.6	*15.0*	14.15
Z90P-20	1	4	0.8	*20.0*	10.75
Z90P-25	1	4	1.0	*25.0*	6.29
Z90P-30	1	4	1.2	*30.0*	-

After the ZIFs were obtained, and prior to any washing of the solids, PXRD was performed for all the solids to ensure all Z90P were consistent with the SOD topology (Figure 30). All pre-washed modified ZIF solids showed a SOD phase, except for Z90P-30, which gave no diffraction signals. This lack of diffraction signals for Z90P-30 could indicate that the solid obtained was amorphous. This non-SOD Z90P-30 requires more studies to determine its nature, but within the scope of this work it was simply discarded. The intensities for all the diffraction peaks on the pre-washed modified ZIF solids decreased as the initial 1-ap increases. The absolute intensities on the diffractograms are not very meaningful since no calibration to relate intensity to mass of ZIF is performed. This decrease of the intensity, however, suggested that a smaller amount of the mass for the solids have the SOD crystal. PXRD analysis of the modified ZIFs solids after washing showed that no change in solid structure occurred during the washing procedure (Figure 31), and that the relative intensities of the peaks is comparable between the different ZIFs. During the washing process for the ZIFs a significant amount of solid mass reduction was observed. To quantity the mass loss during the washing procedure each solid was weighted before and after

washing them, and the mass difference between pre- and post-washed solids, prior to drying of the solids, was quantified (Table 5). There mass difference suggested that the total amount of SOD modified ZIF obtained decreases as a function of the initial available 1-ap. TEM images of the ZIF particle were also measured (Figure 32), accompanied by TEM-EDS quantification for all the solids. TEM images showed that, as the initial available 1ap increases, the particles lose their characteristic rhombic dodecahedra shape for a more pseudospherical shape, as their size shows a tendency to be reduced. EDS quantification showed two important aspects: first, the composition of the ZIF seems to be homogeneous withing one specific ZIF (Tables 9 to 14); second, the composition for all ZIFs determined by TEM-EDS is within the same range of values.

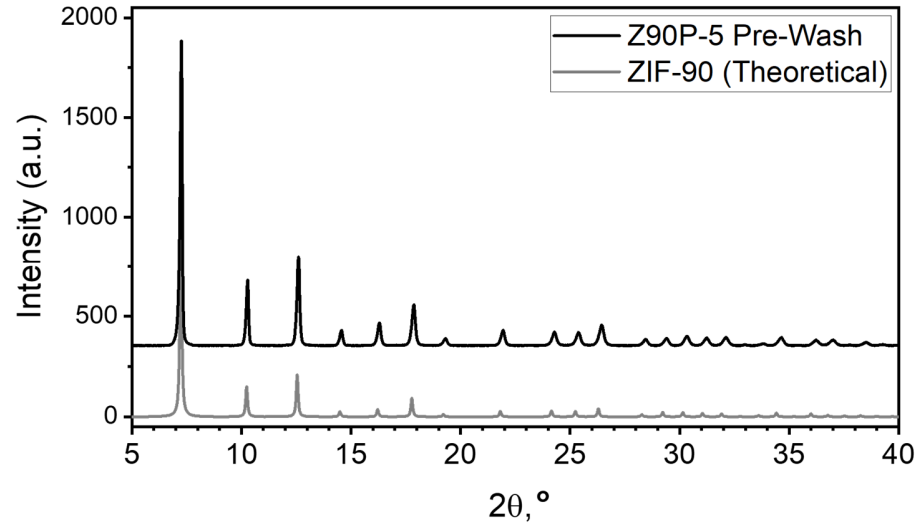

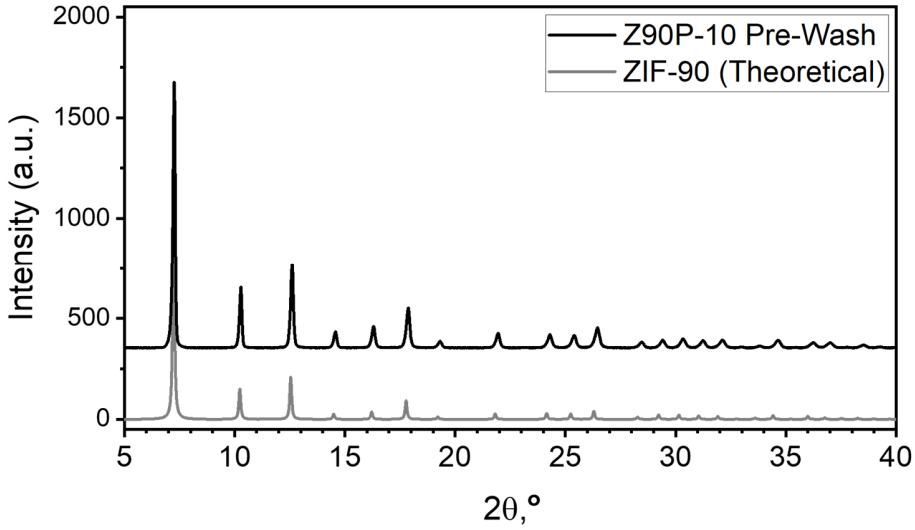

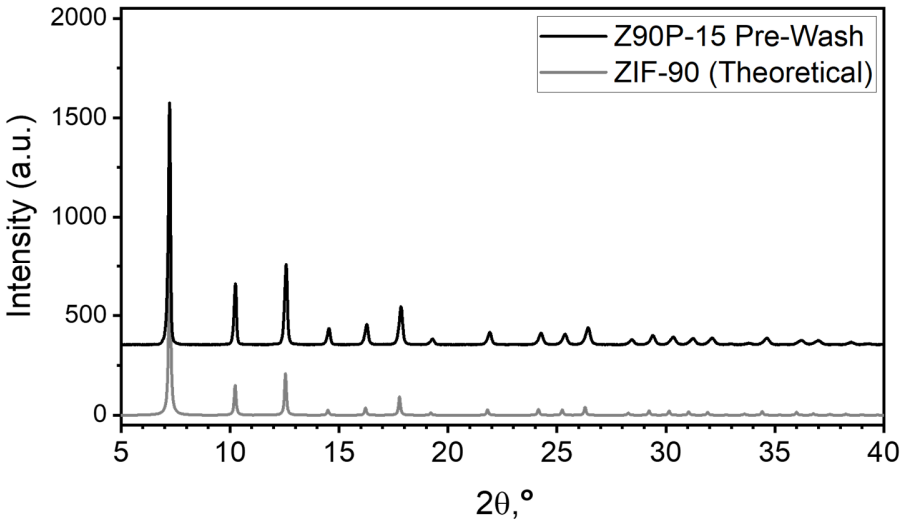
Z90P-15 Pre-Wash
ZIF-90 (Theoretical)
Intensity (a.u.)
2θ,°

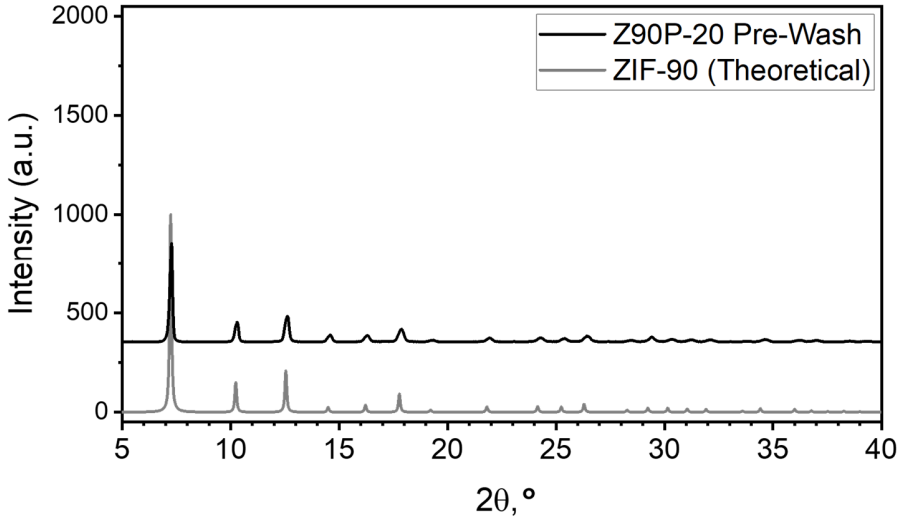
Z90P-20 Pre-Wash
ZIF-90 (Theoretical)
Intensity (a.u.)
2θ,°

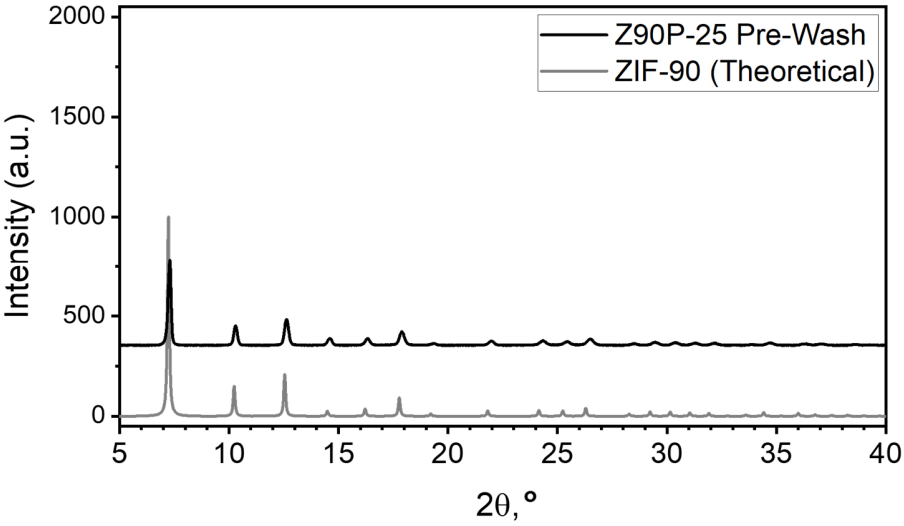
Z90P-25 Pre-Wash
ZIF-90 (Theoretical)
Intensity (a.u.)
2θ,°

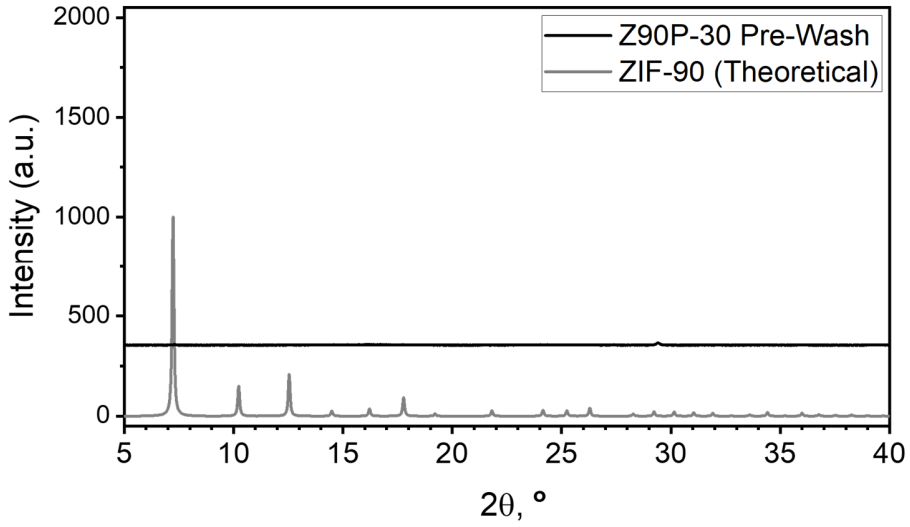

Figure 30 Powder X-ray diffractograms obtained on the Bragg Brentano geometry for each of the synthesised Z90P species before the washing steps, from top to bottom: Z90P-5, Z90P-10, Z90P-15, Z90P-20, Z90P-25, Z90P-30. The diffraction positions for the SOD crystal structure of ZIF-8 is represented on each diffractogram (grey line).

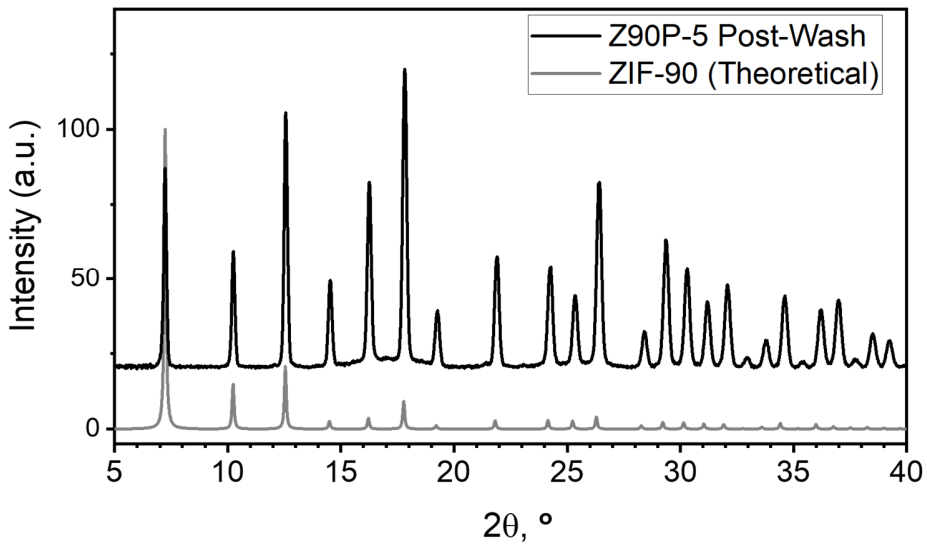

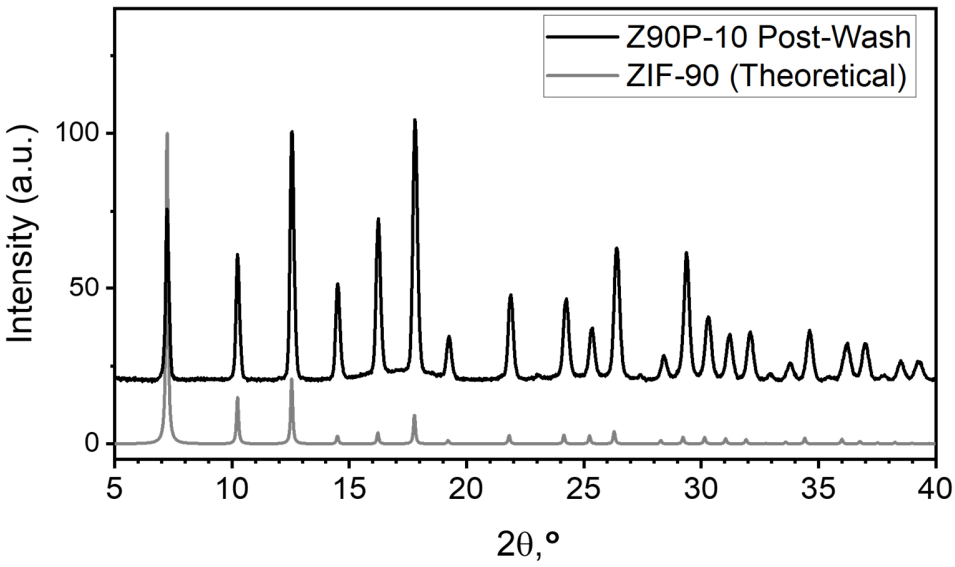
Z90P-10 Post-Wash
ZIF-90 (Theoretical)
Intensity (a.u.)
100
50
0
5
10
15
20
25
30
35
40
2θ,°

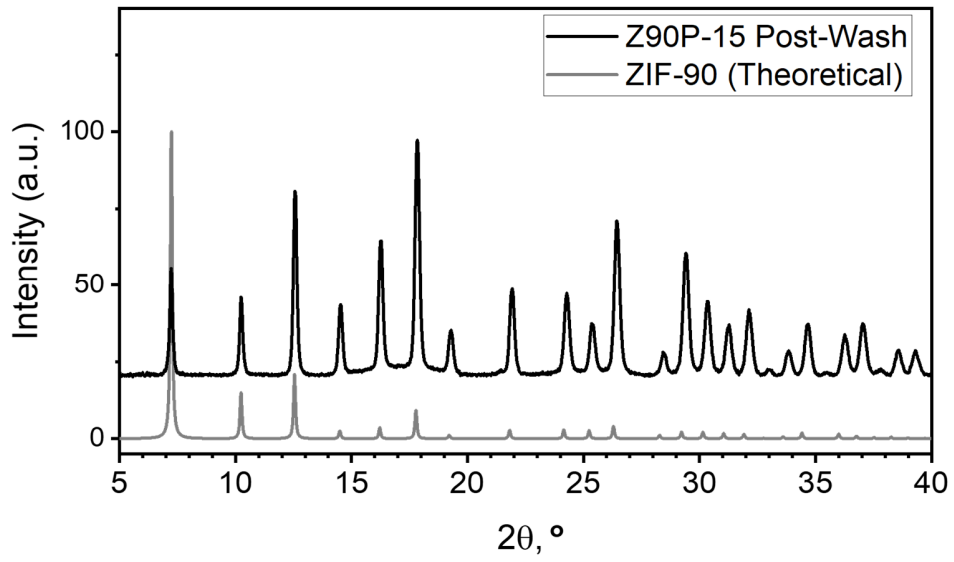
Z90P-15 Post-Wash
ZIF-90 (Theoretical)
Intensity (a.u.)
100
50
0
5
10
15
20
25
30
35
40
2θ, °

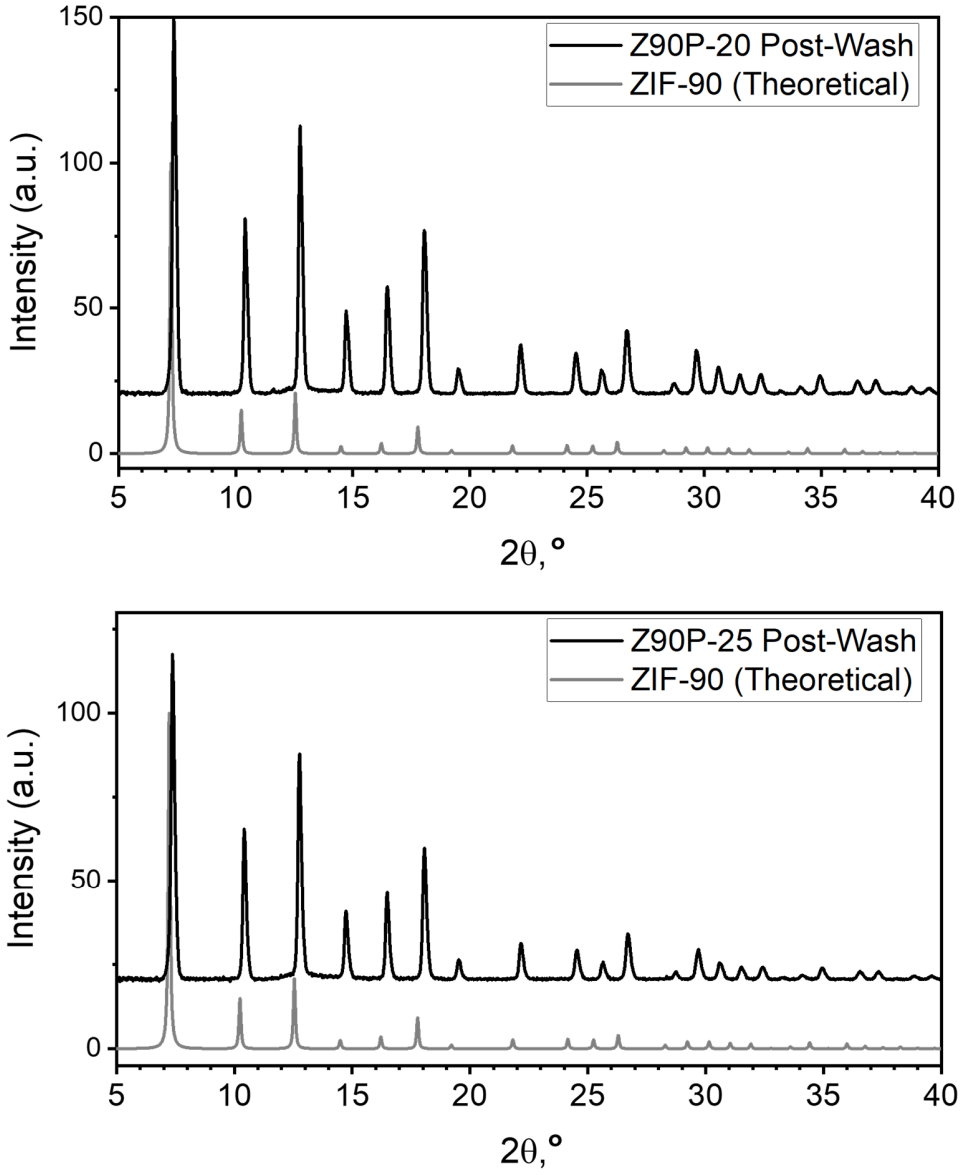

Figure 31 Powder X-ray diffractograms obtained on the Bragg Brentano geometry for each of the synthesised Z90P species after the washing steps, from top to bottom: Z90P-5, Z90P-10, Z90P-15, Z90P-20, Z90P-25. The diffraction positions for the SOD crystal structure of ZIF-8 is represented on each diffractogram (grey line).

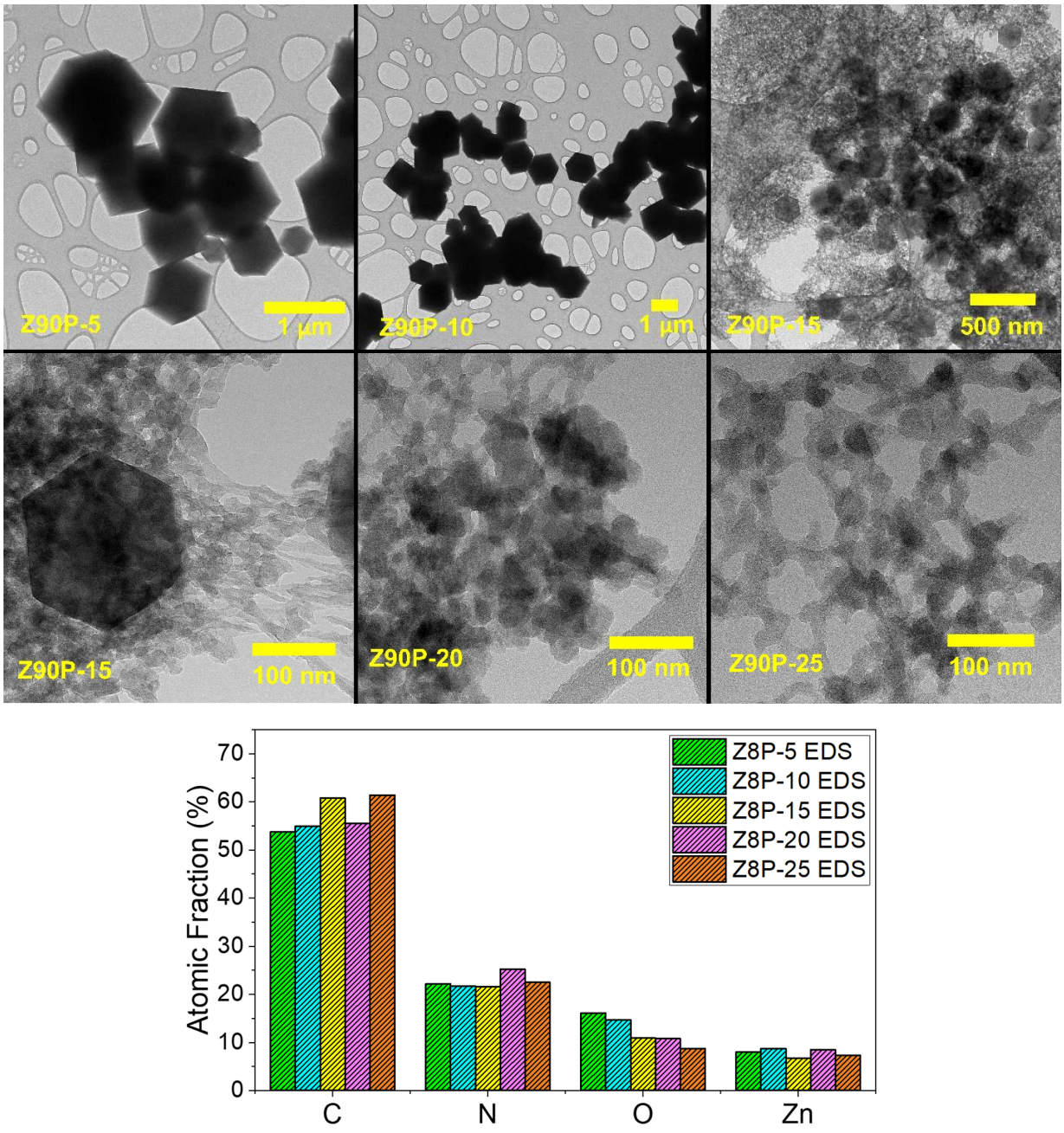

Figure 32 Top: TEM Images of all the synthesised Z90P ZIFs. It shows how, as the imine inclusion increases, the particles lose their characteristic rhombic dodecahedra shape for a more pseudospherical shape, as their size overall suffers a significant reduction in size. Bottom: Column histogram summarizing all the quantification results for the Z90P samples by TEM EDS (section 7.2). Each ZIF is quantified on three different spots of the TEM grid.

The results of the synthesis and characterization for the Z90P family of ZIFs has showed that there is a strong dependency between the initial available 1ap concentration and the final yield and particle size and shape for the final ZIFs. To understand why different concentrations of 1ap affects the final modified ZIFs more characterization must take place.

ZIF composition as a function of initial reagents: Digested ZIFs quantification

The HPLC quantification of the **Z90P-(5-30)$^{210}_{MeONA,1:4}$** family of ZIFs, with the EDTA digestion methodology, employing the acetonitrile HPLC methodology, yielded the results shown in Figure 33. The quantification of the Z90P ZIFs presented on Figure 33a and b were calculated as a % mol for all the directly quantified organic species forming Z90P; no contribution from the mass from the Zinc was considered. The HPLC data showed that the aminopyrene functionality is included in the ZIF as the imine, no significant amount of 1ap being detected. Trace quantities of 1ap were observed in the HPLC but presumably result from slight hydrolyzation for the imine, Figure 33a. This lack of 1ap not detected on the modified ZIFs is proof that there is no 1ap that resulted caged inside of the ZIFs pore structure when the ZIF was formed. Considering that the bulk of the ZIF particles is significantly more hydrophobic that the methanol solution, it was not unexpected to find a significant amount of 1ap caged within the ZIF pores. Should the 1ap preferentially diffuse to the inside of the ZIFs pore structure, then the washing process for the solid ZIFs is pushing the 1ap outside of the ZF structure, hinting that the 1ap can permeate the ZIF pores freely.

Determination of the Zn^{2+} content was performed indirectly from the HPLC quantification, as the mass difference between the total mass weighted for the ZIF prior to the digestion and the total mass for all organic species determined by HPLC. When the Zn^{2+} contribution for the composition of the ZIFs was determined by ICP-OES (Inductively coupled plasma optical emission spectroscopy, a direct quantification methodology) for the digested ZIFs, the results showed a good agreement with the indirect HPLC method (Figure 33c). When the HPLC composition data for each Z90P ZIF are converted to % atomic fraction (section 7.3 shows the equations to convert the HPLC data), a direct comparison to the quantification done by TEM-EDS for the ZIFs is possible. Both quantification methodologies render results over a very similar range of values, proving the strength of the HPLC quantification of the digested ZIFs (Figure 33d). The linear tendency observed when plotting the % mol for the imine inclusion on the synthesised Z90P ZIFs against the %mol for the initial available 1ap prior to the imine condensation reaction (Figure 34 right) suggests a direct dependency between the final imine inclusion on the ZIF and the initial available 1ap during the imine formation reaction. this direct relationship offers the opportunity to predict how much imine will be formed when designing the experiment, as well as offering reproducibility during the synthesis of the ZIFs.

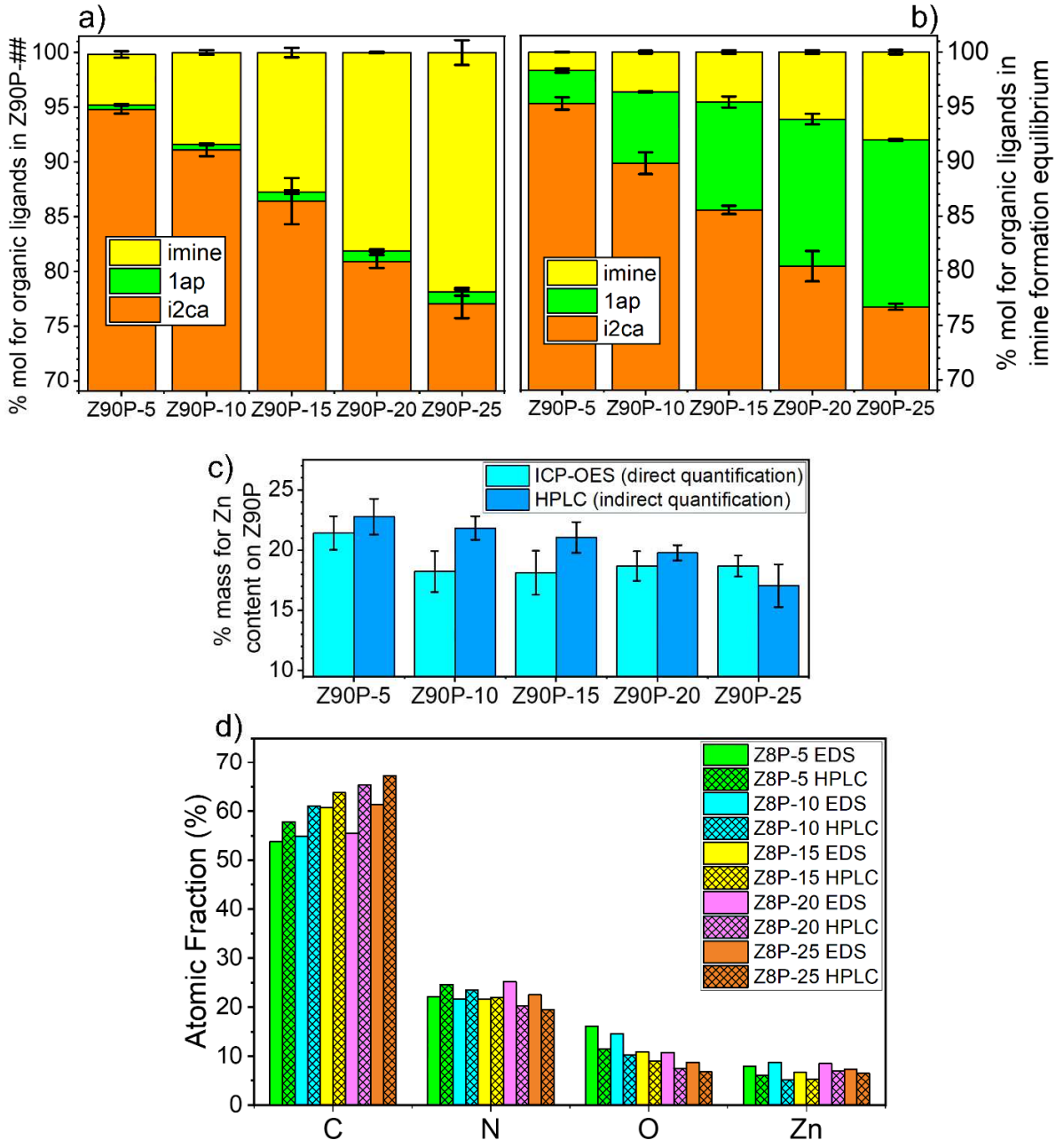

Figure 33 Summary of all the quantification for the ***Z90P-(5-30)$^{210}_{MeONA,1:4}$*** *family of ZIFs. a) Summary of the Z90P EDTA digestion quantification is shown as a % mol for all the directly quantified organic species forming Z90P. when calculating the % mol/g of ZIF only the contribution of the organic constituents was considered; no contribution from the mass from the Zinc was considered. b) Summary of the Z90P imine equilibrium reaction is shown also as a % mol for all the directly quantified organic species involved on the reaction. c) Summary of the comparison of the results for Zn composition, express in % mass, obtained by ICP-OES and HPLC. d) Column histogram summarizing all the quantification results for the Z90P samples by TEM EDS and by HPLC as atomic fraction.*

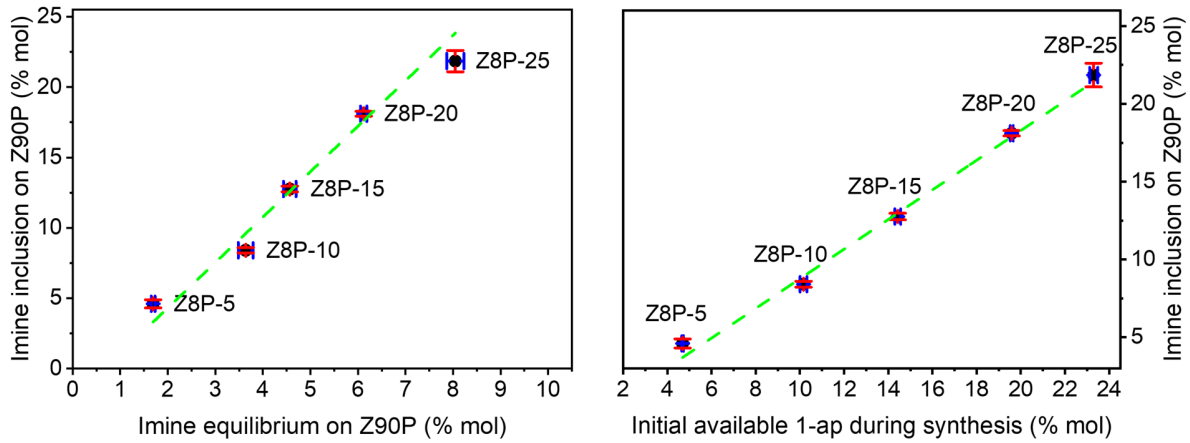

Figure 34 Graphical representation for the % mol for the imine inclusion on the synthesised Z90P ZIFs from Figure 33a are plotted against the %mol for the imine on the imine condensation reaction equilibrium from Figure 33b; the % mol for the imine inclusion on the synthesised Z90P ZIFs from Figure 33a are plotted against the %mol for the initial available 1ap prior to the imine condensation reaction equilibrium.

The HPLC quantification of the **Z90P-(5-30)^{210}$_{MeONA,1:4}$** family of ZIFs, considering the contribution of all the species on the ZIF, organic ligands (direct quantification from HPLC) and metallic node (indirect quantification from HPLC), yields the results shown on Figure 35. Since the obtained ZIFs have the SOD crystal phase (Figure 32) they are conditioned to be constituted by one metallic node for two bridging ligands. In the case of the Z90P ZIFs, the metallic node was Zn^{2+}, and the bridging ligands were i2ca and imine. This specific ratio between imidazolate bridging ligands and zinc metallic nodes was obtained for all the synthesised ZIFs. This confirmation on the ratio between the imidazolates and the zinc is a strong evidence that the imine is forming part of the crystal structure of the ZIFs, which combined with the quantification exclusively of the imine with the EDTA digesting of the ZIFs, is an unambiguous evidence that the imine is included as a structural unit on the modified ZIFs.

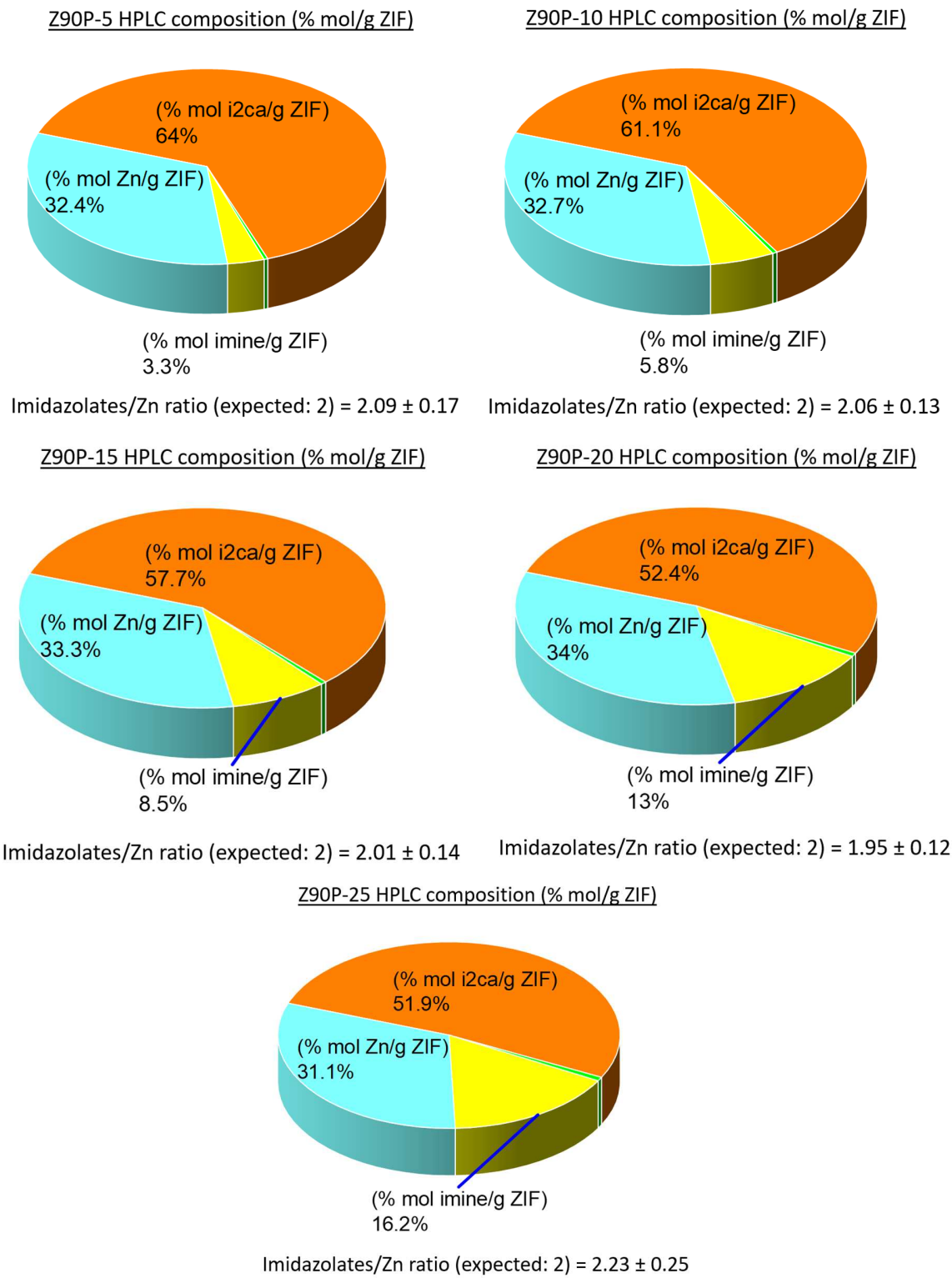

Figure 35 Pie chart representation for the % mol of the Z90P EDTA digestion quantification, shown as a % mol for all the directly quantified organic species forming Z90P, as well as the indirectly calculated % mol/g of the Zn^{2+}. Given the crystallographic nature of the ZIFs, it was also possible to quantify the ratio between the zinc cores and the imidazole bridging ligands. This ratio is expected to be 2.

The developed HPLC quantification methodology to determine the composition for ZIFs has shown its potential when quantifying the composition for the Z90P family of ZIFs. A direct dependency on the inclusion of the imine in the final structure of the modified ZIFs as a function of the initial available 1ap has been found. Strong evidence that the imine is included as a structural unit has also been found.

Insight of a ZIF architecture under sterically constrained conditions

The imine inclusion quantification for the **Z90P-(5-30)^{210}$_{MeONA,1:4}$** family of ZIFs showed a direct correlation between the initial availability of the imine pre ZIF precipitation and the imine inclusion in the final modified ZIF as a function of the initial available imine pre-ZIF formation (Table 6). With all other synthetic conditions kept constant, an increased availability of imine during the formation of the Zn-imidazole coordination monomers implies an increase of the statistical probability of the imine to be part of the coordination sphere of a zinc atom. The formation of the Zn-imidazolates coordination species is the first step for the most accepted formation mechanism for the ZIFs[87] (Figure 4). This increase on the inclusion of the imine within the zinc coordination sphere will be transferred to the formation of the oligomeric nanoclusters that will later reorder into the crystal structure for the ZIF. This increase of the imine contribution on the oligomeric nanoclusters will then render a final crystal structure with a higher inclusion of the imines. The linearity seen on the relationship between the initial amount of 1ap and the final inclusion of the imine on the modified ZIFs allows to design a synthetic methodology to obtain a specific final inclusion of the imine within the modified ZIFs.

Table 6 Summary of the relevant results for the obtained modified ZIFs. The yield is calculated as a ratio between the total mass of solid obtained before and after the washing of the powder with DMF. The imine inclusion is calculated from the EDTA digested HPLC quantification process for the ZIFs. The imine initial availability is calculated from the HPLC data from the Schiff base condensation reaction.

Sample	SOD mass obtained	Imine inclusion on the Z90P crystal structure	Average particle size and shape seen by TEM
	(%)	(% mol)	(nm)
Z90P-5	96.97	4.601 ± 0.022	500-2000, Rhombic dodecahedra
Z90P-10	90.57	8.405 ± 0.014	500-1000, Rhombic dodecahedra
Z90P-i	-	8.33	-
Z90P-15	14.15	12.756 ± 0.031	150-200, Rhombic dodecahedra 50-100; Pseudospherical

Sample	SOD mass obtained	Imine inclusion on the Z90P crystal structure	Average particle size and shape seen by TEM
Z90P-20	10.75	18.104 ± 0.005	50-100; Pseudospherical
Z90P-25	6.29	21.851 ± 0.089	50-100; Pseudospherical

Table 6 shows how a higher inclusion of the imine in the ZIFs lead to a significant reduction in the amount of SOD ZIF obtained, as well as the reduction in size and loss of regular shape. This loss suffered its biggest drop between Z90P-10 (imine inclusion of 8.405 ± 0.014 %mol) and Z90P-15 (imine inclusion of 12.756 ± 0.031 %mol). The explanation proposed on this work to this drop on the obtained SOD yield requires first the theorization of a new member of the ZIFs. **Z90P-i** is an ideal and theoretical Z90P crystal (**Z90P-i**) infinite in size (no surface is considered, only the bulk). To estimate the maximum amount of imine that can be included inside this ideal ZIF-90 crystal the following parameters are considered:

1- The diameter of a ZIF-90 pore is 11 Å[55]; this provides a theoretical maximum spherical volume of 5575 Å^3.
2- From the crystallographic data for 1ap from a reported single crystal structure[175], a molecular volume of 270 Å^3 is theoretically obtained[3] for a single molecule of 1ap. This volume is 5% of the total available volume inside the ZIF pore.
3- The 1ap functionality is included as the imine within the crystal structure of the ZIF. HPLC data strongly suggest that the imidazolic fragment of the imine is part of the crystal structure of the modified ZIFs (section 5.3, "ZIF composition as a function of initial reagents: Digested ZIFs quantification"). Since all aldehyde functionalities point towards the inside of the pore (Figure 36), this will force the 1ap functionality to be located inside the pore pointing towards the centre of the spheric pore. This spatial distribution of the imine inside the ZIF pore makes it unlikely that two aminopyrene functionalities cannot be contained within one pore, since they will suffer a very high steric push.

The proposed disposition of the 1ap inside of the ZIF pore conditions how much 1ap can be included on the pore of the ZIF. Figure 36 shows a simple modelling using Avogadro[176] and the reported cif file for ZIF-90, were the imine was placed substituting one of the i2ca building blocks, facing toward the centre of the pore. After placing the imine, a simple geometry optimization algorithm was run. The most favourable position was shown to be the imine bisecting the ZIF-90 pore, pointing towards the centre of the pore. When two imine functionalities were placed inside, the relative positions of the imidazole building block within the crystal structure determined if the inclusion is stable. Figure 37 shows the only stable conformation found on these simple simulations that allow for the inclusion of two imine functionalities. The imine functionalities were included on the crystal structure anchored to the crystal structure on spatially opposite points of the pore. Any other spatial positioning of the imines withing the ZIF crystal structure rendered an unstable

[3] This theoretical volume was calculated using the reported crystal structure for a cocrystal including 1ap,

final structure. Figure 38 show the simple modelling of the two imine functionalities included on the pore anchored on adjacent windows of the crystal structure; the end result was the two pyrene functionalities clash and repel each other, leading to one of them being pushed within one of the small windows of the pore. A deeper theoretical model is required to better understand exactly how the aminopyrene functionality contained within the imine is oriented within the ZIF pore. However, it is at present sufficient to say that given the spatial disposition of the 1ap within the pore it seems unlikely that two 1ap functionalities can share one pore.

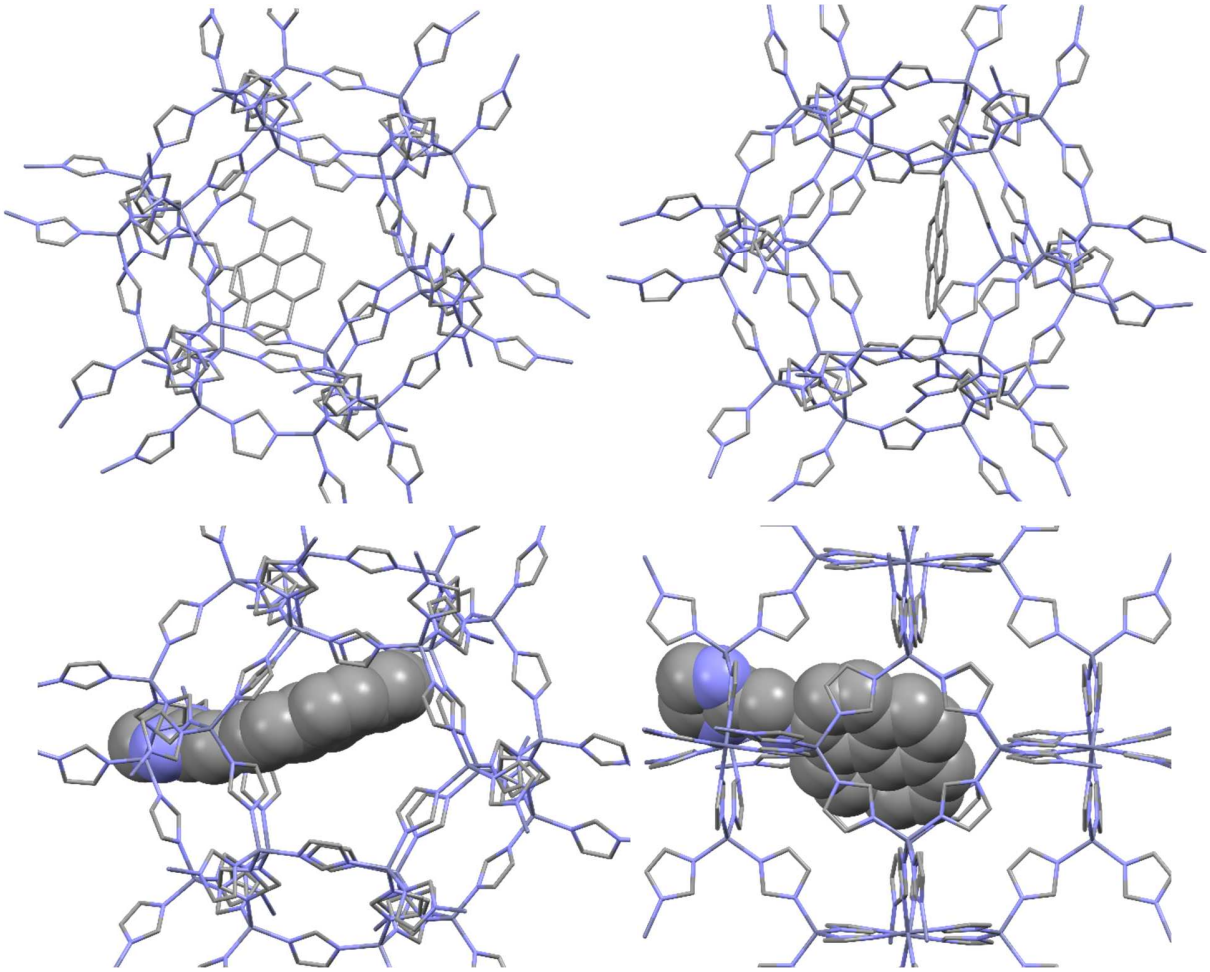

Figure 36 Simple representation of the disposition of the imine as part of the ZIF-90 pore. The representation is done with the ZIF-90 CIF file as a basis, manually including the imine functionality on Avogadro[4] and running a basic geometry optimization. The aldehyde functionality located on the carbon at the N-C-N fragment of the i2ca imidazolic building blocks have been removed to facilitate visualization, as well as the hydrogen atoms.

[4] Avogadro: an open-source molecular builder and visualization tool. Version 1.20. http://avogadro.cc/

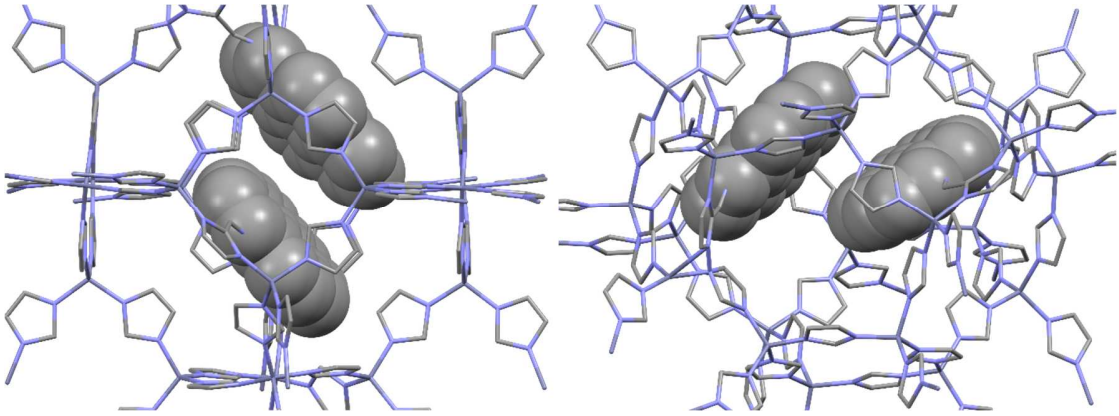

Figure 37 Simple representation of the disposition of two imine functionalities as part of the ZIF-90 pore, placed spatially oppose to each other. The representation is done with the ZIF-90 CIF file as a basis, manually including the imine functionality on Avogadro and running a basic geometry optimization. The aldehyde functionality located on the carbon at the N-C-N fragment of the i2ca imidazolic building blocks have been removed to facilitate visualization, as well as the hydrogen atoms.

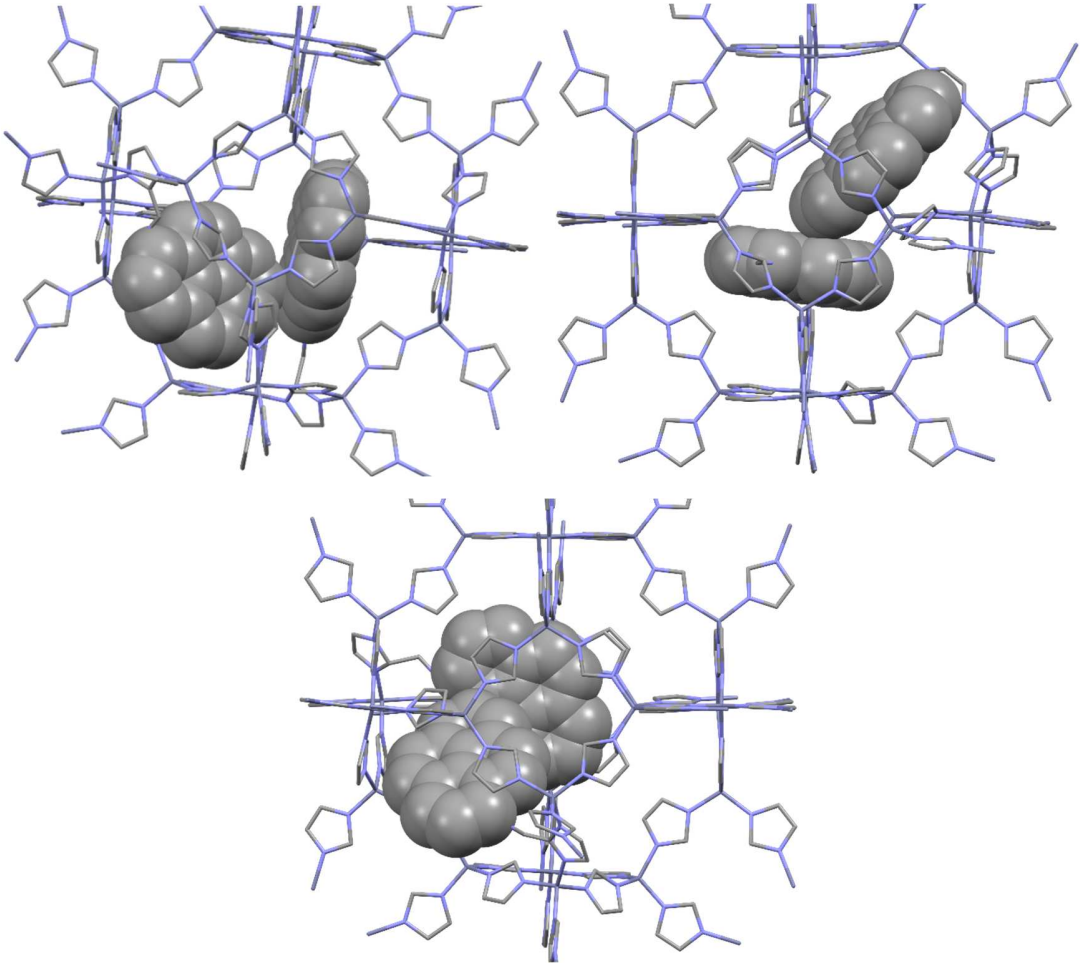

Figure 38 Simple representation of the disposition of two imine functionalities as part of the ZIF-90 pore, placed on contiguous small windows to each other. The representation is done with the ZIF-90 CIF file as a basis, manually including the imine functionality on Avogadro and running a basic geometry optimization. The aldehyde functionality located on the carbon at the N-C-N fragment of the i2ca imidazolic building blocks have been removed to facilitate visualization, as well as the hydrogen atoms.

Assuming then that only 1ap functionality can be contained within one ZIF pore, a unit cell for a theoretical ideal Z90P crystal (**Z90P-i**) including one 1ap functionality per pore is $C_{64}H_{43}N_{25}O_{11}Zn_6$. This means the unit cell formula for **Z90P-i** will be formed by **<u>11</u> i2ca molecules** and **<u>1</u> imine molecule**. From this it is possible to calculate the composition of this Z90P (Table 7).

Table 7 Composition of the idealized Z90P, called "Z90P-i", express as molecules in unit cell and in %mol for its both organic constituents, i2ca and imine.

	Molecules in unit cell of Z90P-i	**Composition of Z90P-i**
	(#)	**(% mol)**
i2ca	11	***91.67***
imine	1	***8.33***
$(\%\ mol\ for\ analyte) = 100 \cdot \frac{molecules\ in\ unit\ cell\ of\ Z90P-i\ for\ analyte}{\sum molecules\ in\ unit\ cell\ of\ Z90P-i\ for\ all\ analytes}$		

The calculated imine inclusion for Z90P-i fits very closely to the real composition obtained of included imine for Z90P-10 (Table 6). This suggests that, considering only inclusion of the imine on the bulk of the crystals for the ZIFs, the distribution of the imine on the crystal tends to fill each pore with one imine functionality. The inclusion of more than one imine on the crystal structure will lead to two imine functionalities on each pore, which simple calculations suggested is not favourable, and will lead to crystal deformations. This crystal deformation due to the overinclusion of imine can be put into context with the ZIF formation mechanism proposed by Cravillon (Figure 4). When the ZIF is reordering itself from the amorphous oligomer to the crystalline structure, it exposes the imines towards the outside of the bulk, and to maximize this the surface must increase, thus the particles become smaller. This unfavoured ordering leads to the abrupt decrease of the SOD mass of ZIF obtained with Z90P-15 and onwards. A higher presence of imine on the oligomer when the ordering is taking place will increase the steric impediment, hindering the formation of the crystal phase.

The data presented here are strong evidence of the imine being included as a building block on the modified ZIFs. The data in this section also suggest a favourable inclusion for the imine in the bulk of the ZIF nanoparticles rather than at the particle surface if the available initial imine is below 8.5% mol (Figure 33 and Table 6). An increase on the initial available imine pre-ZIF formation will generate particles with a bigger exposure of the imine on the surface of the ZIFs, at the expense of reaction yield, particle size, particle regular shape and, most importantly, particle aggregation. Additional techniques must be performed on the particles to have a deeper understanding of the mechanistic inclusion of the imine on the ZIFs. AFM (atomic force microscopy) coupled to fluorescence microscopy[177], can locate areas of the nanoparticle that are fluorescent and with AFM locate the spatial position of the imine within the nanoparticles.

4.4. Fluorescence response of the modified ZIFs against short chained Phthalate acyl esters (PAEs)

To function as sensors for phthalate acyl esters (PAEs), the fluorescence behaviour of the modified ZIFs was investigated. Using the modified ZIFs, it was envisioned to detect the presence of PAEs as a function of the reduction of fluorescence emission for a dispersion of the fluorescent ZIF[178] (Figure 39). The π-π stacking interactions between the chromophore (pyrene covalently bound to the modified ZIF structure) and the aromatic analyte (PAEs), should be responsible for fluorescence relaxation leading to the quenching[122, 179]. For the results presented on this section, **Z8P-15^{30}$_{MeONa,1:2}$** (Z8P) is used as the fluorescent ZIF.

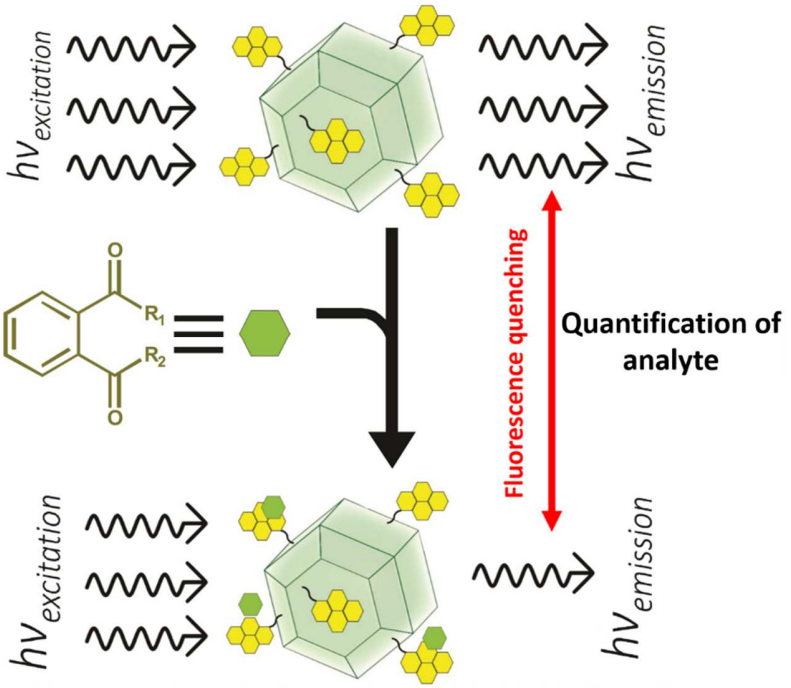

Figure 39 Scheme representing the fluorescence quenching of the modified ZIFs when exposed to PAEs.

The HPLC quantification of the digested **Z8P-15^{30}$_{MeONa,1:2}$** showed that the amount of 1ap present is 3.5% mol/g of ZIF (Figure 40). The quantification of the digested ZIFs when compared with Table 6 suggested that the quantified amount for the imine on the ZIF is then preferentially included on the bulk of the particle, having a tendency for one pyrene functionality per pore as a maximum. The proposed preferential inclusion for the imine functionality inside the pore of the ZIF rather than on the surface of the nanoparticle will condition the fluorescence response of the ZIF and is an aspect that is considered on future discussion.

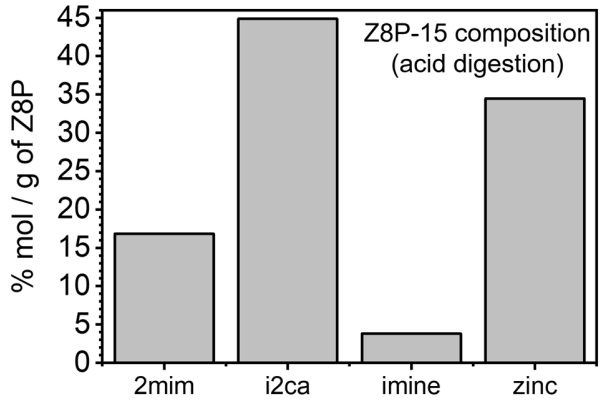

Figure 40 Graphical representation of the results of the chemical composition of Z8P-15 determined by HPLC, and expressed in %mol/mol reactants per g of target Z8P. Zn^{2+} values calculated from the HPLC data is obtained by deducting the total percentage (%g/g Z8P) for 2-mim, i2ca and 1-AP from the total (100%), assuming all the non-accounted for mass on the Z8P-15 comes from Zn^{2+}.

The fluorescence emission spectra for the fluorophore, the imine, was obtained using 335 nm as the excitation wavelength (Figure 41). This excitation wavelength was chosen based on the reported fluorescence absorption spectra for aminopyrene, as described by Soustek et al.[180, 181], that shows the absorption maxima at 355 nm. Instrumental limitations forced the selection of 335 nm as the excitation wavelength instead of the optimal 350 nm. The excitation wavelength must be, at least, 25 nm away from the measured range of emission on the instrument. Measuring the emission spectra from 360 nm to 550 nm meant then the optimal excitation wavelength must be selected at 335 nm. The fluorescence emission spectrum obtained for the modified ZIF is shown in Figure 41, and it had the same profile as the one for the imine. This suggested that there was no difference related to the hydrophobic environment (ZIF bulk) vs hydrophilic environment (ZIF surface) on the intrinsic fluorescence wavelengths of the chromophore.

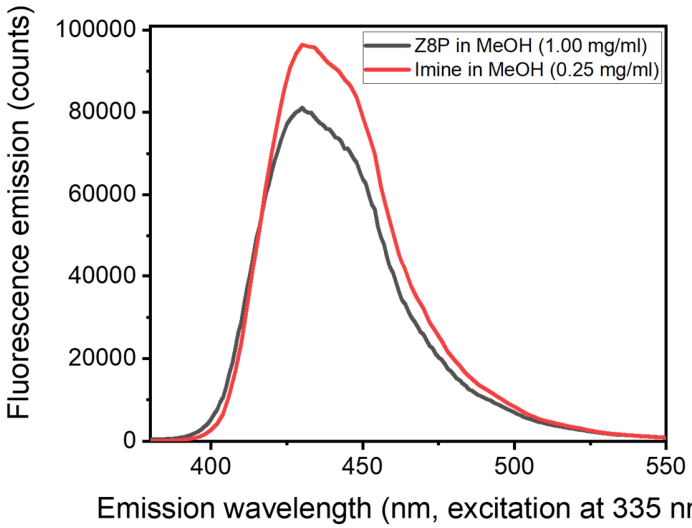

Figure 41 Fluorescence emission spectra for a methanolic dispersion of Z8P (1 mg/mL, grey line) and an imine methanolic solution (0.25 mg/mL, red line), both excited at 335 nm.

The fluorescence quenching response of the Z8P-15 was studied next. The dependence of the fluorescence for Z8P in relation to its concentration showed an intensity increase as the concentration increased from 0.0 to 0.4 mg/mL, until reaching a plateau at 0.2 mg/mL (Figure 42). This fluorescence quenching was an expected behaviour since it is frequent that the fluorescence intensity deviates from a linear dependence at high concentrations and eventually levels off and reaches a plateau. This plateau in the fluorescence emission can be due to "concentration quenching"[117], a reduction caused by self-absorption effects from the dye itself. The quenching can also be due to aggregation-caused quenching (ACQ), a phenomenon responsible for low emission of dyes when in the form of solid state can aggregate and quench[182]. Since a modified ZIF concentration of 0.2 mg/mL showed the beginning of the plateau, this was the maximum concentration for the modified ZIF that was chosen for the quenching experiments, since it was assumed it will minimized quenching by particle aggregation.

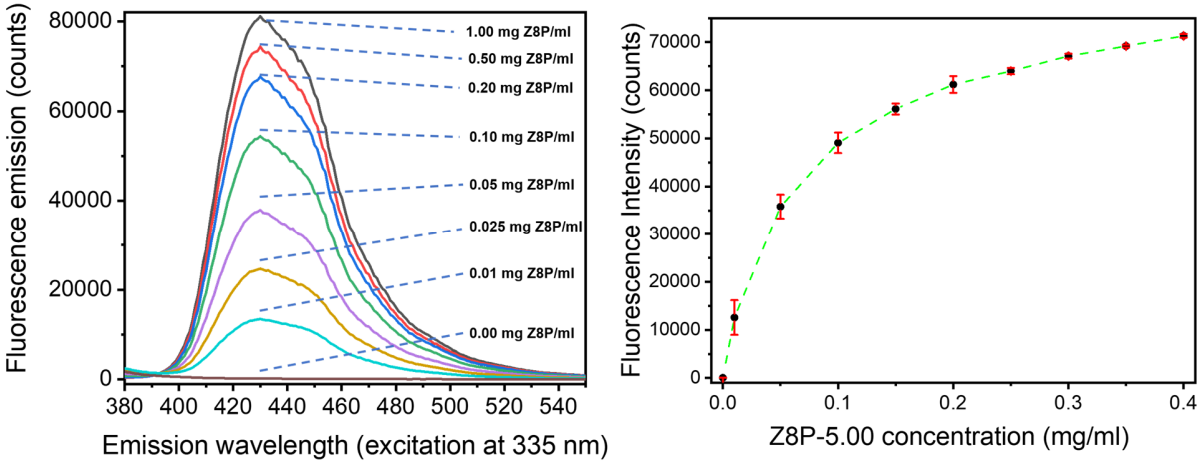

Figure 42 Left: Fluorescence emission spectra for a methanolic dispersion of Z8P-15, excited at 335 nm. Right: Fluorescence emission for Z8P-15 for different concentrations (from 0.00 to 0.4 mg/mL). The intensity is taken from the emission maximum 433 nm. The excitation wavelength is 335 nm. Each point is measured three times and the average results are plotted.

Next, the quenching of the Z8P fluorescence as a function of the concentration of the PAEs was studied. Three Z8P concentrations were chosen (0.20, 0.15 and 0.10 mg/mL), and applied in sensing of dimethyl phthalate (DMP) in a concentration range from 0.00 to 2.00 mg/mL. At low PAE concentrations the quenching was very pronounced. However, with increasing concentration, saturation for the quenching was reached (Figure 43). The rate of the quenching was independent of the concentration for the sensing element within the concentration that is investigated. The same behaviour was also identified for the rest of the chosen PAEs (Figure 44a to c). As a negative control, the fluorescent signal of the PAEs in a water solution (2 g/L) was also measured (Figure 44d). No significant fluorescence could be detected from them, thus not generating any interference with the fluorescence of the ZIF. From the literature it is found that on the excitation and emission wavelengths chosen for the system there is no absorption for the chosen PAEs (Figure 43 bottom). Absorption spectra for 2mim and i2ca (Figure 13) showed that the imidazolic building blocks also did not absorb close to the absorption or emission wavelength range for the imine.

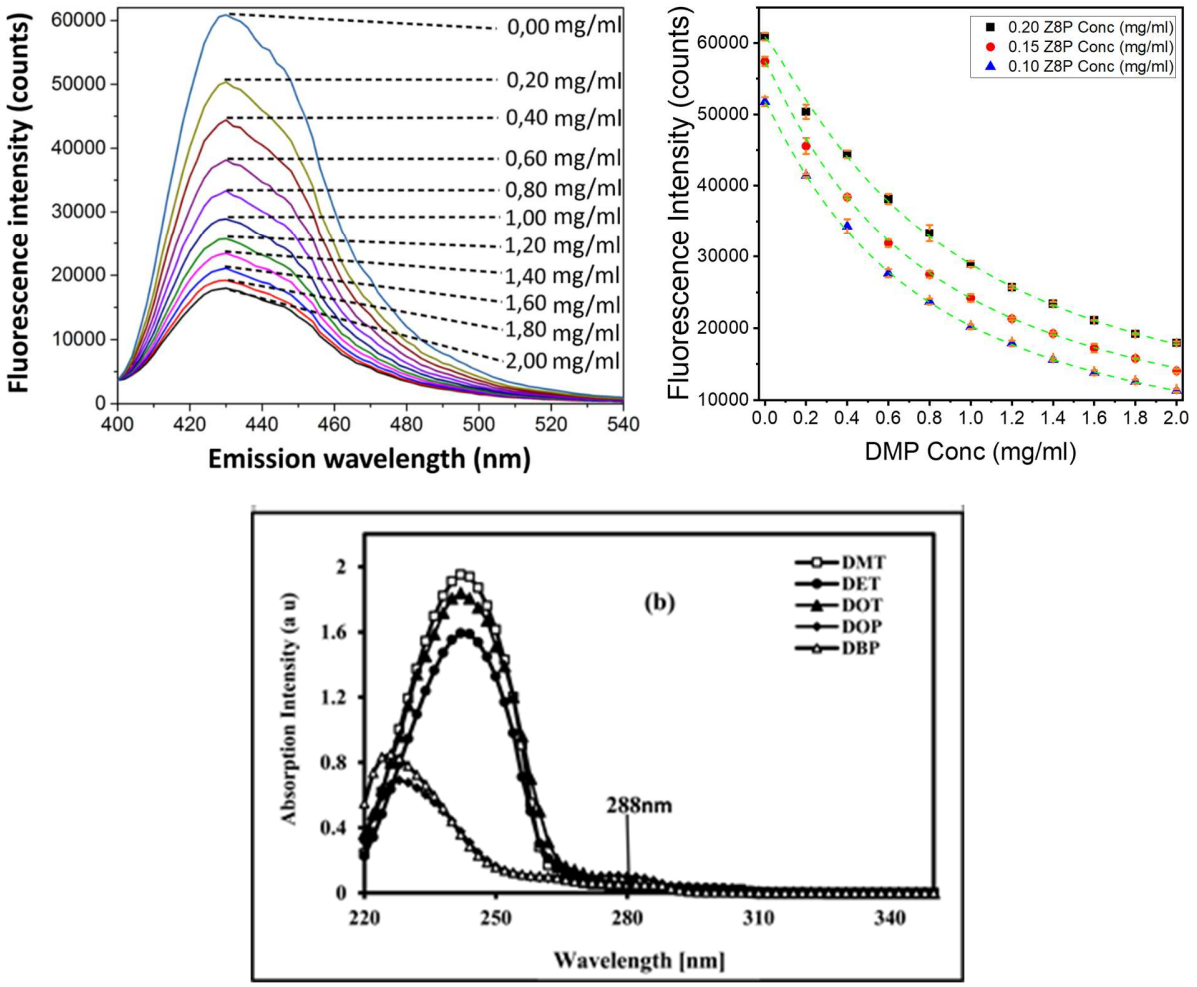

Figure 43 Top Left: Fluorescence quenching measured with a fixed concentration of Z8P (0.2 mg/mL) is suspended in different solutions with varying concentrations of DMP (from 0.00, highest intensity curve, to 2.0 mg/mL, lowest intensity curve). The excitation wavelength is 335 nm. Top Right: Representation of the fluorescence intensity maximum (430 nm) versus the concentration for DMP for three different concentrations for Z8P suspended on methanol. The effect of the quenching is independent of the concentration for the sensing element within the investigated range. Bottom: UV-absorption spectra for Dimethyl terephthalate (DMT), Diethyl terephthalate (DET), Dioctyl terephthalate (DOT), Dioctyl phthalate (DOP, also called DEHP), and Dibutyl phthalate (DBP). Taken under Creative Commons Attribution 4.0 International from[183].

Figure 43 suggested that, given that the concentrations for Z8P used on the Stern-Volmer plots were below 0.2 mg Z8P/mL, there was no particle quenching occurring due to agglomeration. The response of the DMP quenching rate was not dependent on the concentration for Z8P. This constant rate of quenching of Z8P under 0.2 mg/mL was not enough to say whether there is a favouring the quenching on the imines located on the surface of the ZIFs versus the ones on the bulk. It would be reasonable to assume that the quenching happening on the surface of the ZIFs will be predominantly dynamic quenching and the one on the bulk would be static. With the presented data it is unclear whether it should be expected a different fluorescent signal for the fluorophore located on the surface of the particle compared to the fluorophore located in the pores of the ZIF, it requires further explicit studies to determine the exact quenching mechanism.

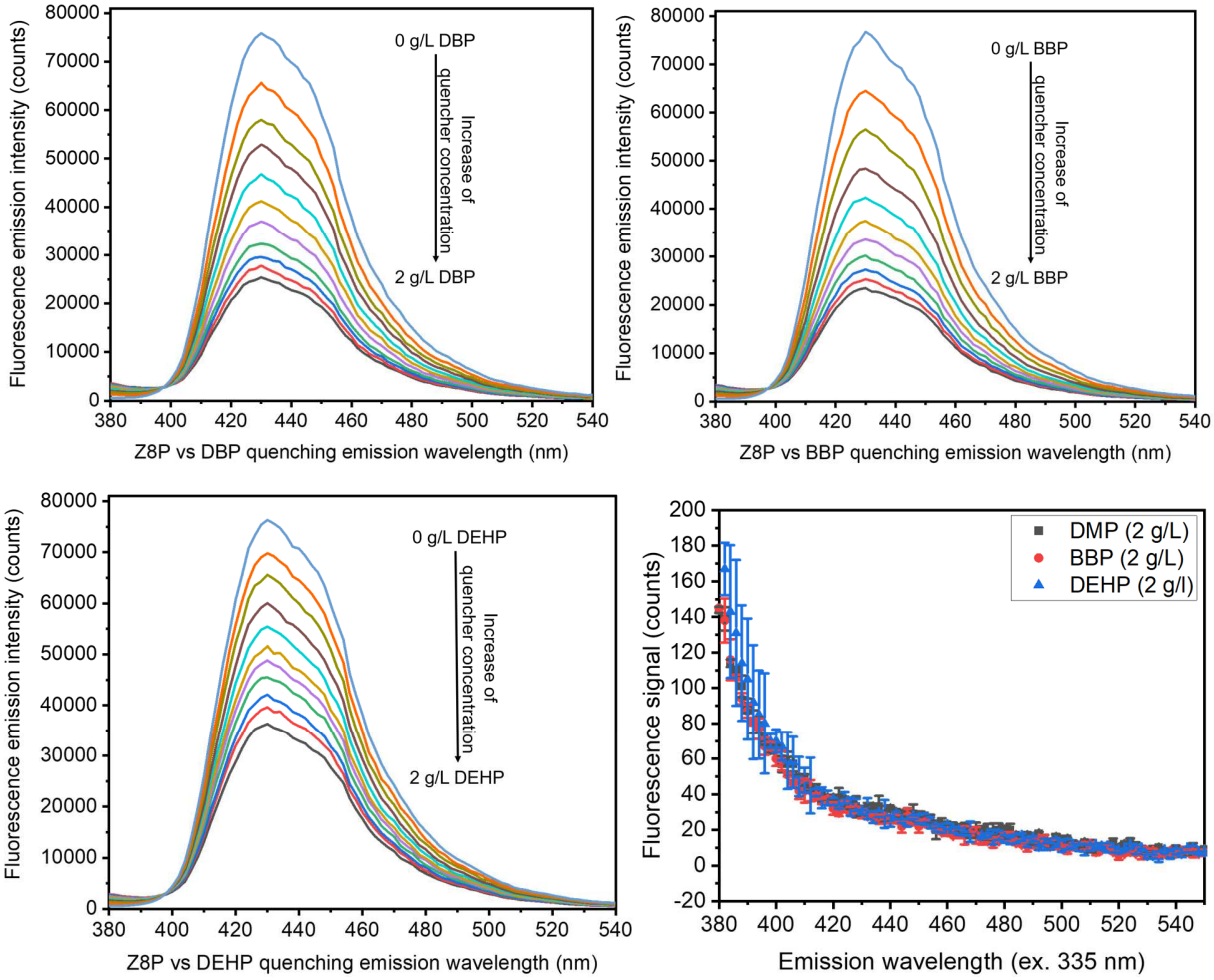

Figure 44 Fluorescence quenching measured with a fixed concentration of Z8P-15.00 (0.2 mg/mL) is suspended in different solutions with varying concentrations of DBP (a), BBP (b) and DEHP (c) (from 0.00, highest intensity curve, to 2.0 mg/mL, lowest intensity curve). Right: Fluorescence emission for the PAEs of interest as a control. Excitation happens at 335 nm.

Testing the fluorescence of Z8P in relation to PAE concentration, a direct dependence between the reduction in fluorescence emission and the increase of the concentration of the analytes was observed. Taking the intensity maximum of the emission at 430 nm for each concentration of PAE in Figure 43 and 44 and plotting it against the PAE concentration corresponding for each point, then applying the modified Stern-Volmer equation for collisional and static fluorescence quenching (equation 2), a calibration curve for each PAE was generated, Figure 45.

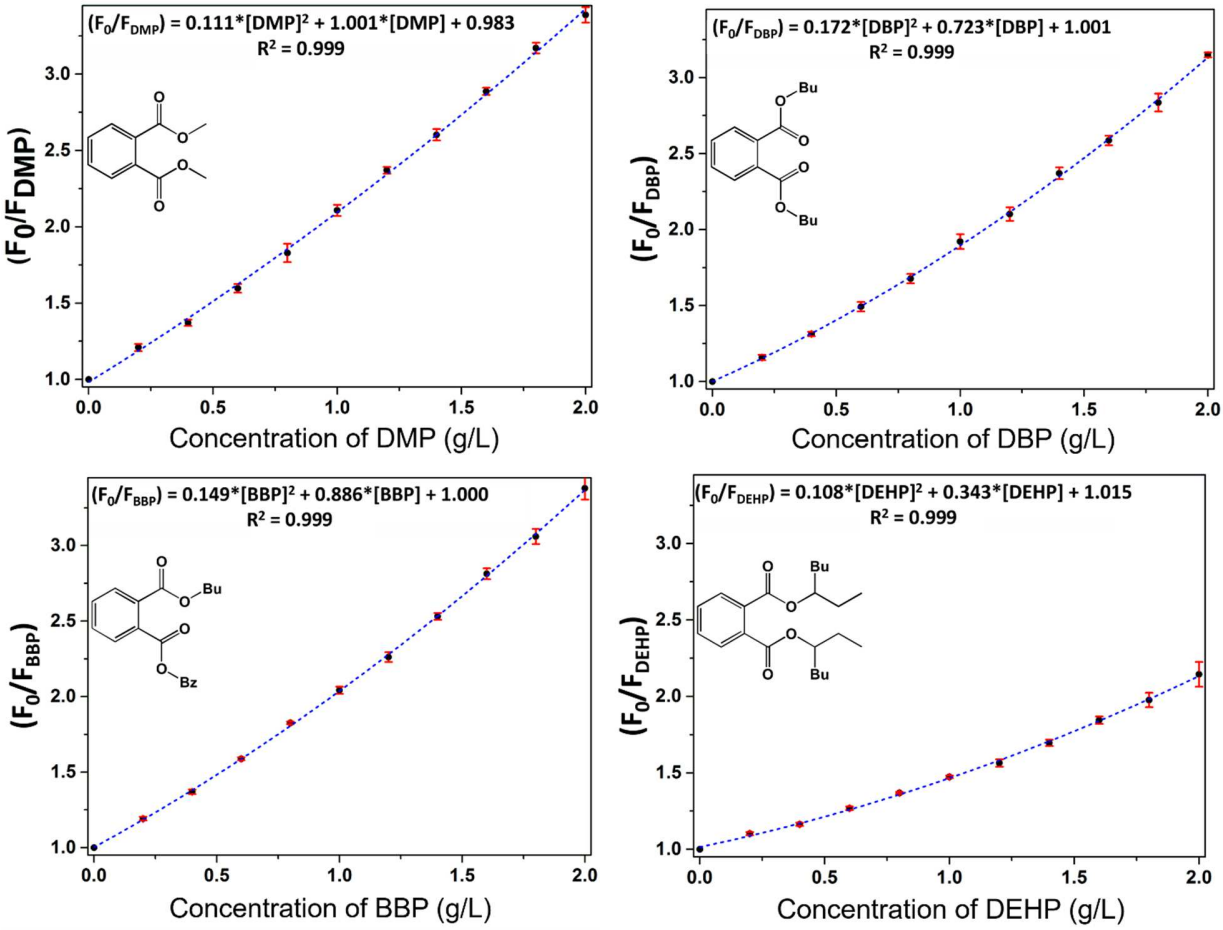

Figure 45 Modified Stern-Volmer fitting for the fluorescence quenching of Z8P at different DMP concentrations (from 0.00 to 2.00 mg/mL). The excitation wavelength is 335 nm, and the emission is recorded at the maximum at 430 nm. Each point is measured three times.

The fact that the modified Stern-Volmer equation fits the data suggested that static and dynamic quenching are happening[114, 117]. This could indicate that the sensing is happening on two different areas of the particle: on the surface, the exposed pyrene cores suffer collisional quenching, this being the dominant contribution, and in the bulk, the phthalates can diffuse through and be trapped with the pyrenes. The absorption spectra for the PAEs (Figure 44 bottom right) and for the imidazolate species forming the modified ZIF (Figure 13) showed they do not absorb at the bands for excitation and emission of the imine, strongly suggesting that the quenching is not due to quenching effects by absorption of the emitted radiation by the imine. Instead, the quenching data suggested a π- π stacking that leads to the formation of an exciton state that no longer absorbs radiation. The formation of a π- π stacking exciplex between the imine and the PAEs is driven by aggregation often due to hydrophobic effects—the dye molecules stack together to minimize contact with water. Planar aromatic molecules that are matched for association through hydrophobic forces can enhance static quenching. The formation of an exciplex via π- π stacking of the PAEs and the imine needs further studies to be confirmed.

The HPLC data of the quantification of Z8P (Figure 40) suggested preferential inclusion of the imine on the bulk of the particle. The preferential inclusion of the imine at the bulk of Z8P seems to support that the permeation of the PAEs withing the ZIF pores is a requirement for the quenching to happen. The permeation of the PAEs within the ZIF pores is also a requisite for the π- π stacking of the PAEs and the imine to occur. The permeation of the PAEs within the ZIF pores via diffusion is theorized only from the presented data, and it requires further explicit studies to determine the exact mechanism.

The upward deviations of the calibration line observed in the Stern-Volmer plots (Figure 45) showed the quenching rate increase accelerates as the concentration of the PAEs increases. This could be attributed to a favoured inclusion of the PAEs within the outer layers of the surface of the ZIFs. Eftink et.al. discuss Stern-Volmer plots having upward deviations to linearity caused by heterogeneities in the quencher concentration and some restrictions in the accessibility of the fluorophores by the quenchers[184] when studying the conformational and/or dynamic changes of proteins in complex macromolecular system. Figures 46 and 47 show the result of simple modelled representations of the disposition of BBP and DEHP inside of a pore for ZIF-90 together with an imine functionality as part of the ZIF-90 pore. These simple models showed that both analytes have enough space inside of the Z8P ZIF to be contained and interact with the imine dye, generating fluorescence quenching. ZIF-90 is a hydrophobic environment[55], which will favour the permeation of the PAEs from the methanolic or water solutions within the ZIF.

The biggest problem this model showed was the permeation of the PAEs within the pore, since the pore opening is very close to the molecular diameter for the PAEs (pore opening of 3.5 Å[55, 185]). The molecular flexibility of the PAEs, combined with the Swing Effect[186-188], and the gate-opening effect observed in ZIF-8[189], supported the idea of the permeation of PAEs and imine, within one pore. The Swing effect is an effect described on literature as a bistable system where the linker, imidazolate, oscillates between two structures: "open window" and "closed window", facilitating a significant increase of the opening window of the pore of up to 2 Å. These two effects, swing effect and gate opening, could lead to a spontaneous opening of the pore window and a widening of the pore, allowing PAE permeation. Once the PAE has permeated, an exciplex formation of the PAEs with the imine contained withing the ZIF pore via diffusion favoured by the hydrophobic environment of the pore could be proposed. This proposed permeation is especially favoured in the outer layer on the surface of the ZIFs.

A third type of quenching exists that could contribute to the behaviour of the quenching, namely “inner-filter quenching”[190]. An inner-filter effect occurs when the total absorbance of the solution is high, leading to a reduction in the intensity of the excitation radiation over the path length. Quenching of this type is not generally categorized among the major quenching process because it is a trivial type of quenching that is not really involved in the radiative and non-radiative transitions in luminescence spectroscopy. On the presented modified ZIF is possible that inner-filter effects occur, since the fluorophores contained on the ZIF nanoparticles can auto-absorb the emitted radiation.

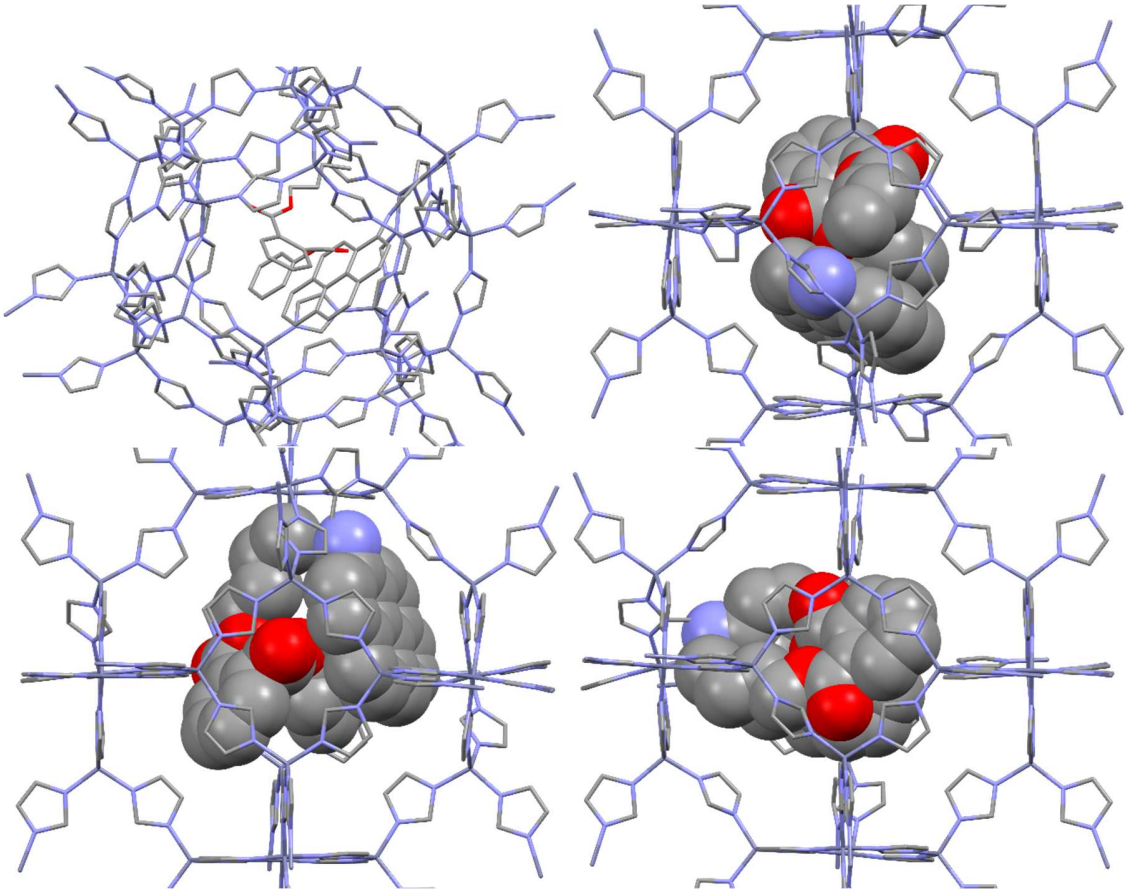

Figure 46 Simple modelled representation the disposition of BBP inside of a pore for ZIF-90 together with an imine functionalities as part of the ZIF-90 pore. The representation is done with the ZIF-90 CIF file as a basis, manually including the imine functionality and the BBP molecule using Avogadro[5] and running a basic geometry optimization. The aldehyde functionality located on the carbon at the N-C-N fragment of the i2ca imidazolic building blocks have been removed to facilitate visualization, as well as the hydrogen atoms

[5] Avogadro: an open-source molecular builder and visualization tool. Version 1.20. http://avogadro.cc/

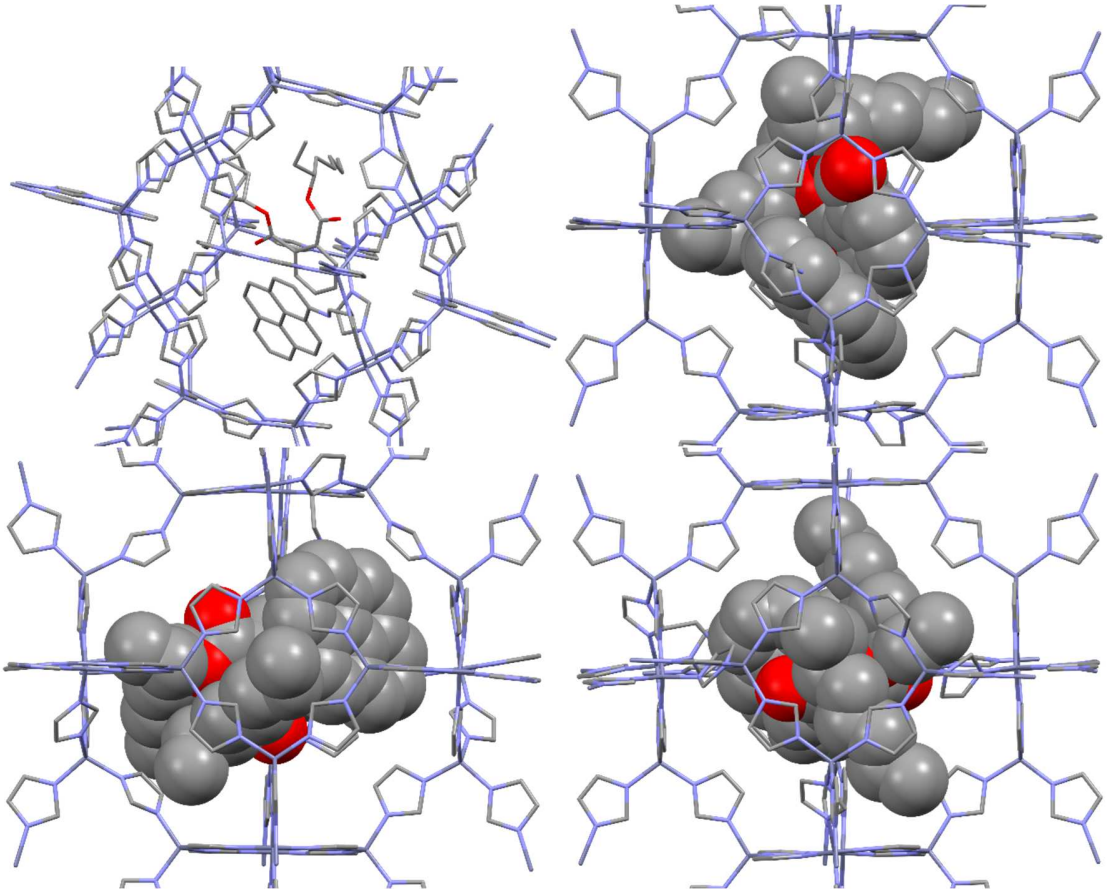

Figure 47 Simple modelled representation the disposition of DEHP inside of a pore for ZIF-90 together with an imine functionalities as part of the ZIF-90 pore. The representation is done with the ZIF-90 CIF file as a basis, manually including the imine functionality and the DEHP molecule using Avogadro and running a basic geometry optimization. The aldehyde functionality located on the carbon at the N-C-N fragment of the i2ca imidazolic building blocks have been removed to facilitate visualization, as well as the hydrogen atoms

Figure 44 showed that the quenching for the bulkier member of the PAEs, DEHP, was significantly reduced when compared to the smaller PAEs, thus, limiting the sensing capacity of the ZIF. This reduction on the quenching capacity was attributed to the bigger molecular size of DEHP (Figure 47). The inclusion within one pore of both the aminopyrene functionality and of one of the PAEs, even the less bulky one, seems highly unlikely to be the favourable phenomena over surface quenching. This exciplex formation would be specially hindered when it comes to the inclusion of the bulkiest species, DEHP, and a significant reduction on the fluorescence quenching is observed on the results. Simple computer models performed (Figures 46 and 47) suggested the inclusion of the PAEs inside of the ZIF pore and the right orientation for the aromatic moieties to be properly oriented to form π- π stacking was allowed. These simple models do not contradict the permeation model proposed; being so bulky when compared to the other PAEs, DEHP is the one with the higher resistance to permeate through the windows of the ZIF pore. Once the DEHP is within the pore, however, they can form the exciplexes with the structural imine. The formation of a ground-state complex between the imine and the PAEs was not proven unambiguously; UV-vis and 1H NMR titration experiments[122] could corroborate the exciplex formation.

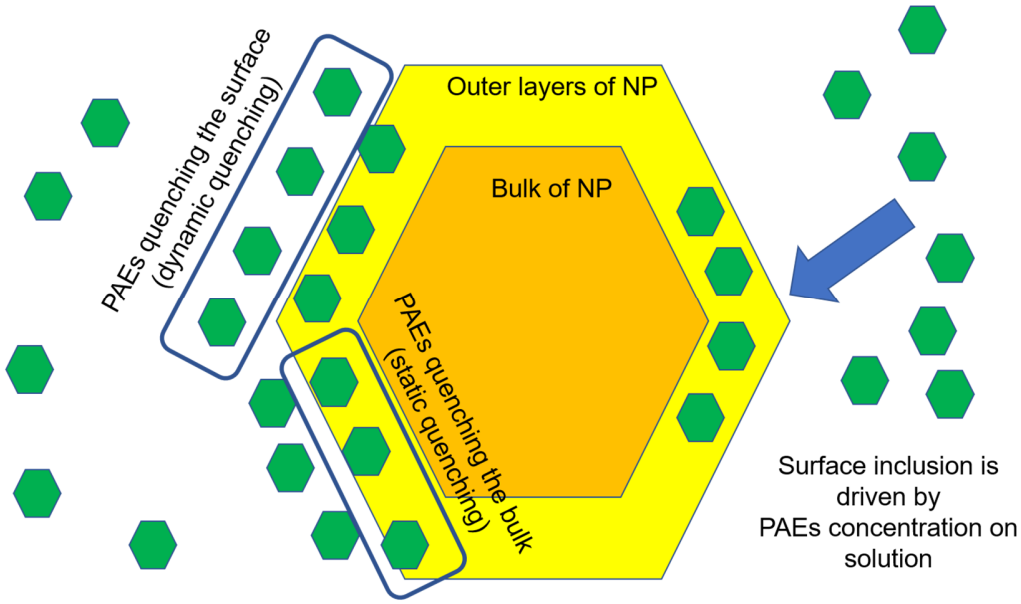

Figure 48 Scheme of the model proposed for the interaction between the PAEs and the Z8P nanoparticles. The PAEs tend to spontaneously migrate from the solution to the surface of the ZIF nanoparticles, then permeating the uttermost layer of the ZIFs. this interaction between the ZIFs and the PAEs will render two distinctive interaction areas between the systems. The PAEs interacting with the surface og the ZIF particles will suffer from collisional quenching, while those permeating the outermost layer of the ZIFs will suffer from static quenching, given the tight fit of the PAEs within the pore of the ZIFs.

With the information that has been gathered, a model to explain the behaviour is possible to be developed (Figure 48). However, in order to obtain conclusive evidence for the interaction between the PAEs and the fluorescent element of the ZIFs a setup where AFM images are correlated with fluorescence microscopy, combined with molecular modelling, would give the evidence required.

4.5. Modified ZIF/antibody conjugation methodology and ELISA and LFIA test of principle for ZIF-IgG conjugates

ZIF-IgG conjugation methodology and structural characterization of the conjugates

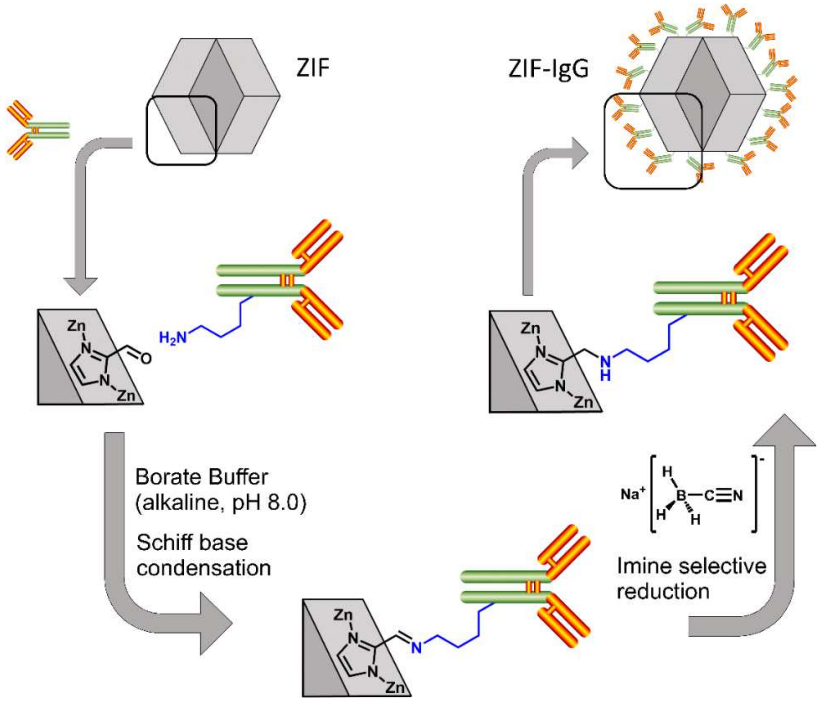

Figure 49 Schematic representation of the conjugation reaction between the ZIFs and the antibodies. In the first step the dispersed particles are mixed in solution with the antibodies. The free amino functionalities from lysine residues side chains in of the antibodies can react with the aldehyde functionality on the ZIF to form an imine bond. Sodium cyanoborohydride is added in the second step to selectively reduce the imine bond to an amine, rendering the conjugation irreversible under assay conditions.

With the synthesis of the modified ZIF stablished and characterized, a methodology to covalently bind them to antibodies was developed (Figure 49). Taking advantage of the free aldehyde functionality, antibodies were covalently bound to the surface of the ZIF particles. This covalent binding was achieved via Schiff base condensation between the aldehydes on the ZIFs and free amino groups present on the antibody's residual amino acids, such as lysine. Once the imine between aldehyde and amine has been formed, it can be selectively reduced using Ciano borohydride, a selective imine reducing agent[191]. Zeta potential measurements for the ZIFs evidence that the ZIF particles are naturally electrostatically charged, as shown by Beyer et al.[192] for ZIF-67 and ZIF-8; this will promote the covering of the surface of the particles by the antibodies once both have been mixed together on an appropriate buffer, promoting any chemical reactivity potential. Subsequent imine to amine transformation was performed to maximise the chemical

stability of the freshly prepared ZIF-antibody conjugates[193]. With this methodology in mind, **Z8P-15^{30}$_{MeONa,1:2}$**, (Z8P) as well as **ZIF-90$_{MeONa,1:2}$**, (Z90) were subsequently reacted with sheep-anti-mouse IgG. PXRD in Bragg-Brentano symmetry and TEM images were taken for these new systems (**ZIF-90** [referred to as ***Z90***], **Z8P-15^{30}$_{MeONa,1:2}$** [referred to as ***Z8P***], the **ZIF-90–IgG conjugate** [referred to as ***Z90–IgG***], and the **Z8P-15^{30}$_{MeONa,1:2}$-IgG conjugate** [referred to as ***Z8P–IgG***]). PXRD showed that the sodalite crystal structure was kept after the conjugation has taken place (Figures 50). TEM images for Z8P-IgG (Figure 52) suggested that the particle size has been retained between before (Figure 51) and after the conjugation takes place. A significant amount of aggregation can be seen for the conjugate Z8P-IgG but is not clear at this point if it was due to the nature of the system or due to sample preparation. Prior to depositing the sample on a TEM grid, a solvent change took place, going from aqueous borate buffer to pure methanol; this change in solvent could trigger the aggregation. NTA (Nanoparticle tracking analysis, Figure 53) for Z90-IgG showed the nanoparticles on dispersion, no aggregation being observed. A size dispersion of 150-300 nm in diameter was observed, which was within range of the results obtained via TEM.

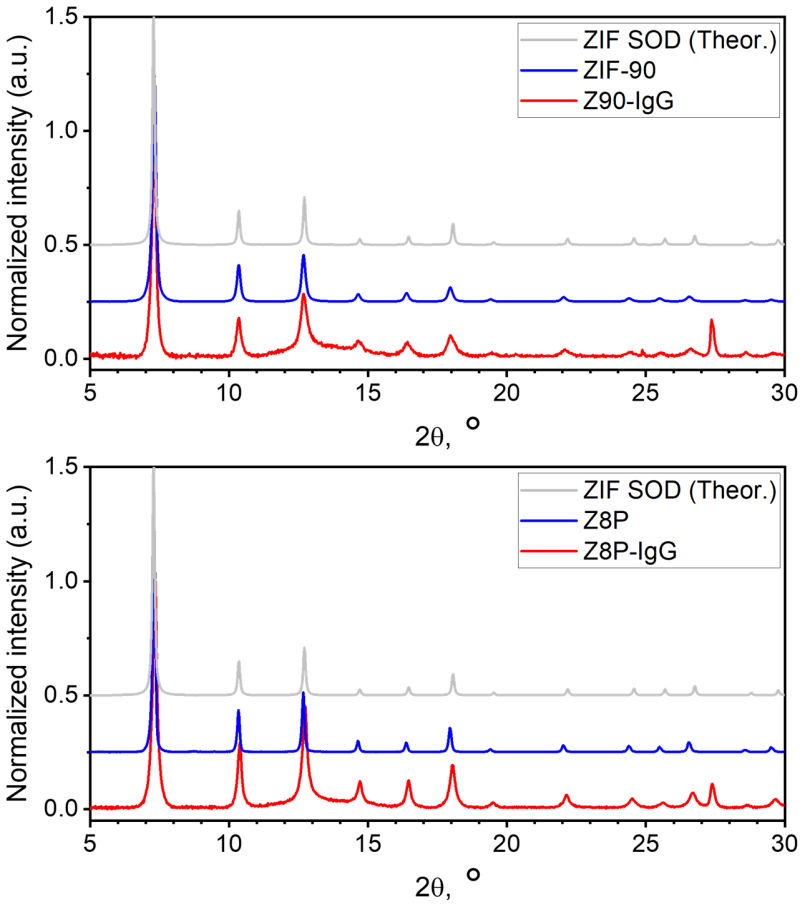

Figure 50 Top: Powder diffractograms for ZIF-90 (blue), the ZIF-90–IgG conjugate [Z90–IgG] (red), both measured in Bragg-Brentano symmetry. Bottom: Powder diffractograms for the modified fluorescent ZIF-8/ZIF-90 hybrid [Z8P] (blue), the ZIF-90–IgG conjugate [Z90–IgG] (red), both measured in Bragg-Brentano symmetry. In both sets of diffractograms the theoretical diffractogram for ZIF-8 is included (grey).

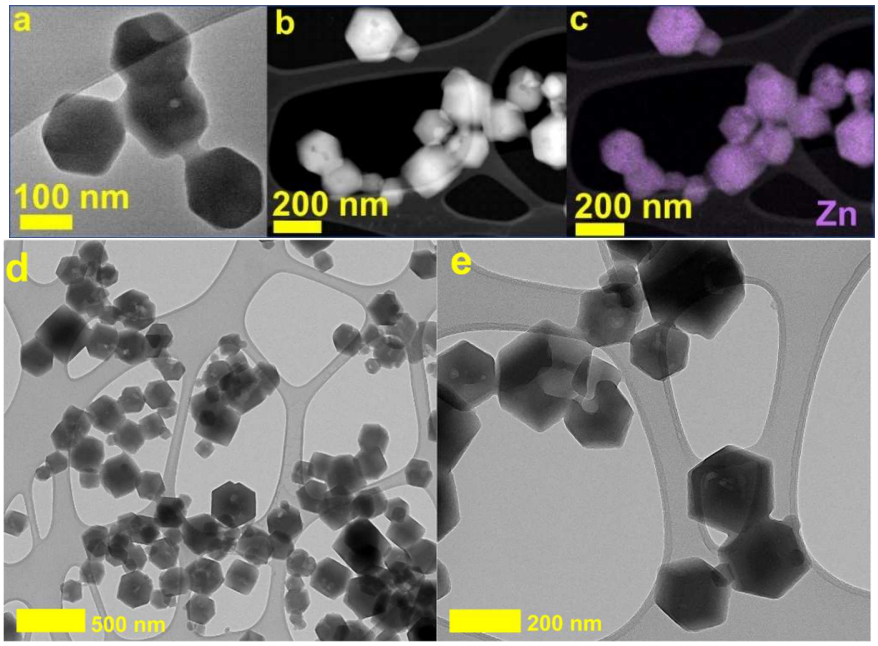

Figure 51 TEM images for Z8P (a-c) and ZIF-90 (d and e). Normal TEM images (a and b) are complemented with a TEM EDS image (c).

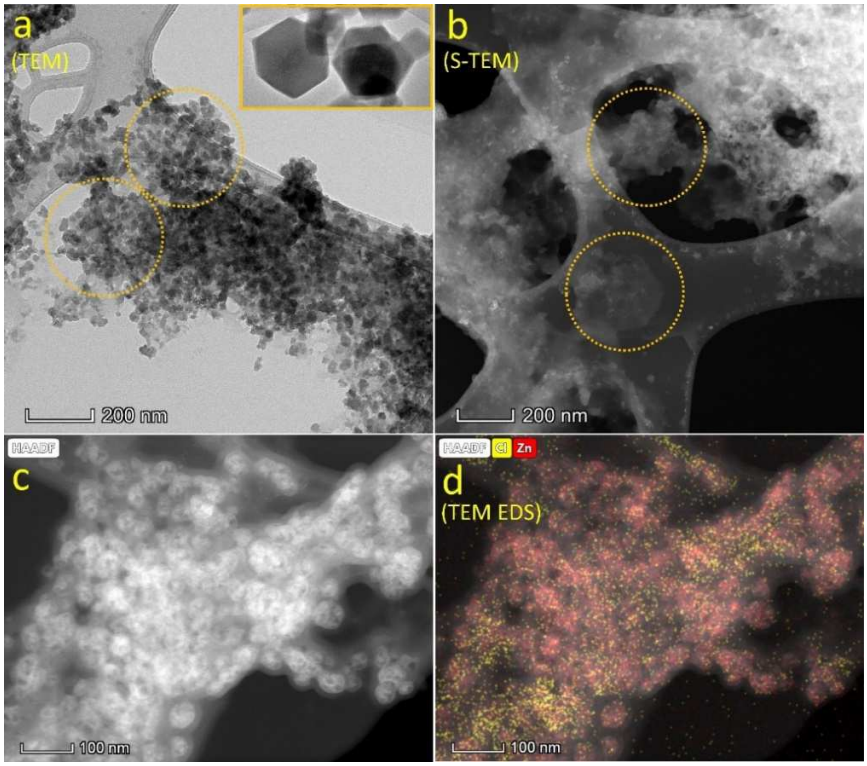

Figure 52 TEM images for Z8P-IgG. Normal TEM images (a and c) are complemented with a STEM image (b), as well as a TEM EDS image (d).

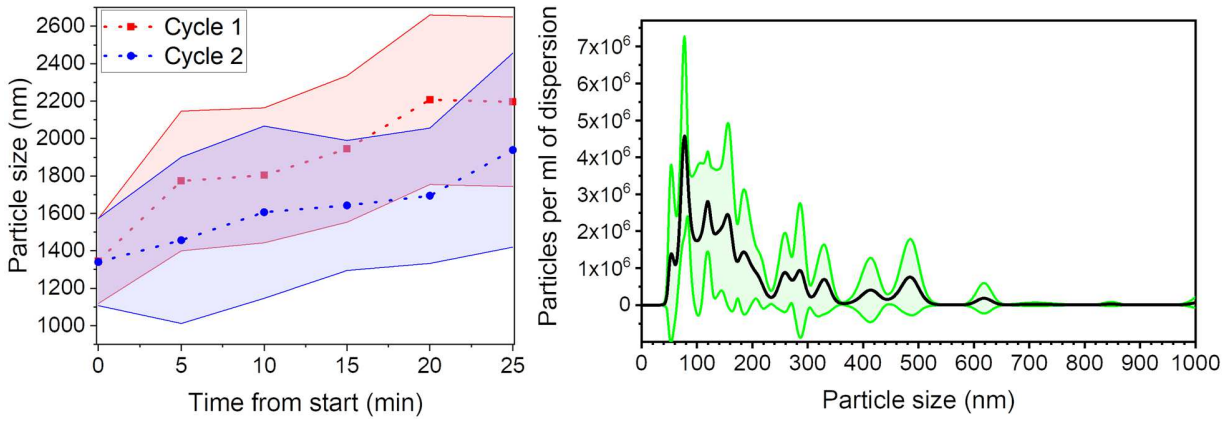

Figure 53 Top: Graphical representation of the results on Table 15 for the Z90-IgG dispersion in borate buffer (200 µg Z90-IgG/mL borate buffer). The coloured area around each line represents the standard deviation for the particle sizes as calculated by DLS. Bottom: Particle size distribution and standard deviation measured by NTA for the Z90-IgG dispersion in borate buffer (20 µg Z90-IgG/mL borate buffer).

NTA results for the Z90-IgG conjugate on borate buffer suggested that the conjugated nanoparticles do not tend to aggregate and remain dispersed and mobile on borate buffer, if the concentration of the ZIF-IgG conjugates does not go over 20 µg/mL. DLS data (Figure 53) for the Z90-IgG conjugate on borate buffer showed two important points: 1) in the measured concentration (0.2 mg/mL), the particles tend to stay as microaggregates of around 1 to 2 µm, even though TEM shows the particles for Z8P-IgG are within a similar size to those of unconjugated Z8P. These microaggregates cannot be broken down by ultrasonication alone, being necessary the introduction of stabilizing agents, such as DMSO or other surfactants. This is likely a hydrophobicity issue, since ZIF-8 and -90 tends to stick together in very polar solvents due to the un-polarity of aged ZIF, which leads to forming colloidosomes. Given that the TEM images for both unconjugated ZIF-90 and Z8P were within the same size ranges and shape (Figure 51), it was extrapolated the same behaviour for both conjugated systems, Z90-IgG and Z8P-IgG; 2) over time the microaggregates tend to increase in size and in size dispersity, hinting a tendency for the system to precipitate overtime. This phenomenon could be easily reverted by sonicating the sample for 3-5 minutes, unlike the microaggregate destruction. This breaking of the sedimented aggregation of the conjugates is important when it comes to conjugate long term storage on high concentrations (0.2-1.0 mg/mL).

The NTA and DLS results hinted that choosing a working concentration for the ZIF-IgG conjugates of over 20 µg/mL is not ideal for applications that demand a high mobility in dispersion. High concentrations of ZIF-IgG in borate buffer (over 0.2 mg/mL) lead to agglomeration and sedimentation. The big ZIF-IgG aggregates that are formed randomly could interact non-homogeneously with the surface. Higher size aggregates are less mobile and have a reduced surface to volume ration, limiting the interactivity with the medium. They can also damage the antibodies deposited on the surface of the microplate well. For this, the ELISA experiments, that require good mobility, were performed with a working concentration of under 20µg of ZIF-IgG/mL of borate buffer.

ZIF-IgG binding nature study via LC-MSMS

To study the nature of the conjugation and seeking for evidence of a successful covalent bond through the imidazole carboxaldehyde moiety of the ZIF particles to a free amino group of the antibody, the idea to digest the conjugate under well stablished specific acidic conditions for proteins was approached (Figure 54). This methodology should completely digest both the antibody and the ZIF to their constituents (amino acids and organic species), but should there be a covalent strong bond between ZIF particle and antibodies, then a new fragment should have been present on the digestion solution as well, specifically the fragment formed between the imidazole moiety and the lysine antibody. Then, a nontargeted liquid chromatography/high-resolution mass spectrometry (LC-HRMS) characterization of the mix should be able to show if these new fragments are present.

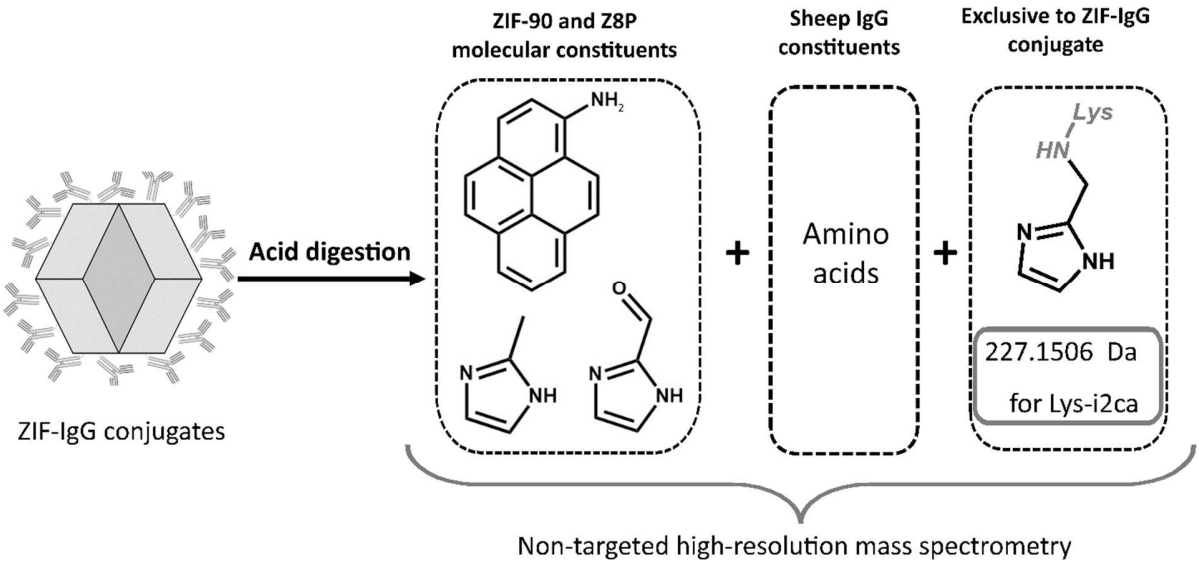

Figure 54 Molecular constituents as expected to be released by the acidic hydrolysis of ZIF−IgG conjugates. The highlighted Lys amino acid imidazole derivatives (m/z 227.1506 Da) accepted to be exclusive obtained from ZIF−IgG conjugates.

First, the efficiency of the hydrolysis was tested, using 0.1 mg sheep-anti-mouse IgG (no ZIF). Extracted ion chromatograms (EICs) of protonated and deprotonated molecular peaks ([M+H]+, [M-H]-) acquired in electrospray positive and negative mode, respectively, suggested the presence of 17 of the 20 proteinogenic amino acids in the sample (Figure 68), indicating efficient protein breakdown. Next, ZIF/IgG conjugates are hydrolysed and subjected to LC-HRMS. Chromatograms of hydrolysed ZIF/IgG conjugates contained approx. 140 chromatographically deconvoluted compounds (“features”) in the mass range of 50-600 Da (Figure 55a). This suggested extensive hydrolytic breakdown of conjugates into smaller molecules. In these chromatograms, ion traces of

possible amino acid imidazole derivatives are traced, using a target list of theoretical precursor ions (Table 15). This approach revealed a potential lysine imidazole derivative at a retention time of 558 s (Figure 55b). The compound is present in both ZIF/IgG conjugates but in none of the control measurements (IgG alone, ZIFs alone), supporting the notion that it is formed exclusively in ZIF/IgG conjugates. Structural evidence for the compound could be obtained from both isotope pattern and MS/MS spectrum. First, isotopologue intensities matched calculated ones within instrument-limited error margins (<2%; Table 16). Second, all major MS/MS fragments could be assigned substructures that explained the putative molecular structure very consistently (Figure 55c). Taken together, while only co-elution of a chemical standard or NMR could give definite structural evidence, covalent bonding of an imidazole carboxaldehyde moiety to an amino acid residue of the antibody was well supported by the present results.

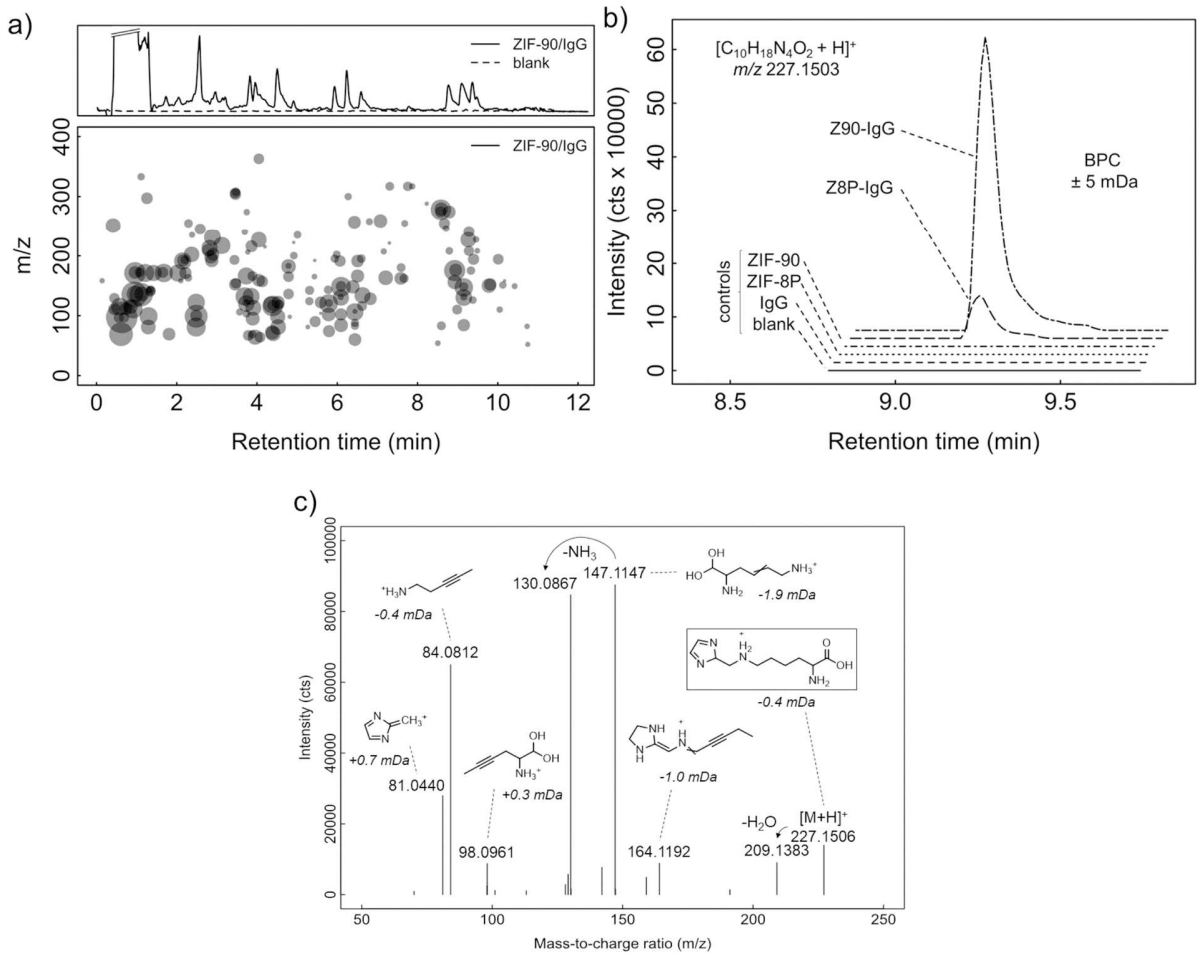

Figure 55 Mass spectrometric characterization of the assumed covalent bond in ZIF-IgG conjugates. (a) Nontargeted (HILIC-)LC-ESI-HRMS of hydrolysis products; representative total ion chromatogram (TIC) and ion map, respectively, demonstrating sample complexity. "m/z" stands for mass to charge ratio. (b) Extraction of a putative lysine imidazolate derivative ($C_{10}H_{18}N_4O_2$, m/z 227.1503). Ion traces are detected in measurements of both ZIF conjugates but not in those of controls. (c) MS/MS spectrum of putative lysine derivative (precursor m/z 227.1503, isolation window 1 Da). MS/MS fragments are assigned most likely molecular structures based on competitive fragmentation modelling (CFM-ID). Deviations of theoretical from measured masses are indicated. Minor fragment annotation left out for clarity. "cts" stands for counts.

ZIF-IgG conjugate particles overtime stability in solution

The experiment developed to study the ZIF-IgG conjugates structural integrity was based on Rietveld methods, by determining the variation of the crystallite sizes over time: should the crystallinity structure of the ZIFs after the conjugation reaction not been heavily affected this would hint the stability of the ZIF particles. For this PXRD measurements of the Z90-IgG and Z8P-IgG conjugates over time were taken for up to 120 hr.

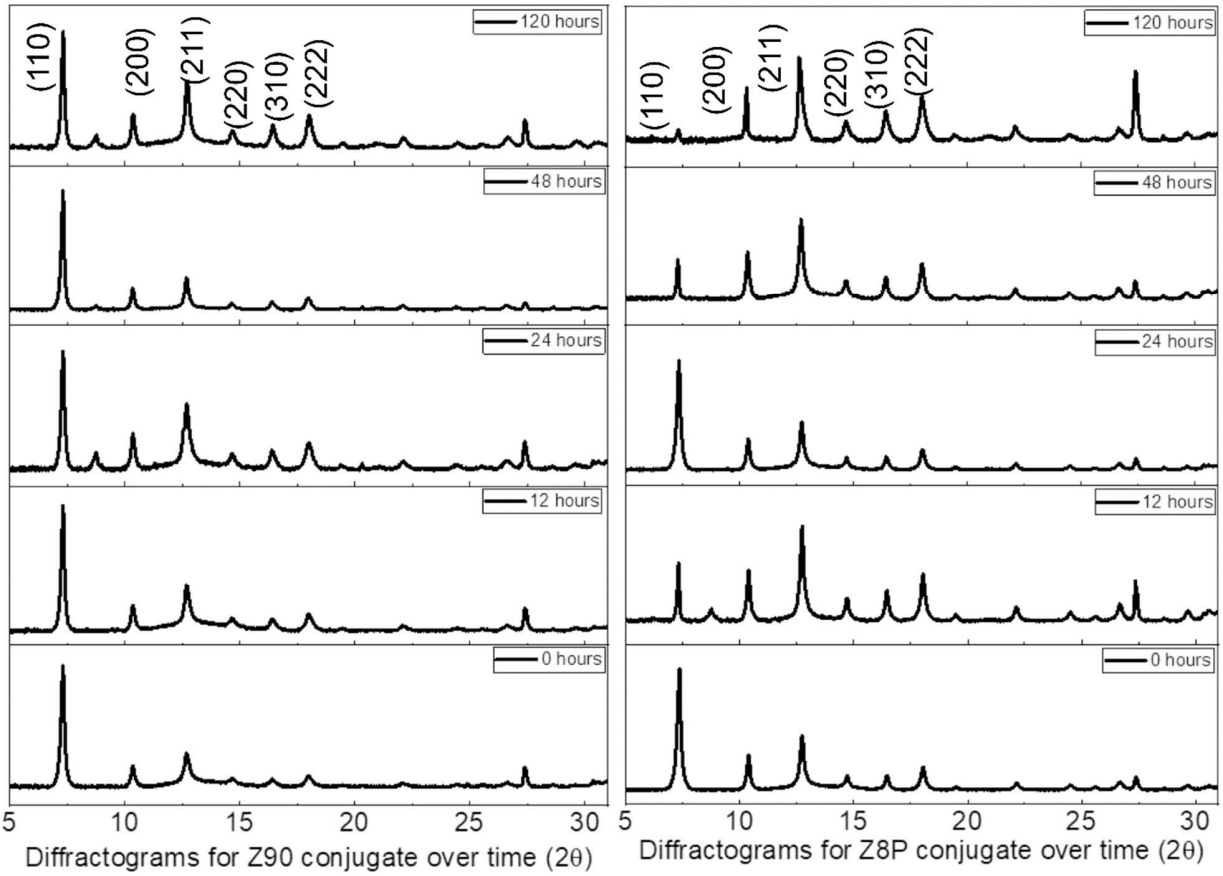

Figure 56 Stacked Diffractograms taken at the times shown from the start of the stability experiments (0 to 120 hours) for both conjugate systems. Z90-IgG conjugate to the left and Z8P-IgG to the right. The background is subtracted from the diffractograms.

Applying the Scherrer equation (Equation 3) to the first three reflections, (110), (200) and (211), for all diffractograms of the ZIF-IgG conjugates (Figure 56) the overall crystallinity of the systems overtime could be assessed. The Scherrer equation is a formula that relates the size of sub-micrometre crystallites in a solid to the broadening of a peak in a diffraction pattern and is used in the determination of size of crystals in the powder[159]. If the Scherrer value remains stable over

time, this is an indication that there is no significant degradation of the ZIF particles in the conjugates. Plotting the crystallite sizes obtained of each diffraction peak versus decomposition time rendered the information needed (Figure 57).

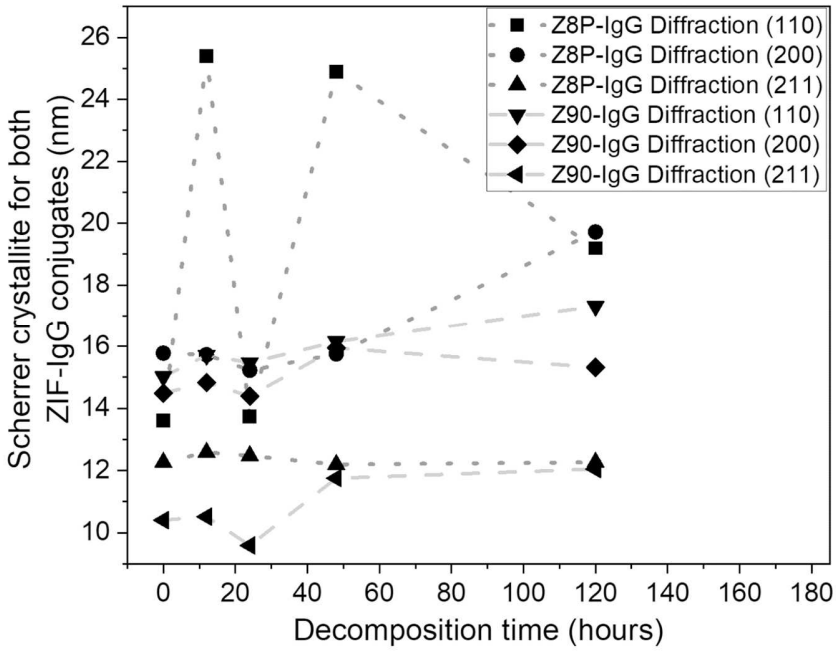

Figure 57 Scherrer crystallite sizes for the first three reflections for the studied ZIF−IgG conjugates, Z8P−IgG and Z90−IgG. No marked changes in crystallite size are observed in the conjugated ZIFs under storage at 4°C for 120 hours using this crystallographic method. The pronounced variation on the (110) reflection for Z8P−IgG does not seem to be representative for the system.

A significant crystallinity degradation over time could not be observed in the studied time frame, since both systems have a similar range of crystallite sizes for all diffractions and over time. The pronounced variation on the diffraction [1,0,0] for Z8P-IgG did not seem to be representative of the system, and is probably caused by the sample not being completely immobilized on the sample holder (is deposited on a water dispersion and started measurement immediately), thus generating the disparity on the first 30 mins of measurement (corresponding to the first 8-9°, approximately).

Overall, the performed experiments strongly suggest that the synthesised conjugates are stable on a borate buffer dispersion. The crystallinity of the ZIFs part of the conjugates did not show any significant damage overtime. The fact that the conjugates tend to precipitate could be easily overcame by sonicating the sample for 5 min prior to use.

ZIF-IgG residual antibody activity and fluorescence properties of the conjugates via ELISA

The antibody residual activity of sheep-anti-mouse IgG bound to the ZIF's surface of the ZIF-IgG conjugates was next measured, via a non-competitive sandwich-ELISA. In indirect ELISA an antigen is adsorbed to a well in an ELISA plate. Detection is a two-step process: (1), an unlabelled primary antibody binds to the specific antigen; (2) an enzyme conjugated secondary antibody that is directed against the primary antibody is applied. This antibody pairs offers an amplification effect, since more than one labelled secondary antibody can bind the primary antibody. Indirect ELISA delivers greater flexibility since different primary antibodies can be used with a single labelled secondary antibody. Sandwich ELISA requires the use of matched antibody pairs (capture and detection antibodies). Each antibody is therefore specific for a different and non-overlapping region of the antigen. The capture antibody binds the antigen that can then be detected in a direct ELISA or in an indirect ELISA configuration. Sandwich ELISA requires the well of an ELISA plate to be coated with a capture antibody as a first step. The key advantage of a sandwich ELISA is its high sensitivity compared to direct or indirect ELISAs. Sandwich ELISA also delivers high specificity as two antibodies are used to detect the antigen. It offers flexibility since both direct and indirect methods can be used. Sandwich ELISA requires an antibody pair to work, which is not always immediately available. Also, antibody optimization must be developed to minimise cross-reactivity between the capture and detection antibodies.

The basic model of ELISA that was used to assess the antibody residual activity of sheep-anti-mouse IgG bound to the ZIF's surface of the ZIF-IgG conjugates was a layered sandwich system which has a base formed by: i) Target: mouse IgG; ii) Primary: sheep anti-mouse IgG; iii) Detector: HRP labelled donkey anti-sheep IgG (Figure 58). This sandwich system was used to characterize the activity response of the primary, analyte-selective antibody. The system was quantified via HRP (Horse Radish Peroxidase) redox reaction driven TMB colour development, in which HRP triggers the conversion of TMB (transparent) to its oxidized coloured product (first intense blue, then bright yellow after the addition of 1M sulfuric acid)[194]; the coloration is proportional to the amount of HRP present on the system which, in turn, is proportional to the amount of primary present on the system.

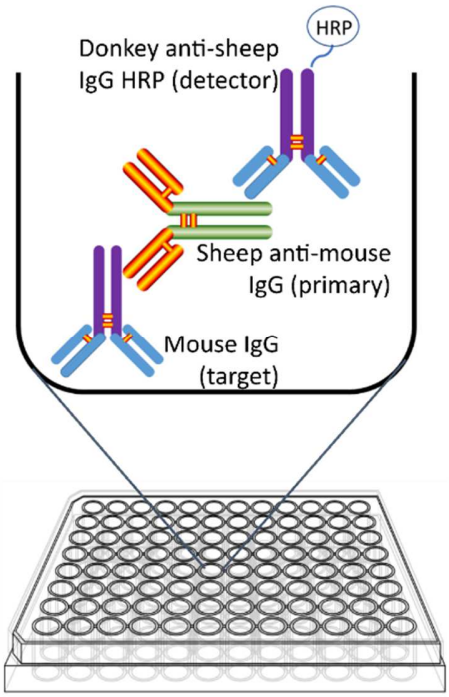

Figure 58 Schematic representation of the general non-competitive indirect ELISA procedure developed to study the antibody activity of the conjugate. The electrostatically charged surface of the high-binding microtiter plates (MTP) is coated with the mouse IgG and incubated on a plate shaker. After washing, the remaining binding sites on the MTP are blocked with casein to avoid any passive adsorption of the conjugates to the surface of the MTP ("non-specific binding"), which would lead to false positive results. After another incubation, the plates are washed again and dilutions of an anti-mouse IgG antibody (or a modified system including anti-mouse IgG) at various concentrations are added and the MTP incubated for 18 hours on a plate shaker. After an additional washing step, a solution with the HRP-labelled detection antibody (anti-sheep IgG) is added and incubated for 1 hour on a microplate shaker. After a final washing step, the substrate 3,3',5,5'-tetramethylbenzidine (TMB) is added to each well and incubated for 15 min on a microplate shaker, then 100 µL of 1 M sulphuric acid is added to each well and the optical density (OD) is measured. The response that should be obtained, should the system response correctly, would be a characteristic sigmoidal calibration curves, obtained by fitting a four-parameter logistic function to the data points.

The calibrating solutions were prepared by making serial dilutions from a stock solution of the antibody species to be assessed (anti-mouse IgG or ZIF-IgG conjugate). The rest of the species taking part on the experiment should be maintained at constant concentrations. To compare accurately the amounts of soluble antibodies, each well was processed under the identical conditions, and 4 replicates of each measurement were performed.

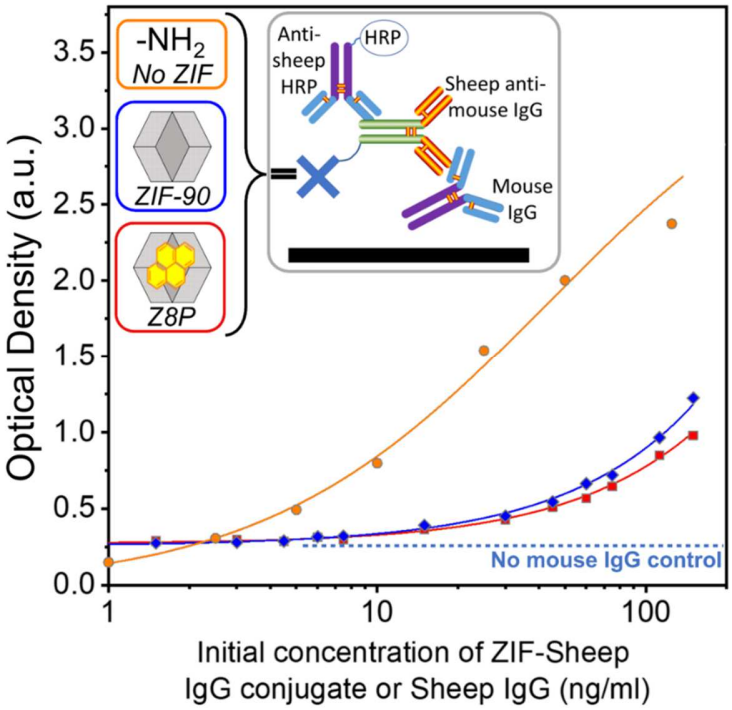

Figure 59 Non-competitive ELISA results. On both the concentration for mouse IgG and anti-sheep IgG Horse Radish Peroxidase (HRP) remains always constant. Orange: Non-competitive sandwich ELISA for the free sheep-anti-mouse IgG used on the posterior coupling to the ZIFs. Blue: Non-competitive sandwich ELISA calibration curves for Z90-IgG. Red: Non-competitive sandwich ELISA calibration curves for Z8P-IgG. The OD (optical density) signal for the blank (coating antibody + blocking agent [casein]) is 0.2633 ± 0.013.

The assay showed the characteristic sigmoidal calibration curve[195] (Figure 59), thus validating the model for further studies. On equal concentrations there is a significant reduction on the activity of the conjugates when compared to the antibodies. This is to be expected since the mobility of the conjugates is significantly reduced given their size. The reproducibility of the replicates for each point on the ELISA curves for the ZIF-IgG conjugates (small standard deviations) was also a strong hint for the good mobility of the colloidal dispersion of the conjugates. If the mobility of the conjugates was not good, then it would be expected to see significantly different results for each replicate, leading to bigger standard deviations.

Controls performed to check any cross reactivity in the indirect ELISA also were performed. All controls have been done with a very high concentration for all the compounds that could show cross-reactivity with the primary (anti-mouse IgG, Table 8). Anti-sheep-HRP had some cross-reactivity against the mouse IgG deposited on the surface of the plate but this was not as strong as to interfere with the signal of the indirect ELISA. The ZIF-IgG conjugates, tested at very high concentrations, showed a residual signal when no mouse IgG is present, but at so low values that there was no real concern of false positive.

Table 8 Controls performed to check any cross reactivity in the indirect ELISA. All controls have been done with a very high concentration for all the compounds that could show cross-reactivity with the primary (anti-mouse IgG). Anti-sheep-HRP has some cross-reactivity against the mouse IgG deposited on the surface of the plate but this is not so strong as to interfere with the signal of the indirect ELISA. The ZIF-IgG conjugates, tested at very high concentrations, show a residual signal when no mouse IgG is present, thus showing non-interaction and potential false positives.

Controls					
	Concentration of Z8P–IgG conjugate (ng/mL)	Concentration of anti-sheep–HRP (ng/mL)	Concentration of Casein (ng/mL)	OD	S.D.
Mouse IgG + casein + anti-sheep IgG–HRP	0	200	1000	**0.191**	**0.002**
Casein + ZIF–IgG conjugate + anti-sheep IgG–HRP	1500	200	1000	**0.085**	**0.007**
	1125	200	1000	**0.079**	**0.008**
	750	200	1000	**0.067**	**0.004**
Casein + anti-sheep IgG–HRP	0	200	1000	**0.057**	**0.003**

The combined strength of antibody specificity and fluorescent Z8P properties was still unproven. To unambiguously prove the combine workings of the selectivity of the antibodies and the ZIF nanoparticles, the inclusion of an imine fluorescent functionality on the ZIF structure was instrumental. This included fluorescent functionality would be used as proof that the conjugate systems retain both key aspects, antibody activity and ZIF crystal structure and usability. The presence of the ZIF element on the conjugate could be detected via the included fluorescence probe and was non-dependent of the antibody activity. While the dual fluorescence and antibody tagged biomaterials would not add immediate value to the LFIA biotest for the colour visualisation of the HRP enzymatic sensor, it was key in the validation of the method to demonstrate that the antibody moves with the fluorescence Z90 antibody conjugate.

To assess this combined antibody-ZIF synergic workings, a parallel two non-competitive sandwich ELISAs were developed, based on the base ELISA previously presented (Figure 58). These experiments will allow to compare the response for Z8P-IgG between non-competitive ELISA and non-competitive fluorescent ELISA. Each well was treated under the same conditions, and each measurement was done in quadruplicate. Both ELISA protocols took place using the exact same concentration for all species. Two measurements took place in parallel:

- Non-competitive ELISA: On a high-binding transparent microtiter plate, where OD is measured as a final step (Figure 60 top)

- Non-competitive fluorescent ELISA: On a high-binding black microtiter plate, are fluorescence is measured as a final step (Figure 60 bottom)

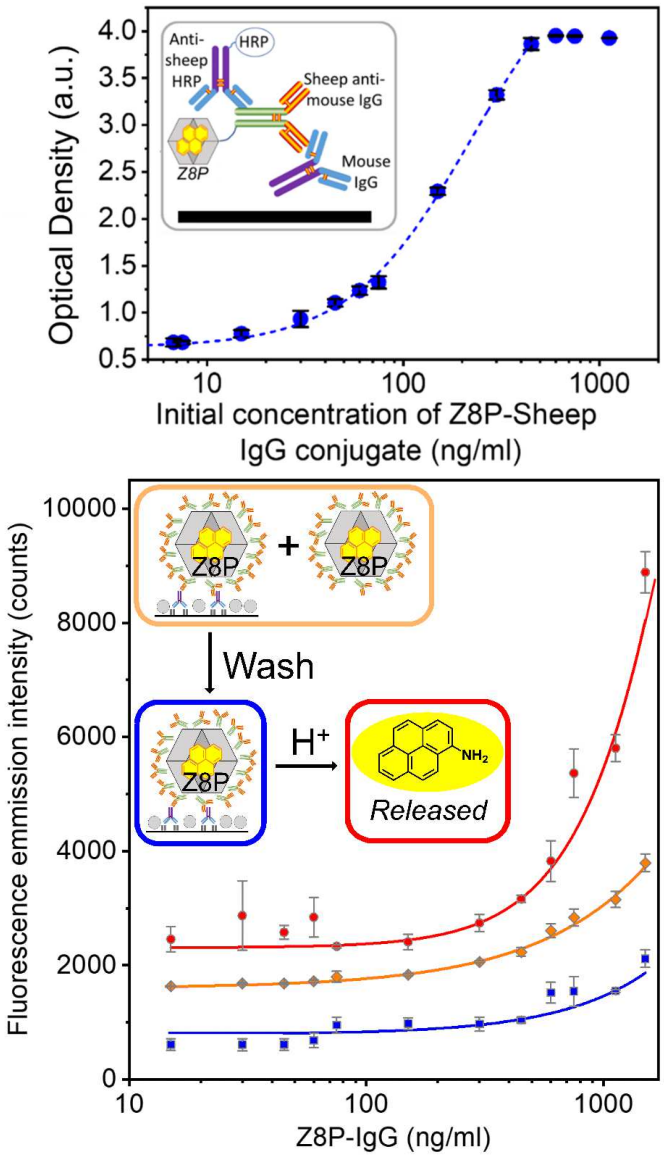

Figure 60 Top: Non-competitive indirect ELISA calibration curves for Z8P-IgG (anti-mouse, from sheep) using high concentrations. The detector reaches saturation at concentrations above 350 ng/mL. The OD signal for the blank (coating antibody + blocking) is 0.72 ± 0.04. Bottom: Fluorescence emission for the non-competitive sandwich ELISA of Z8P sheep anti-mouse IgG conjugate obtained with an excitation wavelength of 335 nm. All the points are blank corrected (the intensity for the blank is subtracted from all points; the blanks' mean intensity is: 168 ± 26 for pre-washing fluorescence, 143 ± 54 for post-washing and 356 ± 5 for the post citric acid induced decomposition). The non-competitive sandwich ELISA calibration curves for Z8P sheep anti-mouse IgG with a very high concentration are also performed. The detector reaches saturation at a concentration of 350 ng/mL. The OD signal for the blank (coating antibody + blocking) is 0.7245 ± 0.043.

The ELISA curve exhibited the expected sigmoidal shape, although an upper limit of analysis was observed at a concentration of 450 ng/mL. These high concentrations oversaturate the photometer (OD above 3.8), but it was a necessity to detect the fluorescence signal, since there is a pronounced difference on the detection sensitivity for both detection methodologies, HRP revealing and fluorescence emission. Attempts at lowering the overall Z8P-IgG concentration to obtain an

unsaturated OD sigmoidal curve reduced the Z8P fluorescence signal below its detection limits. Fluorescence measurements in the non-competitive fluorescence ELISA showed a detectable yet low fluorescence emission intensities (Figure 60, orange line). After a washing step to remove un-bound Z8P particles, the assay gave even lower intensities (Figure 60, blue line). This drop in fluorescence was due to all the non-bonded conjugate particles being removed, only those bonded to the retained antibodies on the surface of the MTP remaining in the well. After the addition of an acidic buffer, a significant increase on the fluorescence can be seen (Figure 60, red line). It was theorized this to be evidence of the inner filter effect being eliminated. This inner-filter effect for Z8P was postulated on section 5.4. This inner filter effect has also been reported for other nanocarrier systems such as liposomes[196]. The breakdown of the Z8P-IgG, and liberation of the dye, eliminates the inner filter effect, leading to an increase of the fluorescence emission by the same amount of fluorophore present.

Non-competitive fluorescence ELISA showed a detectable, yet small, fluorescence signal for the specifically captured conjugate; however, when acid buffer was used to break the system and dismantle the Z8P to is released organic constituents, this upper limit can be overcome, significantly increasing fluorescence for the conjugate. This approach has been employed successfully before on other systems[141, 197], and it shows how both key aspects of the conjugate system, selective binding from the antibodies and fluorescence from the ZIF, can work synergically together.

Z8P-IgG fluorescent response vs DMP

The fluorescent response of the ZIF-IgG conjugate was studied next. The usability of this species as a viable fluorescent bioconjugate was part of the future usability and applicability of Z8P as a biosensor. To this effect, an experiment was designed using the analytical conditions developed previously (section 4.5) to assess the changes in fluorescence quenching of the conjugate, Z8P-IgG, when exposed to a model contaminant, dimethyl phthalate, DMP (Figure 61). A similar response to the one of the Z8P ZIF vs the PAEs (Figure 45) is obtained. This suggests that the antibodies located on the surface of the ZIF were not hindering the detection potential of the Z8P by quenching the fluorescence emission of the ZIF particles. To gather more information regarding the quenching of the Z8P particles by the antibodies, Figure 62 shows a comparative of the fluorescent emission for Z8P, both conjugated and unconjugated. The results of the comparative of conjugated and unconjugated ZIFs show that the antibodies surrounding the Z8P particles quench significantly the fluorescence of the ZIF particles, but do not hinder the usability of the system as a fluorescent detector against PAEs, thus allowing the usability of the ZIFs as bio-labels. Considering the TEM images for the conjugates (Figure 52) the antibodies must be located at the surface of the ZIF nanoparticles, quenching the fluorescence of the fluorophores located at the surface and not at the bulk of the ZIF nanoparticles. These results hint even stronger that the model proposed for the fluorescence mechanism of Z8P vs PAEs (Figure 48) are correct, since the

quenching response of the Z8P part of the conjugate vs the PAEs is not affected by the presence of the antibodies.

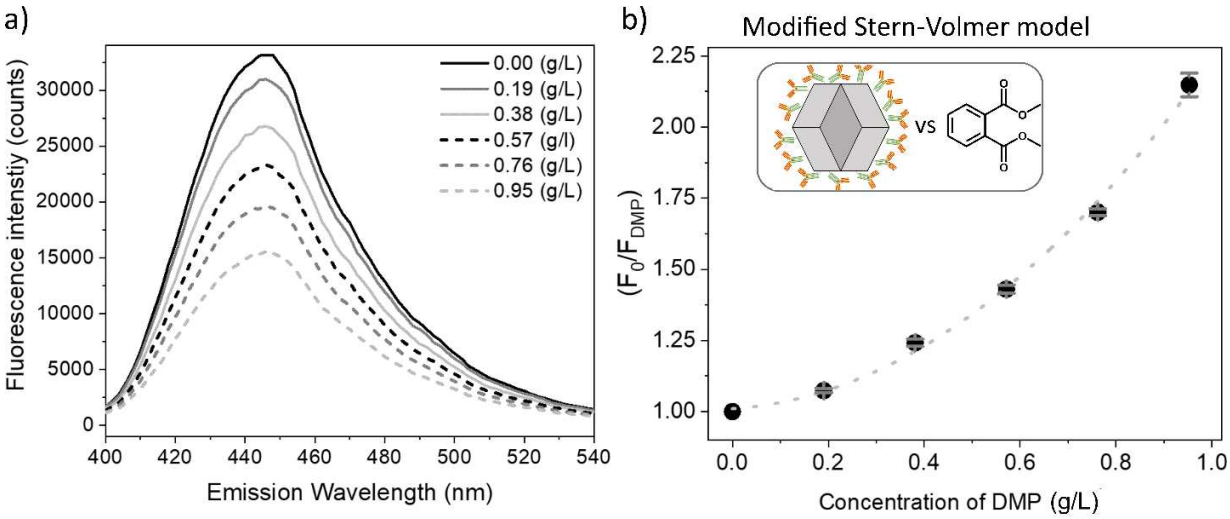

Figure 61 a): Fluorescence spectra for Z8P−IgG (with a constant concentration of 47 µg/mL) when dispersed in borate buffer with increasing concentrations of dimethyl phthalate (DMP, 0.0-1.0 g/mL). b): Modified Stern-Volmer fitting curve for the fluorescence quenching of Z8P−IgG versus the DMP concentrations expressed as g/L. The excitation wavelength is 335 nm, and the emission wavelength maximum is recorded at 445 nm. Each data point represents the mean of duplicate measurements.

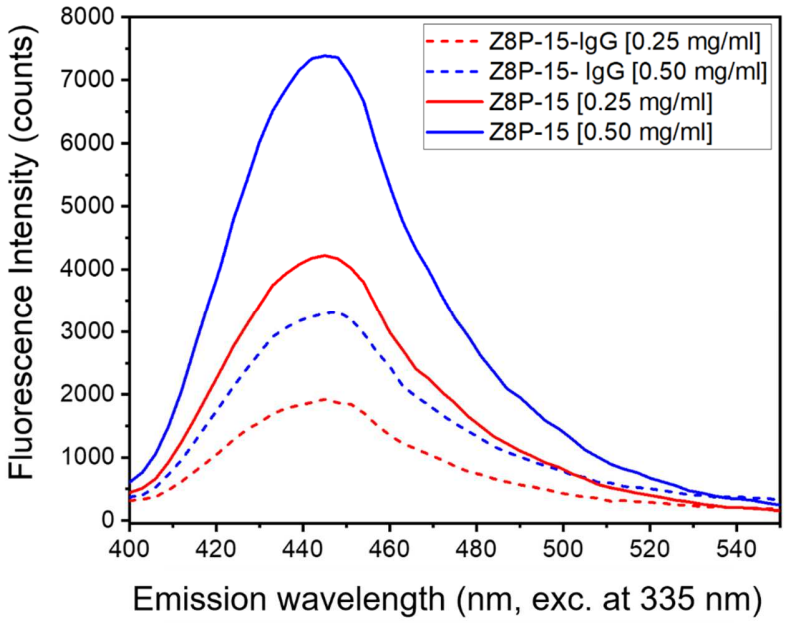

Figure 62 Fluorescence spectra for Z8P and Z8P−IgG, both dispersed in borate buffer with two concentrations of dimethyl phthalate (DMP, 0.25 and 0.50 g/mL). The excitation wavelength is 335 nm, and the emission wavelength maximum is recorded at 445 nm.

Z8P-IgG as a bio-probe in LFIA

Finally, investigating the suitability for the Z8P-IgG system on a lateral flow immunoassay (LFIA) methodology was the last critical step for its potential for future applications[143, 198]. For this, an experiment methodology was developed to test the mobility of the Z8P-IgG conjugates on a solid chromatographic matrix. The matrix chosen for this test was Polyvinylidene fluoride (PVDF). The more tradition nitrocellulose was also tested, but there was a very strong interaction between the ZIF-IgG conjugate and the nitrocellulose matrix, not allowing the free flow of the conjugates. In order to facilitate the experimental setup, a new Z8P-IgG conjugate was synthesized, replacing the anti-mouse IgG by an anti-sheep IgG-HRP conjugate, thus allowing a direct revealing of the presence of the antibodies with the use of TMB without needing an additional antibody. The experiment began by activating the PVDF membrane through submersion in pure ethanol followed by rinsing in deionized water (Figure 63). This turns the surface of the PVDF matrix electrostatically active, allowing it to interact with chemical or biological species. After drying in an open atmosphere, a solution containing sheep IgG was placed on the immobilization point. This is where the target for the antibodies on the ZIF-conjugates will be immobilized and they should be retained, should they flow efficiently. After letting it dry, the PVDF strip with the immobilized sheep IgG was then submerged in a casein solution to block all remaining active sites on the strip, thus eliminating any undesired interaction and retention of the ZIF-IgG conjugate. A volume of the Z8P-IgG HRP dispersion was put on the elution starting point, let dry again and the adsorption pad was attached to the strip. The Z8P-IgG HRP was then eluted using borate buffer and is let dry again.

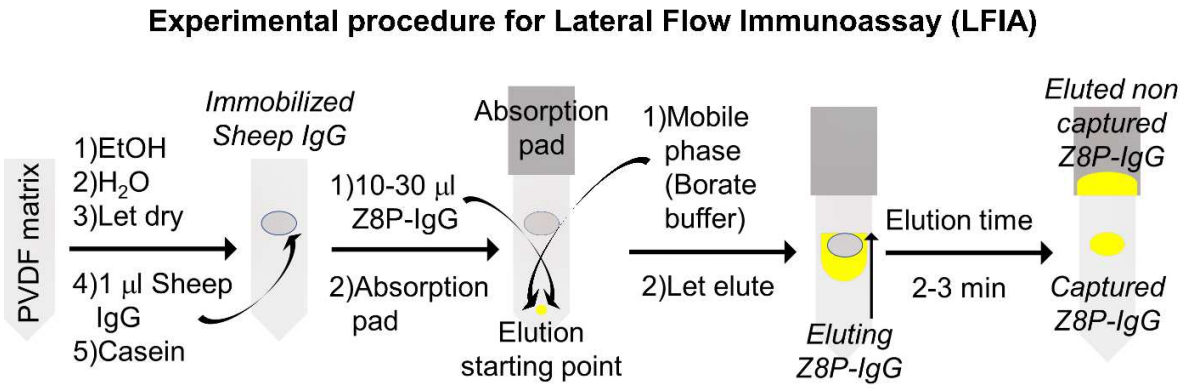

Figure 63 *Basic experimental set-up to use Z8P-IgG on LFIA methodologies.*

At this step it could be seen to the naked eye the yellow colouring of the ZIF part of the conjugate on two areas of the strip: the capture zone and the absorption pad at the end of the strip (Figure 64). For stronger evidence, TMB solution was used to reveal the location of the anti-sheep HRP-labelled antibodies, turning the areas where sheep antibodies part of the conjugate was located to a very intense blue.

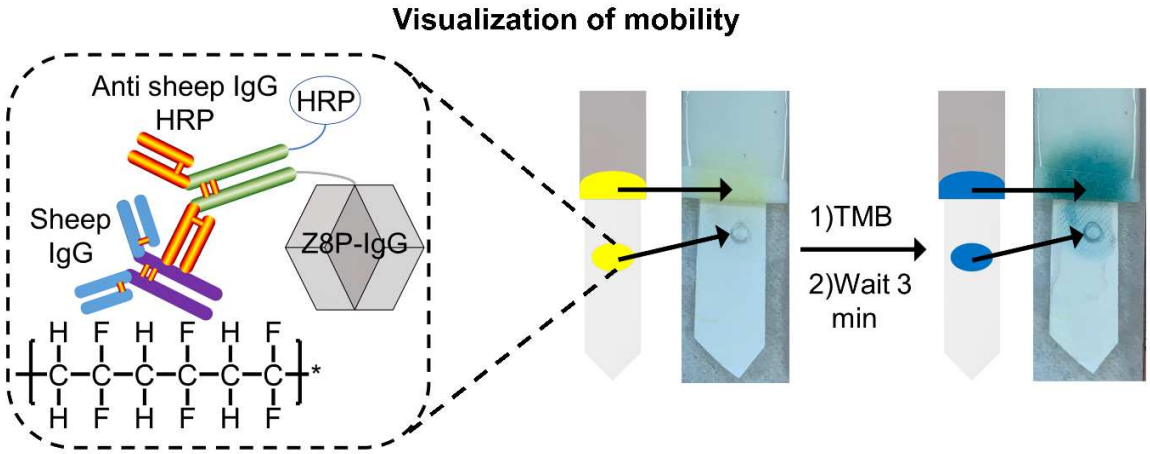

Figure 64 Visualization of the successful selective binding of the ZIF-IgG conjugate.

This proves that the antibodies part of the conjugates had successfully been captured on the area of interest, yet it was not evidence enough to conclusively say the fluorescent ZIF was also retained there. For this, using the same principle used on the non-competitive fluorescent ELISA, a new experiment was developed (Figure 65). On this experiment, the part of the strip where the sheep IgG (target) was immobilized at the beginning of the experiment was cut and was acidly digested to release all the 1ap species present, should there be any Z8P ZIF present on the capture area. Then a fluorescence emission measurement should be able to inform if any fluorescence probe is present on the solution or not, thus proving Z8P was present on the target area.

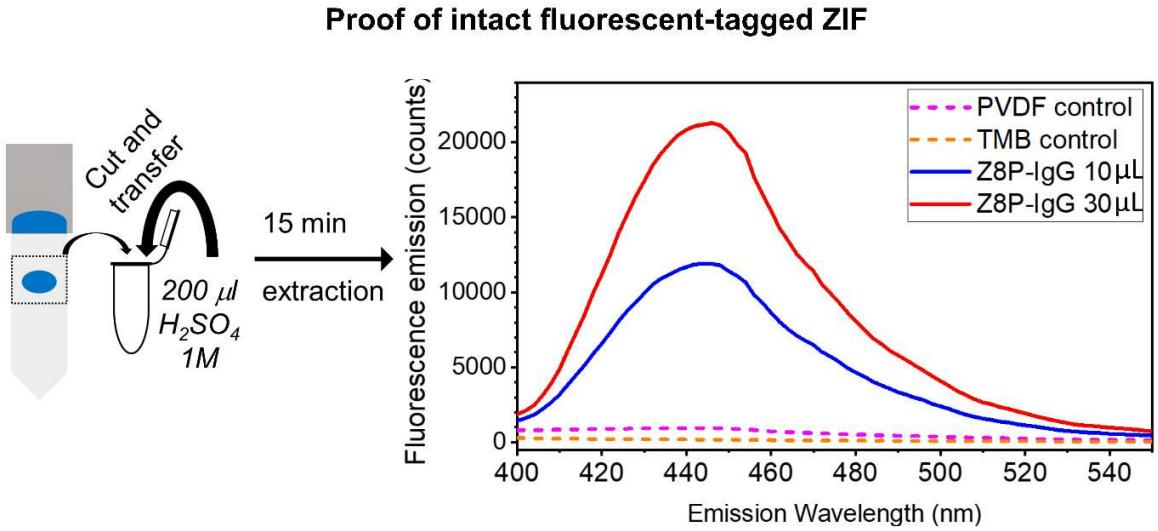

Figure 65 Experiment to study successful presence of the fluorescent Z8P ZIF part of the Z8P-IgG conjugate on the capture area of the LFIA strip.

Results showed a successful identification of the presence of 1ap on the target area. A proportional increase on the fluorescent signal measured as the initial amount of available Z8P-IgG was put at the beginning of the strip prior to any elution of the system was identified.

This set of experiments are evidence that, even though there are still many parameters to optimize, a modified colloidal ZIF shows great potential to act as a bio-label to detect small aromatic molecules while retaining the specific activity of the bound antibody.

5. Conclusions and outlook

This thesis aimed to explore the use of ZIFs as potential bio-compatible materials acting as mobile conjugates with antibodies. The developed ZIF was capable of detecting easily and quickly the concentration of PAEs in a water solution by including a fluorescence functionality on its structure.

As a first step, the methodology to develop a modified fluorescent colloidal ZIF with available reactive functionalities has been shown. The methodology is a two-step one pot reaction, were an imine is synthesized in situ that will later be part of the ZIF crystal structure as a building block. The imine is formed by a Schiff base reaction condensation between the fluorescent functionality, 1-aminopyrene, and the basic building block of the ZIF, imidazole 2-carboxaldehyde. To obtain a final colloidal dispersion of the ZIF of interest several parameters have been considered and studied, finding a compromise between particle size and reaction yield that was satisfactory to the purpose. Two different capping agents were also explored, and advantages and disadvantages for each were presented and explained. N-butylamine leads to smaller, less polydisperse particles, but it blocks the aldehyde functionalities of the ZIFs, hindering their potential post-synthetic modification. Sodium methoxide leads to bigger, more polydisperse particles, but it does not interfere with the chemical functionalities of the final ZIF particles. This ZIF synthesis methodology proved to be easy and safe to use and gave a non-aggregated dispersion of the fluorescent ZIFs of interest. Moreover, parameters able to tune particle size and fluorophore inclusion have been presented. There remains scope to optimize the ZIF synthesis methodology, particularly towards targeting reduced particle sizes (e.g. 100 nm or below) and, more importantly, a lower polydispersity in particle size in the colloid solution.

The extensive use of HPLC as an analytical technique was also explored to obtain accurate chemical composition of the organic ligands forming the presented modified ZIFs. Both mobile phase systems include the use of a phosphate buffered solution in water, a necessity to resolve the imidazolate species (2-methylimidazole and imidazolate 2-carboxaledhyde) and the two pyrene species (1-aminopyrene and the imine). Two organic solvents were tested for the mobile phases, methanol and acetonitrile. Acetonitrile works with a significantly smaller internal pressure during HPLC quantification and is a cleaner solvent when it comes to peak identification. However, the use of acetonitrile can lead to internal precipitation of the phosphate salt if care is not exercised during the HPLC quantification operation. This precipitation hazard is not present when working with methanol as a mobile phase, but the working pressure then reaches dangerously close to the threshold for the safe operation of the HPLC instrument. For the sample preparation for HPLC, two different digestion methodologies were explored. The acid digestion methodology breaks down the ZIF by protonating the imidazolates to imidazole, thus eliminating the Zn-imidazolate coordination. The alkaline digestion methodology breaks down the ZIF by displacing and sequestrating the zinc metallic nodes from the ZIF into the EDTA complexation agent, releasing the imidazolates as anions into solution. The use of the alkaline digestion methodology is more complex and elaborate than the one based in acidic conditions, but it allows to quantify the imine directly as a whole chemical species. In this way, the alkaline digestion approach proved that the imine is part of the modified ZIFs as a component of the crystal structure of the ZIF. By parallel use of HPLC, PXRD and TEM for the development of the synthetic method for the desired ZIF,

the best ratio of the organic ligands can be obtained to give the desired sodalite-like crystalline structure. Important insight into how the fluorescent functionality is included within the ZIF system, as well as how it affects the ZIF formation was gained.

The fluorescence studies resulted in concentration/signal relationships for all the chosen analytes, short chained phthalate acyl esters. The modified Stern-Volmer model fit the calibration relationship. The selectivity of the fluorescent system is something to be optimized, since it relies mostly on sample type and pre-treatment; small aromatic molecules would most likely interfere with the quenching. However, if the treatment of the sample pre-measurement is adequate, this modified ZIF could be part of a continuous, and cost-effective surveillance system, for example with potential applications in monitoring waste waters from industrial processing plants. The obtained fluorescence emission data, combined with very basic computer modelling, points towards the fluorescence quenching relying on the inclusion of the PAEs inside of the ZIF pore and forming an exciplex by π- π stacking with the imine part of the ZIF. A permeation model was proposed showing how the PAEs can permeate within the ZIF pores as a previous step to the exciplex formation. The formation of a ground-state complex between the imine and the PAEs was not proved unambiguously; UV-vis and 1H NMR titration experiments could corroborate the exciton formation. This modified ZIF is a good first step towards the development of a cheap and easy-to-use device to detect the presence of PAEs in environmental samples. More importantly, the potential of colloidal ZIFs as bio-compatible materials has been shown. ZIF-90 as a basic building block could be developed to be used as a selective carrier, targeting a specific area with the use of the antibodies.

Lastly, the methodology for the formation of a stable a ZIF-antibody conjugate is shown, and the formation of a stable covalent linkage is demonstrated. This covalent link was based on an imine link between the free aldehyde functionalities on the ZIF particles surface with an available amino functionality on the antibodies, mainly the one presented on residual lysine. Once the imine was formed, it was irreversibly stabilized by selectively reducing to form an amine bond by using sodium cyanoborohydride. The presence of the linkage was demonstrated by LC-MS/MS analysis of the digested conjugate, proving the strength of the conjugation methodology. In addition to preserving the mobility of the nanoparticle entity the conjugation also prevents protein aggregation of the antibodies and, like an exoskeleton, might elicit protection against degradation. ELISA experiments showed the mobility of the system, as well as proving that the ZIG-antibody conjugates successfully combined the aspects of both the modified ZIFs and the selectivity of the antibodies. These ZIF-antibody conjugates expand drastically the potential of ZIFs to be applied as highly selective bio probes in a variety of analytical and diagnostic applications such as ELISA and LFIA. The potential of ZIFs as compatible biomaterials has been shown. The combination of the activity and selectivity of antibodies with the versatility of structure and composition of ZIFS (chemical reactivity, capture of biological species, a porous carrier, etc) on a final system that is stable and mobile in dispersion has been presented.

6. Additional experimental data

6.1. Imine ^{1}H-NMR spectra

i2ca: ^{1}H NMR (DMSO, 400 MHz): δ 7.308 and 7.531 (2 d, 2H, H3 & H4 respectively; H3 and H4 are two unresolved doublets, theoretical calculations set the J value at approximately 4 Hz), **9.647 (s, 1H, H1)**, 13.501 (s br, 1H, H2; interchangeable proton)

1-AP: ^{1}H NMR (DMSO, 400 MHz): δ **6.31 (s, 2H, NH2)**, 7.38 (d, J = 8.3 Hz, 1H, H2), 7.72 (d, J = 8.8 Hz, 1H, H4), 7.85 (t, J = 7.7 Hz, 1H, H6), 7.89 (d, J = 8.8 Hz, 1H, H3), 7.90 (d, J = 9.3 Hz, 1H, H9), 7.96 (d, J = 8.4 Hz, 1H, H2), 8.00 (d, 1H, H5), 8.27 (d, 1H, J = 9.2, H9)

Imine: ^{1}H NMR (DMSO, 400 MHz): δ 7.2-7.6 (2 d, 2H, H3 &H4 i2ca*), 8.038-8.326 (m, 8H), **8.760 (s, 1H, Imine H1)**, 8.823 (d, 1H, J = 9.2, H9 1-AP), 13.283 (s br, 1H, H2 i2ca)

n-butylamine and i2ca Imine: ^{1}H NMR (DMSO, 400 MHz): δ 0.88-1.33 (several multiples, 7H, alkaline chain of butylamine), 7.11 (s br, 2H, H3 &H4 i2ca*), **8.17 (s, 1H, Imine H1)**, 11.27 (s br, 1H, H2 i2ca, interchangeable proton)

6.2. TEM and TEM-EDS data for the Z90P ZIFs

TEM images for Z90P-5

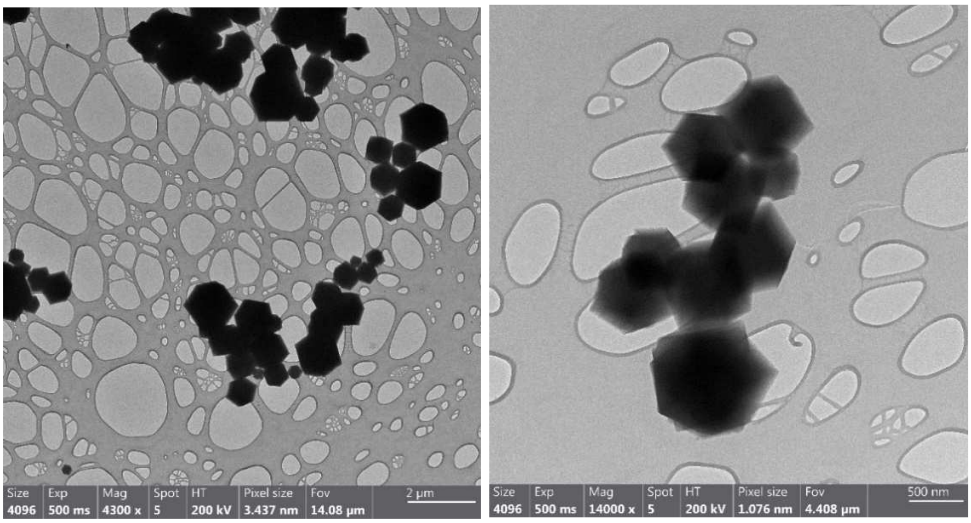

Figure 66 TEM pictures for Z90P-5. The typical shape for ZIF particles[171] can be seen, with some polydispersity in size, between 50 to 2000 nm. This size is determined using only TEM results and are not absolute values.

Table 9 Atomic composition of the rhombic particles observed at TEM for the Z90P-10 sample, quantified via EDS. The results are the average of three different spots on the TEM grid

Z	Element	Family	Atomic fraction	% Re.St.Dev.
-	-	-	%	
6	C	K	53.82	3.05
7	N	K	22.13	4.77
8	O	K	16.06	1.67
30	Zn	K	7.99	18.04

TEM images for Z90P-10

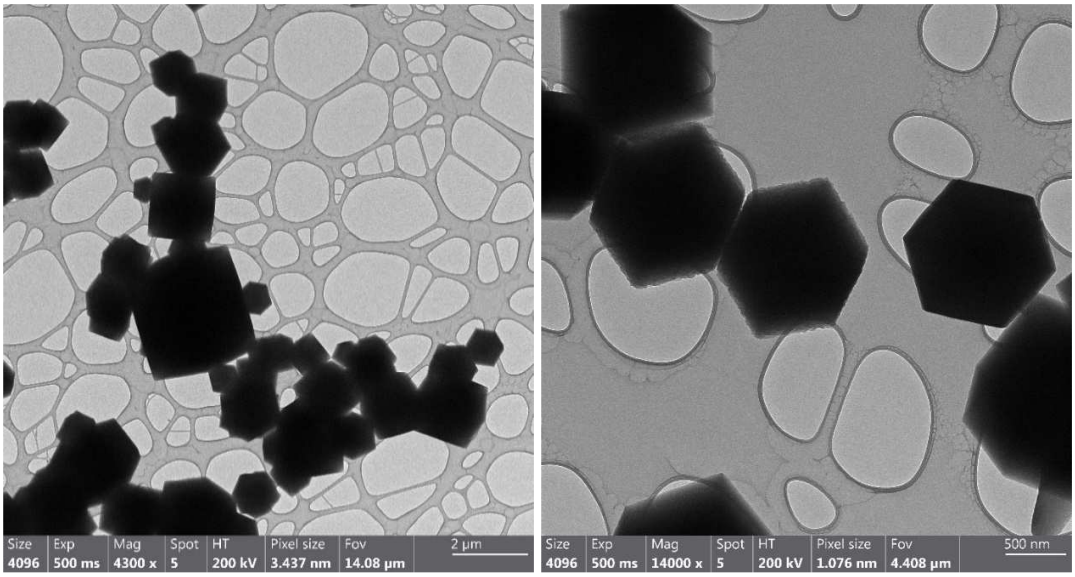

Figure 67 TEM pictures for Z90P-10. The typical shape for ZIF particles[171] can be seen, with some polydispersity in size, between 50 to 2000 nm. This size is determined using only TEM results and are not absolute values.

Table 10 Atomic composition of the rhombic particles observed at TEM for the Z90P-10 sample, quantified via EDS. The results are the average of three different spots on the TEM grid

Z	Element	Family	Atomic fraction	% Re.St.Dev.
-	-	-	%	
6	C	K	54.92	0.38
7	N	K	21.72	4.74
8	O	K	14.64	7.27
30	Zn	K	8.72	2.29

TEM images for Z90P-15

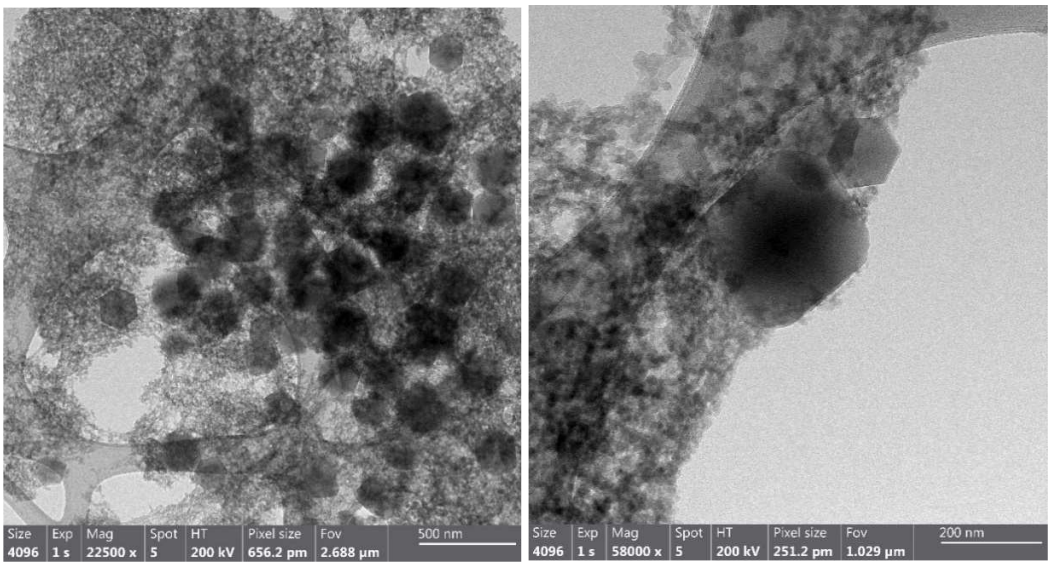

Figure S68 TEM pictures for Z90P-15. The typical shape for ZIF particles[171] can be seen, with an approximate size of 50 nm. Sections with a clearly undefined particles are also observable, with sized of around 30 nm. This size is determined using only TEM results and are not absolute values.

Table 11 Atomic composition of the rhombic particles observed at TEM for the Z90P-15 sample, quantified via EDS. The results are the average of three different spots on the TEM grid

Z	Element	Family	Atomic fraction	% Re.St.Dev.
-	-	-	%	
6	C	K	60.76	8.36
7	N	K	21.64	11.80
8	O	K	10.91	14.07
30	Zn	K	6.70	15.13

Table 12 Atomic composition of the undefined observed at TEM for the Z90P-15 sample, quantified via EDS. The results are the average of three different spots on the TEM grid

Z	Element	Family	Atomic fraction	% Re.St.Dev.
-	-	-	%	
6	C	K	45.60	6.90
7	N	K	29.44	8.00
8	O	K	13.76	17.37
30	Zn	K	11.20	11.04

TEM images for Z90P-20

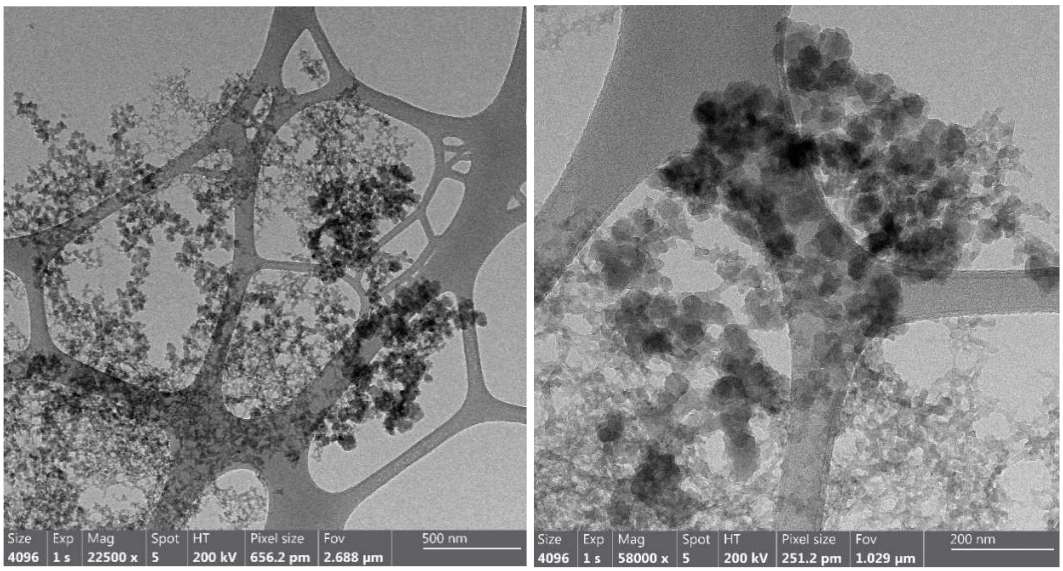

Figure 69 TEM pictures for Z90P-20. Only undefined particles are observable, with sized of around 30 nm. This size is determined using only TEM results and are not absolute values

Table 13 Atomic composition of the undefined observed at TEM for the Z90P-20 sample, quantified via EDS. The results are the average of three different spots on the TEM grid

Z	Element	Family	Atomic fraction	% Re.St.Dev.
-	-	-	%	
6	C	K	55.51	0.43
7	N	K	25.22	1.18
8	O	K	10.78	3.96
30	Zn	K	8.49	3.27

TEM images for Z90P-25

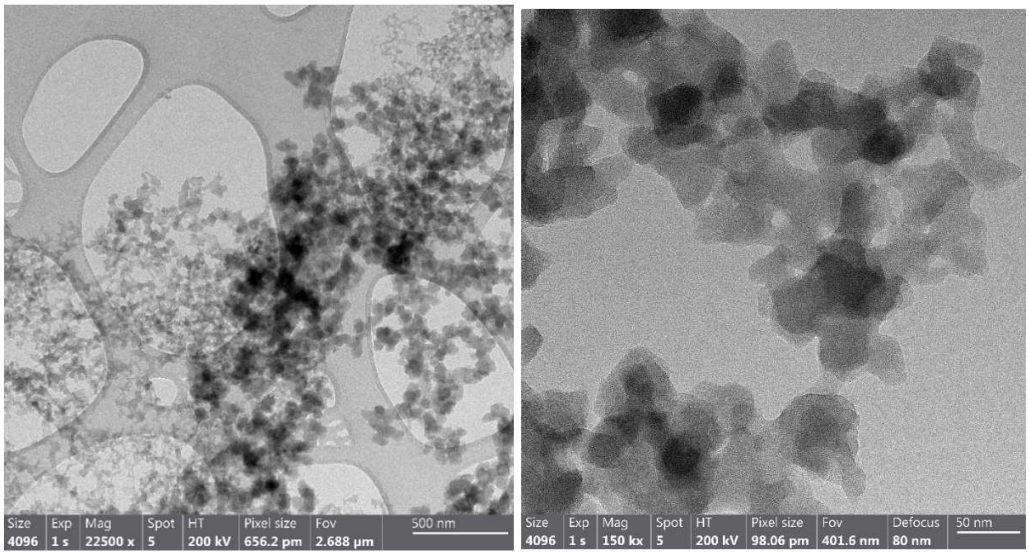

Figure 70 TEM pictures for Z90P-25. Only undefined particles are observable, with sized of around 30 nm. This size is determined using only TEM results and are not absolute values

Table 14 Atomic composition of the undefined observed at TEM for the Z90P-25 sample, quantified via EDS. The results are the average of three different spots on the TEM grid

Z	Element	Family	Atomic fraction	% Re.St.Dev.
-	-	-	%	
6	C	K	61.41	5.52
7	N	K	22.50	8.38
8	O	K	8.74	12.12
30	Zn	K	7.36	8.34

6.3. Converting HPLC data of Z90P-(5-30)$^{210}_{MeONA,1:4}$ family of ZIFs composition to atomic fraction for HPLC/EDS comparison

Using these equations, is possible to convert (µmol/g ZIF) for any organic analyte into its % atomic fraction for all elements forming it: carbon, nitrogen, oxygen and zinc.

$\binom{(\%\ atomic\ fraction}{Carbon} = 100 \cdot \frac{4 \cdot \left(\frac{\mu mol\ \ i2ca}{g\ ZIF}\right) + 16 \cdot \left(\frac{\mu mol\ \ 1ap}{g\ ZIF}\right) + 20 \cdot \left(\frac{\mu mol\ \ imine}{g\ ZIF}\right)}{A}$
$\binom{(\%\ atomic\ fraction}{Nitrogen} = 100 \cdot \frac{2 \cdot \left(\frac{\mu mol\ \ i2ca}{g\ ZIF}\right) + 1 \cdot \left(\frac{\mu mol\ \ 1ap}{g\ ZIF}\right) + 3 \cdot \left(\frac{\mu mol\ \ imine}{g\ ZIF}\right)}{A}$
$\binom{(\%\ atomic\ fraction}{Oxigen} = 100 \cdot \frac{1 \cdot \left(\frac{\mu mol\ \ i2ca}{g\ ZIF}\right)}{A}$
$\binom{(\%\ atomic\ fraction}{Zinc} = 100 \cdot \frac{1 \cdot \left(\frac{\mu mol\ \ Zn}{g\ ZIF}\right)}{A}$
"A" is the sum of all individual atoms for one ZIF $A = \left[4 \cdot \left(\frac{\mu mol\ \ i2ca}{g\ ZIF}\right) + 16 \cdot \left(\frac{\mu mol\ \ 1ap}{g\ ZIF}\right) + 20 \cdot \left(\frac{\mu mol\ \ imine}{g\ ZIF}\right)\right] + \left[2 \cdot \left(\frac{\mu mol\ \ i2ca}{g\ ZIF}\right) + 1 \cdot \left(\frac{\mu mol\ \ 1ap}{g\ ZIF}\right) + 3 \cdot \left(\frac{\mu mol\ \ imine}{g\ ZIF}\right)\right] + [1 \cdot \left(\frac{\mu mol\ \ i2ca}{g\ ZIF}\right)] + \left[1 \cdot \left(\frac{\mu mol\ \ Zn}{g\ ZIF}\right)\right]$

6.4. DLS characterization data

Table 15. Particle size distribution for Z90-IgG dispersed in borate buffer measured in DLS. Before the measurement of cycle 1, 5 min sonication for the sample took place. Cycle 2 happened immediately after cycle 1, with a 5 min sonication step in between cycles.

Cycle 1		
Time from start	**Particle size**	**St Dev**
(min)	(nm)	(nm)
0	1340	233.1
5	1456	444.5
10	1606	460.2
15	1642	347.5
20	1694	361.5
25	1938	518.6
Cycle 2		
Time from start	**Particle size**	**St Dev**
(min)	(nm)	(nm)
0	1345	227.1
5	1773	373.3
10	1803	360.7
15	1944	391.5
20	2207	453
25	2196	453.1

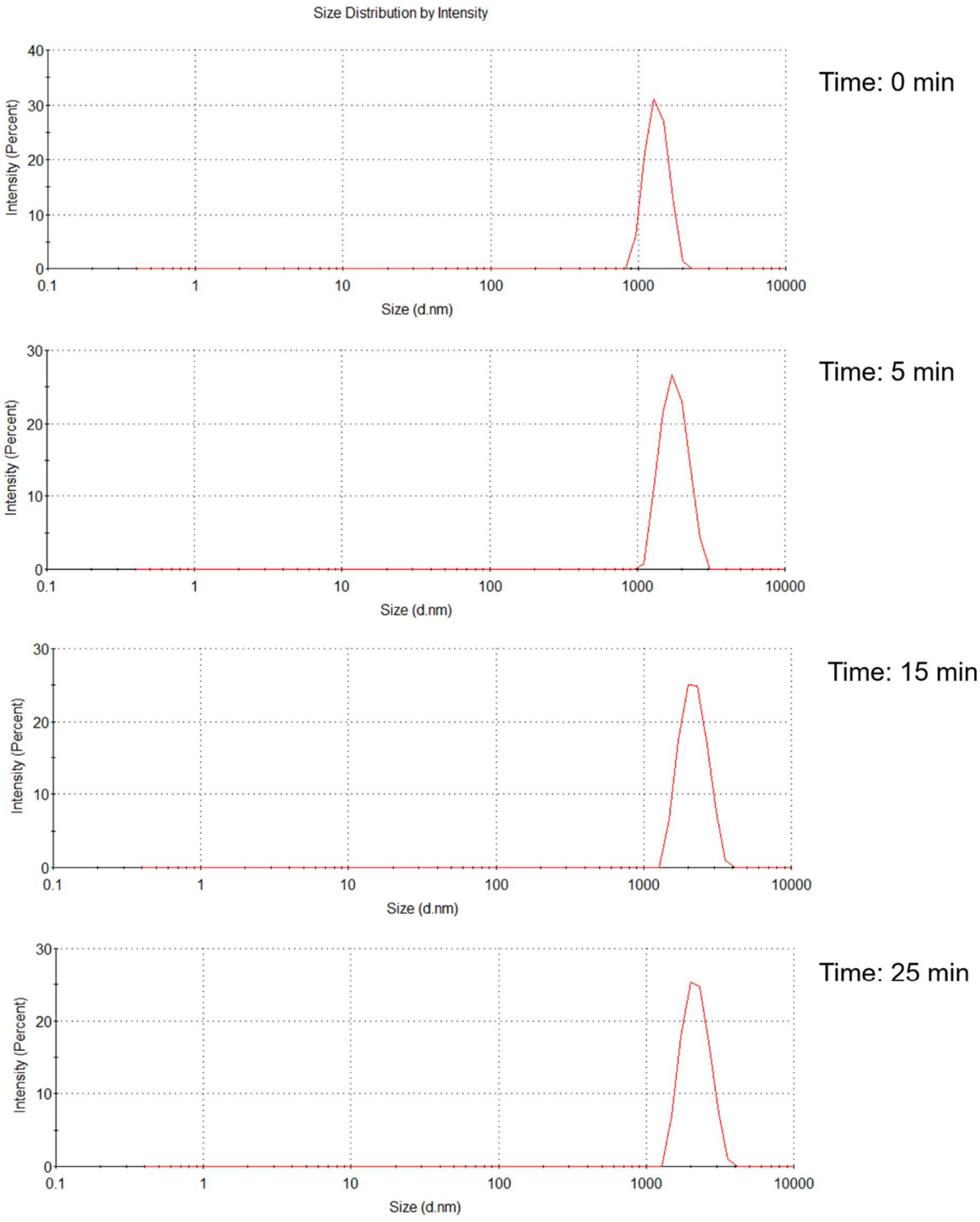

Figure 71 Particle size distribution as a function of time determined by DLS for cycle 1. Same results are observed on cycle 2.

6.5. NTA characterization data

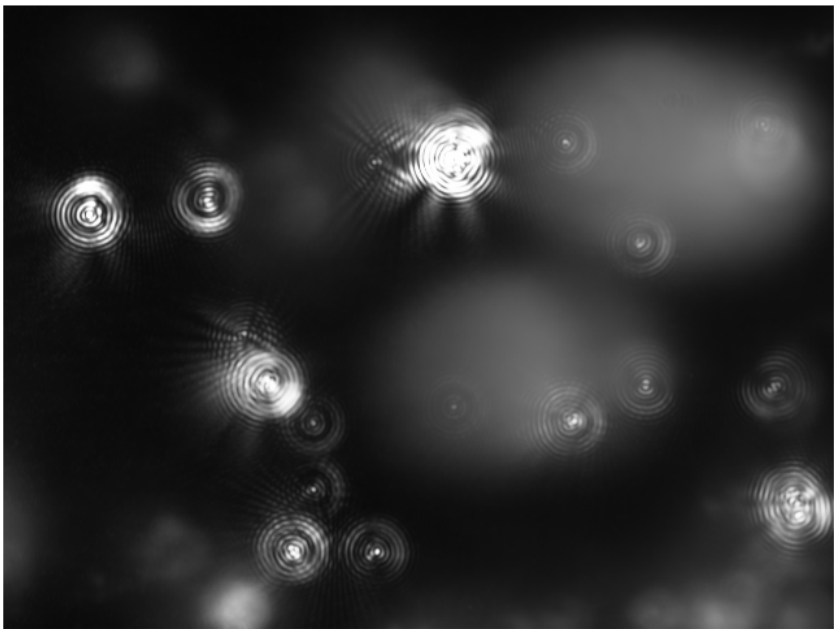

Figure 72 Stationary image of the nanoparticle Z90-IgG dispersion seen through NTA. The rings around the particles are diffraction spheres, due to the crystallographic nature of the conjugate.

6.6. LC-MS/MS characterization of the ZIF-IgG bond: additional data

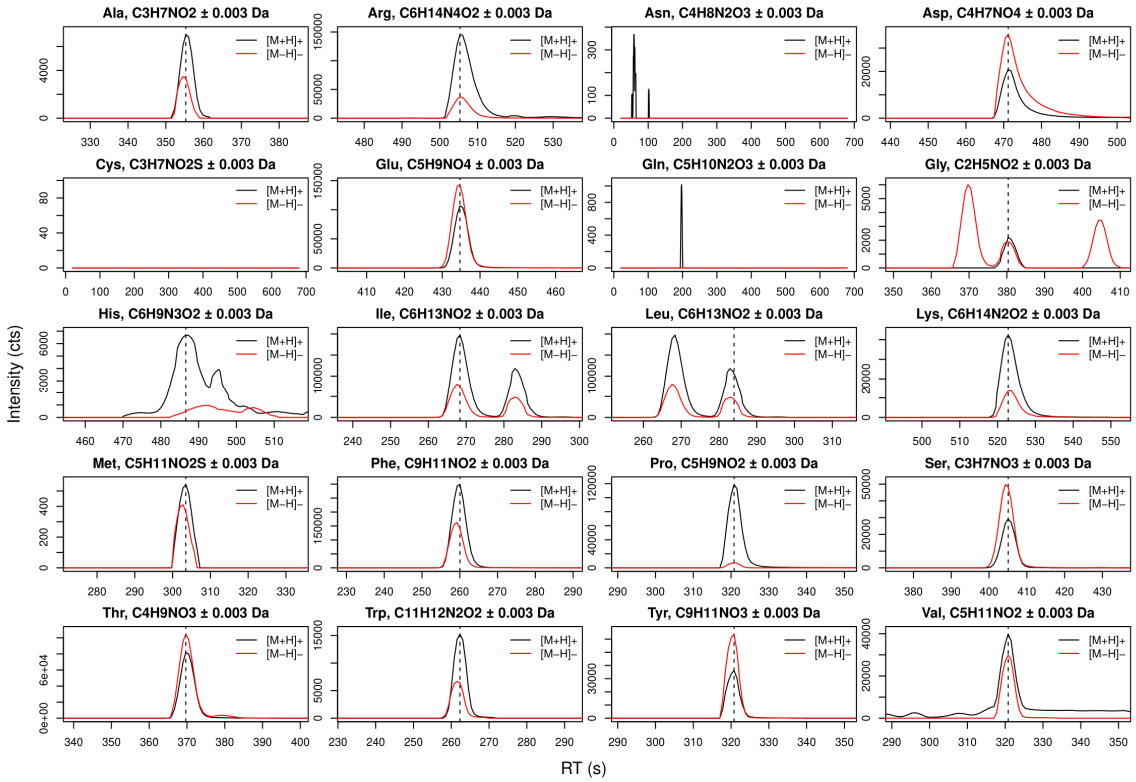

Figure 73 Extracted ion chromatograms for the 20 proteinogenic amino acids released from acidic hydrolysis of 0.01 mg sheep antibody. Extracted ions ($[M+H]^+$, $[M-H]^-$) and mass windows are indicated.

Table 16 LC-MS target list for amino acids and putative amino acid imidazole derivatives.

Name	SMILES	Formula	Neutral mass	$[M+H]^+$	$[M-H]^-$
Ala	CC(C(=O)O)N	C3H7NO2	89.0477	90.0550	88.0404
Ala imidazole derivative 1	CC(C(=O)O)NCC1N=CC=N1	C7H11N3O2	169.0851	170.0924	168.0779
Arg	C(CC(C(=O)O)N)CN=C(N)N	C6H14N4O2	174.1117	175.1190	173.1044
Arg imidazole derivative 1	C(CC(C(=O)O)NCC1N=CC=N1)CN=C(N)N	C10H18N6O2	254.1491	255.1564	253.1418
Arg imidazole derivative 2	C(CC(C(=O)O)N)CN=C(N)NCC1N=CC=N1	C10H18N6O2	254.1491	255.1564	253.1418
Asn	C(C(C(=O)O)N)C(=O)N	C4H8N2O3	132.0535	133.0608	131.0462
Asn imidazole derivative 1	C(C(C(=O)O)NCC1N=CC=N1)C(=O)N	C8H12N4O3	212.0909	213.0982	211.0837
Asn imidazole derivative 2	C(C(C(=O)O)N)C(=O)NCC1N=CC=N1	C8H12N4O3	212.0909	213.0982	211.0837
Asp	C(C(C(=O)O)N)C(=O)O	C4H7NO4	133.0375	134.0448	132.0302

Name	SMILES	Formula	Neutral mass	$[M+H]^+$	$[M-H]^-$
Asp imidazole derivative 1	C(C(C(=O)O)NCC1N=CC=N1)C(=O)O	C8H11N3O4	213.0750	214.0822	212.0677
Cys	C(C(C(=O)O)N)S	C3H7NO2S	121.0197	122.0270	120.0125
Cys imidazole derivative 1	C(C(C(=O)O)NCC1N=CC=N1)S	C7H11N3O2S	201.0572	202.0645	200.0499
Glu	C(CC(=O)O)C(C(=O)O)N	C5H9NO4	147.0532	148.0604	146.0459
Glu imidazole derivative 1	C(CC(=O)O)C(C(=O)O)NCC1N=CC=N1	C9H13N3O4	227.0906	228.0979	226.0833
Gln	C(CC(=O)N)C(C(=O)O)N	C5H10N2O3	146.0691	147.0764	145.0619
Gln imidazole derivative 1	C(CC(=O)NCC1N=CC=N1)C(C(=O)O)N	C9H14N4O3	226.1066	227.1139	225.0993
Gln imidazole derivative 2	C(CC(=O)N)C(C(=O)O)NCC1N=CC=N1	C9H14N4O3	226.1066	227.1139	225.0993
Gly	C(C(=O)O)N	C2H5NO2	75.0320	76.0393	74.0248
Gly imidazole derivative 1	C(C(=O)O)NCC1N=CC=N1	C6H9N3O2	155.0695	156.0768	154.0622
His	C1=C(NC=N1)CC(C(=O)O)N	C6H9N3O2	155.0695	156.0768	154.0622
His imidazole derivative 1	C1=C(NC=N1)CC(C(=O)O)NCC1N=CC=N1	C10H13N5O2	235.1069	236.1142	234.0996
Ile	CCC(C)C(C(=O)O)N	C6H13NO2	131.0946	132.1019	130.0874
Ile imidazole derivative 1	CCC(C)C(C(=O)O)NCC1N=CC=N1	C10H17N3O2	211.1321	212.1394	210.1248
Leu	CC(C)CC(C(=O)O)N	C6H13NO2	131.0946	132.1019	130.0874
Leu imidazole derivative 1	CC(C)CC(C(=O)O)NCC1N=CC=N1	C10H17N3O2	211.1321	212.1394	210.1248
Lys	C(CCN)CC(C(=O)O)N	C6H14N2O2	146.1055	147.1128	145.0983
Lys imidazole derivative 1	C(CCNCC1N=CC=N1)CC(C(=O)O)N	C10H18N4O2	226.1430	227.1503	225.1357
Lys imidazole derivative 2	C(CCN)CC(C(=O)O)NCC1N=CC=N1	C10H18N4O2	226.1430	227.1503	225.1357
Met	CSCCC(C(=O)O)N	C5H11NO2S	149.0510	150.0583	148.0438
Met imidazole derivative 1	CSCCC(C(=O)O)NCC1N=CC=N1	C9H15N3O2S	229.0885	230.0958	228.0812
Phe	C1=CC=C(C=C1)CC(C(=O)O)N	C9H11NO2	165.0790	166.0863	164.0717
Phe imidazole derivative 1	C1=CC=C(C=C1)CC(C(=O)O)NCC1N=CC=N1	C13H15N3O2	245.1164	246.1237	244.1092
Pro	C1CC(NC1)C(=O)O	C5H9NO2	115.0633	116.0706	114.0561
Ser	C(C(C(=O)O)N)O	C3H7NO3	105.0426	106.0499	104.0353
Ser imidazole derivative 1	C(C(C(=O)O)NCC1N=CC=N1)O	C7H11N3O3	185.0800	186.0873	184.0728
Thr	CC(C(C(=O)O)N)O	C4H9NO3	119.0582	120.0655	118.0510
Thr imidazole derivative 1	CC(C(C(=O)O)NCC1N=CC=N1)O	C8H13N3O3	199.0957	200.1030	198.0884
Trp	C1=CC=C2C(=C1)C(=CN2)CC(C(=O)O)N	C11H12N2O2	204.0899	205.0972	203.0826
Trp imidazole derivative 1	C1=CC=C2C(=C1)C(=CN2)CC(C(=O)O)NCC1N=CC=N1	C15H16N4O2	284.1273	285.1346	283.1200
Tyr	C1=CC(=CC=C1CC(C(=O)O)N)O	C9H11NO3	181.0739	182.0812	180.0666
Tyr imidazole derivative 1	C1=CC(=CC=C1CC(C(=O)O)NCC1N=CC=N1)O	C13H15N3O3	261.1113	262.1186	260.1041
Val	CC(C)C(C(=O)O)N	C5H11NO2	117.0790	118.0863	116.0717
Val imidazole derivative 1	CC(C)C(C(=O)O)NCC1N=CC=N1	C9H15N3O2	197.1164	198.1237	196.1092

Table 17 Mass accuracy and isotope pattern analysis for putative lysine imidazole derivative at retention time 558 s (m/z 227.1500).

Isotope	m/z	theoretical m/z	Error (mDa)	Intensity (%)	Theoretical intensity (%)	Difference (%)
M	227.1500	227.1503	0.3	100	100	0
M+1	228.1533	228.1530	0.3	14.26	12.56	-1.69
M+2	229.1567	229.1552	1.5	1.31	1.14	-0.17

6.7. Studies on the decomposition of the ZIF conjugates: additional data

Table 18 Positions for each of the first diffractions for the ZIF−IgG conjugates and its value in radians for use on the Scherrer equation.

Calculation of cosθ in radians			
Diffraction	Angle (°)	Angle (radians)	Cosen angle
[1,1,0]	7.3	0.064	0.998
[2,0,0]	10.4	0.091	0.996
[2,1,1]	12.7	0.111	0.994

Table 19 FWHM for each of the first three diffractions for each conjugate (Z8P-IgG on top, Z90-IgG on bottom) for each of the degradation times studied. To calculate these values, we used the background subtracted diffractograms (Using "Diffrac.EVA") and we fitted a Gaussian model using Origin.

FWHM for each peak for Z8P−IgG			
Decomposition time (hours)	Diffraction [1,1,0]	Diffraction [2,0,0]	Diffraction [2,1,1]
0	0.222	0.192	0.247
12	0.119	0.192	0.241
24	0.220	0.198	0.243
48	0.121	0.192	0.248
120	0.157	0.153	0.247

FWHM for each peak for Z90−IgG			
Decomposition time (hours)	Diffraction [1,1,0]	Diffraction [2,0,0]	Diffraction [2,1,1]
0	0.201	0.209	0.291
12	0.192	0.204	0.288
24	0.195	0.210	0.316
48	0.187	0.190	0.258
120	0.174	0.197	0.251

Table 20 Values for the Scherrer crystallite sizes for all the diffractions chosen on the stability times chosen for our two ZIF−IgG systems. This data is illustrated in Figure S23.

Scherrer crystallite size for Z8P−IgG			
Decomposition time (hours)	Diffraction (1,1,0)	Diffraction (2,0,0)	Diffraction (2,1,1)
0	13.602	15.773	12.264
12	25.394	15.724	12.585
24	13.732	15.225	12.476
48	24.890	15.748	12.195
120	19.187	19.716	12.264
Scherrer crystallite size for Z90−IgG			
Decomposition time (hours)	Diffraction (1,1,0)	Diffraction (2,0,0)	Diffraction (2,1,1)
0	15.019	14.487	10.405
12	15.707	14.828	10.517
24	15.466	14.390	9.590
48	16.145	15.940	11.754
120	17.313	15.317	12.049

7. Acknowledgements

I want to express my deepest gratitude and admiration to my supervisors, Dr Franziska Emmerling and Dr Rudolf Schneider, for their continuous support throughout my doctoral studies. Their expert guidance and patience helped me throughout this challenging experience. I am truly indebted to them and humbled for their commitment and kindness at the toughest of times, and the faith they had in me to complete this journey.

I extend my appreciation to Dr Sebastian Beyer for his guidance the first years of my Ph.D. Dr Ana Belenguer is also specially thanked for all her assistance and guidance on my last years of the Ph.D. Dr Adam Michalchuk is thanked for assistance with reviewing of my thesis, as well as Prof. Dr. Ruediger Tiemann, Prof. Dr. Klaus Rademann and Prof. Dr. Thomas Braun for accepting the roles of committee members.

I gratefully acknowledge the team at the School for Analytical Sciences Adlershof (SALSA) and the Bundesanstalt für Materialforschung und -prüfung (BAM) for their continuous support and being there every step of the way, and for kindly providing me with professional support, as well as the office space. I very much enjoyed my time at grad school, and the immersive experience of interdisciplinarity and internationality it provided for their students.

Special mention goes to Anna Raysyan, Dominik Al-Sabbagh, Dr Inês Catarina Batista Martins, Torvid Feiler, Dr Carsten Jaeger, Teodor Tchipilov, Dr Sigrid Benemann, Carsten Prinz, Dr Carlos Abad, Max Rautenberg, Dr Ralf Bienert, Daniel Geißler, Dr Christian Piechotta, Dr Tanja Westphalen and Dr Claire Murray.

On a personal level, I would like to thank my mother, Ines Maria Arias Arias, for being so patient with me for all her life. Her support proved to be essential for, not only these four years, but all my life. Above all, I am grateful to the person who has been there for me every step of the way and, therefore, should be given an honorary doctorate, Oznur Aglar. I thank you for your constant support, undying patience, and growing up and figuring out things together. We have been together since the beginning of my Ph.D. and your support on all levels have been instrumental for me to make it to this point.

I sincerely thank my close friends for support and kindness throughout the entire journey of my higher education. Words cannot describe the appreciation I have for knowing that I have in my life, people who are always there no matter what, and whose priority above all is my well-being. Special mention in this category goes to Dr. Jose A. Villajos and Victor Rodriguez Zancajo.

I am especially grateful to my SALSA peers for many interesting discussions, shared laughs, and anxieties, and being the only people who “get it.”

8. Statement of Authorship

I declare that I have completed the thesis independently, using only the aids and tools specified. I have not applied for a doctor's degree in the doctoral subject elsewhere and do not hold a corresponding doctor's degree. I have taken due note of the Faculty of Mathematics and Natural Sciences Ph.D. Regulations, published in the Official Gazette of Humboldt-Universität zu Berlin no. 126/2014 on 11.07.2018.

9. References

1. Germany, F. E. A., "Frequently Asked Questions about phthalates and plasticisers". *https://www.umweltbundesamt.de/en/topics/health/environmental-impact-on-people/chemical-substances/plasticisers/frequently-asked-questions-about-phthalates#which-phthalates-are-commonly-used-in-plastics* **5th March 2021, 22:00,** -.
2. Wei, X.-F.; Linde, E.; Hedenqvist, M. S., Plasticiser loss from plastic or rubber products through diffusion and evaporation. *NPJ Mater. Degrad.* **2019,** *3* (1), 1-8.
3. Zhu, X. J.; Qiu, Y. Y. In *Measuring the phthalates of xiangjiang river using liquid-liquid extraction gas chromatography*, Adv Mat Res, Trans Tech Publ: 2011; pp 752-755.
4. Luo, Q.; Liu, Z.-h.; Yin, H.; Dang, Z.; Wu, P.-x.; Zhu, N.-w.; Lin, Z.; Liu, Y., Migration and potential risk of trace phthalates in bottled water: A global situation. *Water research* **2018,** *147*, 362-372.
5. Abdolahnejad, A.; Gheisari, L.; Karimi, M.; Norastehfar, N.; Ebrahimpour, K.; Mohammadi, A.; Ghanbari, R.; Ebrahimi, A.; Jafari, N., Monitoring and health risk assessment of phthalate esters in household's drinking water of Isfahan, Iran. *IJEST* **2019,** *16* (11), 7409-7416.
6. Gani, K. M.; Tyagi, V. K.; Kazmi, A. A., Occurrence of phthalates in aquatic environment and their removal during wastewater treatment processes: a review. *ESPR* **2017,** *24* (21), 17267-17284.
7. Domínguez-Morueco, N.; González-Alonso, S.; Valcárcel, Y., Phthalate occurrence in rivers and tap water from central Spain. *STOTEN* **2014,** *500*, 139-146.
8. Mihovec-Grdiæ, M.; Šmit, Z.; Puntariæ, D.; Bošnir, J., Phthalates in underground waters of the Zagreb area. *Croatian medical journal* **2002,** *43* (4), 493-497.
9. Al-Saleh, I.; Shinwari, N.; Alsabbaheen, A., Phthalates residues in plastic bottled waters. *J. Toxicol. Sci.* **2011,** *36* (4), 469-478.
10. Lü, H.; Mo, C. H.; Zhao, H. M.; Xiang, L.; Katsoyiannis, A.; Li, Y. W.; Cai, Q. Y.; Wong, M. H., Soil contamination and sources of phthalates and its health risk in China: A review. *Environ Res* **2018,** *164*, 417-429.
11. Bach, C.; Dauchy, X.; Chagnon, M.-C.; Etienne, S., Chemical compounds and toxicological assessments of drinking water stored in polyethylene terephthalate (PET) bottles: a source of controversy reviewed. *Water research* **2012,** *46* (3), 571-583.
12. Latini, G., Monitoring phthalate exposure in humans. *Clin. Chim. Acta* **2005,** *361* (1), 20-29.
13. Tollefsen, K.-E., Interaction of estrogen mimics, singly and in combination, with plasma sex steroid-binding proteins in rainbow trout (Oncorhynchus mykiss). *Aquat. Toxicol.* **2002,** *56* (3), 215-225.
14. Albert, O.; Jégou, B., A critical assessment of the endocrine susceptibility of the human testis to phthalates from fetal life to adulthood. *Hum. Reprod. Update* **2013,** *20* (2), 231-249.
15. ECHA, https://eur-lex.europa.eu/legal-content/EN/TXT/PDF/?uri=CELEX:32018R2005&from=EN. *"Commission Regulation (EU) 2018/2005 of 17 December 2018 amending Annex XVII to Regulation (EC) No 1907/2006 of the European Parliament"* **5th March 2020, 22:00**.
16. Liang, D.-W.; Zhang, T.; Fang, H. H.; He, J., Phthalates biodegradation in the environment. *Appl. Microbiol. Biotechnol.* **2008,** *80* (2), 183.
17. Net, S.; Delmont, A.; Sempéré, R.; Paluselli, A.; Ouddane, B., Reliable quantification of phthalates in environmental matrices (air, water, sludge, sediment and soil): A review. *STOTEN* **2015,** *515*, 162-180.
18. Xu, F.; Wang, W.; Jiang, H.; Wang, Z.; Wang, Z.; Guo, P.; Sun, S.; Ding, S., Indirect competitive enzyme-linked immunosorbent assay for the detection of dibutyl phthalate in white wine, compared with GC-MS. *Food Anal. Methods* **2014,** *7* (8), 1619-1626.
19. Zhang, M.-C.; Wang, Q.-E.; Zhuang, H.-S., A novel competitive fluorescence immunoassay for the determination of dibutyl phthalate. *Anal Bioanal Chem* **2006,** *386* (5), 1401-1406.

20. Wei, C.; Ding, S.; You, H.; Zhang, Y.; Wang, Y.; Yang, X.; Yuan, J., An immunoassay for dibutyl phthalate based on direct hapten linkage to the polystyrene surface of microtiter plates. *J PloS one* **2011,** *6* (12), e29196.
21. Sun, R. Y.; Zhuang, H. S., An indirect competitive biotin-streptavidin enzyme-linked immunosorbent assay for the determination of dimethyl phthalate (DMP) in milk and milk products. *J. Environ. Sci. Health B* **2015,** *50* (4), 275-284.
22. Baldofski, S.; Canitz, C. J.; Garbe, L.-A.; Schneider, R. J., Studies on the development of antibodies for the highly hydrophobic plasticizers DINCH and DEHT. *Anal. Biochem.* **2018,** *543*, 90-96.
23. James, S. L., Metal-organic frameworks. *Chem. Soc. Rev.* **2003,** *32* (5), 276-288.
24. Furukawa, H.; Cordova, K. E.; O'Keeffe, M.; Yaghi, O. M., The chemistry and applications of metal-organic frameworks. *Science* **2013,** *341* (6149), 1230444.
25. Kinoshita, Y.; Matsubara, I.; Higuchi, T.; Saito, Y., The crystal structure of bis (adiponitrilo) copper (I) nitrate. *Bull. Chem. Soc. Jpn.* **1959,** *32* (11), 1221-1226.
26. Manousi, N.; Zachariadis, G. A.; Deliyanni, E. A., On the use of metal-organic frameworks for the extraction of organic compounds from environmental samples. *Environ. Sci. Pollut. Res.* **2020**, 1-25.
27. Kumar, G.; Das, S. K., Coordination frameworks containing compounds as catalysts. *Inorg. Chem. Front* **2017,** *4* (2), 202-233.
28. Wen, X.; Zhang, Q.; Guan, J., Applications of metal–organic framework-derived materials in fuel cells and metal-air batteries. *Coord. Chem. Rev.* **2020,** *409*, 213214.
29. Horcajada, P.; Serre, C.; Vallet-Regí, M.; Sebban, M.; Taulelle, F.; Férey, G., Metal–organic frameworks as efficient materials for drug delivery. *Angew. Chem. Int. Ed.* **2006,** *118* (36), 6120-6124.
30. Berenguer Murcia, Á., Ordered porous nanomaterials: The merit of small. *ISRN Nanotechnology* **2013,** *2013*.
31. Guo, M.; Cai, H.-L.; Xiong, R.-G., Ferroelectric metal organic framework (MOF). *Inorg. Chem. Commun* **2010,** *13* (12), 1590-1598.
32. Eddaoudi, M.; Li, H.; Reineke, T.; Fehr, M.; Kelley, D.; Groy, T. L.; Yaghi, O., Design and synthesis of metal-carboxylate frameworks with permanent microporosity. *Topics in Catalysis* **1999,** *9* (1-2), 105-111.
33. Griffin, S. L.; Champness, N. R., A periodic table of metal-organic frameworks. *Coord. Chem. Rev.* **2020,** *414*, 213295.
34. Lu, W.; Wei, Z.; Gu, Z.-Y.; Liu, T.-F.; Park, J.; Park, J.; Tian, J.; Zhang, M.; Zhang, Q.; Gentle Iii, T.; Bosch, M.; Zhou, H.-C., Tuning the structure and function of metal–organic frameworks via linker design. *Chem. Soc. Rev.* **2014,** *43* (16), 5561-5593.
35. Pullen, S.; Clever, G. H., Mixed-Ligand Metal–Organic Frameworks and Heteroleptic Coordination Cages as Multifunctional Scaffolds—A Comparison. *Accounts Chem. Res.* **2018,** *51* (12), 3052-3064.
36. Abednatanzi, S.; Derakhshandeh, P. G.; Depauw, H.; Coudert, F.-X.; Vrielinck, H.; Van Der Voort, P.; Leus, K., Mixed-metal metal–organic frameworks. *Chem. Soc. Rev.* **2019,** *48* (9), 2535-2565.
37. Schröder, F.; Fischer, R. A., Doping of metal-organic frameworks with functional guest molecules and nanoparticles. In *Functional Metal-Organic Frameworks: Gas Storage, Separation and Catalysis*, Springer: 2009; pp 77-113.
38. Li, H.; Eddaoudi, M.; O'Keeffe, M.; Yaghi, O. M., Design and synthesis of an exceptionally stable and highly porous metal-organic framework. *Nature* **1999,** *402* (6759), 276-279.
39. Tafipolsky, M.; Amirjalayer, S.; Schmid, R., Ab initio parametrized MM3 force field for the metal-organic framework MOF-5. *J. Comput. Chem.* **2007,** *28* (7), 1169-1176.
40. Kumar, P.; Deep, A.; Paul, A.; Bharadwaj, L., Bioconjugation of MOF-5 for molecular sensing. *J. Porous Mater* **2014,** *21* (1), 99-104.
41. Rosi, N. L.; Eckert, J.; Eddaoudi, M.; Vodak, D. T.; Kim, J.; O'Keeffe, M.; Yaghi, O. M., Hydrogen storage in microporous metal-organic frameworks. *Science* **2003,** *300* (5622), 1127-1129.

42. Jeremias, F.; Henninger, S. K.; Janiak, C., Ambient pressure synthesis of MIL-100(Fe) MOF from homogeneous solution using a redox pathway. *Dalton Trans.* **2016,** *45* (20), 8637-8644.
43. Fang, Y.; Yang, Z. G.; Li, H. P.; Liu, X. H., MIL-100(Fe) and its derivatives: from synthesis to application for wastewater decontamination. *Environ. Sci. Pollut. Res.* **2020,** *27* (5), 4703-4724.
44. Zhang, F.; Jin, Y.; Shi, J.; Zhong, Y.; Zhu, W.; El-Shall, M. S., Polyoxometalates confined in the mesoporous cages of metal–organic framework MIL-100(Fe): Efficient heterogeneous catalysts for esterification and acetalization reactions. *Chem. Eng. J.* **2015,** *269*, 236-244.
45. Mao, D.; Xie, C.; Li, Z.; Hong, L.; Qu, R.; Gao, Y.; He, J.; Wang, J., Adsorption and controlled release of three kinds of flavors on UiO-66. *Food Sci. Nutr* **2020**.
46. Liu, X. L., Metal-organic framework UiO-66 membranes. *Front Chem Sci Eng.* **2020,** *14* (2), 216-232.
47. González-Rodríguez, G.; Taima-Mancera, I.; Lago, A. B.; Ayala, J. H.; Pasán, J.; Pino, V., Mixed functionalization of organic ligands in UiO-66: A tool to design Metal–Organic Frameworks for tailored microextraction. *Molecules* **2019,** *24* (20), 3656.
48. Gao, G.; Xing, Y.; Liu, T.; Wang, J.; Hou, X., UiO-66(Zr) as sorbent for porous membrane protected micro-solid-phase extraction androgens and progestogens in environmental water samples coupled with LC-MS/MS analysis: The application of experimental and molecular simulation method. *Microchem* **2019,** *146*, 126-133.
49. Cohen, S. M., The Postsynthetic Renaissance in Porous Solids. *J. Am. Chem. Soc.* **2017,** *139*, 2855.
50. Fluch, U.; Paneta, V.; Primetzhofer, D.; Ott, S., Uniform Distribution of Post-Synthetic Linker Exchange in Metal–Organic Frameworks Revealed by Rutherford Backscattering Spectrometry. *Chem. Commun.* **2017,** *53*, 6516.
51. Yuan, S.; Zou, L.; Qin, J. S.; Li, J.; Huang, L.; Feng, L.; Wang, X.; Bosch, M.; Alsalme, A.; Cagin, T.; Zhou, H. C., Construction of hierarchically porous metal–organic frameworks through linker labilization. *Nat. Commun.* **2017,** *8*, 15356.
52. Saha, S.; Regeni, I.; Clever, G. H., Structure Relationships Between Bis-Monodentate Ligands and Coordination Driven Self-Assemblies. *Coord. Chem. Rev.* **2018,** *374*, 1.
53. Deng, H.; Doonan, C. J.; Furukawa, H.; Ferreira, R. B.; Towne, J.; Knobler, C. B.; Wang, B.; Yaghi, O. K., Multiple Functional Groups of Varying Ratios in Metal–Organic Frameworks. *Science* **2010,** *327*, 846.
54. Chapartegui-Arias, A.; Villajos, J. A.; Myxa, A.; Beyer, S.; Falkenhagen, J.; Schneider, R. J.; Emmerling, F., Covalently Fluorophore-Functionalized ZIF-8 Colloidal Particles as a Sensing Platform for Endocrine-Disrupting Chemicals Such as Phthalates Plasticizers. *ACS Omega* **2019,** *4* (17), 17090-17097.
55. Morris, W.; Doonan, C. J.; Furukawa, H.; Banerjee, R.; Yaghi, O. M., Crystals as molecules: postsynthesis covalent functionalization of zeolitic imidazolate frameworks. *JACS* **2008,** *130* (38), 12626-12627.
56. Li, D.; Guo, Z., Metal-organic framework superhydrophobic coating on Kevlar fabric with efficient drag reduction and wear resistance. *Appl. Surf. Sci.* **2018,** *443*, 548-557.
57. Lucier, B. E.; Chen, S.; Huang, Y., Characterization of metal–organic frameworks: Unlocking the potential of solid-state NMR. *Acc. Chem. Res.* **2018,** *51* (2), 319-330.
58. Wong, Y. A.; Martins, V.; Lucier, B. E.; Huang, Y., Solid-State NMR Spectroscopy: A Powerful Technique to Directly Study Small Gas Molecules Adsorbed in Metal–Organic Frameworks. *Chem. Eur. J.* **2019,** *25* (8), 1848-1853.
59. Hayashi, H.; Cote, A. P.; Furukawa, H.; O'Keeffe, M.; Yaghi, O. M., Zeolite A imidazolate frameworks. *Nat. Mater* **2007,** *6* (7), 501-6.
60. Park, K. S.; Ni, Z.; Cote, A. P.; Choi, J. Y.; Huang, R.; Uribe-Romo, F. J.; Chae, H. K.; O'Keeffe, M.; Yaghi, O. M., Exceptional chemical and thermal stability of zeolitic imidazolate frameworks. *PNAS USA* **2006,** *103* (27), 10186-10191.
61. Chen, B.; Yang, Z.; Zhu, Y.; Xia, Y., Zeolitic imidazolate framework materials: recent progress in synthesis and applications. *J. Mater. Chem. A* **2014,** *2* (40), 16811-16831.

62. Kulow, A.; Witte, S.; Beyer, S.; Buzanich, A. G.; Radtke, M.; Reinholz, U.; Riesemeier, H.; Streli, C., A new experimental setup for time-and laterally-resolved X-ray absorption fine structure spectroscopy in a 'single shot'. *J. Anal. At. Spectrom* **2019,** *34* (1), 239-246.
63. Beyer, S.; Prinz, C.; Schürmann, R.; Feldmann, I.; Zimathies, A.; Blocki, A. M.; Bald, I.; Schneider, R. J.; Emmerling, F., Ultra-Sonication of ZIF-67 Crystals Results in ZIF-67 Nano-Flakes. *ChemistrySelect* **2016,** *1* (18), 5905-5908.
64. Kaneti, Y. V.; Dutta, S.; Hossain, M. S. A.; Shiddiky, M. J. A.; Tung, K. L.; Shieh, F. K.; Tsung, C. K.; Wu, K. C.; Yamauchi, Y., Strategies for Improving the Functionality of Zeolitic Imidazolate Frameworks: Tailoring Nanoarchitectures for Functional Applications. *Adv Mater* **2017,** *29* (38).
65. NEWSAM, J. M., The Zeolite Cage Structure. *Science* **1986,** *231* (4742), 1093-1099.
66. Yan, B., Lanthanide-Functionalized Metal-Organic Framework Hybrid Systems To Create Multiple Luminescent Centers for Chemical Sensing. *Acc. Chem. Res.* **2017,** *50* (11), 2789-2798.
67. Jia, H. X.; Yao, Y. C.; Zhao, J. T.; Gao, Y. Y.; Luo, Z. L.; Du, P. W., A novel two-dimensional nickel phthalocyanine-based metal-organic framework for highly efficient water oxidation catalysis. *J. Mater. Chem. A* **2018,** *6* (3), 1188-1195.
68. Maya, F.; Cabello, C. P.; Clavijo, S.; Estela, J. M.; Cerdà, V.; Palomino, G. T., Zeolitic imidazolate framework dispersions for the fast and highly efficient extraction of organic micropollutants. *RSC Acv.* **2015,** *5* (36), 28203-28210.
69. Beldon, P. J.; Fabian, L.; Stein, R. S.; Thirumurugan, A.; Cheetham, A. K.; Friscic, T., Rapid Room-Temperature Synthesis of Zeolitic Imidazolate Frameworks by Using Mechanochemistry. *Angew. Chem. Int. Ed.* **2010,** *49* (50), 9640-9643.
70. Cravillon, J.; Nayuk, R.; Springer, S.; Feldhoff, A.; Huber, K.; Wiebcke, M., Controlling zeolitic imidazolate framework nano-and microcrystal formation: insight into crystal growth by time-resolved in situ static light scattering. *Chem. Mater.* **2011,** *23* (8), 2130-2141.
71. Sajid, M.; Kawde, A.-N.; Daud, M., Designs, formats and applications of lateral flow assay: A literature review. *J. Saudi Chem. Soc.* **2015,** *19* (6), 689-705.
72. Liu, C.; Huang, A., One-step synthesis of the superhydrophobic zeolitic imidazolate framework F-ZIF-90 for efficient removal of oil. *New J Chem* **2018,** *42* (4), 2372-2375.
73. Liu, C.; Liu, Q.; Huang, A., A superhydrophobic zeolitic imidazolate framework (ZIF-90) with high steam stability for efficient recovery of bioalcohols. *ChemComm* **2016,** *52* (16), 3400-3402.
74. Ortiz, A. U.; Freitas, A. P.; Boutin, A.; Fuchs, A. H.; Coudert, F.-X., What makes zeolitic imidazolate frameworks hydrophobic or hydrophilic? The impact of geometry and functionalization on water adsorption. *Phys. Chem. Chem. Phys* **2014,** *16* (21), 9940-9949.
75. Zhang, J.; Tan, Y.; Song, W.-J., Zeolitic imidazolate frameworks for use in electrochemical and optical chemical sensing and biosensing: a review. *Microchimica Acta* **2020,** *187* (4), 1-23.
76. Li, Q.; Wu, J.; Huang, L.; Gao, J.; Zhou, H.; Shi, Y.; Pan, Q.; Zhang, G.; Du, Y.; Liang, W., Sulfur dioxide gas-sensitive materials based on zeolitic imidazolate framework-derived carbon nanotubes. *J. Mater. Chem. A* **2018,** *6* (25), 12115-12124.
77. Liu, Y.; Wang, R.; Zhang, T.; Liu, S.; Fei, T., Zeolitic imidazolate framework-8 (ZIF-8)-coated In2O3 nanofibers as an efficient sensing material for ppb-level NO2 detection. *J. Colloid Interface Sci.* **2019,** *541*, 249-257.
78. Zang, R.; He, Y.; Yuan, R.; Chai, Y., An ultrasensitive electrochemiluminescence immunosensor based on zeolitic imidazolate frameworks encapsulating spherical graphite crystals. *J. Electroanal. Chem.* **2016,** *781*, 284-288.
79. Abuzalat, O.; Wong, D.; Park, S. S.; Kim, S., Highly selective and sensitive fluorescent zeolitic imidazole frameworks sensor for nitroaromatic explosive detection. *Nanoscale* **2020,** *12* (25), 13523-13530.

80. Zhang, Y.-Q.; Wu, X.-H.; Mao, S.; Tao, W.-Q.; Li, Z., Highly luminescent sensing for nitrofurans and tetracyclines in water based on zeolitic imidazolate framework-8 incorporated with dyes. *Talanta* **2019,** *204*, 344-352.
81. McGinty, J.; Yazdanpanah, N.; Price, C.; ter Horst, J. H.; Sefcik, J., Nucleation and Crystal Growth in Continuous Crystallization. **2020**.
82. Lutsko, J. F., How crystals form: A theory of nucleation pathways. *Sci. Adv.* **2019,** *5* (4), eaav7399.
83. Karthika, S.; Radhakrishnan, T.; Kalaichelvi, P., A review of classical and nonclassical nucleation theories. *Cryst. Growth Des.* **2016,** *16* (11), 6663-6681.
84. Pritula, I.; Sangwal, K., Fundamentals of crystal growth from solutions. In *Handbook of crystal growth*, Elsevier: 2015; pp 1185-1227.
85. Schmelzer, J. W.; Abyzov, A. S., How do crystals nucleate and grow: Ostwald's rule of stages and beyond. In *Thermal Physics and Thermal Analysis*, Springer: 2017; pp 195-211.
86. LaMer, V. K.; Dinegar, R. H., Theory, production and mechanism of formation of monodispersed hydrosols. *JACS* **1950,** *72* (11), 4847-4854.
87. Cravillon, J.; Schröder, C. A.; Nayuk, R.; Gummel, J.; Huber, K.; Wiebcke, M., Fast Nucleation and Growth of ZIF-8 Nanocrystals Monitored by Time-Resolved In Situ Small-Angle and Wide-Angle X-Ray Scattering. *Angew. Chem. Int. Ed.* **2011,** *50* (35), 8067-8071.
88. Terban, M. W.; Banerjee, D.; Ghose, S.; Medasani, B.; Shukla, A.; Legg, B. A.; Zhou, Y.; Zhu, Z.; Sushko, M. L.; De Yoreo, J. J., Early stage structural development of prototypical zeolitic imidazolate framework (ZIF) in solution. *Nanoscale* **2018,** *10* (9), 4291-4300.
89. Lim, I. H.; Schrader, W.; Schüth, F., Insights into the molecular assembly of zeolitic imidazolate frameworks by ESI-MS. *Chem. Mater.* **2015,** *27* (8), 3088-3095.
90. Saha, S.; Wiebcke, M.; Huber, K., Insight into Fast Nucleation and Growth of Zeolitic Imidazolate Framework-71 by In Situ Static Light Scattering at Variable Temperature and Kinetic Modeling. *Cryst. Growth Des.* **2018,** *18* (8), 4653-4661.
91. Saha, S.; Springer, S.; Schweinefuß, M. E.; Pontoni, D.; Wiebcke, M.; Huber, K., Insight into fast nucleation and growth of zeolitic imidazolate framework-71 by in situ time-resolved light and X-ray scattering experiments. *Cryst. Growth Des.* **2016,** *16* (4), 2002-2010.
92. Moh, P. Y.; Cubillas, P.; Anderson, M. W.; Attfield, M. P., Revelation of the molecular assembly of the nanoporous metal organic framework ZIF-8. *JACS* **2011,** *133* (34), 13304-13307.
93. Öztürk, Z.; Filez, M.; Weckhuysen, B. M., Decoding Nucleation and Growth of Zeolitic Imidazolate Framework Thin Films with Atomic Force Microscopy and Vibrational Spectroscopy. *Chem. Eur. J.* **2017,** *23* (45), 10915-10924.
94. Cravillon, J.; Munzer, S.; Lohmeier, S. J.; Feldhoff, A.; Huber, K.; Wiebcke, M., Rapid Room-Temperature Synthesis and Characterization of Nanocrystals of a Prototypical Zeolitic Imidazolate Framework. *Chem. Mater.* **2009,** *21* (8), 1410-1412.
95. Yeung, H. H. M.; Sapnik, A. F.; Massingberd-Mundy, F.; Gaultois, M. W.; Wu, Y.; Fraser, D. A.; Henke, S.; Pallach, R.; Heidenreich, N.; Magdysyuk, O. V., Control of Metal–Organic Framework Crystallization by Metastable Intermediate Pre-equilibrium Species. *Angew. Chem. Int. Ed.* **2019,** *58* (2), 566-571.
96. Zhang, Y.; Jia, Y.; Li, M.; Hou, L. a., Influence of the 2-methylimidazole/zinc nitrate hexahydrate molar ratio on the synthesis of zeolitic imidazolate framework-8 crystals at room temperature. *Scientific reports* **2018,** *8* (1), 1-7.
97. Schejn, A.; Balan, L.; Falk, V.; Aranda, L.; Medjahdi, G.; Schneider, R., Controlling ZIF-8 nano- and microcrystal formation and reactivity through zinc salt variations. *CrystEngComm* **2014,** *16* (21), 4493-4500.
98. Bustamante, E. L.; Fernández, J. L.; Zamaro, J. M., Influence of the solvent in the synthesis of zeolitic imidazolate framework-8 (ZIF-8) nanocrystals at room temperature. *J. Colloid Interface Sci.* **2014,** *424*, 37-43.

99. Li, C.-P.; Du, M., Role of solvents in coordination supramolecular systems. *ChemComm* **2011,** *47* (21), 5958-5972.
100. Tian, Y. Q.; Zhao, Y. M.; Chen, Z. X.; Zhang, G. N.; Weng, L. H.; Zhao, D. Y., Design and generation of extended zeolitic metal–organic frameworks (ZMOFs): synthesis and crystal structures of zinc (II) imidazolate polymers with zeolitic topologies. *Chem. Eur. J.* **2007,** *13* (15), 4146-4154.
101. Arjmandi, M.; Pakizeh, M., Effects of washing and drying on crystal structure and pore size distribution (PSD) of Zn 4 O 13 C 24 H 12 framework (IRMOF-1). *Acta Metall Sin-Engl .* **2013,** *26* (5), 597-601.
102. Bux, H.; Liang, F.; Li, Y.; Cravillon, J.; Wiebcke, M.; Caro, J. r., Zeolitic imidazolate framework membrane with molecular sieving properties by microwave-assisted solvothermal synthesis. *JACS* **2009,** *131* (44), 16000-16001.
103. Acuña, A.; Amat-Guerri, F., Early history of solution fluorescence: the Lignum nephriticum of Nicolás Monardes. In *Fluorescence of supermolecules, polymers, and nanosystems*, Springer: 2007; pp 3-20.
104. Renz, M., Fluorescence microscopy—A historical and technical perspective. *Cytometry Part A* **2013,** *83* (9), 767-779.
105. Ceredig, R., George Gabriel Stokes as a biologist. *Phil. Trans. A* **2020,** *378* (2179), 20200105.
106. Wang, Z.; Zheng, Y.; Zhao, D.; Zhao, Z.; Liu, L.; Pliss, A.; Zhu, F.; Liu, J.; Qu, J.; Luan, P., Applications of fluorescence lifetime imaging in clinical medicine. *J. Innov. Opt. Health Sci.* **2018,** *11* (01), 1830001.
107. Ma, S.; Chen, G.; Xu, J.; Liu, Y.; Li, G.; Chen, T.; Li, Y.; James, T. D., Current strategies for the development of fluorescence-based molecular probes for visualizing the enzymes and proteins associated with Alzheimer's disease. *Coord. Chem. Rev.* **2021,** *427*, 213553.
108. McDonagh, C.; Burke, C. S.; MacCraith, B. D., Optical chemical sensors. *Chem. Rev.* **2008,** *108* (2), 400-422.
109. Schäferling, M., The art of fluorescence imaging with chemical sensors. *Angew. Chem. Int. Ed.* **2012,** *51* (15), 3532-3554.
110. Buryakov, I.; Buryakov, T.; Matsaev, V., Optical chemical sensors for the detection of explosives and associated substances. *J. Anal. Chem* **2014,** *69* (7), 616-631.
111. Kikuchi, K.; Nagano, T., Visualization of cellular events using designed fluorescence sensor molecules. *J SYN ORG CHEM JPN* **2004,** *62* (10), 1006-1013.
112. Leiner, M. J., Luminescence chemical sensors for biomedical applications: scope and limitations. *Anal. Chim. Acta* **1991,** *255* (2), 209-222.
113. Suzuki, Y.; Yokoyama, K., Development of functional fluorescent molecular probes for the detection of biological substances. *Biosensors* **2015,** *5* (2), 337-363.
114. Lakowicz, J. R., Quenching of fluorescence. In *Principles of fluorescence spectroscopy*, Springer: 1983; pp 257-301.
115. Kaur, A.; Kaur, P.; Ahuja, S., Förster resonance energy transfer (FRET) and applications thereof. *Anal. Methods.* **2020,** *12* (46), 5532-5550.
116. Zu, F.; Yan, F.; Bai, Z.; Xu, J.; Wang, Y.; Huang, Y.; Zhou, X., The quenching of the fluorescence of carbon dots: a review on mechanisms and applications. *Microchimica Acta* **2017,** *184* (7), 1899-1914.
117. Albrecht, C., Joseph R. Lakowicz: Principles of fluorescence spectroscopy. **2008,** *390* (5), 1223-1224.
118. Kondilenko, V.; Tarasov, I.; Dudnik, V.; Eremenko, A., Donor-acceptor complexes of excited states on silica surface and in hexane solution at liquid nitrogen temperature. *Res. Chem. Intermed.* **1998,** *24* (1), 25-34.
119. Yip, W.; Levy, D. H., Excimer/exciplex formation in van der Waals dimers of aromatic molecules. *Phys. Chem.* **1996,** *100* (28), 11539-11545.

120. Duhamel, J., Pyrene fluorescence to study polymeric systems. *Molecular interfacial phenomena of polymers and biopolymers* **2005**, 214-248.
121. Graceffa, P.; Lehrer, S., The excimer fluorescence of pyrene-labeled tropomyosin. A probe of conformational dynamics. *J. Biol. Chem.* **1980,** *255* (23), 11296-11300.
122. Rochat, S.; Steinmann, S. N.; Corminboeuf, C.; Severin, K., Fluorescence sensing of caffeine in water with polysulfonated pyrenes. *Chem Comm* **2011,** *47* (38), 10584-10586.
123. Lebranchu, Y., Histoire des anticorps thérapeutiques. Elsevier: 2018.
124. Berger, M.; Shankar, V.; Vafai, A., Therapeutic applications of monoclonal antibodies. *Am. J. Med. Sci.* **2002,** *324* (1), 14-30.
125. Yoon, S.; Kim, Y.-S.; Shim, H.; Chung, J., Current perspectives on therapeutic antibodies. *Biotechnol. Bioprocess Eng.* **2010,** *15* (5), 709-715.
126. Hsieh, H. V.; Dantzler, J. L.; Weigl, B. H., Analytical tools to improve optimization procedures for lateral flow assays. *Diagnostics* **2017,** *7* (2), 29.
127. Seidel, M.; Niessner, R., Chemiluminescence microarrays in analytical chemistry: a critical review. *Anal. Bioanal. Chem.* **2014,** *406* (23), 5589-5612.
128. O'Kennedy, R.; Townsend, S.; Donohoe, G. G.; Leonard, P.; Hearty, S.; Byrne, B., Speedy, small, sensitive, and specific—Reality or myth for future analytical methods. *Anal. Lett.* **2010,** *43* (10-11), 1630-1648.
129. Seidel, M.; Niessner, R., Automated analytical microarrays: a critical review. *Anal. Bioanal. Chem.* **2008,** *391* (5), 1521.
130. Sakamoto, S.; Putalun, W.; Vimolmangkang, S.; Phoolcharoen, W.; Shoyama, Y.; Tanaka, H.; Morimoto, S., Enzyme-linked immunosorbent assay for the quantitative/qualitative analysis of plant secondary metabolites. *J. Nat. Med* **2018,** *72* (1), 32-42.
131. Watanabe, E.; Miyake, S.; Yogo, Y., Review of enzyme-linked immunosorbent assays (ELISAs) for analyses of neonicotinoid insecticides in agro-environments. *J. Agric. Food Chem.* **2013,** *61* (51), 12459-12472.
132. Dubois, C.; Marcé, D.; Faivre, V.; Lukaszewicz, A.-C.; Junot, C.; Fenaille, F.; Simon, S.; Becher, F.; Morel, N.; Payen, D., High plasma level of S100A8/S100A9 and S100A12 at admission indicates a higher risk of death in septic shock patients. *Scientific Reports* **2019,** *9* (1), 1-7.
133. Thayer, M. B.; Lade, J. M.; Doherty, D.; Xie, F.; Basiri, B.; Barnaby, O. S.; Bala, N. S.; Rock, B. M., Application of Locked Nucleic Acid Oligonucleotides for siRNA Preclinical Bioanalytics. *Scientific Reports* **2019,** *9* (1), 3566.
134. Oberleitner, L.; Dahmen-Levison, U.; Garbe, L.-A.; Schneider, R. J., Improved strategies for selection and characterization of new monoclonal anti-carbamazepine antibodies during the screening process using feces and fluorescence polarization immunoassay. *Anal. Methods.* **2016,** *8* (38), 6883-6894.
135. Arur, S.; Schedl, T., Generation and purification of highly specific antibodies for detecting post-translationally modified proteins in vivo. *Nature Protocols* **2014,** *9* (2), 375.
136. Stech, M.; Nikolaeva, O.; Thoring, L.; Stöcklein, W.; Wüstenhagen, D.; Hust, M.; Dübel, S.; Kubick, S., Cell-free synthesis of functional antibodies using a coupled in vitro transcription-translation system based on CHO cell lysates. *Scientific Reports* **2017,** *7* (1), 12030.
137. Veldkamp, J.; Visser, A., Application of the enzyme-linked immunosorbent assay (ELISA) in the serodiagnosis of syphilis. *Sexually Transmitted Infections* **1975,** *51* (4), 227-231.
138. Bidwell, D.; Buck, A.; Diesfeld, H.; Enders, B.; Haworth, J.; Huldt, G.; Kent, N.; Kirsten, C.; Mattern, P.; Ruitenberg, E., The enzyme-linked immunosorbent assay (ELISA). *Bull. World Health Organ.* **1976,** *54*, 129-139.
139. Koczula, K. M.; Gallotta, A., Lateral flow assays. *Essays Biochem.* **2016,** *60* (1), 111-120.
140. Darwish, I. A., Immunoassay methods and their applications in pharmaceutical analysis: basic methodology and recent advances. *Int. J. Biomed. Sci.* **2006,** *2* (3), 217.

141. Seydack, M., Nanoparticle labels in immunosensing using optical detection methods. *Biosens. Bioelectron.* **2005,** *20* (12), 2454-2469.
142. Falck, G.; Müller, K. M., Enzyme-based labeling strategies for antibody–drug conjugates and antibody mimetics. *Antibodies* **2018,** *7* (1), 4.
143. Berlina, A. N.; Zherdev, A. V.; Dzantiev, B. B., ELISA and Lateral Flow Immunoassay for the Detection of Food Colorants: State of the Art. *Crit. Rev. Anal. Chem.* **2019,** *49* (3), 209-223.
144. Matsuda, R.; Rodriguez, E.; Suresh, D.; Hage, D. S., Chromatographic immunoassays: strategies and recent developments in the analysis of drugs and biological agents. *Bioanalysis* **2015,** *7* (22), 2947-2966.
145. Arruebo, M.; Valladares, M.; González-Fernández, Á., Antibody-conjugated nanoparticles for biomedical applications. *J. Nanomater* **2009,** *2009*.
146. Jazayeri, M. H.; Amani, H.; Pourfatollah, A. A.; Pazoki-Toroudi, H.; Sedighimoghaddam, B., Various methods of gold nanoparticles (GNPs) conjugation to antibodies. *Sensing and bio-sensing research* **2016,** *9*, 17-22.
147. Saleh, M.; Soliman, H.; Haenen, O.; El-Matbouli, M., Antibody-coated gold nanoparticles immunoassay for direct detection of Aeromonas salmonicida in fish tissues. *J. Fish Dis.* **2011,** *34* (11), 845-852.
148. Parolo, C.; de la Escosura-Muñiz, A.; Merkoçi, A., Enhanced lateral flow immunoassay using gold nanoparticles loaded with enzymes. *Biosens. Bioelectron.* **2013,** *40* (1), 412-416.
149. Lim, P.-L., A one-step two-particle latex immunoassay for the detection of Salmonella typhi endotoxin. *J. Immunol. Methods* **1990,** *135* (1-2), 257-261.
150. Tang, D.; Cui, Y.; Chen, G., Nanoparticle-based immunoassays in the biomedical field. *Analyst* **2013,** *138* (4), 981-990.
151. Banerjee, R.; Jaiswal, A., Recent advances in nanoparticle-based lateral flow immunoassay as a point-of-care diagnostic tool for infectious agents and diseases. *Analyst* **2018,** *143* (9), 1970-1996.
152. Siiman, O.; Wilkinson, J.; Burshteyn, A.; Roth, P.; Ledis, S., Fluorescent neoglycoproteins: antibody-aminodextran-phycobiliprotein conjugates. *Bioconjug. Chem* **1999,** *10* (6), 1090-1106.
153. Guryev, O.; Abrams, B.; Lomas, C.; Nasraty, Q.; Park, E.; Dubrovsky, T., Control of the fluorescence of dye–antibody conjugates by (2-hydroxypropyl)-β-cyclodextrin in fluorescence microscopy and flow cytometry. *Anal. Chem* **2011,** *83* (18), 7109-7114.
154. Das, P.; Bose, M.; Das, A. K.; Banerjee, S.; Das, N. C. In *One-Step Synthesis of Fluorescent Carbon Dots for Bio-Labeling Assay*, Macromolecular Symposia, Wiley Online Library: 2018; p 1800077.
155. Niu, W.; Zhang, L.; Moctar, D. M.; Pan, M.; Chen, Y., Preparation of Water-Soluble CdTe Quantum Dots Based Immunofluorescent Probes and Its Application in Serological Immunoassay. *Integr. Ferroelectr.* **2011,** *128* (1), 142-148.
156. Migneault, I.; Dartiguenave, C.; Bertrand, M. J.; Waldron, K. C., Glutaraldehyde: behavior in aqueous solution, reaction with proteins, and application to enzyme crosslinking. *BioTechniques* **2004,** *37* (5), 790-802.
157. Sanderson, C.; Wilson, D., Methods for coupling protein or polysaccharide to red cells by periodate oxidation. *Immunochemistry* **1971,** *8* (2), 163-168.
158. Park, K. S.; Ni, Z.; Côté, A. P.; Choi, J. Y.; Huang, R.; Uribe-Romo, F. J.; Chae, H. K.; O'Keeffe, M.; Yaghi, O. M., Exceptional chemical and thermal stability of zeolitic imidazolate frameworks. *PNAS USA* **2006,** *103* (27), 10186-10191.
159. Ho, P. H.; Salles, F.; Di Renzo, F.; Trens, P., One-pot synthesis of 5-FU@ ZIF-8 and ibuprofen@ ZIF-8 nanoparticles. *Inorganica Chim. Acta* **2020,** *500*, 119229.
160. Tautenhahn, R.; Boettcher, C.; Neumann, S., Highly sensitive feature detection for high resolution LC/MS. *BMC Bioinformatics* **2008,** *9* (1), 504.

161. Allen, F.; Pon, A.; Wilson, M.; Greiner, R.; Wishart, D., CFM-ID: a web server for annotation, spectrum prediction and metabolite identification from tandem mass spectra. *Nucleic Acids Res.* **2014,** *42* (W1), W94-W99.
162. Latscha, H. P.; Klein, H. A., *Analytische Chemie: Chemie—Basiswissen III*. Springer-Verlag: 2013.
163. NIST Chemistry WebBook, S., "DMF Information" Formamide, N,N-dimethyl-". **2020**.
164. Shimadzu, "Tips for practical HPLC preparation". *LC World Talk Special Issue Volume 2* **2020**.
165. Bae, J.; Choi, J. S.; Hwang, S.; Yun, W. S.; Song, D.; Lee, J.; Jeong, N. C., Multiple coordination exchanges for room-temperature activation of open-metal sites in metal–organic frameworks. *ACS Appl. Mater. Interfaces* **2017,** *9* (29), 24743-24752.
166. Layer, R. W., The Chemistry of Imines. *Chem Rev* **1963,** *63* (5), 489-510.
167. Cunha, E.; Proença, M. F.; Pereira, M. G.; Fernandes, M. J.; Young, R. J.; Strutyński, K.; Melle-Franco, M.; Gonzalez-Debs, M.; Lopes, P. E.; Paiva, M. D. C., Water Dispersible Few-Layer Graphene Stabilized by a Novel Pyrene Derivative at Micromolar Concentration. *Nanomaterials* **2018,** *8* (9).
168. Aires-de-Sousa, J.; Hemmer, M. C.; Gasteiger, J., Prediction of 1H NMR chemical shifts using neural networks. *Anal. Chem* **2002,** *74* (1), 80-90.
169. Castillo, A. M.; Patiny, L.; Wist, J., Fast and accurate algorithm for the simulation of NMR spectra of large spin systems. *J. Magn. Reson.* **2011,** *209* (2), 123-130.
170. Banfi, D.; Patiny, L., www. nmrdb. org: Resurrecting and processing NMR spectra on-line. *Chimia* **2008,** *62* (4), 280-281.
171. Troyano, J.; Carné-Sánchez, A.; Avci, C.; Imaz, I.; Maspoch, D., Colloidal metal–organic framework particles: the pioneering case of ZIF-8. *Chem. Soc. Rev.* **2019,** *48* (23), 5534-5546.
172. Cravillon, J.; Nayuk, R.; Springer, S.; Feldhoff, A.; Huber, K.; Wiebcke, M., Controlling Zeolitic Imidazolate Framework Nano- and Microcrystal Formation: Insight into Crystal Growth by Time-Resolved In Situ Static Light Scattering. *Chem. Mater.* **2011,** *23* (8), 2130-2141.
173. Wu, C.; Liu, Q.; Chen, R.; Liu, J.; Zhang, H.; Li, R.; Takahashi, K.; Liu, P.; Wang, J., Fabrication of ZIF-8@ SiO2 micro/nano hierarchical superhydrophobic surface on AZ31 magnesium alloy with impressive corrosion resistance and abrasion resistance. *ACS Appl. Mater. Interfaces* **2017,** *9* (12), 11106-11115.
174. Kaur, H.; Mohanta, G. C.; Gupta, V.; Kukkar, D.; Tyagi, S., Synthesis and characterization of ZIF-8 nanoparticles for controlled release of 6-mercaptopurine drug. *J. Drug Deliv. Sci. Technol.* **2017,** *41*, 106-112.
175. Mandal, A.; Choudhury, A.; Kumar, R.; Iyer, P. K.; Mal, P., Exploring the semiconductor properties of a charge transfer cocrystal of 1-aminopyrene and TCNQ. *CrystEngComm* **2020,** *22* (4), 720-727.
176. Hanwell, M. D.; Curtis, D. E.; Lonie, D. C.; Vandermeersch, T.; Zurek, E.; Hutchison, G. R., Avogadro: an advanced semantic chemical editor, visualization, and analysis platform. *J. Cheminformatics* **2012,** *4* (1), 1-17.
177. Gómez-Varela, A. I.; Stamov, D. R.; Miranda, A.; Alves, R.; Barata-Antunes, C.; Dambournet, D.; Drubin, D. G.; Paiva, S.; De Beule, P. A., Simultaneous co-localized super-resolution fluorescence microscopy and atomic force microscopy: combined SIM and AFM platform for the life sciences. *Scientific reports* **2020,** *10* (1), 1-10.
178. Rehm, D.; Weller, A., Kinetics of fluorescence quenching by electron and H-atom transfer. *Isr. J. Chem.* **1970,** *8* (2), 259-271.
179. Kowalczyk, T.; Lin, Z.; Voorhis, T. V., Fluorescence quenching by photoinduced electron transfer in the Zn2+ sensor Zinpyr-1: A computational investigation. *Phys. Chem. A* **2010,** *114* (38), 10427-10434.
180. Šoustek, P.; Michl, M.; Almonasy, N.; Machalický, O.; Dvořák, M.; Lyčka, A., The synthesis and fluorescence of N-substituted 1-and 2-aminopyrenes. *Dyes Pigm.* **2008,** *78* (2), 139-147.
181. Berlman, I., *Handbook of florescence spectra of aromatic molecules*. Elsevier: 2012.
182. Huang, Y.; Xing, J.; Gong, Q.; Chen, L.-C.; Liu, G.; Yao, C.; Wang, Z.; Zhang, H.-L.; Chen, Z.; Zhang, Q., Reducing aggregation caused quenching effect through co-assembly of PAH chromophores and molecular barriers. *Nat. Commun.* **2019,** *10* (1), 1-9.

183. Al Ani, K. E.; Ramadhan, A. E.; Khanfar, S., Study the Influence of UV-Irradiation on the Photo Stability of Pure and Plasticized Poly (4-Vinyl Biphenyl) in Solid Films. *MSA* **2017,** *8* (13), 1027.
184. Eftink, M.; Ghiron, C., Fluorescence quenching of indole and model micelle systems. *Phys. Chem.* **1976,** *80* (5), 486-493.
185. Trung, T. K.; Ramsahye, N. A.; Trens, P.; Tanchoux, N.; Serre, C.; Fajula, F.; Férey, G., Adsorption of C5–C9 hydrocarbons in microporous MOFs MIL-100 (Cr) and MIL-101 (Cr): A manometric study. *MICROPOR MESOPOR MAT* **2010,** *134* (1-3), 134-140.
186. Tian, T.; Wharmby, M. T.; Parra, J. B.; Ania, C. O.; Fairen-Jimenez, D., Role of crystal size on swing-effect and adsorption induced structure transition of ZIF-8. *Dalton Trans.* **2016,** *45* (16), 6893-6900.
187. Coudert, F. X., Molecular Mechanism of Swing Effect in Zeolitic Imidazolate Framework ZIF-8: Continuous Deformation upon Adsorption. *Chemphyschem* **2017,** *18* (19), 2732-2738.
188. Zheng, B.; Fu, F.; Wang, L. L.; Yang, L.; Zhu, Y.; Du, H., Investigation of the linker swing motion in the zeolitic imidazolate framework ZIF-90. *Phys. Chem. C* **2018,** *122* (13), 7203-7209.
189. Casco, M. E.; Cheng, Y.; Daemen, L. L.; Fairen-Jimenez, D.; Ramos-Fernández, E. V.; Ramírez-Cuesta, A. J.; Silvestre-Albero, J., Gate-opening effect in ZIF-8: the first experimental proof using inelastic neutron scattering. *ChemComm* **2016,** *52* (18), 3639-3642.
190. Adams, F.; Aime, S.; Andersson, L. A.; Ando, I.; Andrenyak, D. M.; Andrews, D. L.; Andrews, L.; Anthony, S. R.; Appleton, T. G.; Arroyo, C. M., Encyclopedia of Spectroscopy and Spectrometry. **2010**.
191. Hermanson, G. T., *Bioconjugate techniques*. Academic press: 2013.
192. Beyer, S.; Schürmann, R.; Feldmann, I.; Blocki, A.; Bald, I.; Schneider, R. J.; Emmerling, F., Maintaining stable zeolitic imidazolate framework (ZIF) templates during polyelectrolyte multilayer coating. *Colloid Interfac. Sci.* **2018,** *22*, 14-17.
193. Hermanson, B. T., ISBN: 978-0-12-370501-3. *Bioconjugate Techniques* **2008**.
194. Wang, T.-T.; Guo, K.; Hu, X.-M.; Liang, J.; Li, X.-D.; Zhang, Z.-F.; Xie, J., Label-free colorimetric detection of urine glucose based on color fading using smartphone ambient-light sensor. *Chemosensors* **2020,** *8* (1), 10.
195. Cox, K. L.; Devanarayan, V.; Kriauciunas, A.; Manetta, J.; Montrose, C.; Sittampalam, S., Immunoassay methods. In *Assay Guidance Manual [Internet]*, Eli Lilly & Company and the National Center for Advancing Translational Sciences: 2014.
196. Hofmann, C.; Duerkop, A.; Baeumner, A. J., Nanocontainers for analytical applications. *Angew. Chem. Int. Ed.* **2019,** *58* (37), 12840-12860.
197. Trau, D.; Yang, W.; Seydack, M.; Caruso, F.; Yu, N.-T.; Renneberg, R., Nanoencapsulated microcrystalline particles for superamplified biochemical assays. *Anal. Chem* **2002,** *74* (21), 5480-5486.
198. Carrell, C.; Kava, A.; Nguyen, M.; Menger, R.; Munshi, Z.; Call, Z.; Nussbaum, M.; Henry, C., Beyond the lateral flow assay: A review of paper-based microfluidics. *Microelectron. Eng.* **2019,** *206*, 45-54.